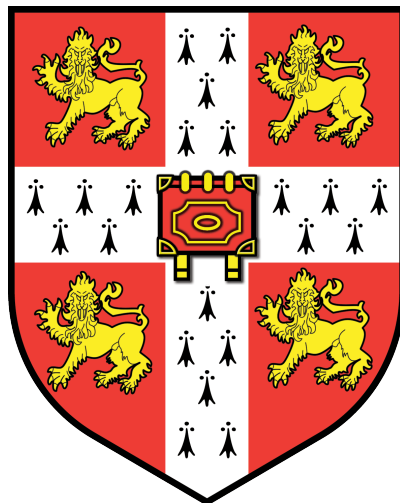


The acoustics of sheared viscous flow over impedance linings

Doran Khamis
Darwin College

A thesis presented for the degree of
Doctor of Philosophy



Department of Applied Mathematics and Theoretical Physics
University of Cambridge
September 2016

Copyright © 2016 Doran Khamis.

Permission granted to reproduce for personal and educational use only

The acoustics of sheared viscous flow over impedance linings

Doran Khamis

This thesis considers the propagation and stability of acoustic perturbations to the steady flow of a perfect gas through a cylindrical duct in the presence of shear and viscosity. Acoustic boundary conditions that account for the physics of both the boundary layer and the lined duct wall are derived and evaluated.

For an inviscid fluid, existing asymptotic results are extended to greatly improve the accuracy of acoustic mode prediction for thin boundary layers, while retaining the regularisation of previous boundary models. A non-asymptotic approach is proposed that performs well for thicker boundary layers and shorter wavelength sound.

Viscothermal effects on the acoustics above an impedance wall, often neglected in aeroacoustic computations, are investigated numerically. It is found that viscosity can be as important as shear, and therefore including shear while neglecting viscothermal effects is questionable. The damping rate of upstream propagating waves is found to be under-predicted by the inviscid theory. The effects of viscosity on stability are also found to be important. It is shown that a viscous flow over an impedance lining supports a greater number of surface wave modes than an inviscid flow.

By assuming a thin boundary layer, asymptotic analysis in both an unrestricted and a high-frequency regime lead to different boundary layer governing equations for the acoustics. The equations for the the first regime must be solved numerically, while the high-frequency limit yields analytical solutions. A closed-form effective impedance boundary condition is derived, suitable for application in frequency-domain numerical simulations, and is shown by comparison with numerical solutions to be highly accurate.

An asymptotic two-deck model for the boundary layer is proposed, using a novel thickness–Reynolds number scaling to allow analytical solution. A closed-form effective impedance boundary condition is derived for an unrestricted frequency. The viscous boundary condition correctly predicts the attenuation of cut-on modes and the position of surface modes, unlike existing inviscid boundary conditions. The temporal stability of the two-deck model is found to be well behaved, allowing a time-domain formulation to be proposed.

Finally, the attenuation predictions for various boundary models are investigated by calculating the reflection coefficients for a plane wave incident on a flat impedance surface. The classical Ingard–Myers boundary condition is shown to incorrectly predict the damping rate of sound in many cases, while it is found once more that viscosity greatly affects the attenuation of upstream propagating sound.

Dedication

To my whole family, near and far

Declaration and Acknowledgements

This dissertation is the result of my own work and includes nothing which is the outcome of work done in collaboration except where specifically indicated in the text. The analysis of chapter 2 has been published (Khamis & Brambley, 2016*a*), and chapters 3–5 have been submitted for publication (Khamis & Brambley, 2016*b,c*). Parts of chapters 3–5 have also been presented at international conferences (Khamis & Brambley, 2015, 2016*d*).

I would like to thank my supervisor, Dr. E. J. Brambley, for his guidance, patience and good humour. I would also like to express my gratitude to Dr. L. J. Ayton for all of our fruitful discussions—and for the fruitless. Thanks must also go to Mr. R. Suliman, who suffered through the sharing of my office in spirit, if luckily rarely in body. Finally, I am indebted to several important people who listened to me consistently throughout my PhD when my confidence wavered, so thank you to those family members and friends who endured, indulged or ignored me.

This work was supported by an EPSRC grant. I would like to thank Darwin College for funding part of my expenses for attending the AIAA/CEAS aeroacoustics conferences in Dallas, TX in May 2015, and in Lyon, France in May 2016.

Contents

1	Introduction	1
1.1	Mathematical preliminaries	5
1.1.1	Thermodynamics and the equations of fluid motion	6
1.1.2	Nondimensionalisation, scaling and linearisation	7
1.2	Introduction to duct acoustics and impedance boundary conditions	9
1.2.1	Solutions in a duct with uniform, inviscid flow	10
1.2.2	Dispersion relations	12
1.2.3	Effective impedance boundary conditions	13
2	Acoustic boundary conditions at an impedance lining in inviscid shear flow	15
2.1	Governing equations	16
2.1.1	The uniform solution	16
2.1.2	An impedance governing equation	17
2.2	Deriving the asymptotic solution	18
2.3	The Runge–Kutta solutions	20
2.3.1	The explicit scheme	21
2.3.2	A single-step implicit scheme	22
2.4	Accuracy of Z_{eff} models	23
2.5	Simplified forms and limiting cases	25
2.5.1	Linear boundary profile	26
2.5.2	Surface modes	26
2.6	Wavenumber spectrum and stability	27
2.6.1	The unstable hydrodynamic mode	30
2.7	Summary	31
	Appendices	32
2.A	Details of the asymptotics of the \tilde{p} and \tilde{v} governing equations	32
2.B	Asymptotics of the impedance governing equation	34
2.C	Surface mode asymptotics of I_j integrals	36
2.D	The implicit scheme	37
3	A numerical study of the effects of shear and viscosity on sound attenuation and flow stability	39
3.1	Governing equations	39
3.1.1	Steady base flow	39
3.1.2	The linearised Navier–Stokes equations	40
3.2	Numerical method	41
3.3	Comparisons of viscous and shear effects	42
3.3.1	Impedance errors	44
3.3.2	Accuracy of modes in the k -plane	47
3.3.3	Surface waves	48
3.3.4	Stability	49
3.4	Summary	50
	Appendices	51
3.A	Details of numerical method	51
3.A.1	Regularity at $r = 0$	51
3.A.2	Mode finding	53
3.A.3	Numerical convergence	54

4	Asymptotic analysis of viscous effects on the acoustics and stability of a shear layer over an impedance wall	55
4.1	Asymptotic analysis	55
4.1.1	Boundary layer asymptotics	56
4.1.2	High frequency asymptotics	57
4.2	Comparison of asymptotic and numerical results	60
4.2.1	k -plane modes	60
4.2.2	ω -plane modes	62
4.2.3	Accuracy of high frequency asymptotics at lower frequencies	63
4.2.4	The ratio Z_{eff}/Z	66
4.3	Summary	69
	Appendices	69
4.A	Numerical boundary conditions and extrapolating to infinity	69
4.B	Solving the high frequency boundary layer equations	71
4.B.1	Matching the high frequency solutions to the outer flow	75
4.B.2	The effective impedance	76
4.C	Alternate high frequency asymptotics: two small parameters	77
5	Analytic solutions for the acoustics in a two-deck viscothermal boundary layer	87
5.1	Governing equations	87
5.2	Main boundary layer solution	88
5.2.1	Matching the main boundary layer solution to the outer flow	90
5.2.2	Behaviour of the main boundary layer solutions near the boundary	91
5.3	Viscous sublayer solution	92
5.3.1	Matching with the main boundary layer solution	93
5.4	Results for the mode shapes	94
5.4.1	Composite solutions	94
5.5	The effective impedance	97
5.5.1	Forming the effective impedance	98
5.6	Results	100
5.6.1	Wavenumber spectra	101
5.6.2	Temporal stability	102
5.7	Suggestion of a time-domain formulation	104
5.8	Summary	106
	Appendices	107
5.A	Determining the sublayer scaling	107
5.B	Solving inside the sublayer	107
5.C	Details of the viscous sublayer–main boundary layer matching	110
6	A study of the attenuation properties of various boundary models via plane wave reflection coefficients	113
6.1	Mathematical formulation	113
6.1.1	Asymptotic reflection coefficients	114
6.1.2	Computational method	116
6.2	Results	119
6.2.1	Two dimensions	120
6.2.2	Three dimensions	120
6.3	Summary	126
7	Conclusion	127
7.1	Further work	134

Chapter 1

Introduction

The propagation of sound is greatly affected by the mean motions of its medium. When a sound wave travels from a region R_1 with mean velocity U_1 to a region R_2 with mean velocity U_2 , refractive and reflective events occur (Ribner, 1957). The vortex sheet interface between the two velocities acts like a permeable wall with a finite acoustic impedance Z . Acoustic information may be passed between the two regions of uniform flow (where the governing equations simplify) via the impedance relation $p = Zv$, where p is the acoustic pressure and v the acoustic velocity normal the interface. The interface between the two fluid layers is susceptible to the Kelvin–Helmholtz instability, the characteristic rolls and billows of which are commonly seen, visualised by clouds, in atmospheric fluid flows. For a vortex sheet interface, the growth rate of the instability is exponential and unbounded with wavenumber.

If the two velocities U_1 and U_2 are separated by a finite region of shear, the non-uniformity of the flow leads to more complicated acoustic behaviour, and closed-form solutions for the acoustics can not be so easily written down. For the particular case $U_2 = 0$, for instance when the region R_2 is a solid object upon the surface of which no slip holds, the shear layer between the two regions is commonly called a boundary layer. Just as the (vortex sheet) interface between two uniform flows can be thought of as having an acoustic impedance, the boundary layer between a uniform flow and a solid wall has its own impedance (Brand & Nagel, 1982) which governs how sound is reflected by and transmitted through it. The solid object R_2 may also have an impedance, for instance if it is an acoustically lined wall. For sound propagating in region R_1 , the joint effects of the boundary layer and wall act as a boundary condition on the acoustic waves. An effective impedance of the boundary layer–wall system may be constructed. If the wall itself does not have a finite impedance (it is acoustically “hard”), the non-uniformity of the boundary layer can still impart a finite effective impedance to the boundary layer–wall system (Nayfeh *et al.*, 1975), and thus the propagating sound behaves as if it sees an acoustically “soft” surface. This thesis investigates how the inclusion of shear and viscosity in the boundary layer above an impedance wall affect the propagation, attenuation and stability of ducted sound, and how the physics of the boundary layer–wall system can be combined into an acoustic boundary condition.

Wave propagation in a steady flow over an acoustically lined wall has been widely studied due to its applications to noise damping in acoustically lined aeroengines (such as that shown in fig. 1.1). With large increases in air traffic projected, and European government targets to reduce aircraft noise by 50% by 2020 compared to 2000 (ACARE, 2001), understanding and reducing overall aircraft noise has become increasingly important. The total sound output from early turbofan engines was dominated by jet noise, and much work over the past half a century has focused on combating jet noise. As a result, the modern-day turbofan engine has an effective perceived noise

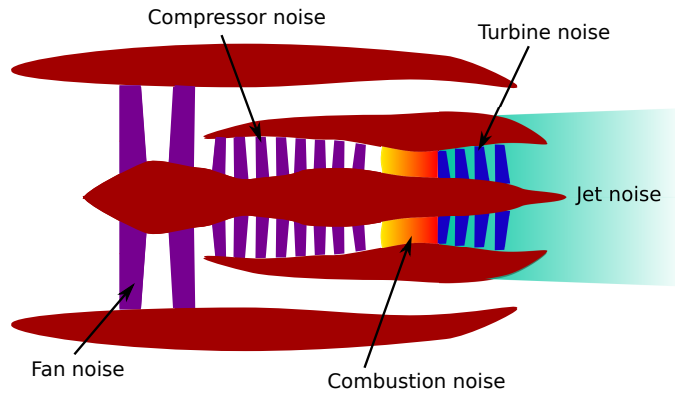


Figure 1.1. Schematic of a typical turbofan engine, displaying the main sources of noise. In this thesis we are concerned mainly with the inlet region before the fan, and the bypass duct after the fan, which surrounds the combustion engine. Taken from Ayton (2014).

level that is spread more evenly between four sources (see fig. 1.2): the fan and compressor in the forward arc; the turbine and combustor; the fan in the rearward arc; and the jet (with the fan now being the most important noise source, Peake & Parry, 2012). Acoustic liners may be used in the cold streams at both the inlet and bypass outlet, and also (less commonly) in the hot stream at the exhaust, and hence may be utilised to directly treat noise from two of these sources, in the forward and rearward arcs. Thus, understanding the effect that acoustic liners have on sound propagating upstream from the compressor and fan, and downstream from the fan, is vital if the 2020 targets are to be met, and is the problem that forms the basis of this thesis.

Early work on wave propagation in a steady flow over an acoustically lined wall considered a uniform inviscid slipping mean flow with fluctuating inviscid acoustic perturbations. This allows analytic solution in terms of trigonometric functions in Cartesian ducts, and Bessel functions in cylindrical or annular ducts. The lined wall was usually modelled by matching normal particle displacement in the fluid to the normal displacement of the wall, now termed the Myers (1980), or Ingard–Myers (Ingard, 1959) boundary condition, although some authors chose to match normal velocity instead (Doak & Vaidya, 1970; Ko, 1971; Rice, 1969). The effect of mean flow shear on the acoustic perturbations has also been studied (e.g. Ko, 1972; Mungur & Gladwell, 1969; Pridmore-Brown, 1958; Tack & Lambert, 1965), usually by Fourier transforming the linearised Euler equations leading to the Pridmore-Brown (1958) equation, which must in general be solved numerically. For a non-slipping inviscid mean flow, it was found independently by Eversman & Beckemeyer (1972) and Tester (1973) that, in the limit of a vanishingly thin inviscid shear layer, continuity of normal displacement is recovered at the lined wall. This proved that the Myers boundary condition was the correct boundary condition for an infinitely thin inviscid slipping flow over a lined wall, and put an end to the confusion surrounding whether displacement or velocity should be matched at the boundary. However, Gabard (2013) showed that, for parameters representative of aeroengines, the Myers boundary condition in some cases over-predicted sound attenuation by over 10dB when compared with the linearised Euler equations, showing that the limit of a vanishingly thin shear layer can be a poor assumption in practice (as was also suggested by Eversman, 1973). A detailed parametric study of the effects of the inviscid mean flow boundary layer on sound propagation was recently performed by Gabard (2016).

The importance of including a finite-thickness shear layer rather than assuming a uniform slipping flow also manifests in the different convective and absolute stability of the two models. Experimental evidence of an instability in flow over an impedance lining has been reported many times (e.g. Aurégan & Leroux, 2008; Marx *et al.*, 2010). Theoretical predictions of the instability

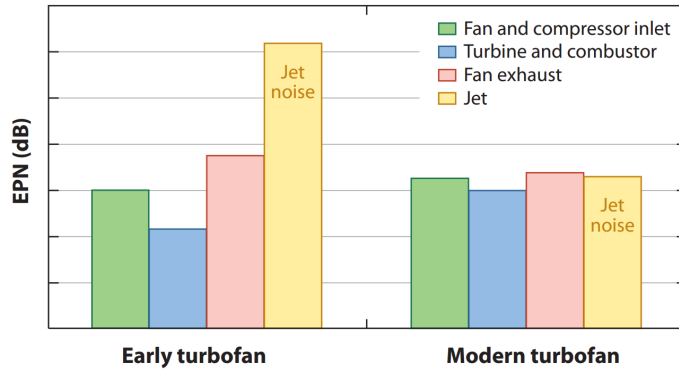


Figure 1.2. Effective perceived noise (EPN) from sound sources in early and modern turbofan engines, taken from Peake & Parry (2012).

that utilise the Myers model found that in the time domain a numerical instability would grow at the grid scale and swamp any meaningful signal, while in the frequency domain an unstable mode was found with a growth rate unbounded with increasing wavenumber. This was due to the ill-posedness of the problem of uniform slipping flow over an impedance lining (Brambley, 2009). The ill-posedness is regularised by considering a non-slipping inviscid mean flow with a finite region of shear (rather than a vortex sheet), and more recent works have sought to modify the Myers boundary condition to account for this thin shear layer (Brambley, 2011*b*; Joubert, 2010; Myers & Chuang, 1984; Rienstra & Darau, 2011). The boundary conditions resulting from these studies are well-posed, and in particular that of Brambley (2011*b*) both matches well with solutions to the linearised Euler equations (Gabard, 2013) and allows for the spatial and temporal stability of inviscid shear flow over a lined wall to be investigated (Brambley, 2013) via rigorous Briggs–Bers (Bers, 1983; Briggs, 1964) analysis (which requires any convectively or absolutely unstable modes to have bounded growth rates; see the appendix of Brambley, 2009). This work is continued here in chapter 2 and has been recently published (Khamis & Brambley, 2016*a*).

The accuracy of the current inviscid models was investigated by Gabard (2013) by considering reflection of acoustic plane waves from an impedance lining in shear flow. It was found that use of the Myers condition can lead to significant errors (of up to 14dB) in predictions of sound attenuation due to the great impact of the boundary layer thickness. Modelling the physics inside the boundary layer more precisely, for instance by expanding to second-order in the boundary layer thickness as is done in chapter 2, should therefore lead to more accurate predictions of the absorption and reflection coefficients for an acoustic liner in flow. The accuracy of current boundary conditions and newly derived conditions are tested in a different way in chapter 2: by comparing with the exact effective impedance found by numerical solution of the Pridmore-Brown equation; and by comparing the prediction of cut-on and cut-off acoustic modes.

Inviscid flow over acoustic liners also supports surface waves – vibrations of the liner and boundary layer – that are not present in the hard-wall case. These waves were classified as surface modes by Rienstra (2003), who used uniform flow and the Myers (or Ingard–Myers) model of the impedance lining to find a possible four surface modes per frequency and circumferential order. This work was extended by Brambley (2013), who accounted for the thin-but-nonzero thickness boundary layer by using the first-order correction terms to the Myers condition (Brambley, 2011*b*) and found the number of possible surface waves increased to six. Because acoustic liners can support surface modes where a hard wall can not, their use could lead to an amplification of noise as well as a reduction due to the possibility of an instability being triggered. Theoretical identification of these unstable modes is therefore of utmost importance. Chapter 2 extends the asymptotics of

Brambley (2011*b*) by solving the inviscid equations to second-order in the boundary layer thickness in order to further investigate surface wave solutions of the Pridmore-Brown equation.

It has been suggested that to accurately correlate theoretical predictions with experimental observations, viscous effects need to be taken into account (Burak *et al.*, 2008, 2009; Renou & Aurégan, 2010, 2011). When Boyer *et al.* (2011) numerically solved the inviscid Euler equations to attempt to identify theoretically an experimentally observed hydrodynamic instability in flow over a lining (Marx *et al.*, 2010), they found they could not predict the growth rate of the unstable mode, whereas the real part of the wavenumber was reasonably well predicted; Boyer *et al.* (2011) did not consider viscous effects, presumably as the Reynolds number of the experiments Marx *et al.* (2010) ($\text{Re} \sim 2.5 \times 10^5$ by the definition in this paper) was considered high enough for viscosity to be negligible, and instead three dimensional and non-parallel flow effects were blamed for the discrepancy. However, Marx & Aurégan (2013) did include viscosity, and found that the unstable surface wave mode found in the experimental study (Marx *et al.*, 2010) is very sensitive to viscosity. In chapter 3 a numerical study of the effects of viscosity on the propagation and stability of acoustic modes is undertaken by solving the linearised compressible Navier–Stokes equations in 1D. The importance of viscosity is quantified by comparing with the corresponding effects of shear by also solving the linearised Euler equations in both shear and uniform flow.

A number of studies have considered the effect of viscous dissipation on sound propagation in shear flow over an impedance lining. Nayfeh (1973) considered the case where the acoustic boundary layer is thin compared with the mean flow boundary layer, expanding to first order in the acoustic boundary layer thickness. Aurégan *et al.* (2001) considered an arbitrary ratio of mean to acoustic boundary layer thickness under the assumption that both were small, but also assumed a low Mach number flow, expanding to first order in the Mach number. They found an effective boundary condition that shifted between continuity of normal displacement and continuity of mass flux across the boundary layer, depending on the ratio of the mean flow and acoustic boundary layer thicknesses. Brambley (2011*a*) extended this work to relax the assumption of low Mach number, with the only remaining assumption being that the boundary layer was thin. High frequency asymptotics of the viscous boundary layer model led to a recovery of the Myers boundary condition to leading order (conservation of normal displacement), while low frequency asymptotics led to conservation of mass flux at leading order, both in agreement with Aurégan *et al.* (2001) (since the acoustic boundary layer thickness scales as $1/\sqrt{\omega}$ for frequency ω). The model of Brambley (2011*a*) was effectively a viscous Myers condition, since it considered viscothermal shear flow in the limit of a vanishingly thin boundary layer thickness. Importantly, the viscous Myers condition does not by itself regularise the ill-posedness of the inviscid Myers boundary condition. Brambley found no closed-form solution for the acoustics in the viscous Myers model, however. The studies by Dokumaci (2014) and Mikhail & El-Tantawy (1994) find analytical solutions for viscous acoustics by making several limiting simplifications. Mikhail & El-Tantawy (1994) considered a hard-walled duct with no mean flow, and assumed the viscous fluid to be non-heat conducting. Dokumaci (2014) assumed a uniform mean flow (invoking the Myers condition at the wall) and appears to neglect viscous dissipation from the acoustic energy equation. Owing to the relatively low Reynolds number $\text{Re} \approx 10^3$ they considered, Mikhail & El-Tantawy (1994) found viscous effects to be felt far outside the acoustic boundary layer, so that their solutions in the core of the duct could not be considered inviscid; in aeroacoustic situations where $\text{Re} \gtrsim 10^5$ are typical, the acoustic mode shapes in the core of the duct have generally converged to the inviscid case (Khamis & Brambley, 2015). In chapter 4 the asymptotics of Brambley (2011*a*) are extended to include the effects of a finite thickness shear layer. A different asymptotic analysis in the high frequency limit is also undertaken, in the pursuit of a closed-form acoustic boundary condition that incorporates

both shear and viscosity.

The analysis of surface waves in the literature to date has been entirely inviscid. It is known that viscosity has the greatest effect very close to a boundary where surface waves exist, and it is therefore likely that viscosity is important for the accurate prediction of both the number and position of surface wave modes. Chapters 3 and 4 study the effect of viscosity on the number and stability of surface wave modes.

Without either making limiting simplifications or taking specific asymptotic limits, there is no known closed-form solutions for the acoustics in a finite-thickness sheared, viscous boundary layer. Reports of boundary layer thicknesses and Reynolds numbers in experimental studies (Marx *et al.*, 2010; Renou & Aurégan, 2011) suggest that the boundary layer momentum thickness is $\delta_m \approx 0.05\text{m}$ in an aeroengine intake 2m in diameter at $\text{Re}_c \approx 2 \times 10^7$ (defined by the centreline speed of sound) or $\text{Re}_u \approx 7 \times 10^6$ (defined by the free stream fluid velocity), so that the boundary layer is thicker than would be predicted assuming a laminar Blasius boundary layer, $\delta \sim 1/\text{Re}^{1/2}$. This could be, for example, due to a turbulent boundary layer where the eddy viscosity (which governs the mean flow) is larger than the molecular viscosity (which is assumed here to govern viscous dissipation for acoustics). Chapter 5 seeks to exploit this difference in viscous lengthscales in order to derive analytical solutions for the acoustics via matched asymptotic expansions in three scaling regions (an outer region and two boundary layer “decks”) that cover an entire cylindrical, acoustically lined duct.

In chapter 6 the work of Gabard (2013) is extended to account for viscothermal effects. A numerical method is proposed for computing the reflection coefficient of a plane wave incident on sheared, viscous boundary layer above an acoustic liner. Comparison is made with the inviscid system, and with the predictions of the ill-posed Myers boundary condition. The numerical method is used to measure the accuracy of analytical expressions for the reflection coefficient that are derived from the new viscous effective impedance boundary conditions proposed in chapters 4 and 5.

Acoustic liners are commonly manufactured using a perforated facing sheet, which is therefore inhomogeneous on the small scale of the distance between perforations. The mean flow above such liners could also be expected to be inhomogeneous at the same small scale. A common simplification in the literature is to average over this small scale and thereby model the liner as a homogeneous boundary, which has been shown to give reasonable accuracy in practice (e.g. Boyer *et al.*, 2011). However, for this assumption to be valid, the acoustic wavelengths and boundary layers considered must lie within limits defined by the hole diameters and spacings of the perforated facing sheet (Dai & Aurégan, 2016). Recent numerical and experimental work on liners in grazing flow has found that small-scale inhomogeneities of the liner may lead to liner self-noise and increased drag when compared with a boundary layer over a flat plate (Tam *et al.*, 2014; Zhang & Bodony, 2016), and shown that nonlinear effects may be important in accurately modelling the liner response (Zhang & Bodony, 2012). In the following chapters we forego the complications of inhomogeneities, while nonlinearity with respect to the interaction between sound field, shear flow and liner is also beyond the scope of this thesis. Furthermore, we neglect any slow axial variation of the mean flow.

1.1 Mathematical preliminaries

Throughout this work we will be concerned with the motion of a fluid acting as a medium for acoustic waves, and the dynamics of these acoustic waves. The subsequent chapters all call upon a few fundamental ideas that we lay out here, to be referred back to when necessary.

1.1.1 Thermodynamics and the equations of fluid motion

We follow the common assumption in aeroacoustic literature that air may be adequately modelled as a perfect gas. Thus, we take the specific heats c_p^* and c_v^* , at constant pressure and volume respectively, to be constants satisfying

$$c_p^* - c_v^* = R_{\text{specific}}^*, \quad (1.1.1)$$

where R_{specific}^* is the specific gas constant and a starred quantity is dimensional. Then, defining $\gamma = c_p^*/c_v^*$ as the ratio of specific heats – and assuming $\gamma = 7/5$ – we may write (1.1.1) as

$$\frac{\gamma - 1}{\gamma} = \frac{1}{c_p^*} R_{\text{specific}}^*. \quad (1.1.2)$$

A perfect gas obeys the ideal gas law

$$p^* V^* = m^* R_{\text{specific}}^* T^*, \quad (1.1.3)$$

where m^* is the mass of gas contained within a volume V^* , and p^* and T^* are the pressure and temperature of the gas. The gas density $\rho^* = m^*/V^*$ may be defined, and used in conjunction with (1.1.2) to rewrite (1.1.3) as

$$\frac{\gamma}{\gamma - 1} p^* = c_p^* \rho^* T^*. \quad (1.1.4)$$

This is our dimensional equation of state, relating the pressure, density and temperature of the gas. We note here that the speed of sound in an ideal gas takes the form $c^{*2} = \gamma p^*/\rho^*$.

To capture the thermodynamics of the fluid, we must enforce conservation of energy. There are many ways to write down a consistent energy equation, in terms of the internal energy, enthalpy or entropy; here we choose to relate the convected change in entropy s^* to the corresponding changes in temperature and pressure, and then subsequently relate these changes to the dissipation of heat by thermal conduction and viscous losses (Landau & Lifshitz, 1987; Pierce, 1994):

$$\rho^* T^* \frac{Ds^*}{Dt^*} = \rho^* c_p^* \frac{DT^*}{Dt^*} - \frac{Dp^*}{Dt^*} = \nabla^* \cdot (\kappa^* \nabla^* T^*) + \sigma_{ij}^* \frac{\partial u_i^*}{\partial x_j^*}, \quad (1.1.5)$$

where $D/Dt^* = \partial/\partial t^* + \mathbf{u}^* \cdot \nabla^*$ is the material derivative; $\mathbf{u}^* = (u^*, v^*, w^*)$ is the fluid velocity vector; and

$$\sigma_{ij}^* = 2\mu^* \left(\frac{\partial u_i^*}{\partial x_j^*} + \frac{\partial u_j^*}{\partial x_i^*} \right) + \mu^{S^*} \nabla^* \cdot \mathbf{u}^* \delta_{ij} \quad (1.1.6)$$

is the Newtonian viscous stress tensor. Here, κ^* is the thermal conductivity, μ^* the shear viscosity, and $\mu^{S^*} = \mu^{B^*} - 2\mu^*/3$ the second viscosity (Tritton, 1988), with μ^{B^*} the bulk viscosity. An important simplification of (1.1.5) occurs in the inviscid limit, in which the specific entropy remains constant for any given fluid particle (Pierce, 1994). Then,

$$\frac{Ds^*}{Dt^*} = 0 \quad \implies \quad \frac{Dp^*}{Dt^*} = c^{*2} \frac{D\rho^*}{Dt^*}, \quad (1.1.7)$$

where we have rewritten the nonzero terms of (1.1.5) in terms of just the density and the pressure. The form (1.1.7) will be used in chapter 2.

The fundamental statements of conservation of mass and momentum for a compressible fluid

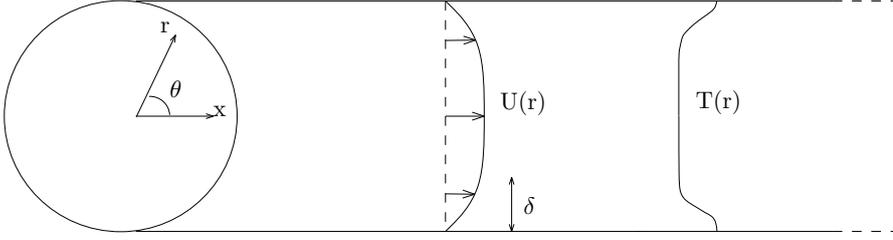


Figure 1.3. Schematic of parallel mean flow in a cylindrical duct with a radially-varying mean temperature.

give us our remaining governing equations as (Landau & Lifshitz, 1987; Stewart, 1942),

$$\frac{\partial \rho^*}{\partial t^*} + \nabla^* \cdot (\rho \mathbf{u}^*) = 0, \quad (1.1.8a)$$

$$\rho^* \frac{D\mathbf{u}^*}{Dt^*} = -\nabla^* p^* + \nabla^* \cdot \sigma^*. \quad (1.1.8b)$$

Along with the statement of conservation of energy and the equation of state, the motion of a fluid may be completely described by the above equations.

1.1.2 Nondimensionalisation, scaling and linearisation

Throughout this work we will treat acoustic waves as linear perturbations to a background flow. This may be justified by comparing the pressure levels we think of as “sound” with ambient atmospheric pressure: normal conversation takes place at $\sim 10^{-2}$ Pa; the pressure disturbance 1m from a jet engine is $\sim 10^2$ Pa; the ambient atmospheric pressure is $\sim 10^5$ Pa. Thus, while a jet engine creates perturbations ten thousand times larger than those we make with our vocal chords, the ambient pressure is a thousand times greater still. This is not to say that nonlinear effects are never important, but we forego their consideration here. We define our mean flow (about which we later linearise) in a cylindrical coordinate system $\mathbf{r}^* = (x^*, r^*, \theta)$ – within which a general velocity vector would be defined $\mathbf{u}^* = (u^*, v^*, w^*)$ – such that our analysis is tuned to the particular geometry of an aeroengine duct. We define an axial, parallel, non-slipping and non-swirling mean flow $\mathbf{U}^* = (U^*(r^*), 0, 0)$, with $U^*(0) = U_0^*$ (the subscript zero denotes a value at the duct centreline $r^* = 0$). Then, the mean pressure is taken as constant across the duct cross-section, $p^*(r^*) \equiv p_0^*$ —this is exact for inviscid flows due to the assumption that streamlines are everywhere parallel, and is a useful approximation in the viscous case (see §3.1.1). The mean temperature and density are allowed to vary only radially, and are related by the equation of state, (1.1.4). Again, we define $T^*(0) = T_0^*$ and $\rho^*(0) = \rho_0^*$ as the reference centreline values. A schematic of the coordinate system and the mean flow is shown in fig. 1.3.

There are natural choices for the length and velocity scales in our problem: the duct radius l^* and the centreline sound speed $c_0^* = \sqrt{\gamma p_0^*/\rho_0^*}$. Time is made dimensionless by combining the length and velocity scales, $t^* = l^*t/c_0^*$. We scale the state variables as follows:

$$p^* = c_0^{*2} \rho_0^* p, \quad \rho^* = \rho_0^* \rho, \quad T^* = \frac{c_0^{*2}}{c_p^*} T, \quad (1.1.9)$$

Coefficients of viscosity (shear and bulk) are scaled by $c_0^* l^* \rho_0^*$, and thermal conductivity by $c_0^* l^* \rho_0^* c_p^*$. The impedance of the acoustic lining is nondimensionalised by $Z^* = \rho_0^* c_0^* Z$. In such a scheme, the dimensionless centreline mean flow density, temperature, pressure and axial velocity take the values $\rho_0 = 1$, $T_0 = 1/(\gamma - 1)$, $p_0 = 1/\gamma$, and $U_0 = M$, respectively, where M is the centreline Mach number. The cylindrical duct has a dimensionless radius of unity.

Using the above scheme, we may rewrite the governing equations (1.1.4), (1.1.5), (1.1.8a) and (1.1.8b) in dimensionless form:

$$\frac{D\rho}{Dt} = -\rho\nabla \cdot \mathbf{u}, \quad (1.1.10a)$$

$$\rho \frac{D\mathbf{u}}{Dt} = -\nabla p + \nabla \cdot \sigma, \quad (1.1.10b)$$

$$\rho \frac{DT}{Dt} - \frac{Dp}{Dt} = \nabla \cdot (\kappa \nabla T) + \sigma_{ij} \frac{\partial u_i}{\partial x_j}, \quad (1.1.10c)$$

$$T = \frac{\gamma}{\gamma - 1} \frac{p}{\rho}. \quad (1.1.10d)$$

This set of governing equations forms the basis of most of the analysis performed in this work. Due to the fact that $p(r) \equiv p_0$, (1.1.10d) tells us that the mean temperature and density profiles are related by $(\gamma - 1)T(r) = 1/\rho(r)$; we will use both interchangeably in later chapters.

Small, unsteady acoustic perturbations are added to the mean flow in the form

$$Q_{\text{tot}}(\mathbf{r}, t) = Q(r) + \epsilon_a q'(\mathbf{r}, t), \quad (1.1.11)$$

where $\epsilon_a \ll 1$ is the acoustic amplitude, and q' is taken to be $\mathcal{O}(1)$. Here, a prime denotes an acoustic perturbation in the time domain. We move to the frequency domain by defining the time-harmonic form $q'(\mathbf{r}, t) = \check{q}(\mathbf{r}) \exp(i\omega t)$, for dimensionless frequency ω (the Helmholtz number). We perform a Fourier transform in the axial coordinate and define a Fourier series in the azimuthal angle, defining the axial and azimuthal wavenumbers (k, m) as the Fourier pairs to the physical variables (x, θ) . Then, we consider a single acoustic mode of the form $\check{q}(\mathbf{r}) = \tilde{q}(r) \exp(-ikx - im\theta)$. Thus, our acoustic perturbations take the modal form

$$q'(\mathbf{r}, t) = \tilde{q}(r) \exp(i\omega t - ikx - im\theta). \quad (1.1.12)$$

Neglecting terms of $\mathcal{O}(\epsilon_a^2)$ or higher – due to our assumption of linear acoustics – the equations (1.1.10) may be linearised to give, with the common exponential factor divided out,

$$\begin{aligned} i\rho(\omega - Uk)\tilde{u} + \rho U_r \tilde{v} &= ik\tilde{p} + \mathcal{V}^u, & i\rho(\omega - Uk)\tilde{v} &= -\tilde{p}_r + \mathcal{V}^v, \\ i\rho(\omega - Uk)\tilde{w} &= \frac{im}{r}\tilde{p} + \mathcal{V}^w, & i\rho(\omega - Uk)\tilde{T} + \rho T_r \tilde{v} &= i(\omega - Uk)\tilde{p} + \mathcal{V}^t, \\ i\rho(\omega - Uk)\gamma\tilde{p} - i\rho^2(\omega - Uk)(\gamma - 1)\tilde{T} - ik\rho\tilde{u} + (\rho\tilde{v})_r + \frac{1}{r}\rho\tilde{v} - \frac{im}{r}\rho\tilde{w} &= 0. \end{aligned} \quad (1.1.13)$$

which we will refer to, as a whole, as the dimensionless linearised compressible Navier–Stokes equations (LNSE). The viscous terms are collected in the \mathcal{V}^j terms, and are defined by

$$\begin{aligned} \mathcal{V}^x &= \frac{1}{\text{Re}} \left\{ (\mathcal{H}\tilde{u}_r + U_r\tilde{\mathcal{H}})_r + \frac{1}{r}(\mathcal{H}\tilde{u}_r + U_r\tilde{\mathcal{H}}) - \frac{m^2}{r^2}\mathcal{H}\tilde{u} - (2 + \beta)k^2\mathcal{H}\tilde{u} \right. \\ &\quad \left. - ik(1 + \beta)(\mathcal{H}\tilde{v})_r + ik\beta\mathcal{H}_r\tilde{v} - \frac{ik}{r}(1 + \beta)\mathcal{H}\tilde{v} - \frac{km}{r}(1 + \beta)\mathcal{H}\tilde{w} \right\} \end{aligned} \quad (1.1.14a)$$

$$\begin{aligned} \mathcal{V}^r &= \frac{1}{\text{Re}} \left\{ (2 + \beta)(\mathcal{H}\tilde{v}_r)_r - \frac{2}{r}\mathcal{H}_r\tilde{v} - \left(k^2 + \frac{m^2}{r^2}\right)\mathcal{H}\tilde{v} + (2 + \beta)\left(\frac{\mathcal{H}\tilde{v}}{r}\right)_r - ik(1 + \beta)(\mathcal{H}\tilde{u})_r \right. \\ &\quad \left. + ik(\mathcal{H}_r\tilde{u} - U_r\tilde{\mathcal{H}}) - im(1 + \beta)\left(\frac{\mathcal{H}\tilde{w}}{r}\right)_r + \frac{im}{r}\mathcal{H}_r\tilde{w} + \frac{2im}{r^2}\mathcal{H}\tilde{w} \right\} \end{aligned} \quad (1.1.14b)$$

Parameter	Value	Parameter	Value
γ	7/5	M	0.1 – 0.5
Pr	0.7	Re	$10^5 - 10^7$
μ_B^*/μ^*	0.6 – 2	β	-1/15 – 4/3

Table 1.1. Typical values of dimensionless parameters used throughout this work.

$$\mathcal{V}^\theta = \frac{1}{\text{Re}} \left\{ -\frac{km}{r}(1+\beta)\mathcal{H}\tilde{u} - \frac{im}{r^2}(3+\beta)\mathcal{H}\tilde{v} - \frac{im}{r}(1+\beta)(\mathcal{H}\tilde{v})_r + \frac{im}{r}\beta\mathcal{H}_r\tilde{v} + (\mathcal{H}\tilde{w}_r)_r \right. \\ \left. + \mathcal{H}\left(\frac{\tilde{w}}{r}\right)_r - \left(k^2 + \frac{m^2}{r^2}\right)\mathcal{H}\tilde{w} - \frac{m^2}{r^2}(1+\beta)\mathcal{H}\tilde{w} - \frac{1}{r}\mathcal{H}_r\tilde{w} \right\} \quad (1.1.14c)$$

$$\mathcal{V}^e = \frac{1}{\text{Re}} \left\{ U_r^2\tilde{\mathcal{H}} + 2\mathcal{H}U_r\tilde{u}_r - 2ik\mathcal{H}U_r\tilde{v} + \frac{1}{\text{Pr}}(\mathcal{H}\tilde{T}_r + T_r\tilde{\mathcal{H}})_r + \frac{1}{r\text{Pr}}(\mathcal{H}\tilde{T}_r + T_r\tilde{\mathcal{H}}) \right. \\ \left. - \frac{1}{\text{Pr}}\left(k^2 + \frac{m^2}{r^2}\right)\mathcal{H}\tilde{T} \right\}. \quad (1.1.14d)$$

In going from (1.1.10) to (1.1.13) and (1.1.14), a number of variables have been introduced or replaced. First, the equation of state (1.1.10d) may be linearised,

$$\tilde{\rho} = \gamma\rho\tilde{p} - (\gamma - 1)\rho^2\tilde{T}, \quad (1.1.15)$$

and subsequently used to eliminate the density perturbation $\tilde{\rho}$. Second, the shorthand $\beta = \mu_0^{B*}/\mu_0^* - 2/3$ has been introduced, where the bulk viscosity fraction $\mu_0^{B*}/\mu_0^* \approx 0.6$ in air (Cramer, 2012; Greenspan, 1959; Pinkerton, 1947). Third, the dimensionless Reynolds and Prandtl numbers have been introduced, which measure the relative strengths of viscous and inertial effects, and viscous and thermal conductive effects, respectively. In terms of dimensional scales, we define the Reynolds number with respect to the centreline sound speed as $\text{Re} = c_0^*l^*\rho_0^*/\mu_0^*$, and the Prandtl number as $\text{Pr} = \mu_0^*c_p^*/\kappa_0^*$. These definitions allow the viscosity and thermal conductivity, assumed to have some dependence on radial position and temperature through the dimensionless $\mathcal{O}(1)$ function $\mathcal{H}(r, T)$, to be expressed in terms of Re and Pr as

$$\mu = \frac{\mathcal{H}}{\text{Re}}, \quad \mu^B = \frac{\mathcal{H}}{\text{Re}} \frac{\mu_0^{B*}}{\mu_0^*}, \quad \kappa = \frac{\mathcal{H}}{\text{Re Pr}}. \quad (1.1.16)$$

Previous studies of viscothermal acoustic propagation have used constant values (Aurégan *et al.*, 2001; Nayfeh, 1973) or a linear temperature dependence (Brambley, 2011a) for the molecular viscosities and thermal conductivity. Radial dependence of the viscosity is important when modelling a turbulent eddy viscosity (Marx & Aurégan, 2013). For now we leave \mathcal{H} as a general function of position and temperature. Typical values of the dimensionless parameters introduced here are given in table 1.1.

1.2 Introduction to duct acoustics and impedance boundary conditions

As discussed above, we use a modal approach to duct acoustics. The set of acoustic modes of the form (1.1.12) define a basis by which a sound field may be represented—though there exist some solutions that may not be described by discrete modes, for instance at the inviscid critical layer

$\omega - U(r_c)k = 0$ (Brambley *et al.*, 2012b). To ascertain the allowable modes in a given system, we must solve for the radial mode shape $\tilde{q}(r)$. Then, applying the relevant boundary conditions to the solution leads to a dispersion relation that links the values of ω and k for a given value of m . Any solution of the dispersion relation $\omega(k, m)$ or $k(\omega, m)$ then defines a single acoustic mode (allowing for double roots, *et cetera*).

1.2.1 Solutions in a duct with uniform, inviscid flow

Commonly, aeroacoustic calculations are performed in the inviscid limit, in which viscous and thermal conductive effects are set to zero. Taking the limit $\text{Re} \rightarrow \infty$ in (1.1.13) we recover the linearised Euler equations (LEE),

$$\begin{aligned} i\rho(\omega - Uk)\tilde{u} + \rho U_r \tilde{v} &= ik\tilde{p}, & i\rho(\omega - Uk)\tilde{v} &= -\tilde{p}_r, \\ i\rho(\omega - Uk)\tilde{w} &= \frac{im}{r}\tilde{p}, & i\rho(\omega - Uk)\tilde{T} + \rho T_r \tilde{v} &= i(\omega - Uk)\tilde{p}, \\ i\rho(\omega - Uk)\gamma\tilde{p} - i\rho^2(\omega - Uk)(\gamma - 1)\tilde{T} - ik\rho\tilde{u} + (\rho\tilde{v})_r + \frac{1}{r}\rho\tilde{v} - \frac{im}{r}\rho\tilde{w} &= 0. \end{aligned} \quad (1.2.1)$$

from which a second-order equation for the acoustic pressure may be derived,

$$\tilde{p}_{rr} + \left(\frac{2U_r k}{\omega - Uk} - \frac{\rho_r}{\rho} + \frac{1}{r} \right) \tilde{p} + \left(\rho(\omega - Uk)^2 - k^2 - \frac{m^2}{r^2} \right) \tilde{p} = 0. \quad (1.2.2)$$

This is a form of the Pridmore-Brown (1958) equation in cylindrical coordinates, and is used abundantly to study acoustics in sheared, inviscid flow (Ko, 1972; Mungur & Gladwell, 1969; Tack & Lambert, 1965). A corresponding equation for the acoustic radial velocity can also be derived (see section 2.1). There is no known closed-form solution to (1.2.2) for a general mean flow.

A simple initial problem to consider is the uniform flow case of (1.2.2), with $(U(r), \rho(r), T(r)) \equiv (U_0, \rho_0, T_0) = (M, 1, 1/(\gamma - 1))$. The mean flow gradients vanish, and the Pridmore-Brown equation reduces to Bessel's equation,

$$\tilde{p}_{rr} + \frac{1}{r}\tilde{p}_r + \left((\omega - Mk)^2 - k^2 - \frac{m^2}{r^2} \right) \tilde{p} = 0. \quad (1.2.3)$$

Equation (1.2.3) has well-known solutions: the cylindrical Bessel functions of the first and second kind. Thus, a general pressure mode may be expressed as a linear superposition of the two Bessel functions,

$$\tilde{p}(r) = EJ_m(\alpha r) + FY_m(\alpha r), \quad \alpha^2 = (\omega - Mk)^2 - k^2, \quad (1.2.4)$$

where the eigenvalue α can be thought of as the radial wavenumber, and E and F are normalisation constants. If we constrain ourselves to cylindrical ducts, the regularity condition at the radial origin requires $F = 0$, since $Y_m(\alpha r)$ is singular at $r = 0$ for all m (for an annular duct, $F \neq 0$ in general). The definition of α in (1.2.4) may also be thought of as an implicit definition of the axial wavenumber k . When k is real the mode is ‘‘cut on’’ and the wave propagates axially along the duct; when k is imaginary the mode is ‘‘cut off’’, and the wave decays exponentially with axial distance travelled. Cut-on modes are generally the most important acoustic modes as their amplitudes are largest, and they are a mechanism of sound propagation away from a source to the far field. The distinction between cut off and cut on becomes blurred when the duct wall is given a finite impedance: all axial wavenumbers are now complex, meaning that no mode propagates axially without attenuating to some degree. We will still use the term cut-on to refer to those

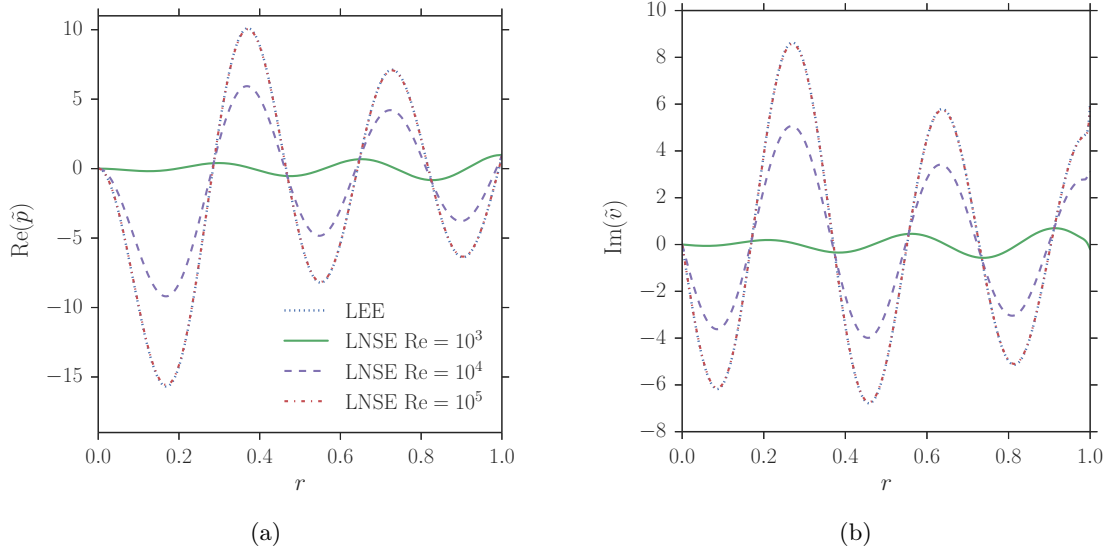


Figure 1.4. Acoustic mode shapes of (a) the pressure, \tilde{p} , and (b) the radial velocity, \tilde{v} , from numerical solutions of the LNSE, (1.1.13), for different values of Re , compared with solutions of the LEE, (1.2.1). For $\text{Re} \gtrsim 10^5$, the inviscid and viscous solutions are very similar outside the boundary layer near $r = 1$. Each solution is normalised by setting the wall-value of the pressure, $\tilde{p}(1) = 1$.

modes that are the *least cut off*.

Using the LEE (1.2.1) we may derive the solutions for all the acoustic quantities corresponding to the pressure (1.2.4) in a cylindrical duct with uniform inviscid flow:

$$\tilde{p}_u = EJ_m(\alpha r), \quad \tilde{v}_u = \frac{iE\alpha J'_m(\alpha r)}{\omega - Mk}, \quad (1.2.5)$$

for the pressure and radial velocity, and

$$\frac{\tilde{u}_u}{k} = \frac{r\tilde{w}_u}{m} = \frac{EJ_m(\alpha r)}{\omega - Mk}, \quad \tilde{\rho}_u = \tilde{T}_u = EJ_m(\alpha r), \quad (1.2.6)$$

for the remaining quantities. These solutions are useful even when considering a flow that is neither uniform nor inviscid: away from the duct wall, the acoustics in a sheared and viscous (yet everywhere parallel) flow are well approximated by the expressions (1.2.5) and (1.2.6), provided the Reynolds number is high enough (Khamis & Brambley, 2015). For the large Reynolds numbers associated with aeroacoustic applications, $10^5 \lesssim \text{Re} \lesssim 10^7$, the effects of shear and viscosity do not extend much past the edge of the boundary layer—that is, wherever the mean flow shear is negligible, the simple solutions (1.2.5) and (1.2.6) are impressively accurate. This is not the case for $\text{Re} \lesssim 10^4$, for which viscous effects alter the behaviour of the solutions in large portions of the duct (Mikhail & El-Tantawy, 1994), as shown in fig. 1.4. Throughout this work we will exploit this feature of high-Reynolds number duct flow; the expressions in (1.2.5) and (1.2.6) will be assumed to hold outside of the mean flow boundary layer, and therefore will be used as outer solutions to which any boundary layer solutions may be asymptotically matched.

When asymptotically matching to an outer solution from an inner region, the behaviour of the outer solution near the inner region must be found (see, for example, Hinch, 1991). In our case, that means determining the behaviour of the outer solutions (1.2.5) near the wall $r = 1$. This may be done by Taylor expanding the Bessel function solutions around $r = 1$ using the substitution $r = 1 - \delta y$ for $\delta \ll 1$:

$$p_u(1 - \delta y) = EJ_m(\alpha) - \delta y \alpha EJ'_m(\alpha) + \mathcal{O}(\delta^2) \quad (1.2.7a)$$

$$v_u(1 - \delta y) = \frac{i\alpha E J'_m(\alpha)}{(\omega - Mk)} + \frac{i\delta y E}{(\omega - Mk)} [\alpha J'_m(\alpha) + (\alpha^2 - m^2) J_m(\alpha)] + \mathcal{O}(\delta^2). \quad (1.2.7b)$$

We can also rewrite (1.2.7) by introducing the constants

$$p_\infty = E J_m(\alpha), \quad v_\infty = \frac{i\alpha E J'_m(\alpha)}{(\omega - Mk)}, \quad (1.2.8)$$

where p_∞ and v_∞ are the wall-values of the uniform flow acoustic pressure and radial velocity, respectively. Thus the near-wall behaviour of the outer solutions may be written as

$$p_u(1 - \delta y) \sim p_\infty + i\delta y(\omega - Mk)v_\infty + \mathcal{O}(\delta^2), \quad (1.2.9a)$$

$$v_u(1 - \delta y) \sim v_\infty + \delta y \left[v_\infty + (\alpha^2 - m^2) \frac{ip_\infty}{(\omega - Mk)} \right] + \mathcal{O}(\delta^2), \quad (1.2.9b)$$

to first order in the boundary layer thickness.

1.2.2 Dispersion relations

A solution of the form (1.2.5) is not necessarily an allowable duct mode; in order to describe a physically realisable acoustic solution, a dispersion relation must be satisfied that links allowable values of the modal quantities (ω, k, m) . Commonly, a dispersion relation may be formed by applying a boundary condition. For the case we are considering here, an allowable mode is found by applying an impedance boundary condition $\tilde{p} = Z \tilde{\mathbf{u}} \cdot \mathbf{n}$ at the wall $r = 1$ with a specific boundary model $Z(\omega, k)$, where \mathbf{n} is the unit surface normal vector pointing out of the fluid (hence in our cylindrical geometry $\tilde{\mathbf{u}} \cdot \mathbf{n} \equiv \tilde{v}$).

As an example, if we use the forms of the acoustic pressure and radial velocity for a uniform inviscid flow from (1.2.5), we may write the dispersion relation $\tilde{p}_u(1) = Z \tilde{v}_u(1)$ as

$$(\omega - Mk) J_m(\alpha) = iZ \alpha J'_m(\alpha). \quad (1.2.10)$$

In the hard-wall limit, when $Z \rightarrow \infty$, (1.2.10) reduces to

$$J'_m(\alpha) = 0, \quad (1.2.11)$$

and the allowable acoustic modes become the zeros of the first derivative of the Bessel function of the first kind, of order m and argument α . That is, for a given azimuthal wavenumber m , the allowable modes are given by (ω_j, k_j) where $J'_m(\alpha_j) = 0$ is the j th zero of $J'_m(\alpha)$, and $\alpha_j^2 = (\omega_j - Mk_j)^2 - k_j^2$. When a wall has zero impedance, $Z = 0$, it is known as a ‘‘pressure release’’ surface. In this case, (1.2.10) reduces to

$$J_m(\alpha) = 0, \quad (1.2.12)$$

and the allowable modes are the zeros of the Bessel function itself. Examples of acoustic modes in the complex k -plane that satisfy the dispersion relations (1.2.11) and (1.2.12) are shown in fig. 1.5. Notice that $\text{Im}(k) = 0$ for the cut-on modes in both cases.

It is known that if the mean flow (with velocity \mathbf{U}) slips along the lining, the acoustic boundary condition $\tilde{p} = Z \tilde{v}$ must be altered (Ingard, 1959; Miles, 1957; Ribner, 1957). Myers (1980) derived (with prior work published in Ingard, 1959; Miles, 1957) the expression

$$i\omega \tilde{\mathbf{u}} \cdot \mathbf{n} = (i\omega + \mathbf{U} \cdot \nabla - (\mathbf{n} \cdot \nabla \mathbf{U}) \cdot \mathbf{n}) \tilde{p} / Z, \quad (1.2.13)$$

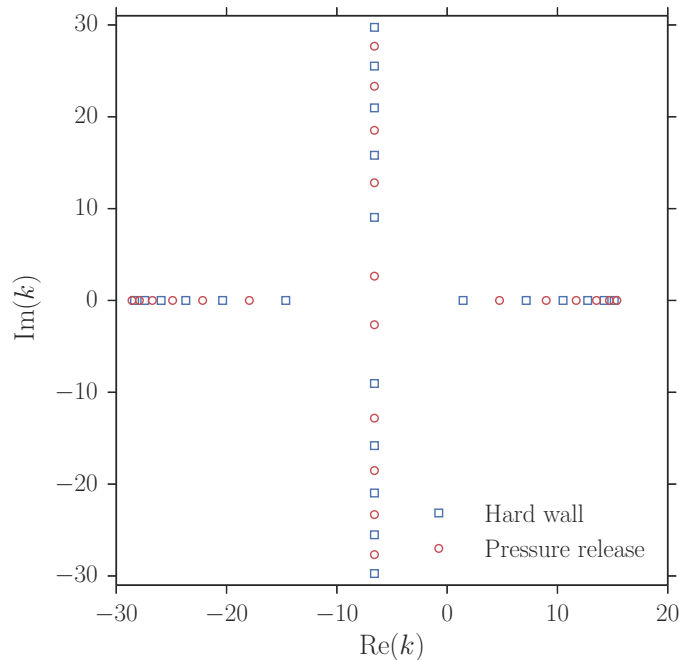


Figure 1.5. A comparison of acoustic modes in the k -plane for the hard wall, (1.2.11), and pressure release, (1.2.12), limits. As the impedance varies between the two limits ($Z \rightarrow \infty$ and $Z = 0$, respectively), the cut-on modes move off the real line and consequently attenuate in the x direction. Parameters are $\omega = 20$, $m = 2$, $M = 0.3$.

for a duct with a general cross-section. In a straight duct the last term in the brackets on the right hand side of (1.2.13) is zero, and in this case the expression (1.2.13) has been shown by Eversman & Beckemeyer (1972); Tester (1973) to be the correct asymptotic limit for a vanishingly thin, inviscid boundary layer (i.e. a vortex sheet an infinitesimal distance from the lining). The Myers boundary condition (1.2.13) (also known as the Ingard–Myers condition Ingard, 1959; Myers, 1980) is discussed in more detail in the next section, and is used as a baseline for comparisons with new acoustic boundary conditions throughout this thesis.

1.2.3 Effective impedance boundary conditions

The previous section discussed acoustic boundary conditions at a liner in isolation from any boundary layer effects. The boundary condition $\tilde{p}(1) = Z\tilde{v}(1)$ is sufficient when no slip enforces a zero mean flow at the wall, or for acoustics in a quiescent medium. However, what do we do when we want to combine the ease of solution of the uniform flow case with the boundary layer complexity that leads to the no slip condition being satisfied? One option is to form an effective impedance boundary condition that accounts for the physics in the boundary layer and the impedance of the liner, and is applicable to a uniform, slipping flow. We may then write the boundary condition as $\tilde{p}_u(1) = Z_{\text{eff}}\tilde{v}_u(1)$, where the effective impedance Z_{eff} differs from the liner impedance Z due to refraction through the sheared boundary layer and any viscothermal effects on the wave propagation.

One way to define Z_{eff} is as the impedance seen by the inviscid, uniform flow acoustics \tilde{p}_u , \tilde{v}_u (that are the correct solutions outside the boundary layer) if they were continued to the duct wall at $r = 1$: $Z_{\text{eff}} = \tilde{p}_u(1)/\tilde{v}_u(1)$. This then allows us, in theory, to choose Z_{eff} such that the easily calculable uniform flow acoustic modes match the modes in the real flow with a sheared (and possibly viscous) boundary layer. Solving the uniform flow problem with a lining impedance of Z_{eff} is equivalent to solving the true (viscous) sheared flow problem with the actual lining impedance Z . We are interested in the relationship between Z and Z_{eff} .

To write the Myers boundary condition (1.2.13) as an effective impedance relation, we imagine a duct with uniform mean flow velocity $\mathbf{U} = (M, 0, 0)$ everywhere except for a vanishingly thin layer next to the wall where the mean velocity is zero. A vortex sheet separates the moving and stationary fluid, across which we assume the continuity of pressure and normal particle displacement. With a subscript f denoting acoustics on the fluid side of the vortex sheet, and a subscript w denoting acoustics on the wall side, at the wall the relationships $Z = \tilde{p}_w/\tilde{v}_w$ and $Z_{\text{eff}} = \tilde{p}_f/\tilde{v}_f$ hold. Continuity of pressure implies $\tilde{p}_w = \tilde{p}_f$. Normal particle displacement ξ is calculated via the relationship $\tilde{v} = D\xi/Dt$. Thus, in the frequency domain we find $\tilde{v}_f = i(\omega - Mk)\xi_f$ and $\tilde{v}_w = i\omega\xi_f$. Continuity of normal particle displacement then gives

$$\xi_w = \xi_f \quad \implies \quad \frac{\tilde{v}_w}{i\omega} = \frac{\tilde{v}_f}{i(\omega - Mk)}. \quad (1.2.14)$$

Now, combining the above relationships for Z , Z_{eff} , \tilde{p}_f , \tilde{p}_w , \tilde{v}_f and \tilde{v}_w , we may write

$$Z_{\text{eff}} = \frac{\tilde{p}_f}{\tilde{v}_f} = \frac{\omega}{\omega - Mk} \frac{\tilde{p}_w}{\tilde{v}_w} = \frac{\omega}{\omega - Mk} Z. \quad (1.2.15)$$

This may be shown to be equivalent to (1.2.13): equation (1.2.13) may be written for a straight duct as

$$i\omega v_f = i(\omega - Mk) \frac{p_f}{Z}, \quad (1.2.16)$$

which upon rearrangement yields

$$Z_{\text{eff}} = \frac{\omega}{\omega - Mk} Z. \quad (1.2.17)$$

The choice of replacing $\tilde{\mathbf{u}} \cdot \mathbf{n}$ with \tilde{v}_f in (1.2.16) is obvious once we acknowledge we are applying the boundary condition to the acoustics in the body of the duct (i.e. the fluid side of the vortex sheet).

It is worth noting that the Myers boundary condition does not confer on the boundary layer (that is, the vortex sheet) an impedance independently from the liner. In the pressure release limit $Z = 0$ and Z_{eff} is also zero; similarly, in the hard wall case $Z = \infty$ and Z_{eff} is also infinite. This is an early sign that the Myers boundary condition does not adequately account for the physics of the boundary layer when applied to a slipping flow.

Many extensions of the Myers boundary condition (often called modified Myers conditions) have been proposed that attempt to account for a finite layer of shear in an inviscid boundary layer. This is usually done by asymptotically expanding inside the boundary layer in the small layer thickness δ , and solving to first order in δ . Gabard (2013) tested the accuracy of two of these first order extensions: the boundary condition of Rienstra & Darau (2011), derived in the incompressible limit, was shown to be inferior to that of Brambley (2011*b*), which assumes a fully compressible fluid. For this reason, in this work we use the term modified Myers condition to refer to the boundary condition proposed by Brambley (2011*b*), which we state here:

$$Z_{\text{eff}} = \frac{\omega}{\omega - Mk} \frac{Z - \frac{i(\omega - Mk)^2}{\omega} \delta I_0}{1 + i\omega Z \frac{k^2 + m^2}{(\omega - Mk)^2} \delta I_1}, \quad (1.2.18)$$

where I_0 and I_1 are integrals across the thin boundary layer,

$$\delta I_0 = \int_0^1 1 - \frac{(\omega - U(r)k)^2 \rho(r)}{(\omega - Mk)^2} dr, \quad \delta I_1 = \int_0^1 1 - \frac{(\omega - Mk)^2}{(\omega - U(r)k)^2 \rho(r)} dr. \quad (1.2.19)$$

Chapter 2

Acoustic boundary conditions at an impedance lining in inviscid shear flow

In this chapter, acoustics in an inviscid boundary layer over an acoustic lining are further investigated. This work has been published in the *Journal of Fluid Mechanics* (Khamis & Brambley, 2016a). In §2.1 the governing Pridmore-Brown equations for the acoustic pressure \tilde{p} and velocity \tilde{v} are stated, and an impedance Riccati equation is derived for $Z(r) = \tilde{p}(r)/\tilde{v}(r)$. Section 2.2 describes the asymptotic analysis leading to a boundary condition that is correct to second-order in the boundary layer thickness. Section 2.3 solves the impedance equation by a single fourth-order explicit Runge–Kutta step across the boundary layer; and by a second-order, single-step implicit scheme. Expressions are given for the effective impedance at the lining seen by the acoustics in a plug flow (uniform mean flow). In §2.4, the accuracy of each of these models is compared against the Ingard–Myers boundary condition, its first-order correction, and numerical simulations. While the second-order boundary condition performs better for thin boundary layers, the single-step implicit Runge–Kutta scheme retains accuracy for high frequencies and short wavelengths, and for thicker boundary layers, making it a viable substitute for the asymptotic boundary conditions outside their regions of validity. In §2.5, simplified forms of the conditions are found both for a specific linear shear profile and for the limiting case $k/\omega \gg 1$ satisfied by surface modes. In §2.6 it is found that the second-order asymptotic condition is extremely accurate when investigating surface modes and their stability, as well as cut-on and cut-off acoustic modes. The second-order condition does, however, support spurious modes far from its region of asymptotic validity.

When applied in shear flow, the Pridmore-Brown equation possesses a singularity, called the critical layer, wherever the phase speed of a wave is equal to the base flow velocity (that is, when a wave is perfectly convected). It has been shown that the contribution to the resultant sound field of the critical layer is modest at most (Brambley *et al.*, 2012a). Here we avoid the critical layer in favour of simplicity. Also omitted from the analysis are viscous effects, which are left to later chapters.

2.1 Governing equations

We are concerned with the dynamics of an inviscid compressible perfect gas, for which the dimensionless governing equations (1.1.10) take the form

$$\frac{\partial \rho}{\partial t} + \nabla \cdot (\rho \mathbf{u}) = 0, \quad \rho \frac{D\mathbf{u}}{Dt} = -\nabla p, \quad \frac{Dp}{Dt} = \frac{\gamma p}{\rho} \frac{D\rho}{Dt}, \quad (2.1.1)$$

where the viscosities and thermal conductivity are set to zero, $\mu = \mu^B = \kappa = 0$. Small, unsteady perturbations to the base flow are considered, of the form (1.1.12), from which the common exponential factor is omitted henceforth. The velocity and density gradients in the base flow boundary layer alter the effect of the acoustic lining on the acoustics. At the lining, the acoustic pressure drives a wall-normal velocity, $\tilde{p} = Z\tilde{v}$, for the given impedance of the lining, Z . Governing equations for the acoustic pressure \tilde{p} and radial velocity \tilde{v} may be derived from (2.1.1):

$$\left(\frac{\tilde{p}'}{Q}\right)' + \frac{\bar{\alpha}^2}{Q}\tilde{p} = 0, \quad \left[\left(\frac{r\tilde{v}}{\omega - Uk}\right)' \frac{Q}{\bar{\alpha}^2}\right]' + Q\left(\frac{r\tilde{v}}{\omega - Uk}\right) = 0, \quad (2.1.2a,b)$$

where a prime denotes differentiation with respect to r , and

$$Q(r) = \frac{\rho(\omega - Uk)^2}{r} \quad \text{and} \quad \bar{\alpha}(r)^2 = \rho(\omega - Uk)^2 - k^2 - \frac{m^2}{r^2}. \quad (2.1.3)$$

It is worth noting that the Pridmore-Brown (1958) equation (2.1.2a) and the corresponding equation for the radial velocity (2.1.2b) are both second-order, in \tilde{p} and \tilde{v} respectively, with the radial momentum equation stating $\tilde{v} \sim \tilde{p}'$. The similarity between the two equations (2.1.2a,b) may be highlighted by defining $\phi = r\tilde{v}/(\omega - Uk)$ and rearranging to give

$$\frac{Q}{\bar{\alpha}^2} \left(\frac{\tilde{p}'}{Q}\right)' + \tilde{p} = 0, \quad \frac{1}{Q} \left(\frac{Q}{\bar{\alpha}^2} \phi'\right)' + \phi = 0. \quad (2.1.4a,b)$$

Inherent in the linearisation of the Euler equation, and thus in (2.1.2a,b), is the so-called critical layer singularity, $\omega - U(r_c)k = 0$, where r_c is the radial location of the critical layer. This occurs when a wave is perfectly convected, and leads to a continuous hydrodynamic spectrum. We neglect the critical layer in this chapter by assuming that r_c does not fall within our physical domain (see Brambley *et al.* (2012a) for a full discussion).

2.1.1 The uniform solution

It is well known (see, e.g., Brambley & Peake, 2008; Vilenksi & Rienstra, 2007) that the acoustic pressure and radial velocity in a duct with inviscid uniform flow can be expressed in terms of Bessel functions as $\tilde{p}_u(r) = EJ_m(\alpha r)$ and $\tilde{v}_u(r) = i\alpha EJ'_m(\alpha r)/(\omega - Mk)$, where $\alpha^2 = (\omega - Mk)^2 - k^2$ and E is a constant amplitude. Modes for such a flow are found by applying a boundary condition at the lined wall, $\tilde{p}_u(1) = Z_{\text{eff}}\tilde{v}_u(1)$. The *effective* impedance Z_{eff} differs from the true lining impedance Z due to refraction through the sheared boundary layer, which is neglected in the uniform flow model. For example, for the Myers boundary condition,

$$Z_{\text{eff}} = \frac{\omega}{\omega - Mk} Z, \quad (2.1.5)$$

where the Doppler factor accounts for refraction across a vortex sheet by enforcing continuity of normal displacement. We would like to choose a Z_{eff} such that the easily calculable uniform

flow acoustic modes match the modes in the real flow with a sheared boundary layer. Thus, Z_{eff} includes information about both the lining impedance Z , and how acoustic modes evolve in shear. This means that solving the uniform flow problem with a lining impedance of Z_{eff} is equivalent to solving the true sheared flow problem with the actual lining impedance Z . We are interested in the relationship between Z and Z_{eff} .

If we knew both ω and k , then we could find Z_{eff} explicitly:

$$Z_{\text{eff}} = (\omega - Mk) \frac{J_m(\alpha)}{i\alpha J'_m(\alpha)}. \quad (2.1.6)$$

We do not know both k and ω a priori, however, and therefore we would like to solve (2.1.6) for the modes $k(\omega)$; a relationship between Z_{eff} and the known Z is then needed. For example, the Ingard–Myers boundary condition modelling an infinitely thin shear layer (Eversman & Beckemeyer, 1972) is given in (2.1.5), while the first-order asymptotic correction to the Ingard–Myers boundary condition in the limit of a thin shear layer (Brambley, 2011b) is given by

$$Z_{\text{eff}} = \frac{\omega}{\omega - Mk} \frac{Z - \frac{i(\omega - Mk)^2}{\omega} \delta I_0}{1 + i\omega Z \frac{k^2 + m^2}{(\omega - Mk)^2} \delta I_1}, \quad (2.1.7)$$

where I_0 and I_1 are integrals across the thin boundary layer,

$$\delta I_0 = \int_0^1 1 - \frac{(\omega - U(r)k)^2 \rho(r)}{(\omega - Mk)^2} dr, \quad \delta I_1 = \int_0^1 1 - \frac{(\omega - Mk)^2}{(\omega - U(r)k)^2 \rho(r)} dr. \quad (2.1.8)$$

2.1.2 An impedance governing equation

Most work concerning acoustic propagation in inviscid fluids begins with equations (2.1.1) and reduces them to a form of the Pridmore–Brown equation (Pridmore–Brown, 1958), e.g. (2.1.2a). Less common is the corresponding governing equation for the radial acoustic velocity \tilde{v} , (2.1.2b). Here, we also work directly with the impedance and derive a new governing equation. We extend the relationship $\tilde{p} = Z\tilde{v}$ at the boundary $r = 1$ to one valid for all r , i.e. $\zeta(r) = \tilde{p}(r)/\tilde{v}(r)$. The same is done for the uniform flow equivalent, i.e. $\zeta_u(r) = \tilde{p}_u(r)/\tilde{v}_u(r)$. Hence, $Z \equiv \zeta(1)$ and $Z_{\text{eff}} \equiv \zeta_u(1)$.

From (2.1.1) and (2.1.2a,b) the following relations may be derived:

$$\frac{\bar{\alpha}^2}{Q} \tilde{p} = i \left(\frac{r\tilde{v}}{\omega - Uk} \right)' \quad \text{and} \quad \tilde{p}' = -iQ \left(\frac{r\tilde{v}}{\omega - Uk} \right). \quad (2.1.9)$$

Guided by the form of (2.1.9), we write

$$\frac{1}{r}(\omega - Uk)\zeta = \frac{\tilde{p}}{r\tilde{v}}. \quad (2.1.10)$$

Taking the derivative with respect to r and using (2.1.9) to eliminate \tilde{p} and \tilde{v} we find a nonlinear Riccati equation for ζ ,

$$\left[\frac{1}{r}(\omega - Uk)\zeta \right]' = -iQ + \frac{i\bar{\alpha}^2}{Q} \left[\frac{1}{r}(\omega - Uk)\zeta \right]^2. \quad (2.1.11)$$

Note that (2.1.11) is a rephrasing of the acoustic equations (2.1.2a,b), and thus $\zeta(r)$ represents the lumped impedance of both the boundary and the fluid in $[r, 1]$. Since (2.1.11) is a first-order equation and at the lining the boundary condition gives $\zeta(1) = Z$, in the uniform flow region the

requirement that $\zeta(r) = \zeta_u(r)$ allows us to find Z_{eff} .

The equation (2.1.11) is exact, and so its numerical solution should correspond with direct solution of the Pridmore–Brown equation. However, its nonlinearity makes it a less attractive candidate for such computations. Instead we solve equation (2.1.11) using two different approximate methods. In §2.3, two single-step Runge–Kutta solutions are found, one explicit and one implicit, which exploit the inherently small step size δ . In §2.B, an alternative asymptotic analysis (to that in §2.2) is performed by expanding (2.1.11) in terms of the small width of the boundary layer, δ . The two methods vary in essence by where we make our approximations: the first approximately solves an exact equation; the second exactly solves an approximate equation.

2.2 Deriving the asymptotic solution

In this section the asymptotic boundary condition for the effective impedance is found to second-order in δ by solving equations (2.1.2a,b) inside the boundary layer and matching to the uniform solutions outside the boundary layer.

Outside the boundary layer, the uniform base flow pressure solution may be written $\tilde{p}_u(r) = EJ_m(\alpha r)$ as described above. Expanding this about the lined wall at $r = 1$ using the boundary layer scaling $r = 1 - \delta y$ as in Brambley (2011*b*), the outer solution for the pressure becomes

$$\tilde{p}_u(1 - \delta y) = EJ_m(\alpha) - \delta y E \alpha J'_m(\alpha) - \frac{1}{2} \delta^2 y^2 E [\alpha J'_m(\alpha) + (\alpha^2 - m^2) J_m(\alpha)] + \mathcal{O}(\delta^3). \quad (2.2.1)$$

Using the notation $p_\infty \equiv \tilde{p}_u(1)$, the pressure at the wall $r = 1$, and $v_\infty \equiv \tilde{v}_u(1)$, (2.2.1) and the equivalent radial velocity expansion may be written as

$$\begin{aligned} \tilde{p}_u(1 - \delta y) = p_\infty + \delta y i(\omega - Mk) v_\infty + \frac{1}{2} \delta^2 y^2 \left[(k^2 + m^2 - (\omega - Mk)^2) p_\infty \right. \\ \left. + i(\omega - Mk) v_\infty \right] + \mathcal{O}(\delta^3) \end{aligned} \quad (2.2.2a)$$

$$\begin{aligned} \tilde{v}_u(1 - \delta y) = v_\infty - \delta y \left(\frac{(\omega - Mk)^2 - k^2 - m^2}{i(\omega - Mk)} p_\infty - v_\infty \right) \\ + \frac{1}{2} \delta^2 y^2 \left[\frac{3m^2 + k^2 - (\omega - Mk)^2}{i(\omega - Mk)} p_\infty \right. \\ \left. + (2 + k^2 + m^2 - (\omega - Mk)^2) v_\infty \right] + \mathcal{O}(\delta^3). \end{aligned} \quad (2.2.2b)$$

Our inner solutions will be matched to (2.2.2) in the limit $y \rightarrow \infty$.

In terms of the boundary layer variable y , equations (2.1.2a,b) become

$$\left(\frac{\tilde{p}_y}{\rho(\omega - Uk)^2} \right)_y = \delta \left(\frac{y \tilde{p}_y}{\rho(\omega - Uk)^2} \right)_y - \delta^2 \left(1 - \frac{k^2 + m^2}{\rho(\omega - Uk)^2} \right) \tilde{p} + \mathcal{O}(\delta^3) \quad (2.2.3)$$

for the pressure, and

$$\begin{aligned} \left[\left(\frac{\tilde{v}}{\omega - Uk} \right)_y \frac{\rho(\omega - Uk)^2}{\rho(\omega - Uk)^2 - k^2 - m^2} \right]_y = \delta \left(\frac{\tilde{v}}{\omega - Uk} \frac{\rho(\omega - Uk)^2}{\rho(\omega - Uk)^2 - k^2 - m^2} \right)_y \\ - \delta \left[\left(\frac{\tilde{v}}{\omega - Uk} \right)_y \frac{2m^2 y \rho(\omega - Uk)^2}{[\rho(\omega - Uk)^2 - k^2 - m^2]^2} \right]_y - \delta^2 \left(\frac{\tilde{v}}{\omega - Uk} \rho(\omega - Uk)^2 \right) \\ + \delta^2 \left(\frac{\tilde{v}}{\omega - Uk} \frac{y \rho(\omega - Uk)^2}{[\rho(\omega - Uk)^2 - k^2 - m^2]^2} (\rho(\omega - Uk)^2 + m^2 - k^2) \right)_y \end{aligned}$$

$$-\delta^2 \left[\left(\frac{\tilde{v}}{\omega - Uk} \right)_y \frac{4m^2 y^2 \rho(\omega - Uk)^2}{[\rho(\omega - Uk)^2 - k^2 - m^2]^3} (\rho(\omega - Uk)^2 - k^2) \right]_y + \mathcal{O}(\delta^3) \quad (2.2.4)$$

for the radial velocity. Here ρ and U are now the corresponding base density and axial velocity as functions of y . A subscript denotes differentiation.

Solving (2.2.3) and (2.2.4) to second-order produces the inner solutions; see §2.A for details. When evaluated at the wall, the second-order correction to the \tilde{v} expansion is singular if $(\omega - Mk)^2 = k^2 + m^2$. Solutions of the Pridmore-Brown equation exist at this point. Thus, the singularity is a consequence of the asymptotic expansion and is spurious. Close to the new singular point one could simply revert to using the first-order expansion as derived by Brambley (2011*b*), which is unaffected by the unphysical singularity.

Matching with the outer solutions (2.2.2) and evaluating at the boundary $y = 0$ gives, after some algebra,

$$\begin{aligned} \tilde{p}(0) = & \tilde{p}_u(0) + i(\omega - Mk)\tilde{v}_u(0)\delta I_0 + i(\omega - Mk)\tilde{v}_u(0)\delta^2 I_2 \\ & + (k^2 + m^2)\tilde{p}_u(0) (\delta I_0 \delta I_1 - \delta^2 I_3) - (\omega - Mk)^2 \tilde{p}_u(0) \delta^2 I_7 + \mathcal{O}(\delta^3), \end{aligned} \quad (2.2.5a)$$

$$\begin{aligned} \tilde{v}(0) = & \frac{\omega}{\omega - Mk} \left\{ \tilde{v}_u(0) - i\tilde{p}_u(0) \frac{k^2 + m^2}{\omega - Mk} \delta I_1 + (\omega - Mk)^2 \tilde{v}_u(0) \delta^2 I_2 \right. \\ & + (k^2 + m^2) \tilde{v}_u(0) \delta^2 I_3 + i\tilde{p}_u(0) \frac{k^2 + m^2}{\omega - Mk} \frac{k^2 - m^2 - (\omega - Mk)^2}{k^2 + m^2 - (\omega - Mk)^2} \delta^2 I_3 \\ & + (k^2 + m^2) \tilde{v}_u(0) (\delta I_0 \delta I_1 - \delta^2 I_2 - \delta^2 I_5) \\ & \left. + \frac{2im^2 \tilde{p}_u(0)}{\omega - Mk} \left(\frac{k^2 + m^2}{k^2 + m^2 - (\omega - Mk)^2} \delta^2 I_6 - \delta^2 I_4 \right) \right\} + \mathcal{O}(\delta^3), \end{aligned} \quad (2.2.5b)$$

where the integrals I_j are

$$\begin{aligned} I_0 &= \int_0^\infty \chi_0(y) dy, & I_1 &= \int_0^\infty \chi_1(y) dy, & I_2 &= \int_0^\infty y \chi_0(y) dy \\ I_3 &= \int_0^\infty y \chi_1(y) dy, & I_4 &= \int_0^\infty y \chi_2(y) dy, & I_5 &= \int_0^\infty \chi_1(y) \int_0^y \chi_0(y') dy' dy \\ I_6 &= \int_0^\infty y \chi_1(y) \chi_2(y) dy, & I_7 &= \int_0^\infty \chi_0(y) \int_0^y \left(1 - \frac{k^2 + m^2}{\rho(y')(\omega - U(y')k)^2} \right) dy' dy \end{aligned} \quad (2.2.6)$$

with

$$\begin{aligned} \chi_0(y) &= \left[1 - \frac{\rho(\omega - Uk)^2}{(\omega - Mk)^2} \right], & \chi_1(y) &= \left[1 - \frac{(\omega - Mk)^2}{\rho(\omega - Uk)^2} \right], \\ \chi_2(y) &= \left[1 - \frac{(\omega - Mk)^2 - k^2 - m^2}{\rho(\omega - Uk)^2 - k^2 - m^2} \right]. \end{aligned} \quad (2.2.7)$$

The impedance of the boundary is the ratio of the acoustic pressure to the normal velocity that it drives, so we write $Z = \tilde{p}(0)/\tilde{v}(0)$ using equations (2.2.5). We identify the effective impedance with the same ratio for the uniform flow variables: $Z_{\text{eff}} = p_\infty/v_\infty$. Using these two relationships we may rearrange the ratio of (2.2.5a) and (2.2.5b) to find an expression for the effective impedance of an acoustic liner with an inviscid sheared boundary layer:

$$Z_{\text{eff}} = \frac{\omega}{\Omega_u} \frac{Z - \frac{i\Omega_u^2}{\omega} (\delta I_0 + \delta^2 I_2) - Z\mu^2 \delta^2 I_2 + \sigma_+ Z (\delta I_0 \delta I_1 + \delta^2 I_3 - \delta^2 I_5)}{1 + i\sigma_+ \frac{\omega Z}{\Omega_u^2} \delta I_1 + \Upsilon_1 \delta^2 I_3 + \Upsilon_2 (\delta^2 I_4 - \frac{\sigma_+}{\mu^2} \delta^2 I_6) + \sigma_+ \delta I_0 \delta I_1 - \Omega_u^2 \delta^2 I_7} + \mathcal{O}(\delta^3), \quad (2.2.8)$$

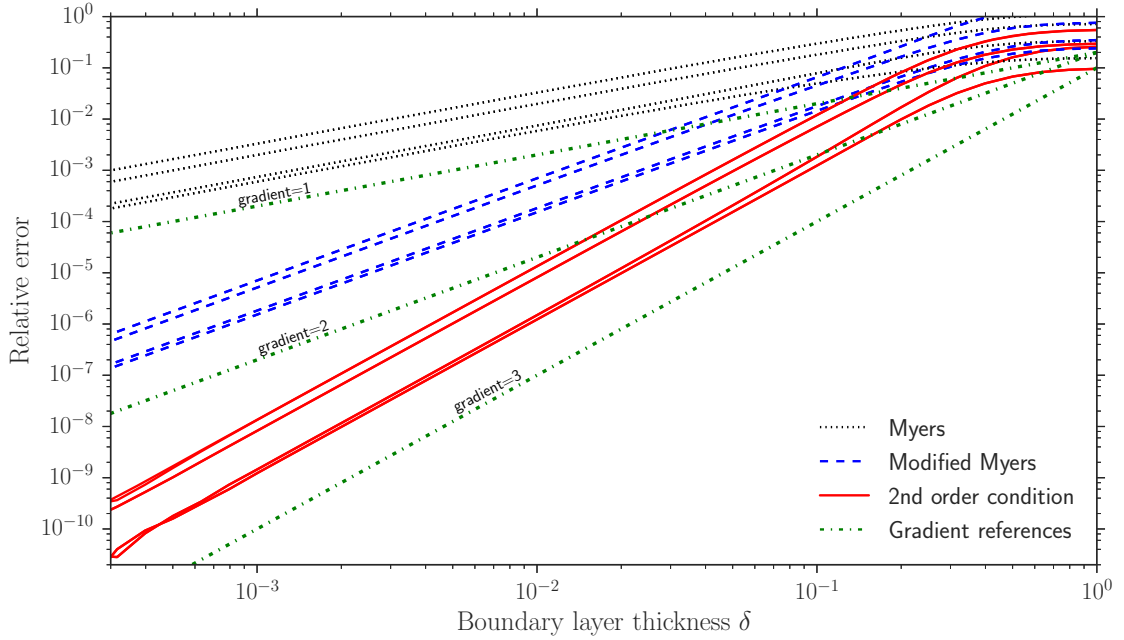


Figure 2.1. The relative errors of the leading (black dotted), first (blue dashed) and second (red solid) orders of the new boundary condition (2.2.8) when compared with numerical solutions of the Pridmore–Brown equation. The green dash-dot lines have gradients of 1, 2 and 3 beginning from the top and moving down. Parameters used are $k = \pm 1 \pm i, \pm 1, \pm i$ and $\omega = 1$, $m = 0$, $M = 0.5$ with the tanh boundary layer profile of (2.4.1). Relative error is defined $|Z^*/Z_{\text{eff}} - 1|$, where Z^* is the approximation from the specified model, and Z_{eff} is the exact result from (2.1.6).

where $\sigma_+ = k^2 + m^2$, $\Omega_u = \omega - Mk$ and $\mu^2 = \sigma_+ - \Omega_u^2$, and where

$$\Upsilon_1 = \frac{i\sigma_+\omega Z}{\Omega_u^2} \left(\frac{2m^2}{\mu^2} - 1 \right) - \sigma_+, \quad \Upsilon_2 = 2im^2 \frac{\omega Z}{\Omega_u^2}.$$

Equation (2.2.8) readily reduces to the modified boundary condition as derived by Brambley (2011*b*) at $\mathcal{O}(\delta)$, (2.1.7), and to the classical Myers condition (2.1.5) in the limit $\delta \rightarrow 0$. Figure 2.1 shows that the condition is correct to the stated asymptotic order.

Equation (2.2.8) may be applied in the physical r domain by transforming the integrals I_j as follows:

$$\begin{aligned} \delta I_0 &= \int_0^1 \chi_0(r) dr, & \delta I_1 &= \int_0^1 \chi_1(r) dr, & \delta^2 I_2 &= \int_0^1 (1-r) \chi_0(r) dr, \\ \delta^2 I_3 &= \int_0^1 (1-r) \chi_1(r) dr, & \delta^2 I_4 &= \int_0^1 (1-r) \chi_2(r) dr, \\ \delta^2 I_5 &= \int_0^1 \chi_1(r) \int_r^1 \chi_0(r') dr' dr, & \delta^2 I_6 &= \int_0^1 (1-r) \chi_1(r) \chi_2(r) dr, \\ \delta^2 I_7 &= \int_0^1 \chi_0(r) \int_r^1 \left(1 - \frac{\sigma_+}{\rho(r') \Omega(r')^2} \right) dr' dr. \end{aligned} \tag{2.2.9}$$

An example of the accuracy of this boundary condition is given in §2.4, and an explicit form for a linear boundary layer profile is given in §2.5.1.

2.3 The Runge–Kutta solutions

Here we derive an expression for Z_{eff} by approximately solving (2.1.11) using a single step of a fourth-order explicit Runge–Kutta method (see Hairer *et al.*, 1993), and a second-order, single-step

implicit scheme.

Equation (2.1.11) may be transformed as follows. Dividing (2.1.11) through by $(\omega - Mk)^2$ produces

$$\frac{1}{\omega - Mk} L' = -i\tilde{Q} + \frac{i\tilde{\alpha}^2}{\tilde{Q}(\omega - Mk)^2} L^2, \quad (2.3.1)$$

where $\tilde{Q} = Q/(\omega - Mk)^2$, an $\mathcal{O}(1)$ quantity for all ω , k , and

$$L = \frac{(\omega - Uk)}{r(\omega - Mk)} \zeta. \quad (2.3.2)$$

The quantity L may be split into a uniform flow value, $L_u = \zeta_u/r$, and a perturbation due to the presence of the boundary layer, \tilde{L} , such that

$$L = L_u + \tilde{L}. \quad (2.3.3)$$

Equation (2.3.1) has the associated data $L_u(1) = Z_{\text{eff}}$, and $L = L_u$ outside the boundary layer. For a uniform flow of Mach number M and constant density $\rho \equiv 1$, (2.3.1) reduces to

$$\frac{1}{(\omega - Mk)} L'_u = -\frac{i}{r} + ir \left(1 - \frac{k^2 + \frac{m^2}{r^2}}{(\omega - Mk)^2} \right) L_u^2. \quad (2.3.4)$$

Equation (2.3.4) may then be used in (2.3.1) along with the decomposition (2.3.3) to form a governing equation for $\tilde{L}(r)$:

$$\begin{aligned} \frac{1}{(\omega - Mk)} \tilde{L}' &= \frac{i}{r} \left[1 - \frac{\rho(\omega - Uk)^2}{(\omega - Mk)^2} \right] + ir \frac{k^2 + \frac{m^2}{r^2}}{(\omega - Mk)^2} \left[1 - \frac{(\omega - Mk)^2}{\rho(\omega - Uk)^2} \right] L_u^2 \\ &+ ir \left[1 - \frac{k^2 + \frac{m^2}{r^2}}{\rho(\omega - Uk)^2} \right] (2L_u \tilde{L} + \tilde{L}^2). \end{aligned} \quad (2.3.5)$$

The asymptotics of equation (2.3.5) may be found in §2.B, where it is shown that the modified Myers (Brambley, 2011*b*) condition may be cleanly reproduced from (2.3.5) but the second-order extension runs into difficulties concerning nonuniqueness. Here, we proceed with approximate solutions to (2.3.5).

2.3.1 The explicit scheme

In order to ensure the correct $\delta \rightarrow 0$ behaviour, we use the decomposition (2.3.3) and solve (2.3.5) for $\tilde{L}(r)$, with the necessary condition that $\tilde{L} = 0$ in uniform flow (for $r < 1 - \delta$). While this is technically only valid for profiles with $U \equiv M$ for $r < 1 - \delta$, for a 99% U_0 boundary layer thickness the approximation $\tilde{L} = 0$ for $r < 1 - \delta$ is a reasonable one. We choose to step from the top of the boundary layer at $r = 1 - \delta$, with the initial condition $\tilde{L}(1 - \delta) = 0$, to the lining at $r = 1$, where the boundary condition $\tilde{L}(1) = \omega Z/(\omega - Mk) - Z_{\text{eff}}$ gives Z_{eff} as a function of Z . Using the analytic uniform solution defined in §2.1.1 we can treat as known the intermediate values of $L_u(r)$ that arise.

To perform the step, we define the fourth-order explicit Runge–Kutta difference equation $\tilde{L}_1 = \tilde{L}_0 + \frac{\delta}{6}(k_1 + 2k_2 + 2k_3 + k_4)$, where $\tilde{L}_0 = \tilde{L}(1 - \delta) = 0$. Defining

$$A = \frac{i(\omega - Mk)}{r} \chi_0, \quad B = ir \frac{k^2 + m^2/r^2}{\omega - Mk} \chi_1, \quad C = ir(\omega - Mk) \left[1 - \frac{k^2 + m^2/r^2}{\rho(\omega - Uk)^2} \right], \quad (2.3.6)$$

with χ_j defined as in (2.2.7), the k_j terms become

$$k_1 = A(1-\delta) + B(1-\delta)L_u(1-\delta)^2, \quad (2.3.7a)$$

$$k_2 = A(1-\delta/2) + B(1-\delta/2)L_u(1-\delta/2)^2 + C(1-\delta/2) \left(2L_u(1-\delta/2)\frac{\delta}{2}k_1 + \frac{\delta^2}{4}k_1^2 \right), \quad (2.3.7b)$$

$$k_3 = A(1-\delta/2) + B(1-\delta/2)L_u(1-\delta/2)^2 + C(1-\delta/2) \left(2L_u(1-\delta/2)\frac{\delta}{2}k_2 + \frac{\delta^2}{4}k_2^2 \right), \quad (2.3.7c)$$

$$k_4 = A(1) + B(1)Z_{\text{eff}}^2 + C(1) (2Z_{\text{eff}}\delta k_3 + \delta^2 k_3^2). \quad (2.3.7d)$$

The decomposition (2.3.3) may then be used to apply the boundary condition at $r=1$, giving

$$Z_{\text{eff}} = \frac{\omega}{\omega - Mk} Z - \frac{\delta}{6}(k_1 + 2k_2 + 2k_3 + k_4). \quad (2.3.8)$$

If we extract the Z_{eff} from k_4 , defining $k_4 = \tilde{k}_4 + [B(1)Z_{\text{eff}} + 2C(1)\delta k_3]Z_{\text{eff}}$, where $\tilde{k}_4 = A(1) + \delta^2 C(1)k_3^2$, we can rearrange (2.3.8) to find

$$Z_{\text{eff}} = \frac{\omega}{\omega - Mk} \frac{Z - \frac{\delta}{6}(1 - Mk/\omega)(k_1 + 2k_2 + 2k_3 + \tilde{k}_4)}{1 + \frac{\delta}{6}(B(1)Z_{\text{eff}} + 2\delta C(1)k_3)}, \quad (2.3.9)$$

which then gives Z_{eff} as a function of Z . To completely isolate Z_{eff} we must multiply up by the denominator on the right hand side and solve the resulting quadratic. In doing so, however, a second root is introduced (leading to a problem similar to that faced in the derivation of the implicit scheme method, below). The classical Myers condition is recovered in the limit $\delta \rightarrow 0$, as we would hope (Eversman & Beckemeyer, 1972; Tester, 1973). The form of (2.3.9) bears a striking resemblance to that of the modified Myers condition.

2.3.2 A single-step implicit scheme

Here we define a trapezoidal second-order, single-step implicit Runge-Kutta scheme and use it for a single step to approximate Z_{eff} . For this scheme, the fundamental difference equation for the differential equation $y' = f(x, y)$ is

$$y_{n+1} = y_n + \frac{h}{2}(f(x_n, y_n) + f(x_{n+1}, y_{n+1})). \quad (2.3.10)$$

The method is implicit due to the appearance of y_{n+1} on both sides of (2.3.10).

We use the scheme to first step back from the boundary, which has a known impedance Z , through the sheared boundary layer profile to the edge of the boundary layer at $r = 1 - \delta$; and then to step forward from $r = 1 - \delta$ to $r = 1$ assuming a uniform flow. The details of these steps are found in §2.D.

The method results in the following effective impedance

$$Z_{\text{eff}} = X_1 + \frac{1}{2}\delta(\tilde{k}_1 + \tilde{k}_2), \quad (2.3.11)$$

where

$$X_1 = X_0 - \frac{1}{2}\delta(k_1 + k_2), \quad \text{and} \quad X_0 = \frac{\omega}{\omega - Mk} Z, \quad (2.3.12)$$

with

$$k_1 = A_1(1) + B_1(1)X_0^2, \quad (2.3.13)$$

$$k_2 = \left(\frac{2}{\delta^2 B_1(1-\delta)} + 2\frac{X_0}{\delta} - k_1 \right) \left(1 - \left\{ 1 - \frac{4A_1(1-\delta)/B_1(1-\delta) + (2X_0 - \delta k_1)^2}{\left(\frac{2}{\delta B_1(1-\delta)} + 2X_0 - \delta k_1 \right)^2} \right\}^{\frac{1}{2}} \right), \quad (2.3.14)$$

for

$$A_1(r) = -\frac{i}{r} \frac{\rho(\omega - Uk)^2}{\omega - Mk}, \quad B_1(r) = ir(\omega - Mk) \left(1 - \frac{k^2 + m^2/r^2}{\rho(\omega - Uk)^2} \right);$$

and

$$\tilde{k}_1 = A_2(1-\delta) + B_2(1-\delta)X_1^2, \quad (2.3.15)$$

$$\tilde{k}_2 = \left(\frac{2}{\delta^2 B_2(1)} - 2\frac{X_1}{\delta} - \tilde{k}_1 \right) \left(1 - \left\{ 1 - \frac{4A_2(1)/B_2(1) + (2X_1 + \delta\tilde{k}_1)^2}{\left(\frac{2}{\delta B_2(1)} - 2X_1 - \delta\tilde{k}_1 \right)^2} \right\}^{\frac{1}{2}} \right), \quad (2.3.16)$$

for

$$A_2(r) = -\frac{i}{r}(\omega - Mk), \quad B_2(r) = ir(\omega - Mk) \left(1 - \frac{k^2 + m^2/r^2}{(\omega - Mk)^2} \right).$$

The two steps used here (back then forward) allow the resulting condition to be a direct map from Z to Z_{eff} (like the asymptotic boundary condition (2.2.8)), without intermediate values of ζ_u having to be used (as in the explicit Runge–Kutta scheme (2.3.9)).

2.4 Accuracy of Z_{eff} models

To measure the accuracy of the boundary conditions derived above, numerical solutions of the full Pridmore-Brown equation were found. This was achieved using a sixth-order finite difference discretisation on a computational grid spaced uniformly in ξ , where $r = \tanh(A\xi)/\tanh(A)$, and A is a stretching parameter, in order to cluster points near $r = 1$ to resolve the boundary layer. Regularity conditions were imposed at $r = 0$, and the wall boundary condition was $\tilde{p}(1) = 1$, with \tilde{v} free. Roots of the dispersion relation $Z = \tilde{p}/\tilde{v}$ were found via Newton–Raphson iteration over k . More details of the numerical method can be found in §3.2 and Appendix 3.A. The tanh velocity profile (Rienstra & Vilenski, 2008)

$$U(r) = M \tanh\left(\frac{1-r}{\delta}\right) + M(1 - \tanh(1/\delta)) \left(\frac{1 + \tanh(1/\delta)}{\delta} r + (1+r) \right) (1-r), \quad (2.4.1)$$

was used to generate the following results, with a constant density $\rho(r) \equiv 1$. This base flow has a displacement thickness

$$\delta^* = \frac{1}{6\delta} (\tanh^2(1/\delta) - 1) + \frac{1}{3} (1 + 2 \tanh(1/\delta)) - \delta \ln(\cosh(1/\delta)), \quad (2.4.2)$$

which for $\delta \in (10^{-7}, 10^{-1})$ gives $\delta^*/\delta = 0.69$ to two decimal places.

A good initial test of the boundary conditions, and one which seems to be missing from the literature concerning such impedance boundary conditions, is to directly check how well the effective impedance is approximated. By solving the Pridmore-Brown equation throughout the complex k -plane for a given ω and m , a boundary impedance Z is generated at each k . This solution has

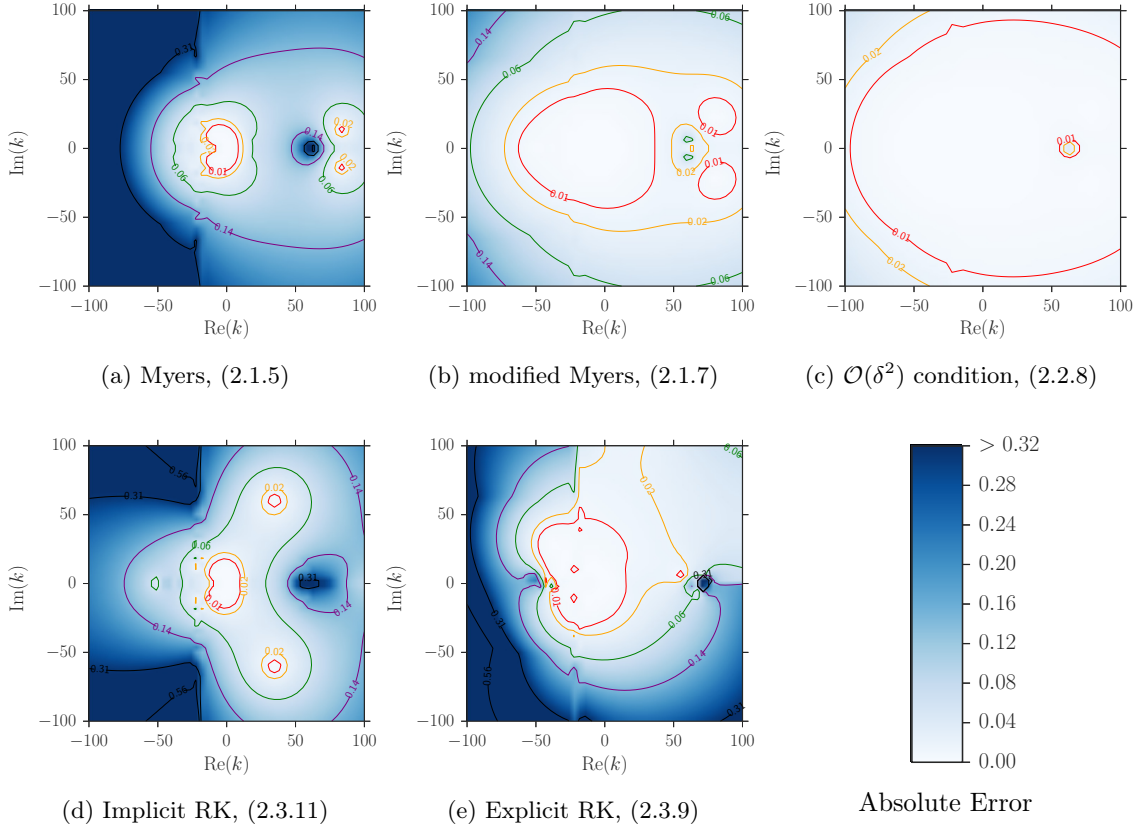


Figure 2.2. Absolute errors in the complex k -plane of the predicted Z_{eff} for each boundary condition. The colour scheme is normalised such that the darkest blue is an error greater than or equal to 1.5 times the mean Myers error. The red contour surrounds errors lower than the lowest quartile of the combined results for the Myers, modified Myers, second-order asymptotic and the single-step implicit Runge–Kutta conditions. Error was calculated as $\min\{|Z_1 - Z_2|, |1/Z_1 - 1/Z_2|\}$. Parameters are $\omega = 31$, $m = 24$, $M = 0.5$, $\delta = 2 \times 10^{-3}$, for a tanh velocity profile (2.4.1) and constant base density $\rho(r) \equiv 1$. The boundary impedance at each point is found from the numerical solution of the Pridmore–Brown equation, (2.1.2a).

a unique uniform flow equivalent and the value of $\zeta_u(1)$ of this uniform flow mode, from (2.1.6), is the Z_{eff} against which we test the models.

Figure 2.2 shows the absolute errors in the complex k -plane of the predicted Z_{eff} for each boundary condition. For the thin boundary layer thickness $\delta = 2 \times 10^{-3}$, the asymptotic conditions perform well. As one would expect, the $\mathcal{O}(\delta^2)$ asymptotic solution, fig. 2.2c, is more accurate throughout the plotted domain than the modified Myers condition, fig. 2.2b, which in turn is more accurate than the Myers condition, fig. 2.2a. For the parameters $\omega = 31$ and $m = 24$ (typical values for rotor-alone noise in an aeroengine bypass duct at take-off (McAlpine *et al.*, 2006)), and the restriction to $\text{Im}(k), \text{Re}(k) \in [-100, 100]$, we are well within the region of asymptotic validity, $\omega, m, k \ll 1/\delta$. The single-step explicit Runge–Kutta scheme, fig. 2.2e, performs well in regions where the scheme is stable, but blows up erratically due to the stiffness of the impedance Riccati equation (2.1.11). The single-step implicit scheme, fig. 2.2d, is reasonably accurate for most of the domain, but has regions where the error is large. Sudden changes inside the boundary layer are not modelled well by the implicit scheme, which utilises data points only at either side of the layer; this suggests the implicit scheme is not suitable for predicting surface modes, and may explain the loss of accuracy of the implicit scheme in the darker regions of fig. 2.2d. The Myers condition, fig. 2.2a, also loses accuracy in these regions due to its vanishingly thin shear layer. The well-posed asymptotic schemes in figs. 2.2b and 2.2c do not have this problem: the bulk treatment of the shear as integrals across the boundary layer, (2.2.6), allow better modelling of variations inside the

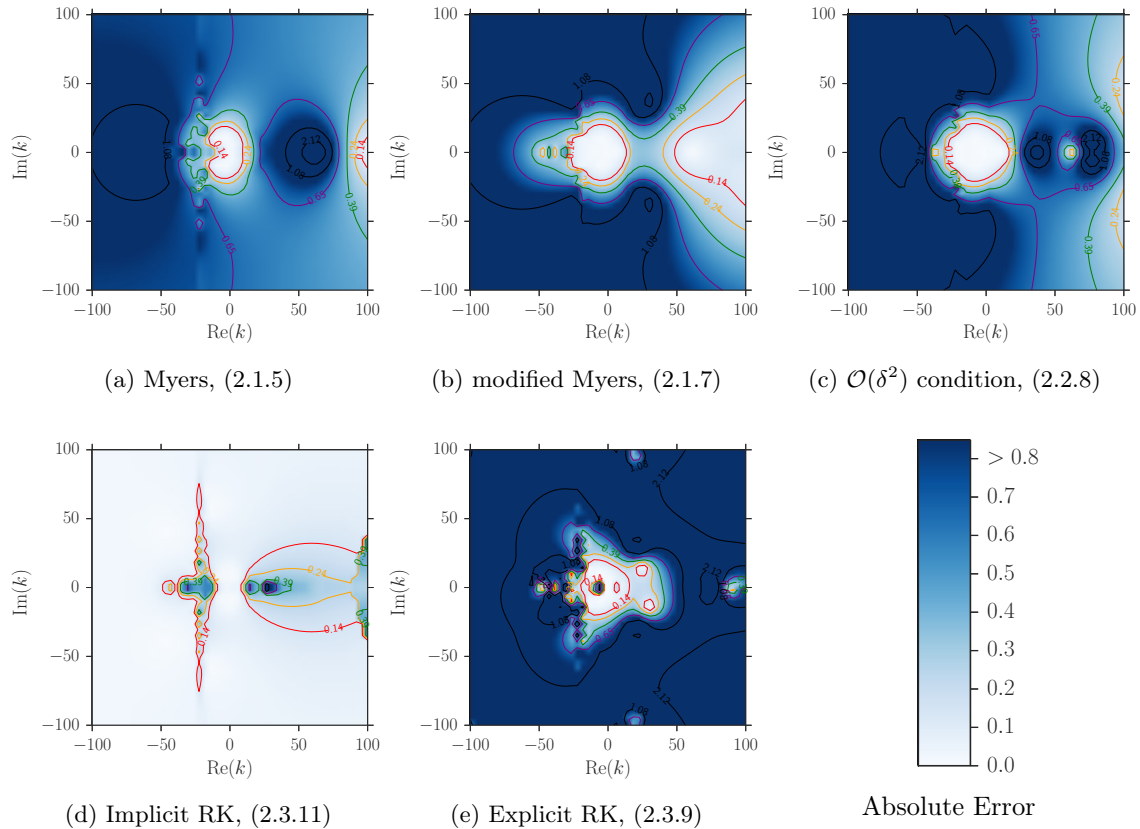


Figure 2.3. As in fig. 2.2, but for a boundary layer thickness $\delta = 3 \times 10^{-2}$. Note also the different error scale compared with fig. 2.2.

boundary layer.

In the bypass duct of an aeroengine the boundary layer may be much thicker than 10^{-3} . Figure 2.3 shows results for $\delta = 3 \times 10^{-2}$, with all other parameters as in fig. 2.2. For this relatively thick boundary layer, the region of asymptotic validity is $k \ll 33$, so it is no surprise that the breakdown of the asymptotic models (figs. 2.3b and 2.3c) occurs within the plotted domain. The Myers condition, fig. 2.3a, is also only usefully accurate in a small region near the origin. The instability of the explicit method makes it unusable in most circumstances (fig. 2.3e). The A-stable single-step implicit scheme, however, comes into its own for thicker boundary layers. Figure 2.3d shows the implicit scheme to be extremely accurate throughout the k domain. Importantly, the accuracy is not lessened as k increases past $1/\delta$, meaning the single-step implicit scheme may also be useful when short-wavelength, high-frequency waves interact with a thick boundary layer. There are, however, larger errors near the Doppler-shifted origin, which is a region important for modes close to cut-on. These errors can manifest as erroneous instabilities of the least cut-off upstream modes, discussed in §2.6.

2.5 Simplified forms and limiting cases

Although expressible analytically, the boundary condition in (2.2.8) contains integrals across the boundary layer that for a general boundary layer profile must be performed numerically. The single-step implicit scheme boundary condition (2.3.11) is also complicated in its most general form. We now investigate specific situations when fully closed, simplified forms of the conditions may be found.

2.5.1 Linear boundary profile

In the case of a linear boundary layer velocity profile

$$U(r) = \begin{cases} M(1-r)/\delta, & (1-r) < \delta \\ M, & (1-r) > \delta \end{cases} \quad (2.5.1)$$

with a constant density $\rho \equiv 1$, the integrals I_j in (2.2.8) may be performed analytically and a closed-form expression for the $\mathcal{O}(\delta^2)$ asymptotic solution can be written:

$$Z_{\text{eff}} = \frac{\omega}{\omega - Mk} \frac{Z + \delta \frac{iMk}{3\omega} (3\omega - 2Mk) + \delta^2 \frac{Mk}{12\omega} (8Z(k^2 + m^2) - (\omega Z - i)(4\omega - 3kM))}{1 + i\delta MkZ \frac{(k^2 + m^2)}{(\omega - Mk)^2} + \delta^2 \Upsilon_3}, \quad (2.5.2)$$

where

$$\begin{aligned} \Upsilon_3 = & \frac{Mk}{12(\omega - Mk)^2} \left(Mk^3 (4 - 3M^2) + 2k^2 (5M^2 - 4) \omega + Mk (4m^2 - 11\omega^2) \right. \\ & \left. - 8m^2\omega + 4\omega^3 \right) - 6iMk\omega Z (m^2 - k^2) (2\omega - 3Mk) \\ & + \frac{i\omega Z}{k^2 M^2} (m^2 - k^2) \ln \left(\frac{\omega}{\omega - Mk} \right). \end{aligned} \quad (2.5.3)$$

Equation (2.5.2), with (2.5.3), may be applied directly as a boundary condition assuming a uniform base flow.

The single-step implicit scheme (2.3.11) simplifies greatly for the specific linear shear profile (2.5.1). Using the sign convention for the roots as discussed in §2.D, the boundary condition reduces to

$$Z_{\text{eff}} = \frac{i\Omega_u}{\delta\mu^2} - \frac{i\Omega_u}{\delta\mu^2} \left\{ 1 + \frac{\delta Z \mu^2}{\Omega_u^2} \left(2i\omega + \delta(\omega^2 - k^2 - m^2)Z \right) - \delta^2 Mk \mu^2 \frac{(2\omega - Mk)}{\Omega_u^2} \right\}^{\frac{1}{2}}, \quad (2.5.4)$$

where, as before, $\Omega_u = \omega - Mk$ and $\mu^2 = k^2 + m^2 - \Omega_u^2$. Expanding the square root in the small- δ limit recovers the Myers condition at leading order.

Previous work has shown that the shape of the boundary layer profile is not as important for attenuation predictions as parameters such as the displacement and momentum thicknesses (Gabard, 2013; Nayfeh *et al.*, 1974). Thus, the explicit forms (2.5.2) and (2.5.4) could be used more generally if the thickness is altered to match the required boundary layer parameters.

As an example, the displacement thickness for a compressible flow may be defined

$$\delta^* = \int_0^1 1 - \frac{\rho(r)U(r)}{\rho_0 U_0} dr, \quad (2.5.5)$$

where a subscript 0 denotes a duct centreline value. Given a displacement thickness of a boundary layer profile that we wish to emulate, we could define a linear profile of the form (2.5.1) with $\delta \rightarrow 2\delta^*$. Momentum thickness and energy thickness might similarly be used.

2.5.2 Surface modes

Surface modes are waves localised near the boundary that decay exponentially into the core of the duct. A surface with a finite impedance (not hard wall) and an infinitesimally thin boundary layer can support up to four surface modes (Rienstra, 2003). Working to first-order in a finite boundary layer thickness above such a surface allows up to six surface modes to be supported (Brambley,

2013). To investigate the effect of the second-order corrections to the surface mode predictions, we utilise the scaling $k/\omega \gg 1$ and the surface mode dispersion relation (Brambley, 2013)

$$\mu - \frac{\omega - Mk}{iZ_{\text{eff}}} = 0, \quad (2.5.6)$$

where Z_{mod} in Brambley (2013) translates to the notation used here as $i\omega Z_{\text{mod}} = i(\omega - Mk)Z_{\text{eff}}$, and $\mu^2 = k^2 + m^2 - (\omega - Mk)^2$, with $\text{Re}(\mu) > 0$. By rearranging (2.2.8) such that we have $i(\omega - Mk)Z_{\text{eff}} = f(Z, Z_{\text{eff}})$, and using from (2.1.6)

$$Z_{\text{eff}} = (\omega - Mk) \frac{J_m(\alpha)}{i\alpha J'_m(\alpha)}, \quad \text{and} \quad \frac{J_m(\alpha)}{\alpha J'_m(\alpha)} \sim \frac{1}{\mu} \quad (2.5.7)$$

in the function $f(Z, Z_{\text{eff}})$, the surface mode dispersion relation (2.5.6) for the $\mathcal{O}(\delta^2)$ asymptotic solution may be written

$$\begin{aligned} 0 = i\omega Z \left[\mu - \mu^3 \delta^2 I_2 + \mu(k^2 + m^2)(\delta I_0 \delta I_1 + \delta^2 I_3 - \delta^2 I_5) \right. \\ \left. - (k^2 + m^2) \left(\delta I_1 + \left(\frac{2m^2}{\mu^2 - 1} \right) \delta^2 I_3 \right) - 2m^2 \left(\delta^2 I_4 - \frac{1}{\mu^2} (k^2 + m^2) \delta^2 I_6 \right) \right] \\ + \mu(\omega - Mk)^2 (\delta I_0 + \delta^2 I_2) + (k^2 + m^2)(\omega - Mk)^2 (\delta^2 I_3 - \delta I_0 \delta I_1) \\ + (\omega - Mk)^4 \delta^2 I_7 - (\omega - Mk)^2. \end{aligned} \quad (2.5.8)$$

To use the dispersion relation (2.5.8), the I_j integral terms must be evaluated in the regime $k/\omega \gg 1$ (or, in some cases, the wavenumber and frequency dependence extracted from the integrals). For the integrals I_0, I_1, I_2, I_4 and I_7 , this may be readily done. For the integrals I_3, I_5 and I_6 , however, global contributions are important and, as such, the k dependence cannot be extracted for a general boundary layer profile. To overcome this problem, the high- k/ω limit of the analytical results for a linear profile are used. This is, of course, detrimental to the resulting surface mode model, but it should give an idea of the number of possible new surface modes predicted by the second-order model. The asymptotic forms of the I_j integrals are shown in §2.C. Using these in (2.5.8) produces a polynomial in k of order 14 if we take Z to be locally reacting (independent of k), meaning that for a given frequency ω the $\mathcal{O}(\delta^2)$ asymptotic solution predicts the existence of a possible 14 surface modes. Not all of these solutions will correspond to real modes, however, since they must satisfy $\text{Re}(\mu) > 0$ in order to decay away from the boundary. The surface mode asymptotics of the modified Myers condition by Brambley (2013) predict only six possible surface modes. This suggests that either the modified Myers condition fails to predict all possible surface modes (through the neglect of important physics, say); or the new second-order model predicts spurious modes that are not shared by the Pridmore-Brown equation.

Repeating the above surface mode analysis for the single-step implicit Runge-Kutta scheme (2.5.4) produces a sixth-order polynomial in k , meaning a possible six surface modes for a given frequency. This matches the number predicted by the modified Myers condition (Brambley, 2013), and suggests that the extra surface modes predicted by the second-order asymptotic condition derived here are in fact spurious. This is investigated further in the next section.

2.6 Wavenumber spectrum and stability

Modes in the k -plane are found for the Myers, modified Myers, single-step implicit scheme (2.3.11), and the $\mathcal{O}(\delta^2)$ asymptotic solution (2.2.8), and compared with those found via numerical solution

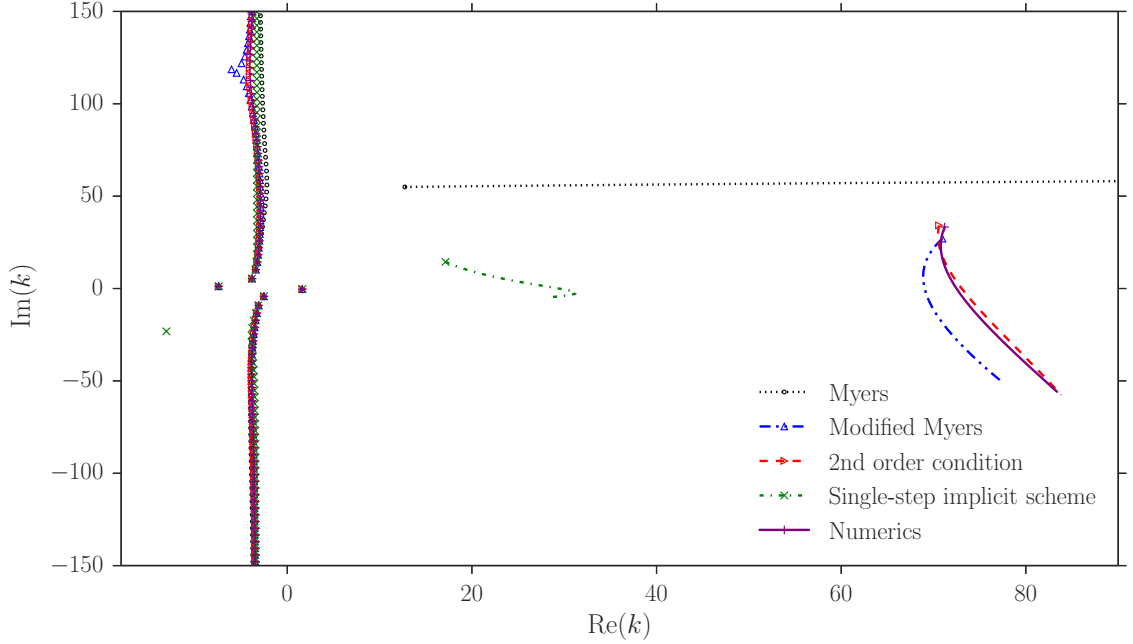


Figure 2.4. Modes in the k -plane of the Myers condition (black circle), modified Myers condition (blue triangle), single-step implicit scheme (2.3.11) (green cross), $\mathcal{O}(\delta^2)$ asymptotic solution (2.2.8) (red right-triangle) and Pridmore-Brown numerics (purple plus). The tanh boundary layer profile (2.5.1) is used, with a constant base density. Parameters are $\omega = 5$, $m = 0$, $M = 0.5$, $\delta = 2 \times 10^{-3}$. The boundary impedance for the markers is $Z = 3 + 0.52i$. The lines track the surface mode for each boundary condition as $\text{Im}(\omega)$ is reduced from zero to -10 , or sufficiently negative, as $\text{Re}(\omega)$ is held constant, and the boundary impedance changes in line with (5.6.1).

of the full Pridmore-Brown equation. The liner model used for all results here (unless specifically stated) is a mass–spring–damper impedance,

$$Z(\omega) = R + i\omega d - ib/\omega, \quad (2.6.1)$$

for $R = 3$, $d = 0.15$ and $b = 1.15$. Figure 2.4 shows the results for a tanh boundary layer profile with a boundary impedance of $Z = 3 - 0.52i$ and parameters $\omega = 5$, $m = 0$ and $\delta = 2 \times 10^{-3}$. In fig. 2.4, the $\mathcal{O}(\delta^2)$ asymptotic solution is seen to reproduce the full numerical modes with great accuracy. The single-step implicit condition predicts poorly the surface mode position in the right half-plane, but this is expected: the method cannot fully resolve a wave existing predominantly in the boundary layer; only information at the top and bottom edges of the boundary layer are used in the numerical scheme. The Myers condition cannot predict the position or behaviour of surface modes (see fig. 2.4), as it neglects boundary layer physics in favour of a vortex sheet.

The lines from the surface modes in the right half-plane of fig. 2.4 are Briggs–Bers (Bers, 1983; Briggs, 1964) contours, and give us information about the stability of the modes (see the appendix of Brambley (2009) for a full discussion). The modes are tracked as $\text{Im}(\omega)$ is reduced from zero to sufficiently negative. The impedance changes with ω via (5.6.1). All of the boundary conditions except the Myers condition predict a downstream propagating convective instability, due to their crossing the real k -axis from the upper to the lower half-planes. This convective instability is also present in the Pridmore-Brown numerics, visible in fig. 2.4.

Figure 2.5 shows the least cut-off modes in the k -plane for parameters typical of rotor–stator interaction in a turbofan engine. The downstream propagating modes in the right half of fig. 2.5 are well approximated by all the tested models. Discrepancies can be seen in the upstream propagating modes of the Myers condition and single-step implicit scheme, however. The Myers condition modes are too cut-off, which could be an explanation for the errors in sound absorption found in Gabard

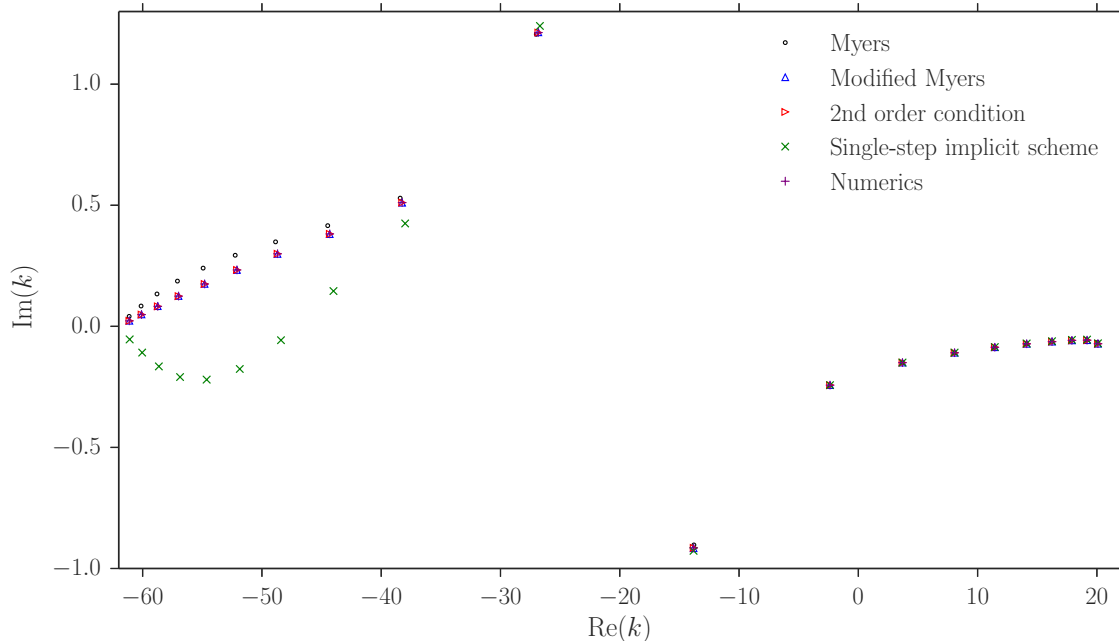


Figure 2.5. Least cut-off modes of the Myers condition (black circle), modified Myers condition (blue triangle), single-step implicit scheme (2.3.11) (green cross), $\mathcal{O}(\delta^2)$ asymptotic solution (2.2.8) (red right-triangle) and Pridmore-Brown numerics (purple plus), for $\omega = 31$, $m = 4$, $M = 0.5$, $\delta = 2 \times 10^{-3}$ and a tanh profile. The boundary impedance is $Z = 3 + 4.61i$.

(2013) when using the Myers condition. In contrast, the single-step implicit scheme modes have destabilised and have the wrong sign for $\text{Im}(k)$; this could be due to either a failing of the method or a wrong choice of sign for the square roots in the derivation (see §2.D for a detailed discussion). Both asymptotic methods correctly predict the Pridmore-Brown result.

Figure 2.6a shows results for $\omega = 10$, $m = 5$ and $\delta = 1 \times 10^{-3}$, with the addition of modes predicted by the $\mathcal{O}(\delta^2)$ asymptotic solution surface mode dispersion relation (2.5.8). The good agreement between the $\mathcal{O}(\delta^2)$ asymptotic solution and its surface mode dispersion relation for the four surface modes near the main spectrum on the right of fig. 2.6a shows that the reduced model (2.5.8) is working as intended. Importantly, the two modes in the lower left corner are unique to the $\mathcal{O}(\delta^2)$ asymptotic solution and its surface mode approximation, with no counterparts found using either the modified Myers condition or the full numerics. These modes also fall outside the range of validity of the asymptotics, since they do not satisfy $|k| \ll 1/\delta$. Figure 2.6b shows the movement of the modes as $\text{Im}(Z)$ is increased from -2.5 to sufficiently positive, where the mass-spring-damper liner model is not used. The four surface modes near the main spectrum join, or interact with, the cut-off modes as the impedance is varied. However, the modes in the lower left do not interact with the other modes in any way. These two pieces of information about the modes in the lower left – their irreproducibility by the numerics; and their unphysical isolation from the main spectrum – suggest they are spurious. Thus, as the surface mode dispersion relation (2.5.8) has been shown to be a valid approximation of (2.2.8), we may use it to suggest that the $\mathcal{O}(\delta^2)$ asymptotic solution predicts eight spurious surface modes. This may not be as harmful to the predictive power of the model as it seems at first: new modes could only exist (for reasonable ω and m) for k values large enough to bring the $\mathcal{O}(\delta^2)$ terms of (2.2.8) into balance with the $\mathcal{O}(\delta)$ or $\mathcal{O}(1)$ terms. This would inherently mean moving outside the region of asymptotic validity of the model, and hence a careful use of the new condition should prevent spurious modes being mistakenly deemed important. Indeed, the spurious modes in fig. 2.6 are outside the region of asymptotic validity, given by $|k| \ll 1000$.

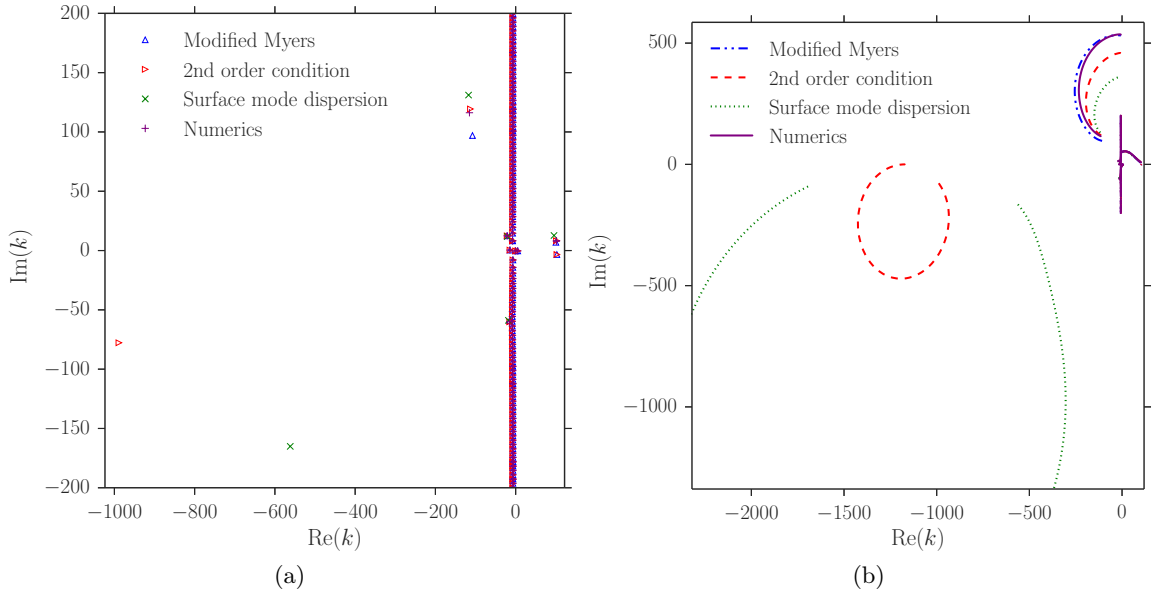


Figure 2.6. (a) Surface modes near the origin for $Z = 1 - 2.5i$, where here the mass-spring-damper model is not used. (b) A larger view of the k -plane, with tracks of surface modes as $\text{Im}(Z)$ is increased from -2.5 with $\text{Re}(Z) = 1$ held constant. A spurious mode can be seen far from the origin. In both plots the parameters are $\omega = 10$, $m = 5$, $\delta = 1 \times 10^{-3}$, for a tanh profile with $M = 0.5$.

2.6.1 The unstable hydrodynamic mode

Surface modes are important for stability analyses. In a laminar boundary layer, linearly unstable surface modes can seed turbulence which subsequently causes the boundary layer to thicken. Instability waves are also known to be a source of sound radiation (e.g. Tam & Morris, 1980), so being better able to predict the linear stability of the boundary layer over a liner is extremely important for aeroacoustic applications where noise suppression is the goal.

The unstable hydrodynamic modes (Brambley & Peake, 2006; Rienstra, 2003) of the asymptotic boundary conditions (2.1.5), (2.1.7) and (2.2.8) are traced for increasing real k in fig. 2.7, and compared with Pridmore-Brown numerics, where now we are solving for ω given k . The growth rate of the mode is $-\text{Im}(\omega)$. The $\mathcal{O}(\delta^2)$ asymptotic solution (dashed) replicates the full numerical solution (solid) accurately for moderate k . In this case, it is a quantitatively better approximation than the modified Myers for $k \lesssim 160$, which would be considered a very large wavenumber for most practical purposes. The $\mathcal{O}(\delta^2)$ asymptotic solution retains the regularisation that results from considering a finite-thickness shear layer; that is, applying the condition (2.2.8) (within its region of asymptotic validity) forms a well-posed system. It is therefore a usefully predictive tool for investigating maximum growth rates and representative wavelengths of the linear instability of an inviscid boundary layer over an impedance lining. For completeness, the Myers boundary condition prediction is plotted in fig. 2.7 (black dotted); its ill-posedness manifests as an unbounded growth rate. The Pridmore-Brown solution asymptotes to $\text{Im}(\omega) = 0$ as $k \rightarrow \infty$ but never becomes stable ($\text{Im}(\omega) > 0$) for any real k . Viscosity controls the restabilisation at small wavelengths (Khamis & Brambley, 2015): we would therefore not expect the inviscid numerics nor the inviscid boundary conditions (2.1.7) and ?? to be stable at large real k without the addition of a small amount of viscosity to stabilise the system for large wavenumbers.

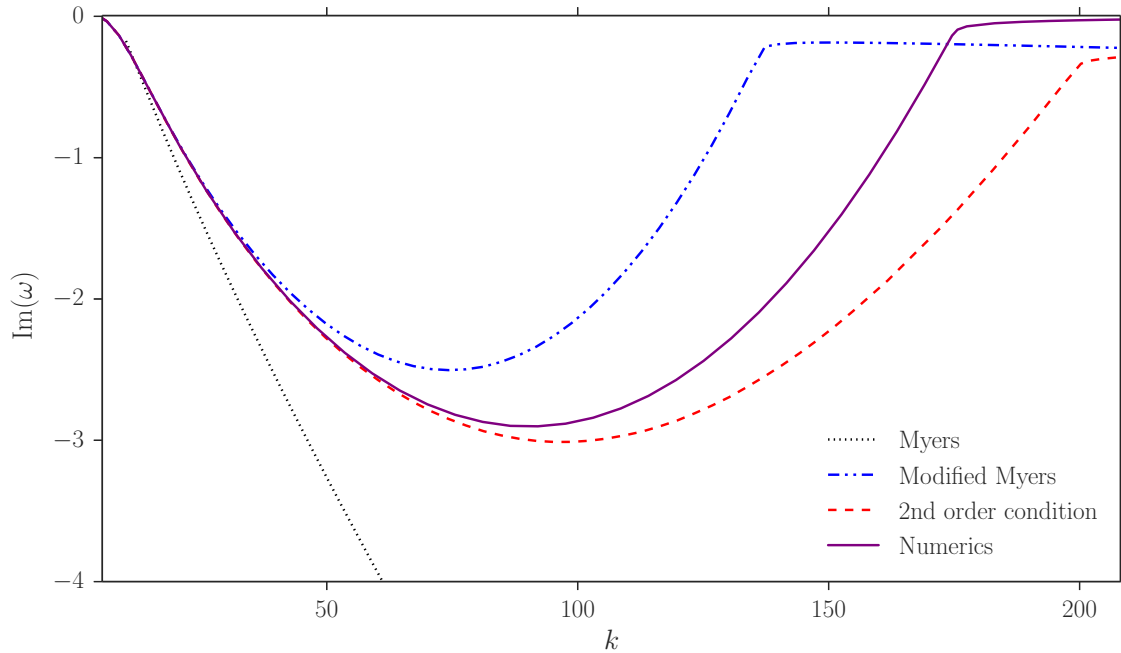


Figure 2.7. The unstable mode growth rate is plotted against real k for parameters $\delta = 2 \times 10^{-3}$, $m = 12$, $M = 0.5$, with a tanh boundary layer profile and a mass–spring–damper impedance, $Z(\omega) = R + i\omega d - ib/\omega$, for $R = 3$, $d = 0.15$, $b = 1.15$, as in (5.6.1).

2.7 Summary

In this chapter, the inviscid theory of sound propagation in an acoustically lined cylindrical duct has been extended. A new effective impedance boundary condition, that accounts for both refraction through the boundary layer and the impedance of the acoustic lining, was derived using matched asymptotic expansions in a thin shear layer at the wall and a uniform outer flow in the core of the duct. The new boundary condition, correct to second order in the boundary layer thickness, showed improvements in accuracy over the Myers (Ingard, 1959; Myers, 1980) condition and its first order correction (Brambley, 2011*b*) when compared with numerical solutions of the linearised Euler equations. The second-order boundary condition out-performed existing boundary conditions in the prediction of cut-on and real surface wave modes in the k -plane, and gave better approximations of the characteristic wavelength and growth rate of instability via stability analysis in the frequency domain. However, the new condition supports spurious surface modes that are not shared by the linearised Euler equations. This result suggests that the physics in the inviscid sheared boundary layer is adequately modelled by the first order modified Myers condition so as to account for all possible surface wave modes—a maximum of six (Brambley, 2013) per frequency and circumferential order, compared to the four supported by the Myers condition (Rienstra, 2003).

The spurious surface wave modes of the new second-order boundary condition occur outside its region of asymptotic validity, $k\delta \ll 1$, $\omega\delta \ll 1$, so their existence is not too damaging to the model. An alternative method was proposed to probe the parameter space outside the region of asymptotic validity of the second-order condition, where short wavelength, high frequency waves interact with a thick boundary layer. A nonlinear Riccati equation governing the evolution of the ratio $Z = \tilde{p}(r)/\tilde{v}(r)$ was derived and subsequently solved via Runge–Kutta integration steps performed analytically. Both a fourth-order explicit integration scheme and a second-order implicit scheme were used, with the explicit scheme shown to be greatly unstable. The implicit scheme was shown to accurately predict the effective impedance of a thick boundary layer at high wavenumbers

(where the asymptotic boundary conditions fail), while failing to predict surface modes due to its poor resolution of the boundary layer.

The general problem of a liner with grazing flow has many facets which themselves are open problems; including viscothermal effects which are in the most part neglected in the literature. It is known that viscosity by itself does not regularise the ill-posedness of the Myers condition (Brambley, 2011a), but that viscous effects can be necessary to accurately predict experimental results (Burak *et al.*, 2008, 2009; Renou & Aurégan, 2010, 2011). The next chapter investigates the effects of viscosity and thermal conduction on sound propagation in an acoustically lined duct, and attempts to quantify their importance in relation to mean flow shear.

Appendix

2.A Details of the asymptotics of the \tilde{p} and \tilde{v} governing equations

We solve (2.2.4) to second order for the inner solution by expanding the radial velocity as $\tilde{v} = \tilde{v}_0 + \delta\tilde{v}_1 + \delta^2\tilde{v}_2 + \mathcal{O}(\delta^3)$. We match to the outer solution

$$\begin{aligned} \tilde{v}_u(1 - \delta y) = v_\infty + \delta y \left(\frac{\mu^2}{i\Omega_u} p_\infty + v_\infty \right) \\ + \frac{1}{2} \delta^2 y^2 \left[(2 + \mu^2) v_\infty + \frac{\mu^2 + 2m^2}{i\Omega_u} p_\infty \right] + \mathcal{O}(\delta^3) \end{aligned} \quad (2.A.1)$$

in the limit $y \rightarrow \infty$, where for brevity $\Omega_u = \omega - Mk$, and $\mu^2 = k^2 + m^2 - \Omega_u^2$. With $\Omega = \omega - Uk$ and $\sigma_+ = k^2 + m^2$, the leading order solution is

$$\tilde{v}_0 = A_0\Omega + B_0\Omega \int_0^y 1 - \frac{\sigma_+}{\rho\Omega^2} dy', \quad (2.A.2)$$

which may be written in terms of bounded integrals as

$$\tilde{v}_0 = A_0\Omega - B_0\Omega y \frac{\mu^2}{\Omega_u^2} + B_0\Omega \frac{\sigma_+}{\Omega_u^2} \int_0^y 1 - \frac{\Omega_u^2}{\rho\Omega^2} dy'. \quad (2.A.3)$$

Upon matching with the leading order of (2.A.1) as $y \rightarrow \infty$ we find $B_0 \equiv 0$ and $A_0 = v_\infty/\Omega_u$. Similarly at first-order,

$$\tilde{v}_1 = A_1\Omega + A_0\Omega y - B_1\Omega y \frac{\mu^2}{\Omega_u^2} + B_1\Omega \frac{\sigma_+}{\Omega_u^2} \int_0^y 1 - \frac{\Omega_u^2}{\rho\Omega^2} dy'. \quad (2.A.4)$$

Matching with (2.A.1) gives $B_1 = ip_\infty$ and $A_1 = -i\sigma_+ I_1 p_\infty / \Omega_u^2$, where

$$I_1 = \int_0^\infty \chi_1(y) dy, \quad \chi_1(y) = 1 - \frac{(\omega - Mk)^2}{\rho(\omega - Uk)^2}. \quad (2.A.5)$$

At second order, we find

$$\begin{aligned} \tilde{v}_2 = A_2\Omega - B_2\Omega y \frac{\mu^2}{\Omega_u^2} + B_2\Omega \frac{\sigma_+}{\Omega_u^2} \int_0^y \chi_1 dy' + A_1\Omega y - B_1\Omega \int_0^y y \frac{\mu^2}{\Omega_u^2} dy' \\ + B_1\Omega \frac{\sigma_+}{\Omega_u^2} \int_0^y \left(\int_0^{y'} \chi_1 dy'' - I_1 \right) dy' + B_1\Omega \frac{\sigma_+}{\Omega_u^2} I_1 y + \frac{1}{2} A_0 \Omega y^2 \end{aligned}$$

$$\begin{aligned}
 & -2m^2\Omega\left(A_0 - B_1\frac{\mu^2}{\Omega_u^2}\right)\int_0^y\frac{y'}{\rho\Omega^2 - \sigma_+}dy' - 2m^2B_1\Omega\frac{\sigma_+}{\Omega_u^2}\int_0^y\frac{y'}{\rho\Omega^2 - \sigma_+}\chi_1dy' \\
 & + A_0\Omega\int_0^1y'\left(1 + \frac{2m^2}{\rho\Omega^2 - \sigma_+}\right)dy' - A_0\Omega\int_0^y\left(1 - \frac{\sigma_+}{\rho\Omega^2}\right)\int_0^{y'}\rho\Omega^2dy''dy'. \quad (2.A.6)
 \end{aligned}$$

In terms of bounded integrals suitable for matching, (2.A.6) may be rewritten as

$$\begin{aligned}
 \tilde{v}_2 = & A_2\Omega - B_2\Omega y\frac{\mu^2}{\Omega_u^2} + B_2\Omega\frac{\sigma_+}{\Omega_u^2}\int_0^y\chi_1dy' + A_1\Omega y - \frac{\mu^2\Omega}{2\Omega_u^2}B_1y^2 - \frac{m^2\Omega}{\Omega_u^2}B_1y^2 \\
 & + B_1\Omega\frac{\sigma_+}{\Omega_u^2}\int_0^y\left(\int_0^{y'}\chi_1dy'' - I_1\right)dy' + B_1\Omega\frac{\sigma_+}{\Omega_u^2}I_1y + \frac{1}{2}A_0\Omega y^2 + \frac{m^2\Omega}{\mu^2}A_0y^2 \\
 & + m^2\Omega\left(\frac{2B_1}{\Omega_u^2} - \frac{A_0}{\mu^2}\right)\int_0^yy'\left(1 - \frac{\Omega_u^2 - \sigma_+}{\rho\Omega^2 - \sigma_+}\right)dy' + \frac{2m^2\sigma_+}{\Omega_u^2}\frac{\Omega}{\mu^2}B_1\int_0^y\chi_1y'dy' \\
 & - \frac{2m^2\sigma_+}{\Omega_u^2}\frac{\Omega}{\mu^2}B_1\int_0^y\chi_1y'\left(1 - \frac{\Omega_u^2 - \sigma_+}{\rho\Omega^2 - \sigma_+}\right)dy' + A_0\sigma_+\Omega\int_0^y\chi_1\int_0^{y'}\chi_0dy''dy' \\
 & - A_0\Omega\mu^2\int_0^y\left(\int_0^{y'}\chi_0dy'' - I_0\right)dy' - A_0\Omega\mu^2I_0y \\
 & \quad - A_0\sigma_+\Omega\int_0^yy'\chi_1dy' + \frac{1}{2}A_0\Omega\mu^2y^2, \quad (2.A.7)
 \end{aligned}$$

where

$$I_0 = \int_0^\infty\chi_0(y)dy, \quad \chi_0(y) = 1 - \frac{\rho(\omega - Uk)^2}{(\omega - Mk)^2}. \quad (2.A.8)$$

At this order in the \tilde{v} expansion we introduce spurious singularities at $\mu^2 = 0$ and $\rho\Omega^2 = \sigma_+$. Taking $y \rightarrow \infty$ and matching with the outer solution gives

$$B_2 = \frac{\Omega_u^2}{\mu^2}A_1 + \frac{\sigma_+}{\mu^2}I_1B_1 - \Omega_u^2I_0A_0 \quad (2.A.9)$$

and

$$\begin{aligned}
 A_2 = & -B_2\Omega\frac{\sigma_+}{\Omega_u^2}I_1 - B_1\frac{\sigma_+}{\Omega_u^2}\int_0^\infty\left(\int_0^y\chi_1dy' - I_1\right)dy - m^2\left(\frac{2B_1}{\Omega_u^2} - \frac{A_0}{\mu^2}\right)\int_0^yy'\chi_2dy' \\
 & - \frac{2m^2\sigma_+}{\Omega_u^2\mu^2}I_3B_1 + \frac{2m^2\sigma_+}{\Omega_u^2\mu^2}B_1\int_0^\infty y\chi_1\chi_2dy - A_0\sigma_+\int_0^\infty\chi_1\int_0^y\chi_0dy'dy \\
 & + A_0\mu^2\int_0^\infty\left(\int_0^y\chi_0dy' - I_0\right)dy + A_0\sigma_+I_3, \quad (2.A.10)
 \end{aligned}$$

where

$$I_3 = \int_0^\infty y\chi_1(y)dy, \quad \text{and} \quad \chi_2(y) = 1 - \frac{(\omega - Mk)^2 - k^2 - m^2}{\rho(\omega - Uk)^2 - k^2 - m^2}. \quad (2.A.11)$$

Evaluating \tilde{v} at the wall, $y = 0$, leads to

$$\begin{aligned}
 \tilde{v}(0) = & \frac{\omega}{\Omega_u}\left\{v_\infty - \frac{i\sigma_+}{\Omega_u}p_\infty\delta I_1 - \sigma_+\left(\frac{2im^2p_\infty}{\Omega_u\mu^2} - v_\infty\right)\delta^2 I_3 + \sigma_+v_\infty\delta I_0\delta I_1\right. \\
 & + \frac{i\sigma_+}{\Omega_u}p_\infty\delta^2 I_3 - \mu^2v_\infty\delta^2 I_2 - \frac{2im^2p_\infty}{\Omega_u}\delta^2 I_4 - \sigma_+v_\infty\delta^2 I_5 \\
 & \left. + \frac{2im^2\sigma_+p_\infty}{\Omega_u\mu^2}\delta^2 I_6\right\} + \mathcal{O}(\delta^3), \quad (2.A.12)
 \end{aligned}$$

where

$$I_4 = \int_0^\infty y\chi_2(y)dy, \quad I_5 = \int_0^\infty\chi_1(y)\int_0^y\chi_0(y')dy'dy, \quad I_6 = \int_0^\infty y\chi_1(y)\chi_2(y)dy. \quad (2.A.13)$$

Equation (2.A.12) is equivalent to (2.2.5b) in the main part of the chapter.

The corresponding problem for \tilde{p} is solved in the same way, using the governing equation (2.2.3) and the outer solution (2.2.2a). The result is given in appendix A of Brambley (2011b) as

$$\begin{aligned} \tilde{p}(0) = p_\infty + i(\omega - Mk)v_\infty \delta I_0 + p_\infty(k^2 + m^2)\delta I_1 \delta I_0 + i(\omega - Mk)v_\infty \delta^2 I_2 \\ - (\omega - Mk)^2 p_\infty \delta^2 I_7 - p_\infty(k^2 + m^2)\delta^2 I_3. \end{aligned} \quad (2.A.14)$$

where

$$I_2 = \int_0^\infty y \chi_0(y) dy, \quad \text{and} \quad I_7 = \int_0^\infty \chi_0(y) \int_0^y \left(1 - \frac{k^2 + m^2}{\rho(y')(\omega - U(y')k)^2}\right) dy' dy. \quad (2.A.15)$$

The effective impedance is formed by taking the ratio $Z = \tilde{p}(0)/\tilde{v}(0)$ and dividing top and bottom by v_∞ . This gives $Z = f(Z_{\text{eff}})$ by virtue of the definition $Z_{\text{eff}} = p_\infty/v_\infty$; rearranging for Z_{eff} produces

$$Z_{\text{eff}} = \frac{\omega}{\Omega_u} \frac{Z + \delta \mathcal{A} + \delta^2 \mathcal{B}}{1 + \delta \mathcal{C} + \delta^2 \mathcal{D}} + \mathcal{O}(\delta^3) \quad (2.A.16)$$

where

$$\begin{aligned} \mathcal{A} &= -\frac{i\Omega_u^2}{\omega} I_0, & \mathcal{B} &= -\frac{i\Omega_u^2}{\omega} I_2 - Z\mu^2 I_2 + \sigma_+ Z(I_0 I_1 + I_3 - I_5), & \mathcal{C} &= i\sigma_+ \frac{\omega Z}{\Omega_u^2} I_1, \\ \mathcal{D} &= \frac{i\sigma_+ \omega Z}{\Omega_u^2} \left(\frac{2m^2}{\mu^2} - 1\right) I_3 + 2im^2 \frac{\omega Z}{\Omega_u^2} \left(I_4 - \frac{\sigma_+}{\mu^2} I_6\right) + \sigma_+(I_0 I_1 - I_3) - \Omega_u^2 I_7 \end{aligned}$$

which is equivalent to (2.2.8).

2.B Asymptotics of the impedance governing equation

Here we derive, asymptotically, two expressions for Z_{eff} from the nonlinear impedance equation (2.3.1), correct to first and second order in δ , respectively.

In the case of a nonuniform flow, where $U = U(r)$ and $\rho = \rho(r)$, we use (2.3.3) in (2.3.1) and substitute for L'_u from (2.3.4) to arrive at (2.3.5) which we repeat here for convenience:

$$\begin{aligned} \frac{1}{(\omega - Mk)} \tilde{L}' &= \frac{i}{r} \left[1 - \frac{\rho(\omega - Uk)^2}{(\omega - Mk)^2}\right] + ir \frac{k^2 + \frac{m^2}{r^2}}{(\omega - Mk)^2} \left[1 - \frac{(\omega - Mk)^2}{\rho(\omega - Uk)^2}\right] L_u^2 \\ &+ ir \left[1 - \frac{k^2 + \frac{m^2}{r^2}}{\rho(\omega - Uk)^2}\right] (2L_u \tilde{L} + \tilde{L}^2). \end{aligned} \quad (2.B.1)$$

The first two square brackets on the right-hand side of (2.B.1) are non-zero only in the thin boundary layer near $r = 1$. This suggests that a power series expansion of \tilde{L} in the boundary layer thickness δ is appropriate, so we write $\tilde{L} = \delta \tilde{L}_1 + \delta^2 \tilde{L}_2 + \mathcal{O}(\delta^3)$. The last square bracket is multiplied by terms proportional to \tilde{L} and \tilde{L}^2 , so the order-of-magnitude assumptions are self-consistent. We again rescale to lie within the boundary layer by writing $r = 1 - \delta y$. Expanding (2.B.1) in terms of y and in powers of δ produces

$$\begin{aligned} \frac{1}{\Omega_u} (\tilde{L}_1 + \delta \tilde{L}_2)' &= -i\chi_0 - i\frac{\sigma_+}{\Omega_u^2} L_u(0)^2 \chi_1 - \delta \left\{ iy\chi_0 + iy\frac{\sigma_-}{\Omega_u^2} L_u(0)^2 \chi_1 \right. \\ &\quad \left. - 2iy\frac{\sigma_+}{\Omega_u^2} L_u(0)L'_u(0)\chi_1 + 2i\left(1 - \frac{\sigma_+}{\rho\Omega^2}\right) L_u(0)\tilde{L}_1 \right\}, \end{aligned} \quad (2.B.2)$$

where $\sigma_\pm = m^2 \pm k^2$, $\Omega(y) = \omega - U(y)k$, $\Omega_u = \omega - Mk$, and the χ_j are defined as in (2.2.7).

Our boundary conditions are $\tilde{L}_j \rightarrow 0$ as $y \rightarrow \infty$ for $j = 1, 2$. In (2.B.2) the Taylor expansion of L_u about the lined wall, $L_u(y) = L_u(0) - \delta y L'_u(0) + \mathcal{O}(\delta^2)$, is used. We note that in this section all arguments are now in terms of y unless explicitly stated; a prime represents a derivative with respect to y , and an argument of $y=0$ relates to a value at the wall, where $r=1$.

We may integrate the leading order terms in (2.B.2) to find an expression for \tilde{L}_1 ,

$$\tilde{L}_1 = i\Omega_u \left[I_0 - \int_0^y \chi_0(z) dz + \frac{\sigma_+}{\Omega_u^2} L_u^2(0) \left(I_1 - \int_0^y \chi_1(z) dz \right) \right], \quad (2.B.3)$$

where the integration constants I_j are defined as in (2.2.6). This ensures that $\tilde{L}_1 \rightarrow 0$ as $y \rightarrow \infty$, such that, as we move into the main body of the duct, where the flow is uniform, our L value tends to its uniform flow value L_u . Evaluating (2.B.3) at $y=0$ causes the integrals to vanish, and thus we find an expression for L at the wall, correct to first order in δ :

$$L(0) = L_u(0) + i\Omega_u \delta \left[I_0 + I_1 \frac{\sigma_+}{\Omega_u^2} L_u^2(0) \right] + \mathcal{O}(\delta^2). \quad (2.B.4)$$

From (2.3.2), no slip at the boundary implies $L(0) = \omega Z / \Omega_u$. Similarly, a uniform slipping flow implies $L_u(0) = Z_{\text{eff}}$. At leading order, then, (2.B.4) becomes

$$Z_{\text{eff}} = \frac{\omega}{\Omega_u} Z + \mathcal{O}(\delta), \quad (2.B.5)$$

which is the Myers effective impedance (2.1.5), as expected (Myers, 1980). If we make the approximation $L_u^2(0) = Z Z_{\text{eff}} / (1 - Mk/\omega) + \mathcal{O}(\delta)$, we can rearrange (2.B.4) at first order to find

$$Z_{\text{eff}} = \frac{\omega}{\Omega_u} \frac{Z - \frac{i}{\omega} \Omega_u^2 \delta I_0}{1 + i\sigma_+ \frac{\omega Z}{\Omega_u^2} \delta I_1} + \mathcal{O}(\delta^2), \quad (2.B.6)$$

which is the modified Myers effective impedance (2.1.7), as derived using matched asymptotic expansions of \tilde{p} in Brambley (2011b).

Continuing, the first-order terms in (2.B.2) may be examined to find the second-order correction terms. Upon integration,

$$\begin{aligned} \tilde{L}_2 = i\Omega_u \left\{ I_2 - \int_0^y z \chi_0(z) dz + \Gamma L_u(0) \left(I_3 - \int_0^y z \chi_1(z) dz \right) \right. \\ \left. + 2L_u(0) \left(I_8 - \int_0^y \tilde{L}_1(z) \left[1 - \frac{\sigma_+}{\rho(z)\Omega(z)^2} \right] dz \right) \right\}, \end{aligned} \quad (2.B.7)$$

where

$$\Gamma = \frac{\sigma_-}{\Omega_u^2} L_u(0) - 2i \frac{\sigma_+}{\Omega_u} \left[1 - \left(1 - \frac{\sigma_+}{\Omega_u^2} \right) L_u(0)^2 \right]$$

and the new integration constant, I_8 , is defined by

$$I_8 = \int_0^\infty \tilde{L}_1 \left[1 - \frac{\sigma_+}{\rho\Omega^2} \right] dy. \quad (2.B.8)$$

As before, this ensures that $\tilde{L}_2 \rightarrow 0$ as $y \rightarrow \infty$ such that we find the correct \tilde{L} behaviour in the uniform core of the duct. Using (2.B.3) and (2.B.7) in (2.3.3) we have, at the boundary,

$$L(0) = L_u(0) + i\Omega_u \left(\delta \left[I_0 + I_1 \frac{\sigma_+}{\Omega_u^2} L_u^2(0) \right] + \delta^2 \left[I_2 + \Gamma L_u(0) I_3 + 2L_u(0) I_8 \right] \right) + \mathcal{O}(\delta^3). \quad (2.B.9)$$

By rearranging (2.B.9) we find the effective impedance,

$$Z_{\text{eff}} = \frac{\omega}{\Omega_u} \frac{Z - \frac{i}{\omega} \Omega_u^2 (\delta I_0 + \delta^2 I_2)}{1 + i \delta \frac{\sigma_{\pm}}{\Omega_u} L_u(0) I_1 + i \Omega_u \delta^2 (\Gamma I_3 + 2I_8)} + \mathcal{O}(\delta^3), \quad (2.B.10)$$

where the values of $L_u(0)$ in the denominator, in the Γ term and in the I_8 integral must be approximated. Herein lies a key issue with this method: the nonlinear L_u terms force approximations to be made for which there is no guiding *modus operandi*. In the matched asymptotic expansions derivation which leads to the condition (2.2.8), no such Z_{eff}^2 splittings have to be made; the linear form falls naturally out of the mathematics. Different asymptotic forms of (2.B.10) may be found by using different approximations, and it transpires that the behaviour of the boundary condition (2.B.10) is heavily dependent on the chosen form. While (2.2.8) and (2.B.10) are asymptotically equivalent, it is difficult to see from (2.B.10) any reason to choose the approximation leading to (2.2.8), although other approximations seem to give worse results than (2.2.8).

We conclude by remarking that although a unique, useful second-order condition does not fall easily out of the impedance governing equation, the derivation of the first-order modified Myers condition is cleaner than that of Brambley (2011*b*).

2.C Surface mode asymptotics of I_j integrals

The integrals I_j are approximated in the $k/\omega \gg 1$ limit as

$$\begin{aligned} \delta I_0 &= \frac{1}{(\omega - Mk)^2} (\omega^2 \delta_{\text{mass}} - 2Mk\omega \delta_{\text{mom}} + M^2 k^2 \delta_{\text{ke}}), & \delta I_1 &\sim \delta_s \frac{Mk}{\omega}, \\ \delta^2 I_2 &= \frac{1}{(\omega - Mk)^2} (\omega^2 \tilde{\delta}_{\text{mass}}^2 - 2Mk\omega \tilde{\delta}_{\text{mom}}^2 + M^2 k^2 \tilde{\delta}_{\text{ke}}^2), \\ \delta^2 I_3 &\sim \delta^2 \left[\frac{3}{2} + \ln \left(\frac{\omega/k}{\omega/k - M} \right) \right], \\ \delta^2 I_4 &\sim \int_0^1 (1-r) \left(1 - \frac{M^2 - 1}{\rho U^2 - 1} \right) dr + \frac{\omega}{k} \int_0^1 \frac{2(1-r)}{\rho U^2 - 1} \left(M - \frac{\rho U (M^2 - 1)}{\rho U^2 - 1} \right) dr, \\ \delta^2 I_5 &\sim \delta^2 \left[\frac{19}{12} M^2 k^2 - \frac{13}{3} Mk\omega + \ln \left(\frac{\omega/k}{\omega/k - M} \right) \right], \\ \delta^2 I_6 &\sim \delta^2 \left[\frac{1}{2} + M^2 + M^2 \ln \left(\frac{\omega/k}{\omega/k - M} \right) + \frac{1 - M^4}{2M^2} \ln \left(1 - \frac{Mk(Mk - 2\omega)}{(\omega - Mk)^2 - k^2 - m^2} \right) \right], \\ \delta^2 I_7 &\sim \frac{\delta_s (k^2 + m^2)}{Mk\omega (\omega - Mk)^2} (\omega^2 \delta_{\text{mass}} - 2Mk\omega \delta_{\text{mom}} + M^2 k^2 \delta_{\text{ke}}), \end{aligned}$$

where I_0 and I_2 are exact, and

$$\begin{aligned} \delta_s &= \frac{-M}{\rho(1)U'(1)}, & \delta_{\text{mass}} &= \int_0^1 (1-\rho) dr, & \delta_{\text{mom}} &= \int_0^1 1 - \frac{\rho U}{M} dr \\ \delta_{\text{ke}} &= \int_0^1 1 - \frac{\rho U^2}{M^2} dr, & \tilde{\delta}_{\text{mass}}^2 &= \int_0^1 (1-r)(1-\rho) dr, \\ \tilde{\delta}_{\text{mom}}^2 &= \int_0^1 (1-r) \left(1 - \frac{\rho U}{M} \right) dr, & \tilde{\delta}_{\text{ke}}^2 &= \int_0^1 (1-r) \left(1 - \frac{\rho U^2}{M^2} \right) dr, \end{aligned}$$

are measures of boundary layer thickness.

2.D The implicit scheme

The second-order trapezoidal single-step implicit scheme is the highest-order such scheme for which a closed-form solution can be written. The fundamental difference equation for the differential equation $y' = f(x, y)$ is

$$y_{n+1} = y_n + \frac{h}{2}(f(x_n, y_n) + f(x_{n+1}, y_{n+1})), \quad (2.D.1)$$

which may be written as

$$y_{n+1} = y_n + \frac{h}{2}(k_1 + k_2), \quad (2.D.2)$$

where

$$k_1 = f(x_n, y_n), \quad k_2 = f\left(x_n + h, y_n + \frac{h}{2}k_1 + \frac{h}{2}k_2\right). \quad (2.D.3)$$

We use this scheme to solve (2.3.1) and (2.3.4), which we rewrite together here in the form

$$L' = A_j(r) + B_j(r)L^2, \quad (2.D.4)$$

for $j = 1, 2$, with

$$\begin{aligned} A_1(r) &= -\frac{i}{r} \frac{\rho(\omega - Uk)^2}{\omega - Mk}, & B_1(r) &= ir(\omega - Mk) \left(1 - \frac{k^2 + m^2/r^2}{\rho\Omega^2}\right), \\ A_2(r) &= -\frac{i}{r}(\omega - Mk), & B_2(r) &= ir(\omega - Mk) \left(1 - \frac{k^2 + m^2/r^2}{(\omega - Mk)^2}\right). \end{aligned}$$

Equation (2.D.4) with $j = 1$ is the impedance governing equation for a sheared flow (our boundary layer), while for $j = 2$ it is the corresponding equation for a uniform flow (our imagined slipping flow with no sheared boundary layer).

This scheme actually performs two steps, one for each boundary layer, sheared and uniform. Starting from the boundary $r = 1$ with the known impedance Z , we step backwards a distance δ through the sheared boundary layer (equation (2.D.4) with $j = 1$):

$$k_1 = A_1(1) + B_1(1)X_0^2, \quad (2.D.5a)$$

$$\begin{aligned} k_{2\pm} &= \frac{2}{\delta^2 B_1(1-\delta)} + 2\frac{X_0}{\delta} - k_1 \\ &\pm \sqrt{\left(\frac{2}{\delta^2 B_1(1-\delta)} + 2\frac{X_0}{\delta} - k_1\right)^2 - \frac{4}{\delta^2} \left(\frac{A_1(1-\delta)}{B_1(1-\delta)} + \left(X_0 - \frac{1}{2}\delta k_1\right)^2\right)}; \end{aligned} \quad (2.D.5b)$$

leading to

$$X_{1\pm} = X_0 - \frac{1}{2}\delta(k_1 + k_{2\pm}). \quad (2.D.6)$$

The quantity $X_0 = \omega Z/(\omega - Mk)$ is $L(1)$ as defined in (2.3.2), and gives the recovery of the Myers condition in the limit $\delta \rightarrow 0$. There are two possible solutions from the square root; however, it is possible to disregard one by considering the small- δ limit. From (2.D.5b), $k_{2\pm}$ may be rewritten

$$k_{2\pm} = Y \pm Y\sqrt{1 + W}, \quad (2.D.7)$$

where

$$Y = \frac{2}{\delta^2 B_1(1-\delta)} + 2\frac{X_0}{\delta} - k_1, \quad W = -\frac{4}{\delta^2 Y^2} \left(\frac{A_1(1-\delta)}{B_1(1-\delta)} + (X_0 - \delta k_1/2)^2\right). \quad (2.D.8)$$

Since Y is $\mathcal{O}(1/\delta^2)$, the term inside the square root in (2.D.7) may be Taylor-expanded as $\sqrt{1 + \delta^2 W} \sim 1 + \delta^2 W/2 + \mathcal{O}(\delta^4)$. Taking the positive root leads to $k_{2+} = \mathcal{O}(1/\delta^2)$, while taking the negative root gives $k_{2-} = \mathcal{O}(1)$. Considering (2.D.6), the single implicit Runge–Kutta step would produce an $\mathcal{O}(1/\delta)$ change between the quantities X_1 and X_0 if k_{2+} was chosen, and an $\mathcal{O}(\delta)$ change if k_{2-} was chosen. Over a small distance we expect a stable solution to change by a small amount; thus, we disregard the positive root and write $X_{1\pm} \equiv X_1$. Note, this assumption may break down if $\delta^2 W$ is not a small quantity, or if a mode oscillates rapidly within the boundary layer.

When computing the value of k_2 , we rewrite (2.D.7) to eliminate the possibility of rounding errors for small W . The square root may be expanded as a binomial series when $|W| < 1$,

$$(1 + W)^{\frac{1}{2}} = \sum_{n=0}^{\infty} \binom{1/2}{n} W^n. \quad (2.D.9)$$

The leading coefficient of (2.D.9) is unity, which, when multiplied by the Y outside the root, cancels with the first Y term in (2.D.7) when the correct negative root is taken (by the scaling argument above). The remaining terms in the series, $n \in [1, \infty)$, may be approximated by the Padé approximant $r(z) = p(z)/q(z)$ (for polynomials p, q) with the zeroth-order coefficient of $p(z)$ set to zero. Then, $k_2 = -Yp(W)/q(W)$. If $|W| \geq 1$, the explicit square root form (2.D.7) may be used.

Next, we step forward from the edge of the boundary layer at $r = 1 - \delta$ through the imagined uniform boundary layer (equation (2.D.4) with $j = 2$) to the boundary, where the impedance is the effective impedance Z_{eff} . The quantity X_1 serves as our initial condition, and generates a further two solutions:

$$\tilde{k}_1 = A_2(1 - \delta) + B_2(1 - \delta)X_1^2, \quad (2.D.10a)$$

$$\tilde{k}_{2\pm} = \tilde{Y} \pm \tilde{Y} \sqrt{1 + \tilde{W}}, \quad (2.D.10b)$$

where

$$\tilde{Y} = \frac{2}{\delta^2 B_2(1)} - 2 \frac{X_1}{\delta} - \tilde{k}_1, \quad \tilde{W} = -\frac{4}{\delta^2 \tilde{Y}^2} \left(\frac{A_2(1)}{B_2(1)} + \left(X_1 + \frac{1}{2} \delta \tilde{k}_1 \right)^2 \right), \quad (2.D.11)$$

and where we again take the negative root of $\tilde{k}_{2\pm}$ in (2.D.10b), writing $\tilde{k}_{2\pm} \equiv \tilde{k}_2$. The computation of \tilde{k}_2 may again be done via Padé approximation if $|\tilde{W}| < 1$. Since we have a binomial series with index $1/2$, the same polynomials $p(z)$ and $q(z)$ from above may be used, and evaluated at the new argument \tilde{W} . We arrive at a single value for Z_{eff} ,

$$Z_{\text{eff}} = X_1 + \frac{1}{2} \delta (\tilde{k}_1 + \tilde{k}_2), \quad (2.D.12)$$

which is the result in the main part of the chapter.

Chapter 3

A numerical study of the effects of shear and viscosity on sound attenuation and flow stability

In this chapter, the effects of viscosity and thermal conduction on the propagation of sound in a lined duct with shear flow are analysed by numerically solving the linearised Navier–Stokes equations (given in §3.1). The work presented in this chapter has been submitted for publication in the *Journal of Fluid Mechanics* (Khamis & Brambley, 2016*b*); some of this work was presented at the AIAA Aeroacoustics conference (Khamis & Brambley, 2015). Details of the numerical solution are given in §3.2. Comparisons are made with inviscid computations in inviscid shear flow in §3.3. To quantify the results, separate comparisons are made between the inviscid shear flow computations and analytical solutions for the acoustics in inviscid uniform flow. Since it is widely accepted that the effects of shear are important to the acoustics in a duct (Gabard, 2013), we use this second comparison as a baseline against which to judge the relative importance of viscosity.

3.1 Governing equations

A fluid can be described by six variables: three orthogonal components of the velocity $\mathbf{u} = (u, v, w)$, and three state variables (P, ρ, T) , the pressure, density, and temperature respectively. The dynamics of a viscous, compressible perfect gas are governed by the Navier–Stokes equations (1.1.10).

Each flow variable Q_{total} is assumed to have a time-averaged base flow part and a time harmonic acoustic part, such that $Q_{\text{total}}(\mathbf{r}, t) = Q(\mathbf{r}) + \epsilon_a q(\mathbf{r}) \exp\{i\omega t\}$, where $\epsilon_a \ll 1$ is the magnitude of acoustic oscillations, and ω is the dimensionless frequency (the Helmholtz number).

3.1.1 Steady base flow

Rather than solve the steady Navier–Stokes equations, or indeed solve the unsteady Navier–Stokes equations (possibly together with a sub-grid-scale turbulence model) and then time average, we approximate the steady base flow as a simple analytic profile, which we do not therefore require to satisfy (1.1.10). This is in order to compare with inviscid results with similar assumptions and with empirical profiles derived from experiments. We consider flow along a cylinder with coordinate system $\mathbf{r} = (x, r, \theta)$, as shown in fig. 1.3, and take the steady base flow velocity and temperature to be independent of x and θ , and the base flow velocity to be in the axial direction. This is a

reasonable approximation for viscous flow provided we are sufficiently far from a leading edge that the boundary layer varies little over the x range to be considered (Brambley, 2011a). At the duct wall, we require no slip, $U(1) = 0$, and thermal equilibrium, $T_r(1) = 0$, where a subscript denotes differentiation. Subject to these constraints, no restriction is placed on the mean flow velocity profile $U(r)$ and temperature profile $T(r)$. The base flow density is given by $1/\rho(r) = (\gamma - 1)T(r)$ from the constitutive law (1.1.10d) and the fact that the base flow pressure is constant. Note that if $T(r)$ were a constant independent of r then the base flow sound speed $c_0(r)$ would also be constant, although this is not assumed in what follows.

All results presented here are for a hyperbolic velocity and temperature profile,

$$U(r) = M \tanh\left(\frac{1-r}{\delta}\right) + M\left(1 - \tanh\left(\frac{1}{\delta}\right)\right)\left(\frac{1 + \tanh(1/\delta)}{\delta}r + (1+r)\right)(1-r) \quad (3.1.1a)$$

$$T(r) = T_0 + \tau\left(\cosh\left(\frac{1-r}{\delta}\right)\right)^{-1}, \quad (3.1.1b)$$

where δ is a measure of boundary layer thickness, with $U(1-\delta) \approx 0.76M$ and $U(1-3\delta) \approx 0.995M$. Motivated by the compressible Blasius boundary layer temperature profile, we take $\tau = 0.104$ to three significant figures in what follows. We vary M and δ later.

3.1.2 The linearised Navier–Stokes equations

To derive the linearised Navier–Stokes equations (LNSE) we Fourier transform the acoustic quantities in the axial coordinate, and define a Fourier series in the azimuthal coordinate. Then we consider a single mode as in (1.1.12). Linearising (1.1.10) about the base flow leads to (1.1.13), which we rewrite here for convenience as

$$0 = i(\omega - Uk)\gamma\tilde{p} - i(\omega - Uk)(\gamma - 1)\rho\tilde{T} - ik\tilde{u} + T\left(\frac{\tilde{v}}{\tilde{T}}\right)_r + \frac{1}{r}\tilde{v} - \frac{im}{r}\tilde{w} \quad (3.1.2a)$$

$$0 = i\rho(\omega - Uk)\tilde{u} + \rho U_r\tilde{v} - ik\tilde{p} - \frac{1}{\text{Re}}\left\{(\mathcal{H}\tilde{u}_r + U_r\tilde{\mathcal{H}})_r + \frac{1}{r}(\mathcal{H}\tilde{u}_r + U_r\tilde{\mathcal{H}}) - \frac{m^2}{r^2}\mathcal{H}\tilde{u}\right. \\ \left. - (2 + \beta)k^2\mathcal{H}\tilde{u} - ik(1 + \beta)(\mathcal{H}\tilde{v})_r + ik\beta\mathcal{H}_r\tilde{v} - \frac{ik}{r}(1 + \beta)\mathcal{H}\tilde{v} - \frac{km}{r}(1 + \beta)\mathcal{H}\tilde{w}\right\} \quad (3.1.2b)$$

$$0 = i\rho(\omega - Uk)\tilde{v} + \tilde{p}_r - \frac{1}{\text{Re}}\left\{(2 + \beta)(\mathcal{H}\tilde{v}_r)_r - \frac{2}{r}\mathcal{H}_r\tilde{v} - \left(k^2 + \frac{m^2}{r^2}\right)\mathcal{H}\tilde{v} + (2 + \beta)\left(\frac{\mathcal{H}\tilde{v}}{r}\right)_r\right. \\ \left. - ik(1 + \beta)(\mathcal{H}\tilde{u})_r + ik(\mathcal{H}_r\tilde{u} - U_r\tilde{\mathcal{H}}) - im(1 + \beta)\left(\frac{\mathcal{H}\tilde{w}}{r}\right)_r + \frac{im}{r}\mathcal{H}_r\tilde{w} + \frac{2im}{r^2}\mathcal{H}\tilde{w}\right\} \quad (3.1.2c)$$

$$0 = i\rho(\omega - Uk)\tilde{w} - \frac{im}{r}\tilde{p} - \frac{1}{\text{Re}}\left\{-\frac{km}{r}(1 + \beta)\mathcal{H}\tilde{u} - \frac{im}{r^2}(3 + \beta)\mathcal{H}\tilde{v} - \frac{im}{r}(1 + \beta)(\mathcal{H}\tilde{v})_r\right. \\ \left. + \frac{im}{r}\beta\mathcal{H}_r\tilde{v} - \left(k^2 + \frac{m^2}{r^2}\right)\mathcal{H}\tilde{w} + (\mathcal{H}\tilde{w}_r)_r - \frac{m^2}{r^2}(1 + \beta)\mathcal{H}\tilde{w} + \mathcal{H}\left(\frac{\tilde{w}}{r}\right)_r - \frac{1}{r}\mathcal{H}_r\tilde{w}\right\} \quad (3.1.2d)$$

$$0 = i\rho(\omega - Uk)\tilde{T} + \rho T_r\tilde{v} - i(\omega - Uk)\tilde{p} - \frac{1}{\text{Re}}\left\{U_r^2\tilde{\mathcal{H}} + 2\mathcal{H}U_r\tilde{u}_r - 2ik\mathcal{H}U_r\tilde{v}\right. \\ \left. + \frac{1}{\text{Pr}}\left((\mathcal{H}\tilde{T}_r + T_r\tilde{\mathcal{H}})_r + \frac{1}{r}(\mathcal{H}\tilde{T}_r + T_r\tilde{\mathcal{H}}) - \left(k^2 + \frac{m^2}{r^2}\right)\mathcal{H}\tilde{T}\right)\right\}, \quad (3.1.2e)$$

The system (3.1.2) is closed by assigning a functional form to $\mathcal{H}(r, T)$, introduced in (1.1.16), and Taylor expanding; to leading order in the acoustic perturbations we find

$$\tilde{\mathcal{H}} = \left. \frac{\partial \mathcal{H}(r, T)}{\partial T} \right|_{(r, T)} \tilde{T}. \quad (3.1.3)$$

In this chapter we forego the radial dependence of the viscosity and choose a linear temperature dependence as a ‘leading order’ approximation of the true dependence (Kadoya *et al.*, 1985).¹ Thus, we define

$$\mathcal{H}(r, T) = \frac{T}{T_0}. \quad (3.1.4)$$

The shear and bulk viscosities are assigned the same temperature dependence, as their ratio μ^{B*}/μ^* is relatively insensitive to temperature variations in both air and water (Pierce, 1994, chap. 10).

The LNSE, as given in (3.1.2) with (3.1.4), form a system of five linear ordinary differential equations in r for the five acoustic quantities $(\tilde{p}, \tilde{u}, \tilde{v}, \tilde{w}, \tilde{T})$. The system is first order in \tilde{p} and second order in $\tilde{u}, \tilde{v}, \tilde{w}$ and \tilde{T} so we may apply nine boundary conditions. At $r = 0$, each variable must satisfy a regularity condition. At the duct wall $r = 1$, no slip specifies $\tilde{u}(1) = \tilde{w}(1) = 0$ while the isothermal assumption of the duct wall specifies $\tilde{T}(1) = 0$. As the ninth boundary condition we choose to normalise our solution by specifying $\tilde{p}(1) = 1$ in order to force a nonzero solution, which therefore leaves $\tilde{v}(1)$ unconstrained. Note that a unique solution with these boundary conditions may be expected for any values of ω, k and m .

At the wall, the acoustic pressure drives a nonzero radial velocity given by the impedance Z (nondimensionalised by $Z^* = \rho_0^* c_0^* Z$). Because of the no slip condition, this unambiguously implies the additional boundary condition

$$\frac{\tilde{p}(1)}{\tilde{v}(1)} = Z, \quad (3.1.5)$$

which is a dispersion relation relating allowable values for ω, k and m . Each allowable value of (ω, k, m) is referred to as a duct mode. The impedance Z may depend upon ω, k or m through an appropriate, causal liner model (Rienstra, 2006). For example, a mass–spring–damper model of the boundary with a mass d , spring constant b and damping coefficient R gives the impedance

$$Z(\omega) = R + i\omega d - ib/\omega. \quad (3.1.6)$$

However, for now we make no assumption of the specific form of $Z(\omega, k)$.

3.2 Numerical method

Here, we describe the method used here to solve the LNSE (3.1.2) numerically. The domain of the problem is $r \in [0, 1]$, although near the wall at $r = 1$ we will consider a thin boundary layer. We therefore choose to discretise the domain non-uniformly, with more grid points clustered near the boundary $r = 1$. This non-uniform grid is then mapped to a uniformly-spaced computational grid, $\psi \in [0, 1]$, using the map

$$r = \frac{\tanh S\psi}{\tanh S}, \quad (3.2.1)$$

¹The reference gives the viscosity of dry air as $\mu = B(A_1 T + A_{0.5} T^{0.5} + \sum_{i=0}^{-4} A_i T^i) + \Delta\mu_\rho$, where B and the A_j are empirical fitting parameters and the $\Delta\mu_\rho$ is some small ‘‘excess’’ viscosity that depends on the density.

where $S > 0$ is a stretching parameter. Larger values of S allow more points to be clustered near $r = 1$. The LNSE (3.1.2) are then rewritten using ψ as the independent variable using

$$\frac{d}{dr} = \frac{\partial \psi}{\partial r} \frac{d}{d\psi}. \quad (3.2.2)$$

It was found that this mapping allowed the numerical derivatives to be calculated more stably than using directly a nonuniform computational discretisation for r .

The computational domain is then discretised into N equally spaced points, forming a matrix equation $\mathbf{A}\mathbf{x} = \mathbf{b}$ where A is a $5N \times 5N$ sparse matrix and \mathbf{x} is the solution vector. The vector \mathbf{b} contains zeros in $5N - 1$ entries (the homogeneous equations and eight boundary conditions), with the the pressure normalisation being enforced by the remaining (nonzero) entry. In forming A , radial derivatives are approximated using a sixth-order seven-point centred finite difference stencil (Brambley, 2015, 2016), since exponential growth and decay is expected in the r -direction as well as oscillations. The system is solved using a sparse matrix solver, with in general $N = 8000$ being sufficient for convergence to typical errors of $\lesssim 10^{-8}$ (see §3.A), and S chosen large enough to place at least 400 points inside the boundary layer irrespective of its thickness. The convergence of the numerical method is further evidenced by the good agreement with the asymptotics seen in §4.2.

The same solver may be used to produce the inviscid results by numerically setting $1/\text{Re} = 0$. In the inviscid case, only two boundary conditions may be applied, which we take to be the $\tilde{p}(1) = 1$ normalisation and the $\tilde{v}(0)$ regularity condition, with regularity of the other variables at $r = 0$ following automatically in this case.

For a given azimuthal mode m and impedance model for Z , a Newton–Raphson iteration is used to find complex values of k (or ω) given ω (or k) such that the dispersion relation (3.1.5) is satisfied. More information is given in §3.A.

3.3 Comparisons of viscous and shear effects

We make two types of comparisons in this study: comparing sheared viscous solutions of the LNSE (labelled sv) with sheared inviscid solutions (labelled si), both of which are found using the numerical method described above; and comparing sheared inviscid (si) solutions with uniform flow inviscid solutions (labelled ui). The uniform inviscid solutions are found analytically by setting $(U(r), \rho(r), T(r), 1/\text{Re}) = (M, 1, 1/(\gamma - 1), 0)$, giving solutions in terms of Bessel functions,

$$\tilde{p}_{\text{ui}}(r) = \frac{J_m(\alpha r)}{J_m(\alpha)}, \quad \tilde{v}_{\text{ui}}(r) = \frac{i\alpha J'_m(\alpha r)}{(\omega - Mk)J_m(\alpha)}, \quad \alpha^2 = (\omega - Mk)^2 - k^2, \quad (3.3.1)$$

where $J'_m(\alpha r)$ denotes the first derivative of J_m with respect to its argument. In equations (3.3.1) we make no assumption about the impedance boundary at $r = 1$.

As an initial illustrative example, fig. 3.1 compares the mode shapes of the three solutions, the uniform inviscid solutions rescaled (by varying $\tilde{p}(1)$) to match the numerical solutions in the core of the duct $r < 1 - 3\delta$ where shear and viscothermal effects are negligible (as anticipated from Khamis & Brambley, 2015). Shear and viscothermal effects are seen only to be significant within the boundary layer region $r > 1 - 3\delta$, where they produce $\mathcal{O}(1)$ effects at the wall $r = 1$. The plots in fig. 3.1 would correspond to a mode (i.e. a solution of the dispersion relation (3.1.5)) if $Z = -1.27 + 0.97i$ for the sheared, viscous numerics, if $Z = -0.64 + 0.02i$ for the sheared, inviscid numerics, and if $Z = 0.12 + 0.35i$ for the inviscid uniform flow solution. This suggests that these three solutions will have significantly different interactions with an impedance wall, as we see next.

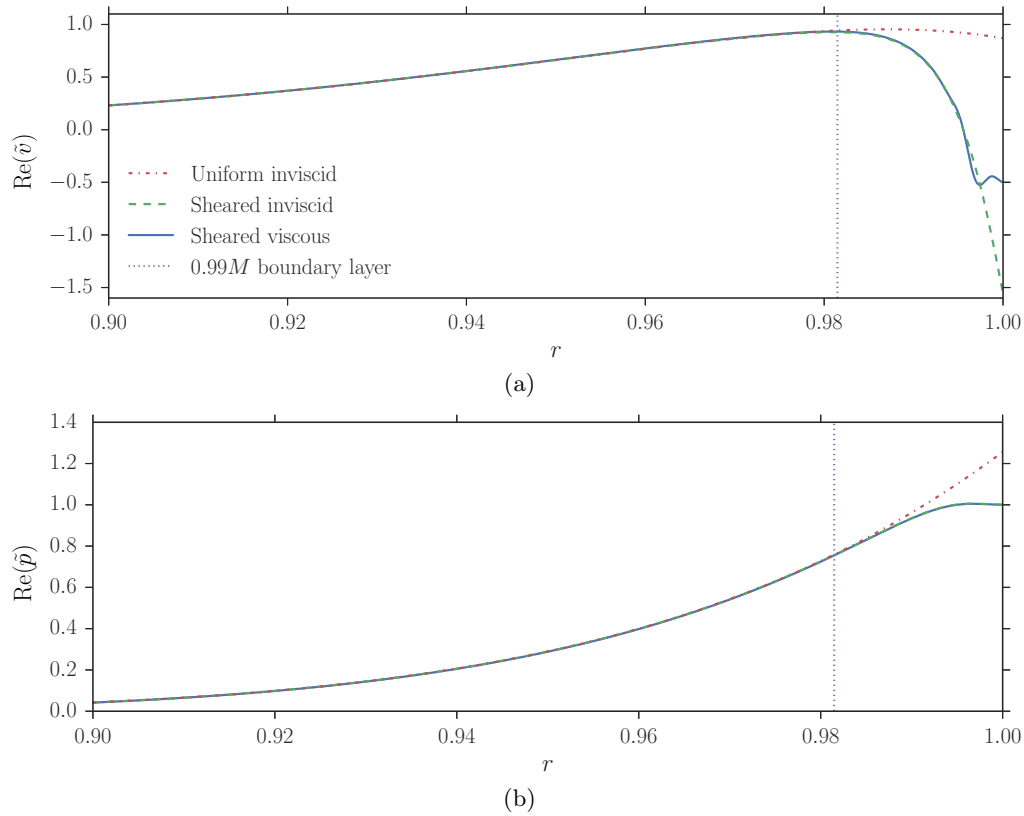


Figure 3.1. The (a) $\mathbb{R}e(\tilde{v})$ and (b) $\mathbb{R}e(\tilde{p})$ mode shapes of the three solutions: \tilde{q}_{ui} (uniform inviscid, dashdot), \tilde{q}_{si} (sheared inviscid, dashed), and \tilde{q}_{sv} (sheared viscous, solid) where in (a) $\tilde{q} = \tilde{v}$ and in (b) $\tilde{q} = \tilde{p}$. The dotted vertical line lies at $r = 1 - 3\delta$, where $U \simeq 0.99M$. Parameters are $\omega = 5$, $k = 26 - 14i$, $m = 12$, $M = 0.5$, $\delta = 7 \times 10^{-3}$, $\text{Re} = 1 \times 10^6$, with the hyperbolic base flow (3.1.1). The mean squared error between the solutions for $r < 1 - 5\delta$ is 10^{-6} .

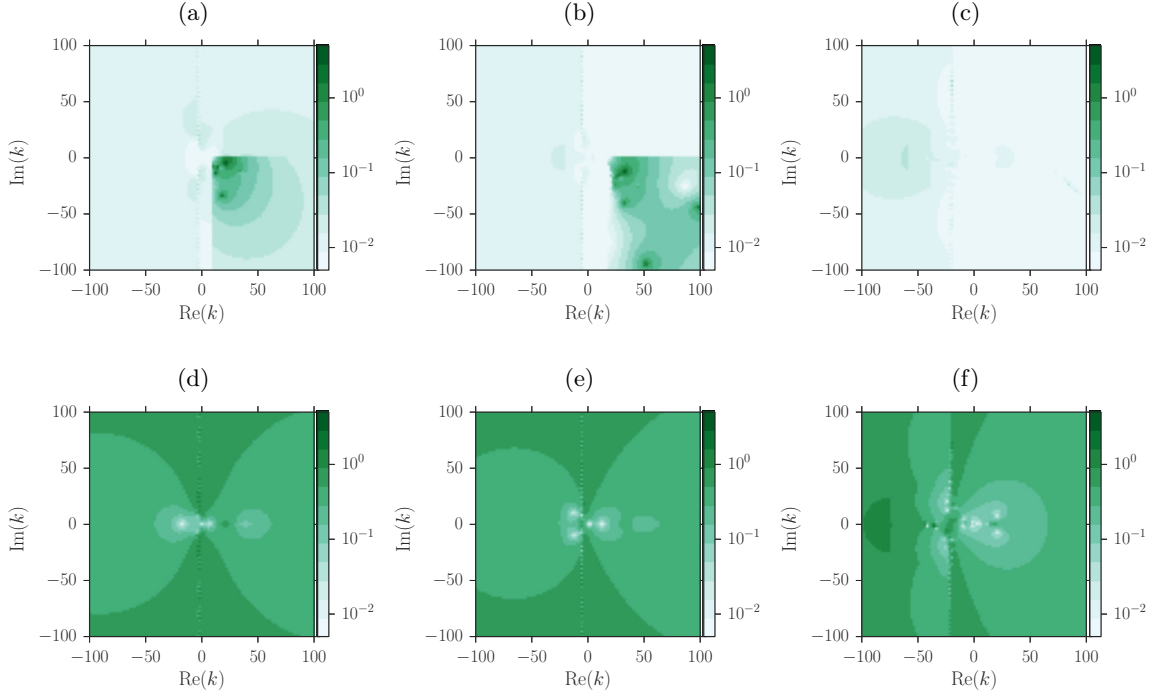


Figure 3.2. (a,b,c) viscous impedance error, comparing the sheared inviscid numerics with the sheared viscous numerics. (d,e,f) shear impedance error, comparing the uniform inviscid numerics with the sheared inviscid numerics. (a,d) $\omega = 4 + 0.04i$; (b,e) $\omega = 8 + 0.08i$; (c,f) $\omega = 31 + 0.31i$. Parameters are $m = 6$, $M = 0.5$, $\text{Re} = 5 \times 10^5$, $\delta = 3 \times 10^{-2}$. Base profiles as in (3.1.1).

3.3.1 Impedance errors

Setting $Z_{sv} = \tilde{p}_{sv}(1)/\tilde{v}_{sv}(1)$ and $Z_{si} = \tilde{p}_{si}(1)/\tilde{v}_{si}(1)$, we define the impedance error due to assuming an inviscid fluid (henceforth referred to as viscous impedance error) as

$$\min\{|Z_{sv} - Z_{si}|, |1/Z_{sv} - 1/Z_{si}|\}, \quad (3.3.2)$$

which was chosen to handle correctly near-zero and near-infinite impedances. With this definition, this impedance error is also the admittance error for the admittance $Y = 1/Z$. Note that, since we are not solving the dispersion relation (3.1.5), the impedance Z at the wall is not prescribed here; we are merely comparing the impedance produced by the viscous and inviscid equations. Similarly, the impedance error associated with neglecting base flow shear in an inviscid system (henceforth referred to as shear impedance error) is given by

$$\min\{|Z_{si} - Z_{ui}|, |1/Z_{si} - 1/Z_{ui}|\}, \quad (3.3.3)$$

where $Z_{ui} = \tilde{p}_{ui}(1)/\tilde{v}_{ui}(1)$. To avoid division by zero in the calculation of Z_{ui} , a small imaginary part is added to the frequency in the following computations, equal to 1% of $\text{Re}(\omega)$.

There are many parameters that affect the acoustics in the boundary layer, and the importance of both shear and viscosity will depend on the particular values used. In order to draw meaningful conclusions, we calculate the impedance error for axial wavenumbers across a section of the complex plane $|\text{Re}(k)| \leq 100$, $|\text{Im}(k)| \leq 100$, and choose two main parameters to investigate: the frequency and Mach number.

The impedance errors are plotted in the wavenumber plane in fig. 3.2 for $M = 0.5$, $\delta = 3 \times 10^{-2}$ and $\text{Re} = 5 \times 10^5$. For these parameters, for large sectors of the k -plane and for all three frequencies,

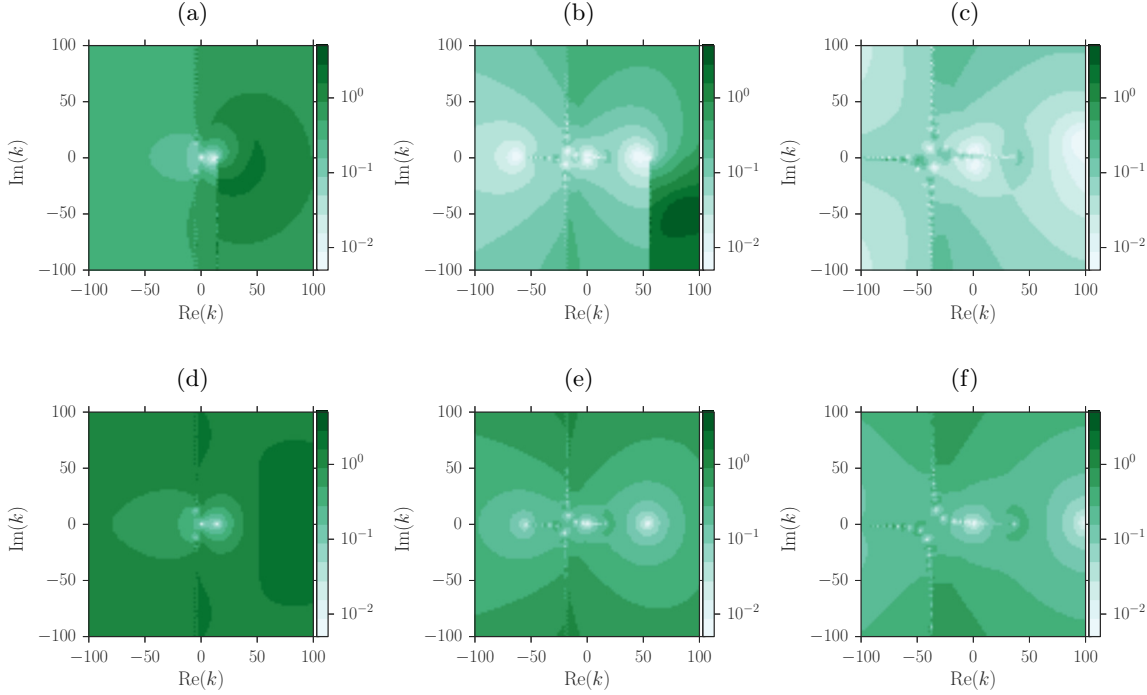


Figure 3.3. (a,b,c) viscous impedance error. (d,e,f) shear impedance error. (a,d) $\omega = 7 + 0.07i$; (b,e) $\omega = 28 + 0.28i$; (c,f) $\omega = 56 + 0.56i$. Parameters are $m = 12$, $M = 0.5$, $\text{Re} = 1 \times 10^5$, $\delta = 2 \times 10^{-3}$. Base profiles as in (3.1.1).

the shear error is an order of magnitude larger than the viscous error. However, at low frequencies, figs. 3.2a and 3.2b, the viscous error in the region $\text{Re}(k) > \omega/M$, $\text{Im}(k) < 0$ is comparable to the shear error in the same region, figs. 3.2d and 3.2e. This region, bounded by the viscous branch cut $k = \omega/M - iq$ and inviscid branch cut $k = \omega/M + q$ was labelled the “anomalous region” by Brambley (2011a), as the behaviour in this region is unlike the rest of the k -plane and its origin is unknown.

Figure 3.3 shows, for a thinner boundary layer $\delta = 2 \times 10^{-3}$, the viscous errors become more prevalent than before, as can be seen by comparing fig. 3.3a with fig. 3.3d. At lower frequencies, the viscous error is significant throughout the wavenumber plane, not just in the anomalous region. Figure 3.3a shows large regions of the k -plane suffer from $\mathcal{O}(1)$ viscous errors, with a median error (calculated using all values in the plotted domain) of 0.5 to one decimal place (compared to the median shear error of 1.3 in fig. 3.3d). As the frequency increases, the viscous error becomes smaller, with the median error reducing to 0.05 in fig. 3.3c (compared to the median shear error of 0.27 in fig. 3.3f). This could be attributed to the dependence of the acoustic boundary layer thickness δ_{ac} on frequency: a larger ratio δ_{ac}/δ occurs at lower frequencies, hence viscous effects are stronger.

Figures 3.4 and 3.5 show the effect of increasing Mach number on the error, with the Reynolds number held fixed². As the Mach number increases, so too does the shear error, as might be anticipated since a higher Mach number means neglecting larger velocity gradients in the uniform flow case. However, it is seen (particularly in figs. 3.5a–3.5c) that increasing the Mach number leads to larger viscous errors throughout the k -plane and not just inside the anomalous region, with the median error increasing from 0.02 in fig. 3.5a to 0.14 in fig. 3.5c.

²Recall that Re is defined here with respect to the sound speed, $\text{Re} = c_0^* l^* \rho_0^* / \mu_0^*$, rather than with respect to the flow speed, $\overline{\text{Re}} = U_0^* l^* \rho_0^* / \mu_0^* = M \text{Re}$. Hence, figs. 3.4 and 3.5 show that, for a given fluid with fixed μ_0^* and c_0^* , increasing the flow speed U_0^* leads to increasing $\overline{\text{Re}}$ but, confusingly, larger viscous error, justifying our previous choice of Re as the Reynolds number.

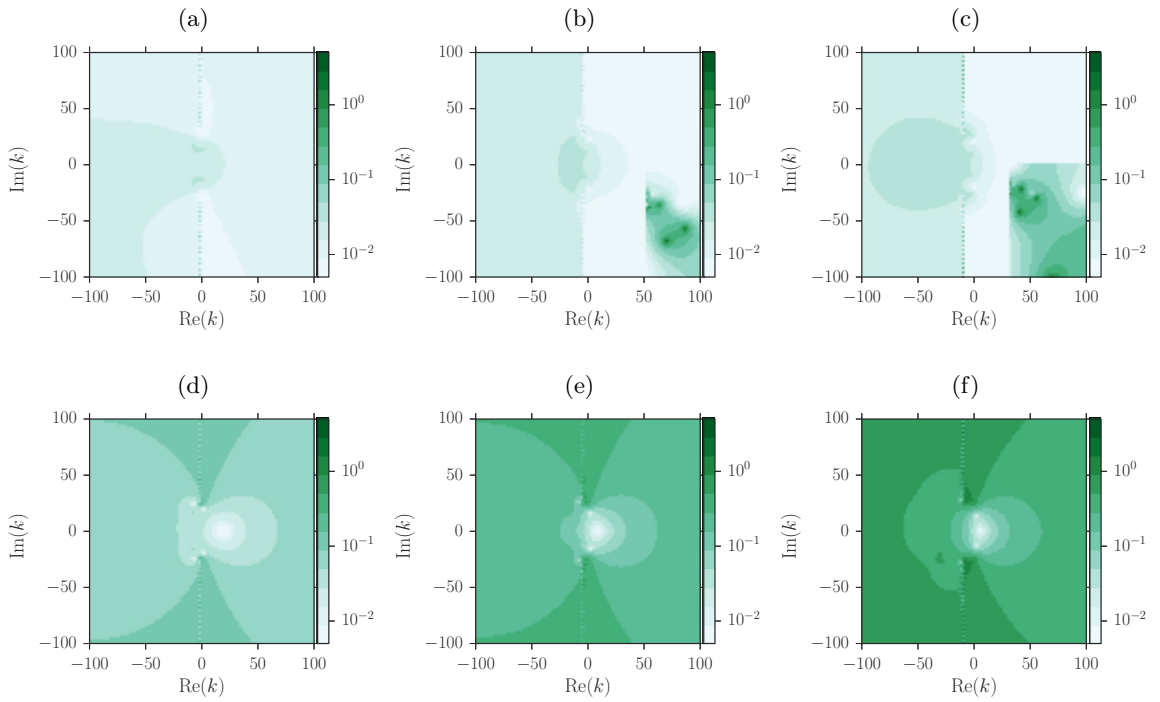


Figure 3.4. (a,b,c) viscous impedance error. (d,e,f) shear impedance error. (a,d) $M = 0.1$; (b,e) $M = 0.3$; (c,f) $M = 0.5$. Parameters are $\omega = 15 + 0.15i$, $m = 24$, $\text{Re} = 1 \times 10^5$, $\delta = 3 \times 10^{-2}$. Base profiles as in (3.1.1).

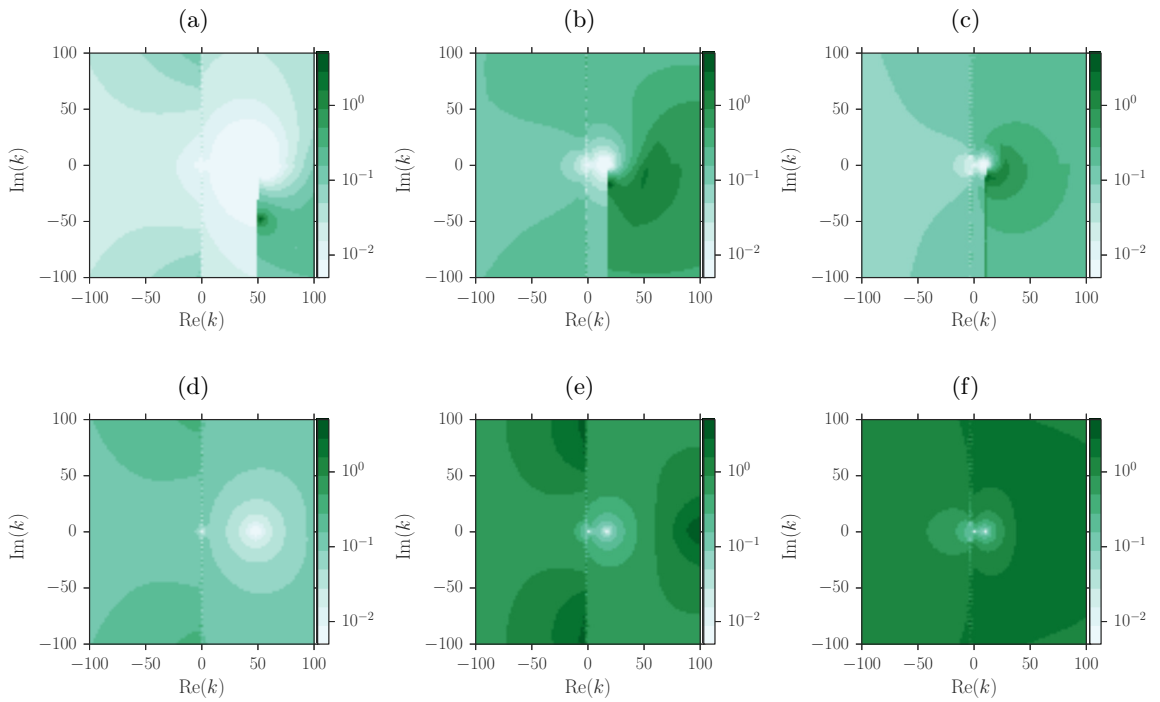


Figure 3.5. (a,b,c) viscous impedance error. (d,e,f) shear impedance error. (a,d) $M = 0.1$; (b,e) $M = 0.3$; (c,f) $M = 0.5$. Parameters are $\omega = 5 + 0.05i$, $m = 7$, $\text{Re} = 5 \times 10^6$, $\delta = 2 \times 10^{-3}$. Base profiles as in (3.1.1).

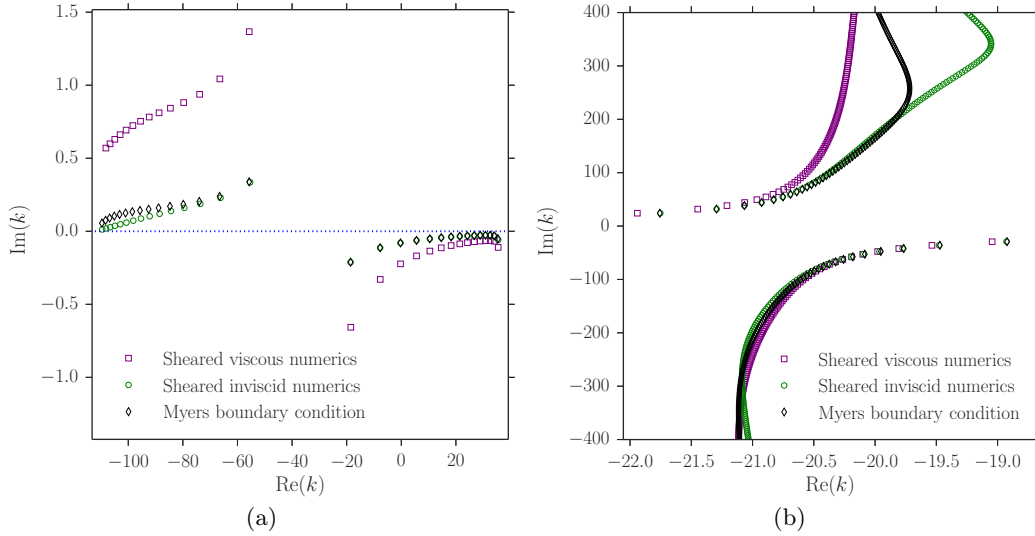


Figure 3.6. (a) Cut-on modes of the Myers boundary condition, sheared inviscid numerics (LEE), and sheared viscous numerics (LNSE), for $\omega = 56$, $m = 12$, $M = 0.5$, $\delta = 2 \times 10^{-3}$, $\text{Re} = 1 \times 10^5$ with a mass–spring–damper boundary impedance (3.1.6) with $R = 3$, $d = 0.15$ and $b = 1.15$ giving $Z = 3 + 8.38i$. (b) Cut-off modes for $\omega = 31$, $m = 24$, $M = 0.5$, $\delta = 2 \times 10^{-4}$, $\text{Re} = 2.5 \times 10^7$ with a boundary impedance of $Z = 2 + 0.6i$. In both (a) and (b) the hyperbolic boundary layer profiles in (3.1.1) are used.

3.3.2 Accuracy of modes in the k -plane

As described in the introduction, the Myers (Ingard, 1959; Myers, 1980) boundary condition corresponds to the limit of a sheared inviscid boundary layer with a vanishing thickness (Eversman & Beckemeyer, 1972; Tester, 1973), and for the situation considered here may be written as

$$\omega \tilde{v}(1) = (\omega - Mk) \tilde{p}(1) / Z \quad \Rightarrow \quad Z_{\text{eff}} = \frac{\omega}{\omega - Mk} Z, \quad (3.3.4)$$

where Z_{eff} is the effective impedance for which the Myers boundary condition is $\tilde{p}(1)/\tilde{v}(1) = Z_{\text{eff}}$. We use the Myers condition here to find k -plane modes under the uniform inviscid assumption. For the sheared viscous and sheared inviscid results, the numerics of §3.2 are used along with the dispersion relation (3.1.5). Unless stated, the impedance boundary model (3.1.6) is used in the following computations.

Figure 3.6 plots the solutions to the dispersion relations (3.1.5) for the sheared viscous and sheared inviscid numerics, together with the solutions to the dispersion relation (3.3.4) for the uniform inviscid solution together with the Myers boundary condition. The modes near the real axis may be considered propagating (cut on), with $|\text{Im}(k)|$ giving the axial decay rate of the mode due to the lined wall; $|\text{Im}(k)|$ is therefore extremely important in aeroengine design, as it predicts how much of the engine noise is absorbed by the liner and how much is available to propagate to the far field. One effect of a thin sheared boundary layer is to change the impedance of the wall as seen by the acoustics outside the boundary layer (Brambley, 2011a), thus changing the amount by which the nearly propagating modes are damped. Figure 3.6a shows that viscosity can also play a vital role in determining the damping rate of the modes, even at the high frequency of $\omega = 56$ used in this case, and that inviscid calculations underestimate the decay rate of these cut-on modes. This may also explain the result in Boyer *et al.* (2011) where the growth rate of the surface wave was overestimated by inviscid computations.

Figure 3.6b shows viscosity has less of an effect on the well cut-off modes, although the agreement is parameter dependent. Accurate prediction of these cut-off modes is far less important in aeroengine design than that of the nearly cut-on modes, since all models predict the cut-off modes

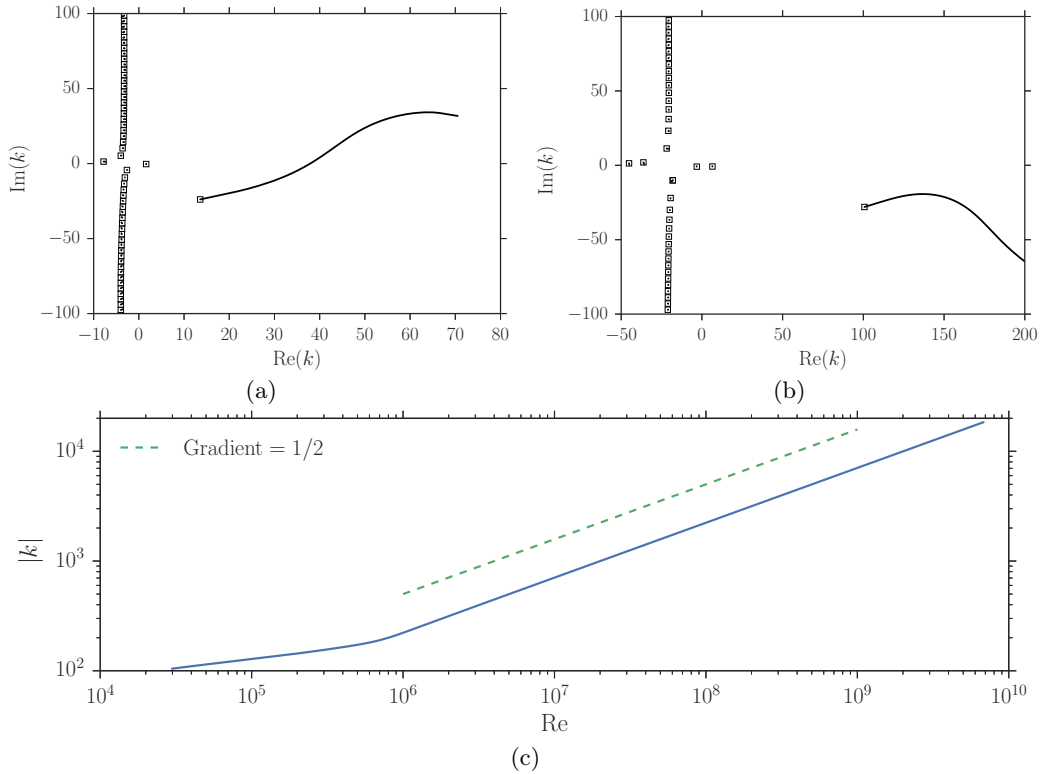


Figure 3.7. In (a) and (b), markers show modes in the k -plane for the viscous sheared numerics, tracks follow surface wave modes as Re is increased. At the end of the tracks the computations are purely inviscid. Parameters are: (a) $\omega = 5$, $m = 0$, $M = 0.5$, $\delta = 2 \times 10^{-3}$, $Z = 3 + 0.52i$ calculated using (3.1.6), markers at $\text{Re} = 2.5 \times 10^5$; (b) $\omega = 31$, $m = 24$, $M = 0.5$, $\delta = 5.8 \times 10^{-3}$, $Z = 3 + 4.61i$ calculated using (3.1.6), markers at $\text{Re} = 3.0 \times 10^4$. In both (a) and (b) the hyperbolic boundary layer profiles in (3.1.1) are used. (c) shows the behaviour of the surface mode k_{sm} on the right side of (b) as Re is increased on a log–log scale, demonstrating that $|k_{\text{sm}}|$ is tending to infinity as $1/\text{Re} \rightarrow 0$.

to decay extremely fast along the axis of the duct.

3.3.3 Surface waves

Surface waves (Rienstra, 2003) are an important consideration when investigating lined surfaces, as certain surface waves may represent a hydrodynamic instability of flow over the surface (Brambley, 2011b; Rienstra, 2003). Asymptotic analysis has shown that an inviscid finite thickness boundary layer can support a maximum of six modes localised near the boundary (Brambley, 2013) while a vanishingly thin boundary layer can support only up to four (Rienstra, 2003). Here, we investigate whether the inclusion of viscosity changes the number or character of the surface wave modes, by tracking the modes as viscosity is turned off in the computations ($1/\text{Re} \rightarrow 0$).

Figure 3.7 shows the behaviour of modes of the viscous linearised Navier–Stokes equations as the Reynolds number is increased. The markers signify the most viscous point (lowest Re) considered, and the lines end where $1/\text{Re} = 0$ (inviscid). In both fig. 3.7a and fig. 3.7b the change in the acoustic modes is small compared to that in the surface wave modes. Figure 3.7a is an example where the viscous surface wave mode (marker in the bottom right quadrant) moves substantially as Re is increased, crossing the real axis at $\text{Re} \simeq 1.35 \times 10^6$ and therefore changing in character from being exponentially decaying as x increases to being exponentially growing. Figure 3.7b shows a viscous surface wave mode originating in the lower right quadrant and tending to infinity as $1/\text{Re} \rightarrow 0$, as confirmed in fig. 3.7c. This mode therefore has no inviscid equivalent, and hence the inclusion of viscosity in the boundary layer is seen to support a greater number of surface waves

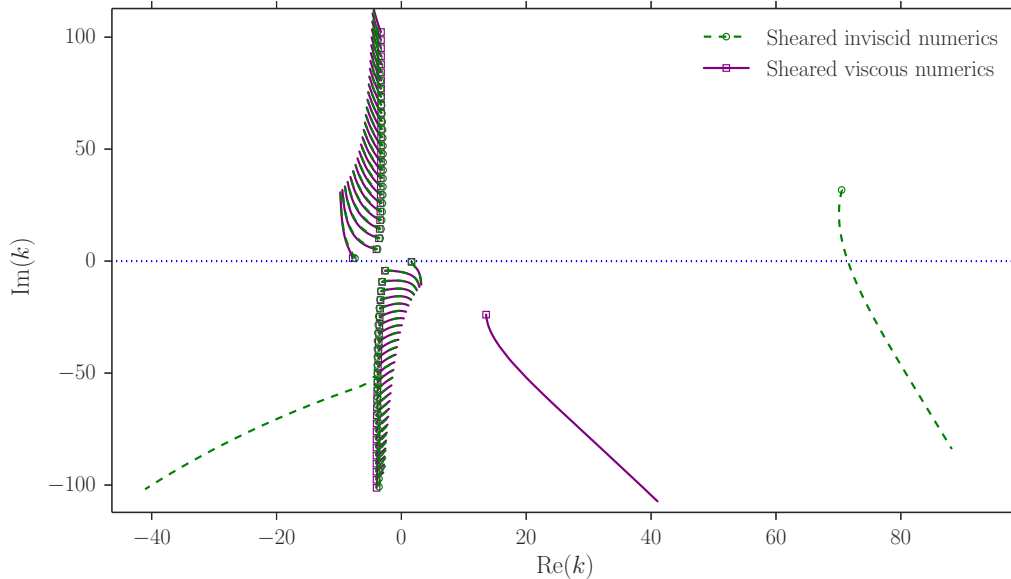


Figure 3.8. Briggs-Bers trajectories in the k -plane for inviscid and viscous sheared numerics. Markers at $\omega = 5$, $Z = 3 + 0.52i$; lines showing trajectories as $\Im(\omega)$ is reduced from zero to -15 with $\Re(\omega) = 5$ held constant. The boundary impedance evolves as in (3.1.6), with $R = 3$, $d = 0.15$, $b = 1.15$. Parameters are $m = 0$, $M = 0.5$, $\delta = 2 \times 10^{-3}$, $\text{Re} = 2.5 \times 10^5$. The hyperbolic base profiles (3.1.1) are used.

modes than a purely inviscid boundary layer.

3.3.4 Stability

Viscosity is intrinsically linked to stability in shear flow. For example, it was reported by Brambley (2011a) that viscous effects change the growth rate of the Myers vortex sheet instability from having a $k^{1/2}$ to a $k^{1/3}$ wavenumber dependence. In the previous section, a surface wave mode was found as the Reynolds number was increased to switch from exponential decay to exponential growth as x increases. We further investigate stability here by performing a Briggs-Bers (Bers, 1983; Briggs, 1964) stability analysis, reducing $\Im(\omega)$ from zero with $\Re(\omega)$ held fixed, for a mass-spring-damper impedance (3.1.6) with $R = 3$, $d = 0.15$, and $b = 1.15$. The resulting Briggs-Bers trajectories for the k -plane modes are shown in fig. 3.8. All of the viscous modes are stable for the plotted parameters, since the trajectories do not cross the $\Re(k)$ axis. All but one of the inviscid modes are stable, with the surface wave in the right half plane crossing the $\Re(k)$ axis as $\Im(\omega)$ is reduced from zero, indicating the mode to be a right-running convective instability. Importantly, this mode is found to stabilise as the Reynolds number is decreased past a critical value $\text{Re} \simeq 1.35 \times 10^6$, well within the normal operating range of an aircraft engine.

A temporal stability analysis may also be performed by choosing a real wavenumber k and solving the dispersion relation (3.1.5) for the complex frequency $\omega(k)$, with $-\Im(\omega(k))$ then giving the growth rate at that wavenumber. Figure 3.9 shows the behaviour of the growth rate of the unstable surface wave as the (real) wavenumber is increased. The Myers boundary condition displays the well-known instability, the growth rate of which is unbounded in k . The inviscid sheared numerics have an instability for all real k , with $\Im(\omega)$ asymptoting to zero but remaining negative. Results for the viscous sheared numerics are shown for three Reynolds numbers. At the highest value, $\text{Re} = 1 \times 10^6$, it can be seen that: viscosity stabilises short wavelengths; the most unstable wavelength is altered from the inviscid value; and the maximum growth rate is reduced in the viscous case, although there are possibly some wavenumbers where the viscous system gives faster growing instability than the inviscid system. As the Reynolds number is reduced (below

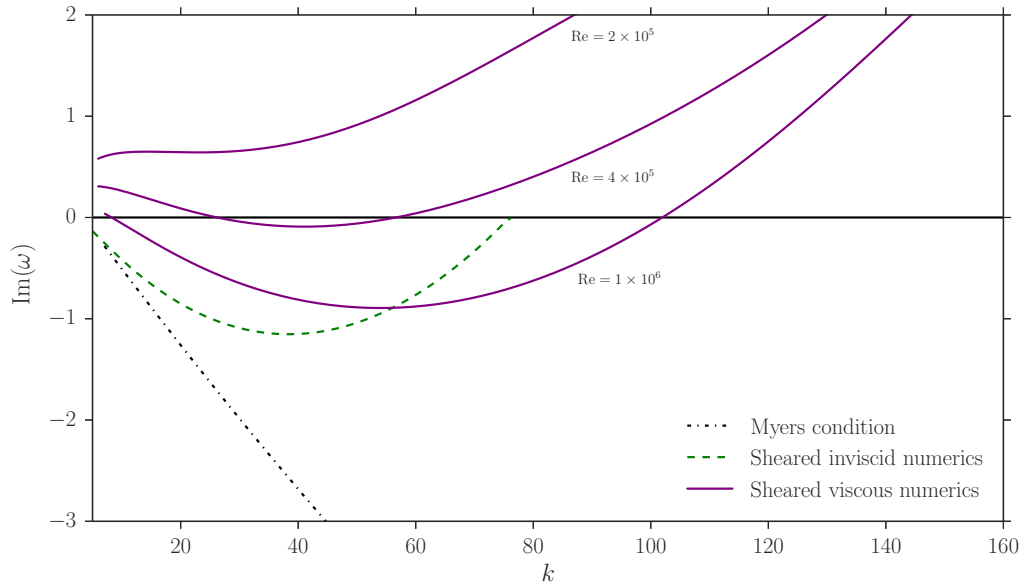


Figure 3.9. The decay rate $\text{Im}(\omega)$ of the unstable mode is plotted as the real wavenumber k increases. The mode stabilises as Re is decreased past $\text{Re} = 4 \times 10^5$. Parameters are $m = 0$, $M = 0.5$, $\delta = 5 \times 10^{-3}$, with the mass–spring–damper liner model of (3.1.6), with $R = 3$, $d = 0.15$, $b = 1.15$. The hyperbolic base profiles (3.1.1) are used.

$\text{Re} = 4 \times 10^5$ for these parameters) the flow becomes stable for all real k (as shown by the stable $\text{Re} = 2 \times 10^5$ mode). This may explain the apparent difficulty, expressed in the literature, of observing this instability experimentally.

It is important to remember that absolute, as well as convective, instabilities could be present. Absolute instabilities occur when two surface modes, one originating in the upper–half k -plane for $\text{Im}(\omega) = 0$ and one originating in the lower–half plane, collide for $\text{Im}(\omega) < 0$, causing a pinch at the resulting double root in the k -Fourier inversion contour (Bers, 1983; Briggs, 1964). These absolute instabilities would dominate any convective instability at large times. Brambley (2013) showed asymptotically and numerically that for an inviscid sheared flow, the boundary layer must be extremely thin ($\delta \sim 10^{-4}$) for an absolute instability to arise. In the viscous case, we conjecture that absolute instabilities require a large Re (i.e. weak viscosity) coupled with a thin boundary layer; however, this is purely a conjecture, and in the present chapter we do not investigate absolute instabilities.

3.4 Summary

Numerical solutions of the linearised compressible Navier–Stokes equations and the linearised Euler equations were used in this chapter to investigate the effects of viscosity and thermal conduction on sound propagation in an acoustically lined duct, and quantify their importance in relation to mean flow shear. It was shown that viscosity has greatest effect in thin boundary layers, at low frequencies, and at high flow rates (high centreline Mach numbers). In some cases, the inclusion of viscosity can be as important for accuracy as the inclusion of mean flow shear, in particular for upstream propagating cut-on modes.

Viscosity also changes the stability properties of the boundary layer. In the k -plane, surface modes that are convectively unstable in an inviscid system are stable for a low enough Reynolds number in the viscous system. In the ω -plane, unstable modes are seen to stabilise past a critical wavenumber, in contrast to the inviscid instability mode for which the inviscid critical layer prevents

the mode becoming stable. The number of surface modes, as well as their stability, is altered by viscosity. By tracing a viscous surface mode as $\text{Re} \rightarrow \infty$, it was shown that the mode tends to infinity in the inviscid limit. The conclusion may thus be drawn that a viscous sheared boundary layer supports a greater number of possible surface wave modes than a corresponding inviscid boundary layer.

The following two chapters aim to include viscous and thermal conductive effects in theoretical models of a sheared boundary layer above an acoustic lining. This is done with the aim that the important effects of viscosity on flow stability and mode attenuation (as described in the current chapter) may be captured by an effective impedance boundary condition, applicable to an inviscid plug flow.

Appendix

3.A Details of numerical method

Details of our numerical method are given below.

3.A.1 Regularity at $r = 0$

The behaviour of the acoustics near $r = 0$ are investigated by assuming for each acoustic quantity a series expansion in r , $\tilde{q} \sim \alpha_0 + \alpha_1 r + \dots$, and analysing the $\mathcal{O}(1/r^n)$ terms of the viscous governing equations (3.1.2). By ensuring cancellation at $\mathcal{O}(1/r^n)$ for each governing equation, consistent regularity conditions are derived. Below, each equation is considered in turn. In this derivation we assume $m \geq 0$, but the same results hold for negative m .

Irregular terms appear in the continuity equation (3.1.2a) only at $\mathcal{O}(1/r)$:

$$\frac{\tilde{v}}{r} - \frac{im}{r}\tilde{w} = 0 \quad \implies \quad \begin{cases} \tilde{v}(0) = 0, & m = 0, & \tilde{v} \sim b_1 r + \dots \\ \tilde{v}(0) = im\tilde{w}(0), & m \neq 0. \end{cases} \quad (3.A.1)$$

No other information may be gathered from this equation.

In the axial momentum equation (3.1.2b), the most singular terms at $r = 0$ are $\mathcal{O}(1/r^2)$, which gives us

$$\frac{m^2}{r^2}\tilde{u} = 0 \quad \implies \quad \begin{cases} \text{Identically true,} & m = 0, \\ \tilde{u}(0) = 0, & m \neq 0, & \tilde{u} \sim a_1 r + \dots \end{cases} \quad (3.A.2)$$

where we have set $a_0 = 0$ in the \tilde{u} expansion for $m \neq 0$, but left $a_1 \neq 0$ to provide a contribution at $\mathcal{O}(1/r)$. The $\mathcal{O}(1/r)$ terms of (3.1.2b) give

$$\frac{1}{r}(\mathcal{H}\tilde{u}_r + U_r\tilde{\mathcal{H}}) - \frac{m^2}{r^2}\mathcal{H}\tilde{u} - (1 + \beta)\frac{1}{r}\mathcal{H}(ik\tilde{v} + km\tilde{w}) = 0. \quad (3.A.3)$$

In the $m = 0$ case, we may use (3.A.1) and the fact that $U_r \rightarrow 0$ as $r \rightarrow 0$ to find $\tilde{u}_r(0) = 0$. If $m \neq 0$, (3.A.1) and (3.A.2) imply

$$\frac{(1 - m^2)}{r}\mathcal{H}\tilde{u}_r = 0 \quad \implies \quad \begin{cases} \text{Identically true,} & m = 1, \\ \tilde{u}_r(0) = 0, & m > 1. \end{cases} \quad (3.A.4)$$

At $\mathcal{O}(1/r^2)$ the radial momentum equation (3.1.2c) behaves like

$$-\frac{m^2}{r^2}\mathcal{H}\tilde{v} - (2 + \beta)\mathcal{H}\frac{\tilde{v}}{r^2} + (3 + \beta)\frac{im}{r^2}\mathcal{H}\tilde{w} = 0, \quad (3.A.5)$$

from which in the $m = 0$ case we recover (3.A.1). If $m \neq 0$, we use the expansions

$$\tilde{v} \sim b_0 + b_1r + \dots, \quad \tilde{w} \sim c_0 + c_1r + \dots \quad (3.A.6)$$

in (3.A.5), with (3.A.1) implying $b_0 = imc_0$, to find

$$\frac{(1 - m^2)}{r^2}\tilde{v} = 0 \quad \implies \quad \begin{cases} \text{Identically true,} & m = 1, \\ \tilde{v}(0) = 0, & m > 1, \end{cases} \quad \tilde{v} \sim b_1r + \dots \quad (3.A.7)$$

where again b_1 is left to contribute to the $\mathcal{O}(1/r)$ system. At $\mathcal{O}(1/r)$ we find, with $\mathcal{H}_r \rightarrow 0$ as $r \rightarrow 0$,

$$-\frac{m^2}{r^2}\mathcal{H}\tilde{v} + (2 + \beta)\mathcal{H}\left(\frac{\tilde{v}_r}{r} - \frac{\tilde{v}}{r^2}\right) + (3 + \beta)\frac{im}{r^2}\mathcal{H}\tilde{w} - (1 + \beta)\frac{im}{r}\mathcal{H}\tilde{w}_r = 0. \quad (3.A.8)$$

If $m = 0$, the left hand side is identically zero by the \tilde{v} expansion in (3.A.1). If $m \neq 0$ we use (3.A.6) and (3.A.1) in (3.A.8) to find $mb_1 = 2ic_1$, implying

$$m\tilde{v}_r(0) = 2i\tilde{w}_r(0). \quad (3.A.9)$$

Now, since for $m = 0$ the $\mathcal{O}(1/r)$ system was redundant, we may use the $\mathcal{O}(1)$ system to derive a boundary condition for \tilde{p} . Using (3.A.2) and setting the derivatives of the base flow to zero at $r = 0$, we find for $m = 0$

$$\tilde{p}_r = \frac{\mathcal{H}}{\text{Re}}(2 + \beta)\left(\tilde{v}_{rr} - \frac{\tilde{v}}{r^2} + \frac{\tilde{v}_r}{r}\right). \quad (3.A.10)$$

Now, using $\tilde{v} \sim b_1r + b_2r^2 + \dots$ from the $m = 0$ case of (3.A.1), the $\mathcal{O}(1)$ contribution of the large bracket is simply $3b_2$. This implies

$$\tilde{p}_r(0) = \frac{3}{2}\frac{\mathcal{H}}{\text{Re}}(2 + \beta)\tilde{v}_{rr}(0), \quad m = 0. \quad (3.A.11)$$

The azimuthal momentum equation (3.1.2d) at $\mathcal{O}(1/r^2)$ is

$$-(3 + \beta)\frac{im}{r^2}\mathcal{H}\tilde{v} - \frac{m^2}{r^2}\mathcal{H}\tilde{w} - (1 + \beta)\frac{m^2}{r^2}\mathcal{H}\tilde{w} - \frac{1}{r^2}\mathcal{H}\tilde{w} = 0. \quad (3.A.12)$$

When $m = 0$ (3.A.12) simply reduces to $\tilde{w}(0) = 0$ (and indeed $\tilde{w}(r) \equiv 0$). If $m \neq 0$, we may use (3.A.1) to derive the relation

$$\frac{(m^2 - 1)}{r^2}\tilde{w} = 0 \quad \implies \quad \begin{cases} \text{Identically true,} & m = 1, \\ \tilde{w}(0) = 0, & m > 1, \end{cases} \quad \tilde{w} \sim c_1r + \dots \quad (3.A.13)$$

where c_1 contributes at $\mathcal{O}(1/r)$, and the $m > 1$ series expansion is also valid for $m = 0$. At $\mathcal{O}(1/r)$, setting gradients of mean flow quantities to zero, (3.1.2d) reduces to

$$\frac{im}{r}\tilde{p} = -\frac{\mathcal{H}}{\text{Re}}\left\{-\left(1 + \beta\right)\frac{km}{r}\tilde{u} - \left(3 + \beta\right)\frac{im}{r^2}\tilde{v} - \left(1 + \beta\right)\frac{im}{r}\tilde{v}_r - \left(2 + \beta\right)\frac{m^2}{r^2}\tilde{w} + \frac{\tilde{w}_r}{r} - \frac{\tilde{w}}{r^2}\right\}, \quad (3.A.14)$$

which is identically zero when $m = 0$ and the series expansion (3.A.13) for $m > 1$ is assumed.

When $m \neq 0$, we may use (3.A.2) and the expansions (3.A.6), along with (3.A.9) which implies $mb_1 = 2ic_1$, to form the boundary condition

$$\tilde{p}(0) = \frac{\mathcal{H}}{2\text{Re}}(2 + \beta)(4 - m^2)\tilde{v}_r(0), \quad m \neq 0. \quad (3.A.15)$$

The energy equation (3.1.2e) is relatively simple. At $\mathcal{O}(1/r^2)$ we find

$$\frac{m^2}{r^2}\mathcal{H}\tilde{T} = 0 \quad \Longrightarrow \quad \begin{cases} \text{Identically true,} & m = 0, \\ \tilde{T}(0) = 0, & m \neq 0, \end{cases} \quad \tilde{T} \sim d_1 r + \dots \quad (3.A.16)$$

while at $\mathcal{O}(1/r)$ we find

$$\frac{1}{r}(\mathcal{H}\tilde{T}_r + T_r\tilde{H}) - \frac{m^2}{r^2}\mathcal{H}\tilde{T} = 0, \quad (3.A.17)$$

where the $\mathcal{O}(1/r)$ contribution of the term $\propto \tilde{T}/r^2$ is considered. Now, $T_r \rightarrow 0$ as $r \rightarrow 0$, which leads to

$$\frac{(1 - m^2)}{r}\mathcal{H}\tilde{T}_r = 0 \quad \Longrightarrow \quad \begin{cases} \text{Identically true,} & m = 1, \\ \tilde{T}_r(0) = 0, & m > 1. \end{cases} \quad (3.A.18)$$

Collecting the information above, our regularity conditions at $r = 0$ are:

$$\tilde{p}_r = \frac{3}{2}\frac{\mathcal{H}}{\text{Re}}(2 + \beta)\tilde{v}_{rr}, \quad \tilde{u}_r = 0, \quad \tilde{v} = 0, \quad \tilde{w} = 0, \quad \tilde{T}_r = 0, \quad (3.A.19)$$

for $m = 0$, and

$$\begin{aligned} \tilde{p} &= \frac{1}{2}\frac{\mathcal{H}}{\text{Re}}(2 + \beta)(4 - m^2)\tilde{v}_r, \\ \tilde{u} &= 0, \quad \tilde{v} = im\tilde{w}, \quad \tilde{w}_r = -\frac{im}{2}\tilde{v}_r, \quad \tilde{T} = 0, \end{aligned} \quad (3.A.20)$$

for $m \geq 1$.

3.A.2 Mode finding

To find acoustic modes, we solve the dispersion relation (3.1.5) numerically. This is done by iterating on k (or ω) via a Newton–Raphson procedure, given a fixed ω (or k). For the majority of modes (e.g. the cut-off and cut-on acoustic modes in the k -plane) the solutions of the Ingard–Myers dispersion relation

$$Z = \frac{(\omega - Mk)^2}{i\omega} \frac{J_m(\alpha)}{\alpha J'_m(\alpha)} \quad (3.A.21)$$

are used as an initial guess. Then, to find surface modes in the k -plane and unstable modes in the ω -plane, a fine two-dimensional mesh of complex-valued initial guesses is fed into the Newton–Raphson solver. This is done to minimise the chance of missing solutions.

The following test gives an example of the time taken to find modes using the dispersion relation (3.1.5). To find 102 acoustic modes (not surface waves) with Myers condition modes as initial guesses, the time taken was 1416.5s for the LNSE numerics (3.1.2). For comparison we list here the time taken by the asymptotic models derived in the next chapter, for which modes are found using the asymptotic dispersion relation (5.6.2): we find 40.7s for the high frequency model (4.1.13) and 527.4s for the $\mathcal{O}(\delta)$ model (4.1.2). This test was performed on a laptop with a 2.5GHz Intel i5 processor.

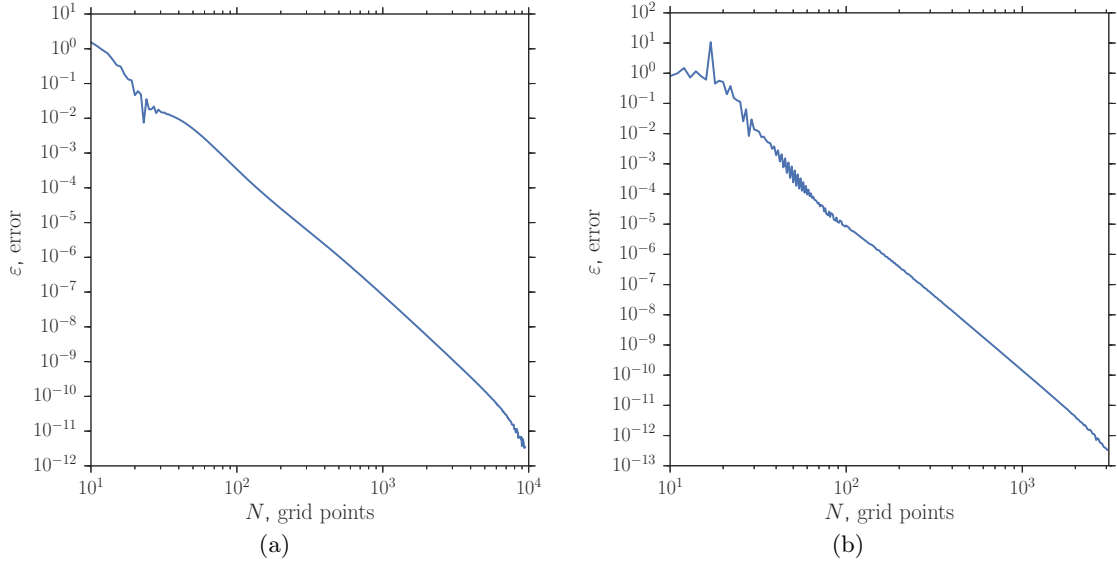


Figure 3.A.1. Relative error $\varepsilon = |Z/Z_c - 1|$ of calculated impedance value as number of grid points N is increased, with respect to a well-converged case with $N = 50000$. (a) Viscous numerics with $\omega = 31$, $k = 15 + 5i$, $m = 12$, $M = 0.5$, $\delta = 7 \times 10^{-3}$, $\text{Re} = 10^6$. (b) Inviscid numerics with $\omega = 5$, $k = 3 - 15i$, $m = 4$, $M = 0.5$ and $\delta = 2 \times 10^{-3}$. In both (a) and (b) the hyperbolic boundary layer profiles in (3.1.1) are used.

3.A.3 Numerical convergence

The numerical solver was checked for consistency and convergence in a number of ways: by comparison with analytical solutions in the inviscid uniform flow case; by comparison with asymptotic mode shapes in the boundary layer; by checking convergence of the solver with respect to number of grid points used; and by checking that the asymptotics agree with the numerics to the stated order of accuracy. The first of these is trivial – the cylindrical solution $\tilde{p} = J_m(\alpha r)$ in the uniform inviscid case is well known – and will not be discussed further. The second point may be verified by comparing the numerics to the asymptotic models derived in the next chapter (see fig. 4.2—it is clear that the numerical and asymptotic solutions have the same near-wall behaviour).

The third point may be assessed by varying the number of grid points and checking the values of Z calculated at the wall in each case, and calculating the relative error with respect to some well-converged case. The convergence plots in fig. 3.A.1 show that for $N \approx 8000$ the numerics are achieving errors of $\lesssim 10^{-8}$ in both the viscous and inviscid cases. The rate of convergence is set by the treatment of the end-points of the numerical domain, where the sixth-order stencil is reduced to fourth order to retain the use of central difference approximations close to the domain edge. Upwind and downwind fourth-order stencils are used at the boundary points.

The final point is addressed by checking the convergence of the asymptotic models derived in the next chapter, see fig. 4.1. This may be thought of conversely as a consistency check for the numerical solver. The correct gradients of asymptotic error shown in the figure indicate that the numerical solver is consistent down to very small errors ($\sim 10^{-8}$ or smaller).

Chapter 4

Asymptotic analysis of viscous effects on the acoustics and stability of a shear layer over an impedance wall

In this chapter the acoustics of a viscothermal sheared boundary layer above a lined wall are investigated asymptotically for a boundary layer of thickness $0 < \delta \ll 1$, for both an $\mathcal{O}(1)$ frequency and in a high frequency limit. In the latter case, analytical forms for the acoustics in the boundary layer are found, and a closed-form effective impedance boundary condition is derived which includes the effects of both shear and viscosity. The accuracy of these asymptotics are compared in §4.2, together with their predictions for surface waves on the lined surface. The work presented in this chapter has been submitted for publication in the *Journal of Fluid Mechanics* (Khamis & Brambley, 2016*b*); some of this work was presented at the AIAA Aeroacoustics conference (Khamis & Brambley, 2015).

Several simplified boundary conditions have been proposed which take account of near-wall effects on the wall impedance. These include: models based on an inviscid fluid with a vanishingly thin shear layer (Myers, 1980), meaning $\mathcal{O}(\delta)$ quantities are neglected; an inviscid fluid with a finite-thickness shear layer (Brambley, 2011*b*; Myers & Chuang, 1984), meaning $\mathcal{O}(\delta)$ quantities are included but viscosity is neglected; a viscous fluid with a vanishingly thin shear layer (Brambley, 2011*a*), meaning $\mathcal{O}(\delta)$ quantities are neglected; or other restrictive simplifying assumptions (e.g. Aurégan *et al.*, 2001; Nayfeh *et al.*, 1974). In this chapter we derive a simplified boundary layer model capable of reproducing the important effects of both shear and viscosity seen in the previous chapter, both including finite-thickness shear by including $\mathcal{O}(\delta)$ quantities and including viscosity.

4.1 Asymptotic analysis

We first present asymptotics based on a reasonably straightforward rescaling in §4.1.1. Because these result in equations that still need to be solved numerically, an alternative asymptotic solution in the high frequency limit is presented in §4.1.2 that yields tractable equations with analytic solutions. Both asymptotic solutions are subsequently compared with full LNSE solutions in §4.2.

4.1.1 Boundary layer asymptotics

We analyse asymptotically the near-wall behaviour of the linearised Navier–Stokes equations (3.1.2) by rescaling into the boundary layer,

$$r = 1 - \delta y, \quad \text{with} \quad \mu = \frac{\mathcal{H}}{\text{Re}} = \mathcal{H}\xi\delta^2, \quad (4.1.1)$$

where ξ measures the magnitude of the molecular viscosity, μ , compared with that expected from a Blasius boundary layer of thickness δ . We assume here $\xi \leq \mathcal{O}(1)$, with $\xi = \mathcal{O}(1)$ for a Blasius boundary layer, $\xi \ll 1$ for a turbulent boundary layer, and $\xi = 0$ for an inviscid boundary layer. These scalings are supplemented by $\hat{u} = \delta\tilde{u}$ and $\hat{T} = \delta\tilde{T}$, which are required to balance the viscous with the inertial terms at leading order in the axial momentum, energy, and continuity equations (Brambley, 2011a). These scalings lead to a system of ordinary differential equations in the boundary layer variable y and in powers of the boundary layer thickness δ . Brambley (2011a) keeps only the leading order terms. As a direct extension of that work, and in order to model the effects of both the shear and the viscosity, we work here to $\mathcal{O}(\delta)$. We find

$$i(\omega - Uk)\hat{T} + ikT\hat{u} + T^2\left(\frac{\tilde{v}}{\tilde{T}}\right)_y = \delta[\gamma i(\omega - Uk)T\tilde{p} + T\tilde{v} - imT\tilde{w}], \quad (4.1.2a)$$

$$\begin{aligned} i(\omega - Uk)\hat{u} - U_y\tilde{v} - \xi(\gamma - 1)^2T(T\hat{u}_y + U_y\hat{T})_y = \\ \delta\left[i(\gamma - 1)kT\tilde{p} - \xi(\gamma - 1)^2T(T\hat{u}_y + U_y\hat{T})\right], \end{aligned} \quad (4.1.2b)$$

$$\begin{aligned} \tilde{p}_y = \delta\left[i\rho(\omega - Uk)\tilde{v} - \xi(2 + \beta)(\gamma - 1)(T\tilde{v}_y)_y \right. \\ \left. - i\xi\beta k(\gamma - 1)(T\hat{u})_y - i\xi k(\gamma - 1)(T\hat{u}_y + U_y\hat{T})\right], \end{aligned} \quad (4.1.2c)$$

$$\xi(T\tilde{w}_y)_y - \frac{i(\omega - Uk)}{(\gamma - 1)^2T}\tilde{w} + \frac{im}{\gamma - 1}\tilde{p} = \mathcal{O}(\delta), \quad (4.1.2d)$$

$$\begin{aligned} i(\omega - Uk)\hat{T} - T_y\tilde{v} - \frac{1}{\text{Pr}}\xi(\gamma - 1)^2T(T\hat{T})_{yy} - \xi(\gamma - 1)^2T(U_y^2\hat{T} + 2TU_y\hat{u}_y) = \\ \delta\left[(\gamma - 1)i(\omega - Uk)T\tilde{p} - \frac{1}{\text{Pr}}\xi(\gamma - 1)^2T(T\hat{T})_y\right]. \end{aligned} \quad (4.1.2e)$$

Note that the azimuthal momentum equation (4.1.2d) is written to leading order as the azimuthal acoustic velocity \tilde{w} appears only in the first order forcing in the continuity equations (4.1.2a). If the parameter ξ were set to zero in (4.1.2), an inviscid system would be recovered which, when solved, would lead to the modified Myers condition as derived by Brambley (2011b). Immediately deducible from (4.1.2c) is that, in contrast with the leading order viscous model of Brambley (2011a), the pressure is not constant across the boundary layer; instead, variation in the pressure appears at first order as an integral across the boundary layer. The system (4.1.2) may be solved asymptotically assuming expansions of the acoustic quantities of the form $q = q_0 + \delta q_1 + \mathcal{O}(\delta^2)$.

The acoustic axial and azimuthal velocities satisfy no slip at the lining $r = 1$, $y = 0$, to all orders, and the acoustic temperature satisfies the isothermal wall condition to all orders. The leading order pressure is a constant, and our chosen normalisation therefore dictates that $\tilde{p}_0 \equiv 1$ and $\tilde{p}_1(0) = 0$. Similarly, we choose for the impedance boundary condition to be satisfied exactly, such that $\tilde{v}_0(0) = 1/Z$ and $\tilde{v}_1(0) = 0$. Prohibiting exponentially growing solutions as $y \rightarrow \infty$ gives

further boundary conditions, as described in Appendix 4.A. This leads to

$$\begin{aligned} \hat{u}_0(0) = 0, \quad \hat{T}_0(0) = 0, \quad \tilde{w}_0(0) = 0, \quad \tilde{p}_0 \equiv 1, \quad \tilde{v}_0(0) = \frac{1}{Z}, \\ \hat{u}_0(y) \rightarrow 0, \quad \hat{T}_0(y) \rightarrow 0, \quad \tilde{w}_0(y) \rightarrow \frac{m}{\omega - Mk} \quad \text{as } y \rightarrow \infty, \end{aligned} \quad (4.1.3)$$

at $\mathcal{O}(1)$, and

$$\begin{aligned} \hat{u}_1(0) = 0, \quad \hat{T}_1(0) = 0, \quad \tilde{p}_1(0) = 0, \quad \tilde{v}_1(0) = 0, \\ \hat{u}_1(y) \rightarrow \frac{k}{\omega - Mk}, \quad \hat{T}_1(y) \rightarrow 1, \quad \text{as } y \rightarrow \infty, \end{aligned} \quad (4.1.4)$$

at $\mathcal{O}(\delta)$. The limit $y \rightarrow \infty$ of this boundary layer solution must match to the uniform inviscid acoustics outside the boundary layer, (3.3.1). Defining p_∞ and v_∞ as the values of pressure and normal velocity of the uniform inviscid solution at the lining $r = 1$, we expand $p_\infty = p_\infty^{(0)} + \delta p_\infty^{(1)}$ and similarly for v_∞ , so that the uniform inviscid solutions (3.3.1) close to the lining may be expanded as

$$p_{\text{ui}}(1 - \delta y) = p_\infty^{(0)} + \delta p_\infty^{(1)} + \delta y i(\omega + Mk)v_\infty^{(0)} + \mathcal{O}(\delta^2), \quad (4.1.5a)$$

$$v_{\text{ui}}(1 - \delta y) = v_\infty^{(0)} + \delta v_\infty^{(1)} + \delta y \left(v_\infty^{(0)} - \frac{(\omega - Mk)^2 - k^2 - m^2}{i(\omega - Mk)} p_\infty^{(0)} \right) + \mathcal{O}(\delta^2). \quad (4.1.5b)$$

In practice, the system (4.1.2), (4.1.3) and (4.1.4) is solved across the boundary layer for a finite range $y \in [0, Y]$, with the values of \tilde{p}_0 , \tilde{p}_1 , \tilde{v}_0 , \tilde{v}_1 at $y = Y$ extrapolated to infinity (see Appendix 4.A) and matched with the relations (4.1.5) to find $p_\infty^{(j)}$ and $v_\infty^{(j)}$; the effective impedance $Z_{\text{eff}} = (p_\infty^{(0)} + \delta p_\infty^{(1)}) / (v_\infty^{(0)} + \delta v_\infty^{(1)})$ may then be formed.

The system (4.1.2), (4.1.3) and (4.1.4) must in general be solved numerically. It does not, therefore, suggest an easily applicable closed-form boundary condition capable of capturing the behaviour of the acoustics in a sheared viscothermal boundary layer. With this in mind, we now consider the high frequency limit of the LNSE.

4.1.2 High frequency asymptotics

We now consider the limits $\omega \gg 1$ and $\delta \ll 1$ with $\omega\delta \sim \varepsilon \ll 1$ (where ε is not to be confused with the acoustic amplitude ϵ_a used earlier). If we were to expand the outer solutions (3.3.1) near the wall $r = 1 - \delta y$ in powers of ω and δ , then at order n (in δ) the largest term would be of the form $(\omega\delta)^n$. Thus, for a useful outer expansion, we need $\delta \sim 1/\omega^a$ with $a > 1$. We choose here the distinguished scaling $\varepsilon = 1/\sqrt{\omega}$ (informed by the expansion of the outer solution near the boundary, (4.1.6) below), and hence the two small parameters are related by $\delta = \varepsilon^3 \bar{\delta}$ where $\bar{\delta} = \mathcal{O}(1)$.¹ This scaling agrees well with reported parameters for a turbofan intake (Gabard, 2013), with a blade passing frequency $\omega = 28$ and upstream boundary layer thickness $\delta = 7 \times 10^{-3}$ giving $\bar{\delta} \approx 1.04$. With the above scaling choices, the outer solutions expand as

$$p_{\text{ui}}(1 - \delta y) = p_\infty + i\varepsilon \bar{\delta} (1 - ML)y v_\infty + \frac{1}{2} \varepsilon^2 \bar{\delta}^2 (N^2 - \bar{\alpha}^2) y^2 p_\infty + \mathcal{O}(\varepsilon^3), \quad (4.1.6a)$$

$$v_{\text{ui}}(1 - \delta y) = v_\infty + i\varepsilon \bar{\delta} \frac{\bar{\alpha}^2 - N^2}{1 - ML} y p_\infty + \frac{1}{2} \varepsilon^2 \bar{\delta}^2 (N^2 - \bar{\alpha}^2) y^2 v_\infty + \mathcal{O}(\varepsilon^3), \quad (4.1.6b)$$

where

$$\bar{\alpha}^2 = (1 - ML)^2 - L^2, \quad (4.1.7)$$

¹An alternative scaling is given in Appendix 4.C in which both small parameters are left in the problem, connected by a weaker constraint than the one used here: $\delta \sim \varepsilon^{(2+n)}$ for $n \in \mathbb{R}^+$. The two methods result in solutions that are asymptotically equivalent to at least first order in ε .

and $L = k/\omega$, $N = m/\omega$ with L, N assumed to be $\mathcal{O}(1)$.

To find the inner solution, we follow Brambley (2011a) in introducing a multiple scales WKB ansatz for the acoustic quantities,

$$\frac{d}{dy} = \frac{\partial}{\partial \bar{y}} + \frac{1}{\varepsilon} \eta(\bar{y}) \frac{\partial}{\partial \theta}, \quad \text{with} \quad \bar{y}(y) = y, \quad \theta(y) = \frac{1}{\varepsilon} \int_0^y \eta(y') dy', \quad (4.1.8)$$

then relabel \bar{y} to y . The function $\eta(y)$ is a combination of base flow quantities,

$$\eta^2(y) = \frac{i(1 - U(y)L)}{\xi(\gamma - 1)^2 T^2(y)}, \quad (4.1.9)$$

with $\text{Re}\{\eta(y)\} > 0$ as $y \rightarrow \infty$, and represents the viscous decay rate of vorticity away from the boundary. The acoustic quantities are assumed to vary over both the short length-scale, θ , and the long length-scale, y . The base flow quantities vary only over the long length-scale, y . The short length-scale θ can be thought of as equivalent to the classical acoustic boundary layer scaling $r = 1 - \delta\theta/\sqrt{\omega\eta}$ (Ingard, 2010, chap. 2, pg. 11). From the system (3.1.2), we make the pre-emptive scalings

$$\tilde{u} = \frac{\check{u}}{\omega\delta}, \quad \tilde{T} = \frac{\check{T}}{\omega\delta}, \quad (4.1.10)$$

and expand in powers of ε ,

$$\begin{aligned} \check{u}_{\theta\theta} - \check{u} &= \frac{iU_y \check{v}}{1 - UL} - \frac{\varepsilon \bar{\delta} L}{\rho(1 - UL)} \check{p} - \frac{\varepsilon}{\eta^2 T} \left[(\eta T \check{u}_{\theta})_y + \eta T \check{u}_{\theta y} + \eta U_y \check{T}_{\theta} \right] \\ &\quad - \frac{\varepsilon^2}{\eta^2 T} \left[(T \check{u}_y)_y + (U_y \check{T})_y \right] - \varepsilon^3 \left[\bar{\delta}^2 (1 + \beta) \frac{iL}{\eta} \check{v}_{\theta} \right] + \mathcal{O}(\varepsilon^4), \end{aligned} \quad (4.1.11a)$$

$$\begin{aligned} \frac{1}{\text{Pr}} \check{T}_{\theta\theta} - \check{T} &= \frac{iT_y \check{v}}{1 - UL} - \varepsilon \frac{\bar{\delta}}{\rho} \check{p} - \frac{\varepsilon}{\eta^2 T} \left[\frac{1}{\text{Pr}} (\eta T \check{T}_{\theta})_y + \frac{1}{\text{Pr}} \eta (T \check{T}_{\theta})_y + 2\eta T U_y \check{u}_{\theta} \right] \\ &\quad - \frac{\varepsilon^2}{\eta^2 T} \left[\frac{1}{\text{Pr}} (T \check{T})_{yy} + 2T U_y \check{u}_y + U_y^2 \check{T} \right] + \mathcal{O}(\varepsilon^4), \end{aligned} \quad (4.1.11b)$$

$$\check{v}_{\theta} = -\varepsilon \left[\frac{i(1 - UL)}{\eta T} \check{T} + \frac{iL}{\eta} \check{u} + \frac{T}{\eta} \left(\frac{\check{v}}{T} \right)_y \right] + \varepsilon^2 \left[i(1 - UL) \frac{\bar{\delta}\gamma}{\eta} \check{p} - \frac{i\bar{\delta}N}{\eta} \check{w} \right] + \mathcal{O}(\varepsilon^4), \quad (4.1.11c)$$

$$\begin{aligned} \check{p}_{\theta} &= -\varepsilon \frac{\check{p}_y}{\eta} - \frac{\bar{\delta} i \rho (1 - UL)}{\eta} \left\{ \varepsilon^2 \left[(2 + \beta) \check{v}_{\theta\theta} - \check{v} \right] \right. \\ &\quad \left. + \varepsilon^3 \left[\frac{(2 + \beta)}{\eta^2 T} \left((\eta T \check{v}_{\theta})_y + \eta T \check{v}_{\theta y} \right) + (1 + \beta) \frac{iL}{\eta} \check{u}_{\theta} \right] \right\} + \mathcal{O}(\varepsilon^4), \end{aligned} \quad (4.1.11d)$$

$$\begin{aligned} \check{w}_{\theta\theta} - \check{w} &= -\frac{N}{\rho(1 - UL)} \check{p} - \frac{\varepsilon}{\eta^2 T} \left[(\eta T \check{w}_{\theta})_y + \eta T \check{w}_{\theta y} \right] \\ &\quad - \frac{\varepsilon^2}{\eta^2 T} \left[(T \check{w}_y)_y + i\bar{\delta}N(1 + \beta) \eta T \check{v}_{\theta} \right] + \mathcal{O}(\varepsilon^3). \end{aligned} \quad (4.1.11e)$$

The equations (4.1.11) are not quite a high frequency expansion of the boundary layer equations (4.1.2); the high frequency has caused some terms to jump order, and consequently we retain some terms that are absent in the standard $\mathcal{O}(\delta)$ analysis in §4.1.1. Also note that in contrast with the high frequency asymptotics of Brambley (2011a), the model proposed here has variation in the acoustic pressure at $\mathcal{O}(\varepsilon)$, and ‘finite thickness shear’ terms (i.e. first order in the boundary layer thickness, δ) appearing at $\mathcal{O}(\varepsilon^2)$.

Solving the system (4.1.11) for the inner solutions leads to the acoustic pressure and radial

velocity

$$\tilde{p}(y, \theta) = F_0(y) + \varepsilon F_1(y) + \varepsilon^2 F_2(y), \quad (4.1.12a)$$

$$\begin{aligned} \tilde{v}(y, \theta) = & A_0(y) + \varepsilon \left[A_1(y) + \frac{iL}{\eta(y)} B_0(y) e^{-\theta} + \frac{i(1-U(y)L)}{\sigma\eta(y)T(y)} D_0(y) e^{-\sigma\theta} \right] \\ & + \varepsilon^2 \left[A_2(y) + \frac{iL}{\eta} B_1(y) e^{-\theta} + a_0(y) e^{-\theta} + \frac{i(1-U(y)L)}{\sigma\eta(y)T(y)} D_1(y) e^{-\sigma\theta} \right]. \end{aligned} \quad (4.1.12b)$$

where $\sigma^2 = \text{Pr}$. The functions $F_j(y)$, $A_j(y)$, $B_j(y)$, $D_j(y)$ and $a_0(y)$ are determined by boundary, secularity and matching conditions, as described in Appendix 4.B. We note that \tilde{p} does not vary on the short length scale θ until $\mathcal{O}(\varepsilon^3)$, which is beyond the order of solution we present here. We asymptotically match (4.1.12) with the outer solutions (4.1.6) in the limit $y \rightarrow \infty$ (see section 4.B.1), which, using the definitions $Z = \tilde{p}(0)/\tilde{v}(0)$ and $Z_{\text{eff}} = p_\infty/v_\infty$, leads to the effective impedance

$$Z_{\text{eff}} = \frac{1}{\omega - Mk} \frac{\omega Z - \frac{kU_y(0)}{\sqrt{\omega\eta(0)}} Z - i\delta I_0(\omega - Mk)^2 + \omega \mathcal{B}Z}{1 + i\omega Z \delta I_1 \frac{k^2 + m^2}{(\omega - Mk)^2} + \mathcal{A} + \mathcal{C}Z}, \quad (4.1.13)$$

where

$$\mathcal{A} = (\delta I_0 \delta I_1 + \delta^2 I_{11} - \delta^2 I_{01})(k^2 + m^2) - \delta^2 I_2((\omega - Mk)^2 - k^2 - m^2), \quad (4.1.14a)$$

$$\begin{aligned} \mathcal{B} = & (\delta I_0 \delta I_1 + \delta^2 I_3 - \delta^2 I_{10})(k^2 + m^2) - \delta^2 I_{00}((\omega - Mk)^2 - k^2 - m^2) \\ & - i \frac{(\gamma - 1)^2}{\omega \text{Re}} \left[\frac{I_\mu}{\delta^2} + 2 \frac{\sigma}{1 + \sigma} T(1) U_r(1)^2 - \frac{5k^2}{4\omega^2} T(1)^2 U_r(1)^2 \right], \end{aligned} \quad (4.1.14b)$$

$$\mathcal{C} = \frac{(\gamma - 1)T(1)}{\sqrt{i\omega \text{Re}}} \left[ik U_r(1) \delta I_1 \frac{k^2 + m^2}{(\omega - Mk)^2} + \frac{i}{\omega} (k^2 + m^2)(\gamma - 1)T(1) + \frac{i\omega}{\sigma} (\gamma - 1) \right], \quad (4.1.14c)$$

and I_j are the integrals

$$\begin{aligned} \delta I_0 &= \int_0^1 \chi_0 \, dr, & \delta I_1 &= \int_0^1 \chi_1 \, dr, & \delta^2 I_2 &= \int_0^1 (1-r) \chi_0 \, dr, \\ \delta^2 I_3 &= \int_0^1 (1-r) \chi_1 \, dr, & \frac{I_\mu}{\delta^2} &= \int_0^1 \frac{\chi_\mu}{\delta^3} \, dr, & \delta^2 I_{01} &= \int_0^1 \chi_0(r) \int_r^1 \chi_1(r') \, dr' \, dr, \\ \delta^2 I_{10} &= \int_0^1 \chi_1(r) \int_r^1 \chi_0(r') \, dr' \, dr, & \delta^2 I_{00} &= \int_0^1 \left(\int_r^1 \chi_0(r') \, dr' - \delta I_0 \right) \, dr, \\ & & \delta^2 I_{11} &= \int_0^1 \left(\int_r^1 \chi_1(r') \, dr' - \delta I_1 \right) \, dr, \end{aligned}$$

with

$$\begin{aligned} \chi_0 &= 1 - \frac{\rho(\omega - Uk)^2}{(\omega - Mk)^2}, & \chi_1 &= 1 - \frac{(\omega - Mk)^2}{\rho(\omega - Uk)^2} \\ \frac{\chi_\mu}{\delta^3} &= \frac{-\omega}{\omega - Uk} \left[\frac{1}{2\sigma^2} (T^2)_{rrr} + (TU_r^2)_r + \frac{kT}{\omega - Uk} (TU_r)_{rr} \right]. \end{aligned}$$

At leading order, the boundary condition (4.1.13) reduces to the Myers condition, (3.3.4). At $\mathcal{O}(\varepsilon)$, and in the limit of a vanishingly thin shear layer $\delta \rightarrow 0$, (4.1.13) reduces to the $\mathcal{O}(\varepsilon)$ high frequency result presented in Brambley (2011a), while at $\mathcal{O}(\varepsilon)$ in the limit of infinite Reynolds number ($\xi = 0$) (4.1.13) reduces to the modified Myers boundary condition (Brambley, 2011b).

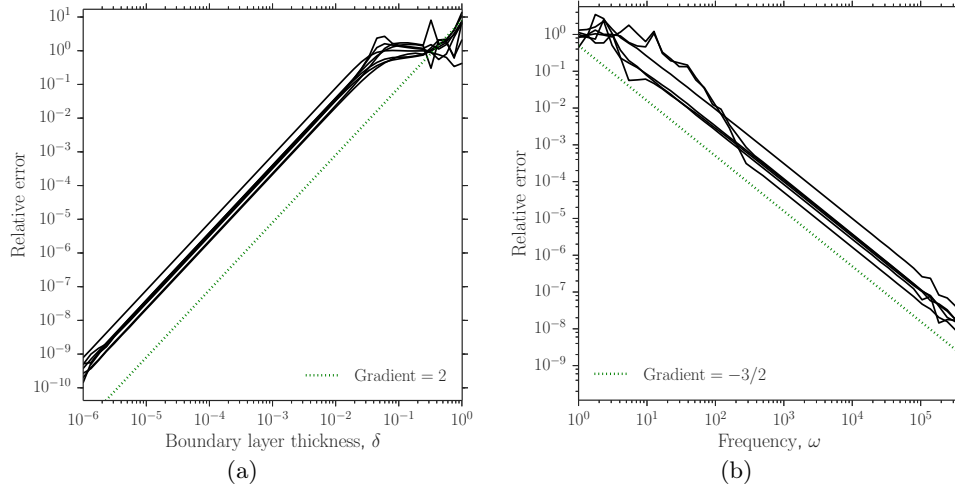


Figure 4.1. Asymptotic accuracy plots with relative error defined as $|Z_{\text{eff}}(Z)/(\tilde{p}_{ui}(1)/\tilde{v}_{ui}(1)) - 1|$, where the function $Z_{\text{eff}}(Z)$ is the asymptotic effective impedance (from either §4.1.1 or §4.1.2) with the input boundary impedance $Z = \tilde{p}_{sv}(1)/\tilde{v}_{sv}(1)$. (a) accuracy of the reduced boundary layer model (4.1.2), (4.1.3) and (4.1.4) with respect to δ . The first order solution has an error of $\mathcal{O}(\delta^2)$ (gradient 2). Parameters are $\omega = 10$, $m = 0$, $M = 0.5$, $k = \pm 1 \pm i$, ± 1 , $\pm i$, $\text{Re} = 1/\delta^2$. (b) accuracy of the high frequency effective impedance (4.1.13) with respect to ω ; the error is $\mathcal{O}(\varepsilon^3) = \mathcal{O}(\omega^{-3/2})$ (gradient $-3/2$). Parameters are $M = 0.5$, $\delta = \omega^{-3/2}$, $\text{Re} = 1/\delta^2$, $m/\text{int}(\omega) = 1$, $k/\omega = \exp\{i \arg(\tilde{k})\}$ where $\tilde{k} = \pm 1 \pm i$, 1 , $-i$. In both (a) and (b) the hyperbolic base flow profiles (3.1.1) are used.

4.2 Comparison of asymptotic and numerical results

The two asymptotic boundary layer models presented above are compared here against numerical solutions of the linearised Navier–Stokes equations, (1.1.13). Figure 4.1 shows that the two models are correct to their stated order of accuracy in their respective limits $\delta \rightarrow 0$ and $\omega \rightarrow \infty$.

Figure 4.2 shows the mode shapes of the acoustic radial velocity of the two asymptotic solutions, $\mathcal{O}(\delta)$ (4.1.2) and high frequency (4.1.12b), compared with viscous numerics. For reference, the inviscid uniform flow solution, \tilde{v}_{ui} in (3.3.1), to which the asymptotic solutions match, is also plotted. Both models replicate the viscous mode shape well inside the boundary layer. It appears in fig. 4.2b that the high frequency asymptotics outperform the $\mathcal{O}(\delta)$ asymptotics due to the high frequency ($\omega = 31$) used in this case.

4.2.1 k -plane modes

To find duct modes for the asymptotic models, a dispersion relation must be satisfied,

$$Z_{\text{eff}}(Z) = \frac{\tilde{p}_{ui}(1)}{\tilde{v}_{ui}(1)}, \quad (4.2.1)$$

where the effective impedance $Z_{\text{eff}}(Z)$ is the result of the asymptotic model (e.g. from (4.1.13)) given the actual boundary impedance Z as input (see Appendix 3.A for more information). In this section, we choose a frequency ω and find complex $k(\omega)$ that satisfy (5.6.2).

The asymptotic models are seen in fig. 4.3 to replicate the k -plane modes of the LNSE well. As with fig. 3.6, the attenuation (given by $\text{Im}(k)$) of the nearly propagating upstream modes is badly predicted by the Myers condition. The effect of viscosity is to increase the attenuation of these cut-on modes, as seen in fig. 4.3a, while the effect of shear is to reduce attenuation (for modes travelling upstream). Both asymptotic models perform well, suggesting the physics of both the shear and the viscosity have been correctly captured in both asymptotic formulations. In fig. 4.3b, the asymptotic boundary conditions accurately predict the viscous surface wave mode in the upper left quadrant, unlike either the inviscid numerics or the Myers condition.

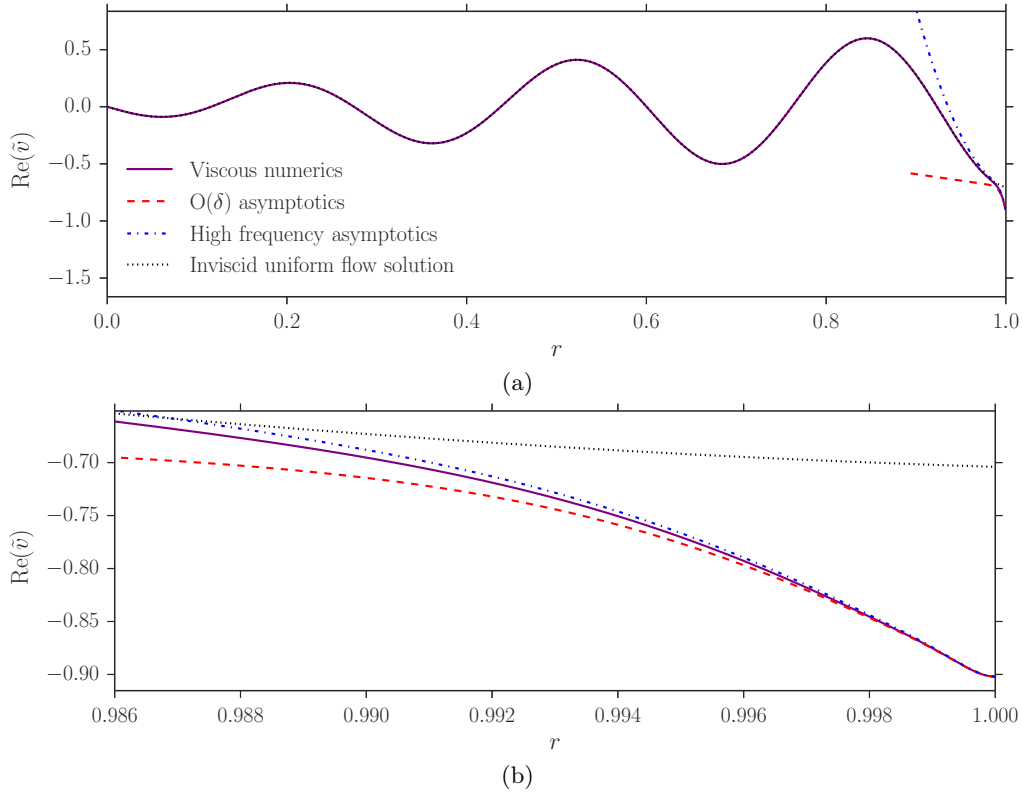


Figure 4.2. Acoustic radial velocity mode shapes of the viscous numerics, the $\mathcal{O}(\delta)$ boundary layer asymptotics (4.1.2), the high frequency boundary layer asymptotics (4.1.12b), and the inviscid uniform outer solution (3.3.1) to which the asymptotic solutions match in the limit $y \rightarrow \infty$. The asymptotic solutions are defined in the space of a boundary layer variable y , and plotted in the r domain using $r = 1 - \delta y$. (a) shows the full duct, (b) shows the boundary layer. Parameters are $\omega = 31$, $k = 14 + i$, $m = 2$, $M = 0.5$, $\delta = 7 \times 10^{-3}$, $\text{Re} = 5 \times 10^5$; the hyperbolic base flow (3.1.1) is used.

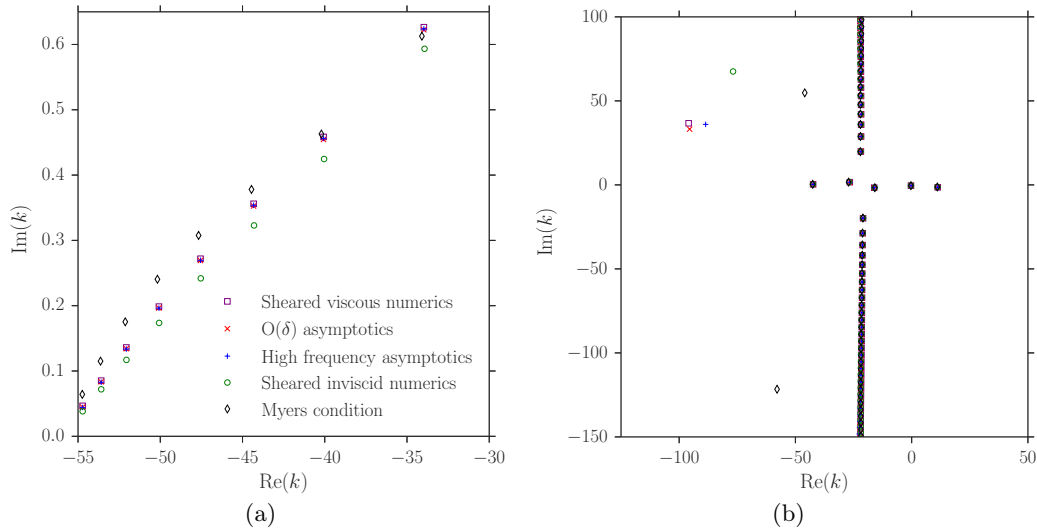


Figure 4.3. (a) Upstream cut-on modes of the two asymptotic models (4.1.2) and (4.1.13), the viscous and inviscid numerics, and the Myers boundary condition, for $\omega = 28$, $m = 0$, $M = 0.5$, $\delta = 2 \times 10^{-3}$, $\text{Re} = 5 \times 10^6$ with a boundary impedance of $Z = 3 + 4.16i$ (calculated using the mass-spring-damper impedance (5.6.1)). (b) Mode spectra showing one surface wave mode in the upper left quadrant. Parameters are $\omega = 31$, $m = 24$, $M = 0.5$, $\delta = 1 \times 10^{-3}$, $\text{Re} = 1 \times 10^6$, with a boundary impedance of $Z = 0.6 - 2i$. In both (a) and (b) the hyperbolic boundary layer profiles in (3.1.1) are used.

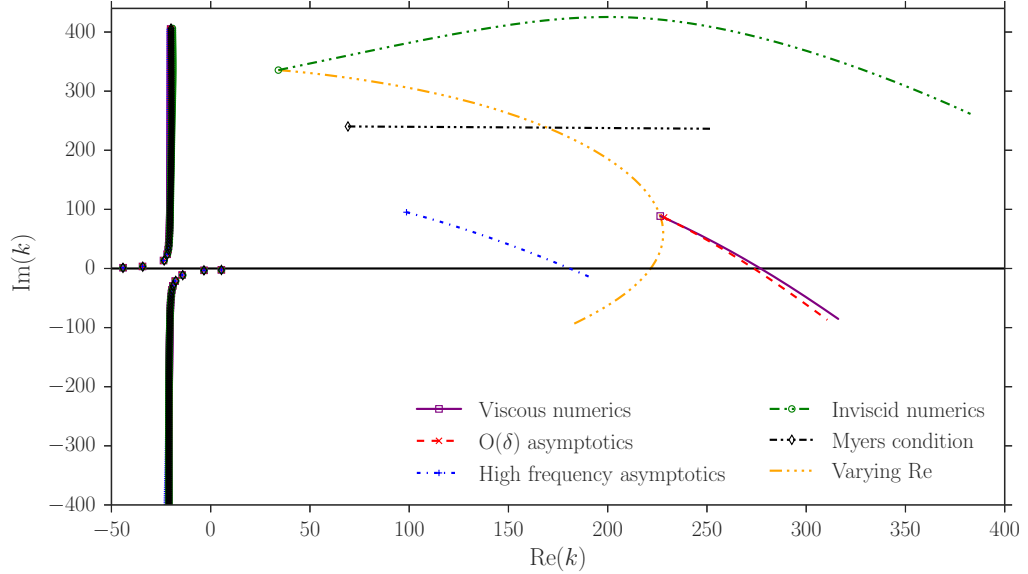


Figure 4.4. Markers show modes in the k -plane of the two asymptotic models (4.1.2) and (4.1.13), the viscous and inviscid numerics, and the Myers boundary condition, for $\omega = 31$, $m = 24$, $M = 0.5$, $\delta = 2 \times 10^{-4}$, $\text{Re} = 2.5 \times 10^7$ with a boundary impedance of $Z = 2 + 0.6i$. Also shown are Briggs–Bers trajectories of the surface wave modes in the upper right quadrant as $\text{Im}(\omega)$ is reduced from zero to around -20 with $\text{Re}(\omega) = 31$ held fixed. The impedance is governed by a mass–spring–damper model $Z(\omega) = R + i\omega d - ib/\omega$, with $R = 2$, $d = 0.02$, $b = 0.62$, such that $Z = 2 + 0.6i$ at $\omega = 31$. The track labelled “Varying Re” follows the inviscid numerical surface wave mode as the Reynolds number is reduced from $\text{Re} = \infty$; it passes through the viscous mode at $\text{Re} = 2.5 \times 10^7$ and crosses the real axis when $\text{Re} \simeq 1.04 \times 10^7$. The hyperbolic boundary layer profiles in (3.1.1) are used.

In fig. 4.4 the inviscid numerics and Myers boundary condition again predict a surface wave in a very different position to the viscous numerical surface wave (upper right quadrant). The dashed “Varying Re” line traces the movement of this surface wave mode as the Reynolds number is decreased from infinity; as both the inviscid and the viscous surface wave mode lie along this line, we identify the viscous surface wave mode as the viscous equivalent of the inviscid surface wave mode. The $\mathcal{O}(\delta)$ asymptotics (4.1.2) perform very well, while the high frequency asymptotics (4.1.13) do not do so well in predicting the position of the LNSE surface wave mode. This can be explained by the large value of the axial wavenumber at the LNSE surface wave mode being outside the range of validity of the high-frequency asymptotics, since $k \simeq 226 + 88i$ for this mode gives $|L| = 1.6/\varepsilon$, contradicting the assumption of $L = k/\omega$ being $\mathcal{O}(1)$ following (4.1.7).

Also shown in fig. 4.4 are the Briggs–Bers trajectories of the surface wave modes as $\text{Im}(\omega)$ is reduced from zero to around -10 . The LEE mode (sheared inviscid numerics) remains far above the real k axis as $\text{Im}(\omega)$ is reduced, while the LNSE mode (viscous numerics) crosses the real axis, indicating a downstream propagating convective instability. The two asymptotic models predict the correct convective instability, although the high frequency asymptotics are inaccurate for the reasons discussed in the previous paragraph.

4.2.2 ω -plane modes

The temporal stability properties of the new asymptotic models are investigated here. We choose a real k and solve the dispersion relation (5.6.2) to find complex frequency roots $w(k)$. The exponential factor $\exp\{i\omega t\}$ implies that the temporal growth rate of a mode is given by $-\text{Im}(\omega)$.

Figure 4.5 compares the behaviour of the ω modes as k , real, is increased for the LNSE, $\mathcal{O}(\delta)$ asymptotics, and high frequency asymptotics. As in §3.3.4, the LNSE displays an instability that has a well-defined maximum growth rate and restabilises at a finite k . The $\mathcal{O}(\delta)$ asymptotic model reproduces this behaviour: the growth rate of the instability is bounded (due to the regularising

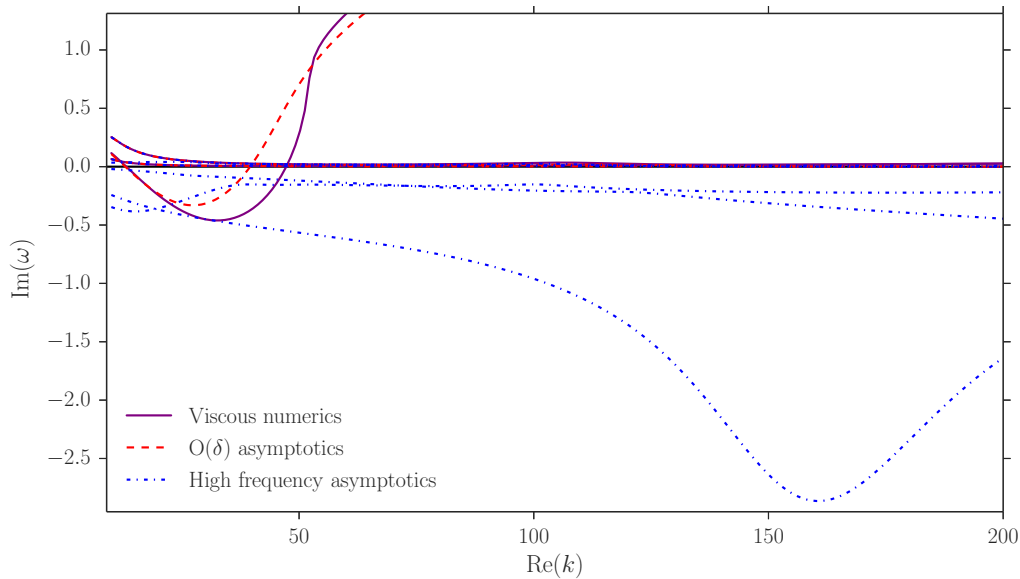


Figure 4.5. Temporal growth rates, $-\Im(\omega)$, of modes as k , real, is increased. A mode below the k axis is a growing instability. Plotted are modes for the LNSE, $\mathcal{O}(\delta)$ asymptotics (4.1.2), and high frequency asymptotics (4.1.13). Parameters are $m = 0$, $M = 0.5$, $\text{Re} = 3 \times 10^6$, $\delta = 7 \times 10^{-3}$ with the hyperbolic base flow (3.1.1). The boundary impedance is modelled as a mass–spring–damper (5.6.1) with a mass $d = 0.01$, spring $b = 10$ and damping $R = 0.75$.

effect of a finite thickness shear layer), and the mode restabilises for small enough wavelength (due to the small-scale damping by viscosity); this model is well-posed. Recall that neither the Myers boundary condition (Ingard, 1959; Myers, 1980) nor the leading order viscous boundary condition (Brambley, 2011a) lead to a bounded growth rate, while the first order inviscid boundary correction (Brambley, 2011b) gives a bounded growth rate that remains unstable for all k . Figure 4.5 also shows that the high frequency viscous asymptotics of §4.1.2 perform poorly with regard to temporal instability, so there is no guarantee of well-posedness; this is because the temporal instability occurs either for low frequencies or for $|k/\omega| \gg 1$, which are both outside the region of asymptotic validity of the high frequency boundary condition (4.1.13).

4.2.3 Accuracy of high frequency asymptotics at lower frequencies

In §4.2.1 it was shown that the high frequency asymptotics (4.1.13) are efficient in predicting cut-off and cut-on acoustic modes at high frequencies, but that the model can fail relative to the $\mathcal{O}(\delta)$ asymptotics in its prediction of surface waves. Here, we investigate the accuracy of the high frequency asymptotics at moderate to low frequencies for the cut-off and cut-on acoustic modes.

For the nearly cut-on acoustic modes, the parameter of most interest is the rate of attenuation per axial distance travelled. The accuracy of the asymptotic models with respect to the LNSE numerics can be expressed as the difference in the predicted attenuation rate, given in decibels per duct radius as

$$\Delta\text{dB} = 20 \log_{10} \left[\frac{\Im(k)}{\Im(k_{\text{LNSE}})} \right]. \quad (4.2.2)$$

Table 4.1 shows that the attenuation rate of the cut-on modes is well predicted by the high frequency asymptotics (4.1.13), and even at the low frequency of $\omega = 5$ the $\mathcal{O}(\delta)$ asymptotics are only marginally more accurate.² For $\omega = 2$, the $\mathcal{O}(\delta)$ asymptotics are significantly more accurate than the high frequency asymptotics, but the high frequency asymptotics still predict the attenuation of the two cut-on modes to within 1dB per duct radius travelled—that is, with much

²For a duct of radius $l^* = 1\text{m}$, a dimensionless frequency $\omega = 5$ corresponds to a sound frequency of $f^* \approx 270\text{Hz}$. The value $\omega = 31$ gives $f^* \approx 1.6\text{kHz}$.

greater accuracy than the Myers boundary condition. A similar situation is shown in table 4.2 for different parameters. We see that the high frequency asymptotics can achieve impressive accuracy even at low frequencies, and may even out-perform the $\mathcal{O}(\delta)$ asymptotics.

	k ($\omega = 10$)	ΔdB	k ($\omega = 5$)	ΔdB	k ($\omega = 2$)	ΔdB
LNSE	5.9042-0.4802i -18.6182+0.1565i		2.6441-0.6808i -6.4055+2.2000i		-0.9533-1.0094i -3.3209+1.9036i	
Myers	5.9456-0.4706i -18.6321+0.1259i	-0.1756 -1.8948	2.6555-0.6043i -6.5494+1.7036i	-1.0354 -2.2212	-0.8293-0.8665i -3.1805+3.1690i	-1.3261 4.4269
HF	5.9046-0.4748i -18.6189+0.1451i	-0.0992 -0.6587	2.6309-0.6817i -6.3715+2.2413i	0.0115 0.1616	-1.0158-0.9550i -2.9887+1.7280i	-0.4815 -0.8407
OD	5.9043-0.4790i -18.6186+0.1472i	-0.0219 -0.5317	2.6422-0.6781i -6.4053+2.2004i	-0.0336 0.0016	-0.9675-1.0079i -3.3079+1.9001i	-0.0127 -0.0159

Table 4.1. Wavenumbers of the most cut-on modes, using the LNSE numerics, the Myers boundary condition, the high frequency (HF) asymptotics (4.1.13) and the $\mathcal{O}(\delta)$ (OD) asymptotics (4.1.2). Parameters are $\omega = 5$, $m = 2$, $\text{Re} = 1 \times 10^5$, $\delta = 4 \times 10^{-3}$. The boundary impedance Z is found using (5.6.1) with $d = 0.08$, $b = 6$ and $R = 1.6$. Base profiles as in (3.1.1). The same parameters were used for fig. 4.6. The errors in the attenuation predicted by the approximate models are expressed in decibels per radius in the ΔdB columns, calculated using (4.2.2).

	k ($\omega = 15$)	ΔdB	k ($\omega = 10$)	ΔdB	k ($\omega = 5$)	ΔdB
LNSE	-26.5036+0.2031i -26.5169+0.2312i		-13.8888+1.0301i -13.8435+1.0375i		-0.5166-3.4788i -0.5106-3.4081i	
Myers	-26.5039+0.2026i -26.5077+0.2070i	1.1256 -0.0214	-13.8893+1.0295i -13.8420+1.0351i	0.0618 -0.0054	-0.5166-3.4783i -0.5211-3.4781i	-0.1783 -0.0012 -0.0016

Table 4.2. As for table 4.1, but with $m = 6$, $\text{Re} = 8 \times 10^6$, $\delta = 5 \times 10^{-3}$.

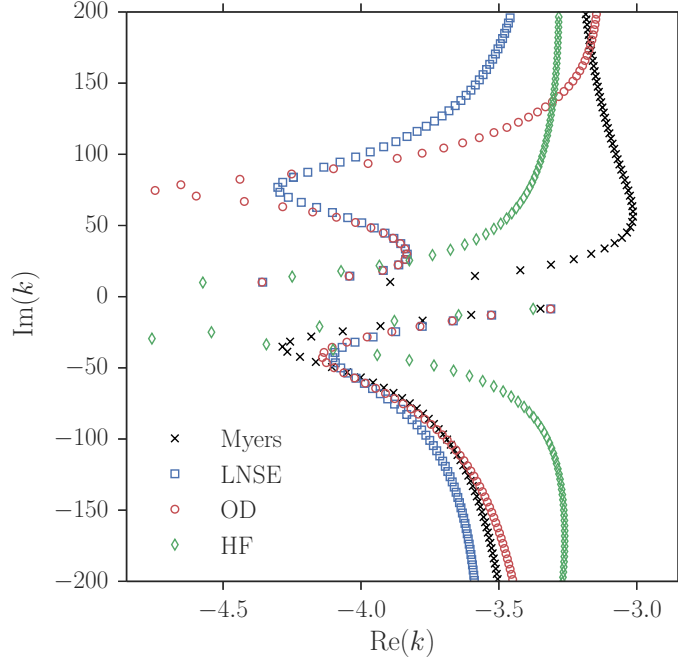


Figure 4.6. Cut-off modes in the k -plane of the Myers boundary condition, the LNSE numerics, the high frequency (HF) asymptotics (4.1.13) and the $\mathcal{O}(\delta)$ (OD) asymptotics (4.1.2) for $\omega = 5$, $m = 2$, $\text{Re} = 1 \times 10^5$, $\delta = 4 \times 10^{-3}$. The boundary impedance Z is found using (5.6.1) with $d = 0.08$, $b = 6$ and $R = 1.6$. Base profiles as in (3.1.1).

In fig. 4.6, the spectra of cut-off acoustic modes in the k -plane is plotted for the LNSE numerics, the Myers boundary condition and the two new asymptotic models, for the relatively low frequency $\omega = 5$. The accuracy of the high frequency asymptotics is seen to have dropped with this reduction in frequency, although the behaviour of these cut-off modes is far less important than that of the cut-on modes considered above.

4.2.4 The ratio Z_{eff}/Z

In this section the effective impedance Z_{eff} predicted by the high frequency asymptotics (4.1.13) – which accounts for a sheared and viscous boundary layer over an acoustic lining – is compared with the boundary impedance Z . This is done by considering the values of $|Z_{\text{eff}}/Z|$ and $\arg(Z_{\text{eff}}/Z)$ over the complex k -plane for a given set of parameters. The parameters $(Z, \omega, M, \text{Re}, \delta)$ are chosen to correspond to typical experimental facilities (e.g. Aurégan & Leroux, 2008; Jones *et al.*, 2005; Marx *et al.*, 2010; Renou & Aurégan, 2011). Due to our scheme of nondimensionalisation, in which the frequency is scaled by the ratio of the speed of sound and the radius of the duct, c_0^*/l^* , the small ducts typically used in such facilities ($\sim 1\text{cm}$ wide) lead to dimensionless frequencies that are too small to satisfy the asymptotic regimes assumed in the derivation of (4.1.13). Therefore, we choose to scale the system up to the size of a typical aeroengine, where the fan diameters are typically 2–3.5m. The mean flow profiles used to evaluate (4.1.13) are boundary layer expansions of the hyperbolic profiles (3.1.1),

$$U(y) = M \tanh(y), \quad T(y) = T_0 + \tau (\cosh(y))^{-1}, \quad (4.2.3)$$

where $y \in [0, 16]$ is sufficient to capture the boundary layer, and we identify δ with the momentum thicknesses of the experimentally determined (fully turbulent) profiles.

Figures 4.7–4.10 display results for two different experimental setups, with two parameter sets for each (details are given in the figure captions). Figures 4.7a and 4.8a show that for the zeroth-

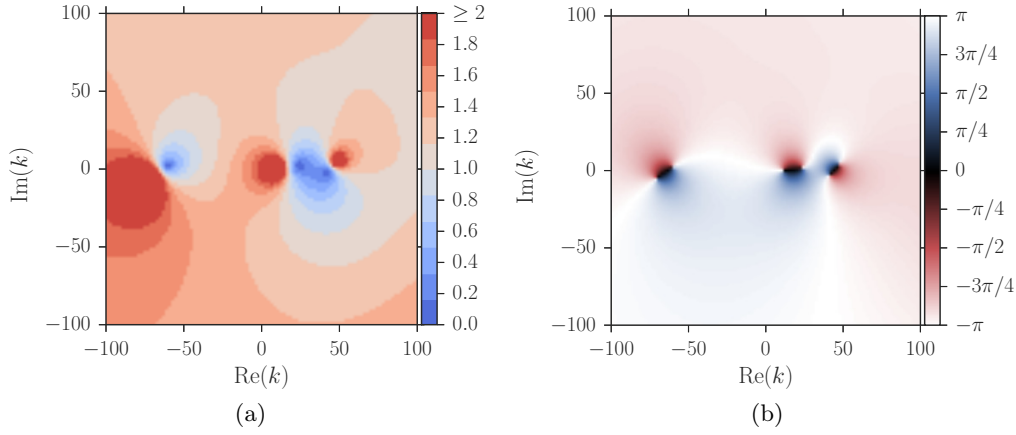


Figure 4.7. Contour plots in the k -plane of (a) $|Z_{\text{eff}}/Z|$, (b) $\arg(Z_{\text{eff}}/Z)$ for the experimental setup of Jones *et al.* (2005), with $f^* = 2500\text{Hz}$, $Z = 0.93 - 1.43i$, $M = 0.335$. For a duct radius $l^* = 1.5\text{m}$ and sound speed $c_0^* = 340\text{ms}^{-1}$, our dimensionless parameters are $\omega = 69.3$, $m = 0$, $\text{Re} = 3.4 \times 10^7$, $\delta = 9\%$. Base profiles as in (4.2.3).

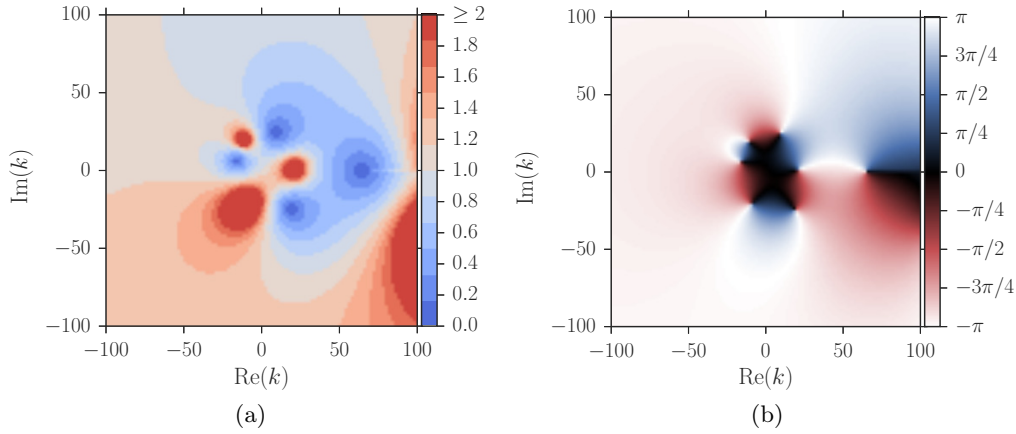


Figure 4.8. Contour plots in the k -plane of (a) $|Z_{\text{eff}}/Z|$, (b) $\arg(Z_{\text{eff}}/Z)$ for the experimental setup of Marx *et al.* (2010), with $f^* = 1200\text{Hz}$, $Z = 0.25 - 0.39i$ and $M = 0.32$. For a duct radius $l^* = 1\text{m}$ and sound speed $c_0^* = 363\text{ms}^{-1}$, dimensionless parameters are $\omega = 20.8$, $m = 0$, $\text{Re} = 2.4 \times 10^7$, $\delta = 5\%$. Base profiles as in (4.2.3).

order azimuthal mode ($m = 0$) there can occur large areas of the complex k -plane where $|Z_{\text{eff}}/Z|$ lies close to unity. However, the corresponding plots of $\arg(Z_{\text{eff}}/Z)$, figs. 4.7b and 4.8b, show that Z_{eff} and Z commonly lie in different quadrants of the complex plane, hence their close relative magnitudes belie their disparity. For the higher azimuthal order shown in figs. 4.9a and 4.10a, $|Z_{\text{eff}}/Z| \gtrsim 2$ over large sections of the k -plane. This suggests that modes that rapidly vary in the azimuthal direction – $m = 24$ is indeed rapidly varying, but typical of rotor-alone noise at take-off (McAlpine *et al.*, 2006) – interact differently with the coupled boundary layer–acoustic lining system to a plane wave, say, and hence see an appreciably different effective impedance.

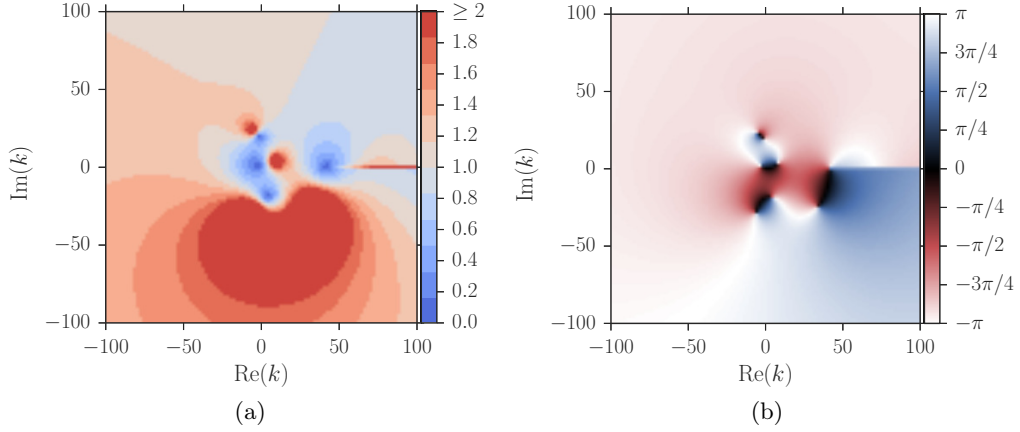


Figure 4.9. Contour plots in the k -plane of (a) $|Z_{\text{eff}}/Z|$, (b) $\arg(Z_{\text{eff}}/Z)$ for the experimental setup of Jones *et al.* (2005), with $f^* = 500\text{Hz}$, $Z = 0.61 - 0.59i$ and $M = 0.335$. For a duct radius $l^* = 1.5\text{m}$ and sound speed $c_0^* = 340\text{ms}^{-1}$, dimensionless parameters are $\omega = 13.9$, $m = 24$, $\text{Re} = 3.4 \times 10^7$, $\delta = 9\%$. Base profiles as in (4.2.3).

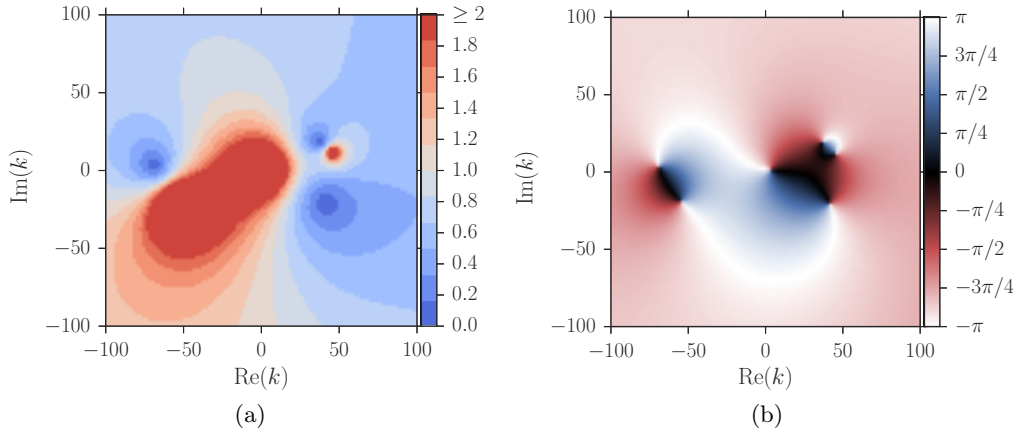


Figure 4.10. Contour plots in the k -plane of (a) $|Z_{\text{eff}}/Z|$, (b) $\arg(Z_{\text{eff}}/Z)$ for the experimental setup of Marx *et al.* (2010), with $f^* = 5000\text{Hz}$ and $M = 0.32$. The impedance $Z = 3.33 + 1i$ was found by extrapolating to a higher frequency the expression of Aurégan & Leroux (2008): $Z = -i\check{a} \cot(\check{b}\omega^* + (1 - i)\check{c}\sqrt{\omega^*})$, where $\check{a} = 1.25$, $\check{b} = 1.85 \times 10^{-4}$ and $\check{c} = 2 \times 10^{-3}$. For a duct radius $l^* = 1\text{m}$ and sound speed $c_0^* = 363\text{ms}^{-1}$, dimensionless parameters are $\omega = 86.5$, $m = 24$, $\text{Re} = 2.4 \times 10^7$, $\delta = 5\%$. Base profiles as in (4.2.3).

4.3 Summary

In this chapter we have used matched asymptotic expansions and the WKB multiple scales method to solve for the acoustics in a finite-thickness sheared, viscous boundary layer above an acoustic lining. The first asymptotic regime, using a relatively simple boundary layer rescaling, resulted in a simplified set of governing equations for the acoustics that must be solved numerically. The second asymptotic regime, which linked the modal frequency and boundary layer thickness via a non-trivial asymptotic scaling, resulted in an analytically tractable system of equations that when solved led to a closed-form expression for the effective impedance of a sheared and viscous boundary layer above an acoustic lining, valid at high frequencies.

The high frequency regime is usually relevant in aeroacoustic applications, but this may not always be the case. Also, attempting to reformulate a frequency-domain boundary condition that was derived in the high-frequency limit in the time domain leads to troubling questions. The next chapter seeks to address these two problems by abusing the different lengthscales associated with eddy and molecular viscosity to derive an analytical effective impedance boundary condition that does not rely on an asymptotically large frequency.

Appendix

4.A Numerical boundary conditions and extrapolating to infinity

Equation (4.1.2) gives the governing equations for the acoustics in a thin boundary layer $y > 0$, $r = 1 - \delta y$. Outside this boundary layer, as $y \rightarrow \infty$, the mean flow is considered uniform and the outer inviscid acoustic solution is given in (3.3.1). Here we consider matching the two. To aid this matching, we assume that the mean flow varies within the boundary layer only for $y < Y$, within which region (4.1.2) must be solved numerically. For $y > Y$, however, the governing equations may be solved analytically. The solutions may be used to extend the numerical solutions found in $y \in [0, Y]$ and extrapolate them in the limit $y \rightarrow \infty$ in order to match with the outer inviscid acoustic solution (3.3.1). For $y > Y$, the governing equations (4.1.2) reduce to

$$\xi \hat{u}_{yy} - i(\omega - Mk)\hat{u} = \delta [\xi \hat{u}_y - ik\tilde{p}], \quad (4.A.1a)$$

$$\frac{\xi}{\text{Pr}} \hat{T}_{yy} - i(\omega - Mk)\hat{T} = \delta \left[\frac{\xi}{\text{Pr}} \hat{T}_y - i(\omega - Mk)\tilde{p} \right], \quad (4.A.1b)$$

$$\xi \tilde{w}_{yy} - i(\omega - Mk)\tilde{w} = -im\tilde{p}, \quad (4.A.1c)$$

$$\tilde{v}_y = -i(\omega - Mk)(\gamma - 1)\hat{T} - ik\hat{u} + \delta [i\gamma(\omega - Mk)\tilde{p} + \tilde{v} - im\tilde{w}], \quad (4.A.1d)$$

$$\tilde{p}_y = \delta [i(\omega - Mk)\tilde{v} - \xi(2 + \beta)\tilde{v}_{yy} - ik\xi(1 + \beta)\hat{u}_y], \quad (4.A.1e)$$

which are uncoupled. At leading order these have the bounded solutions

$$\hat{u}_0(y) = \bar{u}_0 e^{-\eta_\infty y}, \quad \hat{T}_0(y) = \bar{T}_0 e^{-\sigma \eta_\infty y}, \quad \tilde{w}_0(y) = \bar{w} e^{-\eta_\infty y} + \frac{mp_0}{\omega - Mk}, \quad (4.A.2a)$$

$$\tilde{v}_0(y) = \bar{v}_0 + i(\omega - Mk) \frac{(\gamma - 1)}{\sigma \eta_\infty} \bar{T}_0 e^{-\sigma \eta_\infty y} + \frac{ik}{\eta_\infty} \bar{u}_0 e^{-\eta_\infty y}, \quad \tilde{p}_0 = p_0, \quad (4.A.2b)$$

for some constants $\bar{u}_0, \bar{T}_0, \bar{w}, \bar{v}_0$. At first order the solutions are

$$\hat{u}_1(y) = \bar{u}_1 e^{-\eta_\infty y} + \frac{1}{2} \bar{u}_0 y e^{-\eta_\infty y} + \frac{k p_0}{\omega - M k}, \quad (4.A.3a)$$

$$\hat{T}_1(y) = \bar{T}_1 e^{-\sigma \eta_\infty y} + \frac{1}{2} \bar{T}_0 y e^{-\sigma \eta_\infty y} + p_0, \quad (4.A.3b)$$

$$\begin{aligned} \tilde{v}_1(y) = \bar{v}_1 + \left(\bar{v}_0 + \frac{(\omega - M k)^2 - k^2 - m^2}{\omega - M k} i p_0 \right) y + i(\omega - M k) \frac{(\gamma - 1)}{\sigma \eta_\infty} (\hat{T}_1 - p_0) \\ + \frac{i k}{\eta_\infty} \left(\hat{u}_1 - \frac{k p_0}{\omega - M k} \right) + \frac{i m}{\eta_\infty} \left(\tilde{w}_0 - \frac{m p_0}{\omega - M k} \right) - \frac{\xi(\gamma - 1)}{2\sigma^2} \hat{T}_0 - \frac{\xi k}{2(\omega - M k)} \hat{u}_0, \end{aligned} \quad (4.A.3c)$$

$$\tilde{p}_1(y) = \bar{p}_1 + i(\omega - M k) \bar{v}_0 y + i \xi (\omega - M k) (\gamma - 1) (2 + \beta - 1/\text{Pr}) \hat{T}_0, \quad (4.A.3d)$$

where $\sigma^2 = \text{Pr}$ and $\eta_\infty^2 = i(\omega - M k)/\xi$, with $\Re(\eta_\infty) > 0$, and some constants $\bar{u}_1, \bar{T}_1, \bar{v}_1$ and \bar{p}_1 . Note that η_∞ has a branch cut along $k = \omega/M - iq$ for $q \geq 0$ to ensure that the solutions remain bounded as $y \rightarrow \infty$. In the limit $y \rightarrow \infty$, the relations (4.A.2a), (4.A.3a) and (4.A.3b) give boundary conditions on \hat{u}, \hat{T} and \tilde{w} ,

$$\hat{u}_0(y) \rightarrow 0, \quad \hat{T}_0(y) \rightarrow 0, \quad \tilde{w}_0(y) \rightarrow \frac{m p_0}{\omega - M k}, \quad \text{as } y \rightarrow \infty, \quad (4.A.4)$$

at $\mathcal{O}(1)$, and

$$\hat{u}_1(y) \rightarrow \frac{k p_0}{\omega - M k}, \quad \hat{T}_1(y) \rightarrow p_0, \quad \text{as } y \rightarrow \infty, \quad (4.A.5)$$

at $\mathcal{O}(\delta)$.

To form the effective impedance we match the solutions (4.A.2b), (4.A.3c) and (4.A.3d) in the limit $y \rightarrow \infty$ to the outer solutions, which are the uniform inviscid acoustics outside the boundary layer, (3.3.1). The outer solutions may be expanded near the lining to give

$$\tilde{p}_{\text{ui}}(1 - \delta y) = p_\infty - \delta y p'_\infty + \mathcal{O}(\delta^2), \quad \tilde{v}_{\text{ui}}(1 - \delta y) = v_\infty - \delta y v'_\infty + \mathcal{O}(\delta^2), \quad (4.A.6)$$

where the derivatives p'_∞, v'_∞ may be rewritten

$$p'_\infty = -i(\omega - M k)v_\infty, \quad v'_\infty = \frac{(\omega - M k)^2 - k^2 - m^2}{i(\omega - M k)} p_\infty - v_\infty. \quad (4.A.7)$$

Since we have applied a known normalisation at the lining – causing constant terms to arise at $\mathcal{O}(\delta)$ in the boundary layer solutions – we must expand $p_\infty = p_\infty^{(0)} + \delta p_\infty^{(1)}$ and similarly for v_∞ . Hence the expansions (4.A.6) become

$$p_{\text{ui}}(1 - \delta y) = p_\infty^{(0)} + \delta p_\infty^{(1)} + \delta y i(\omega + M k) v_\infty^{(0)} + \mathcal{O}(\delta^2), \quad (4.A.8a)$$

$$v_{\text{ui}}(1 - \delta y) = v_\infty^{(0)} + \delta v_\infty^{(1)} + \delta y \left(v_\infty^{(0)} + \frac{(\omega - M k)^2 - k^2 - m^2}{(\omega - M k)} i p_\infty^{(0)} \right) + \mathcal{O}(\delta^2). \quad (4.A.8b)$$

These are the outer solutions to which we match our numerical solutions of (4.1.2) in the limit $y \rightarrow \infty$, via the analytical solutions for $y > Y$. The numerical solutions may be found by, for instance, discretising the domain and approximating the y derivatives using finite differences.

If we are solving in a finite numerical domain $y \in [0, Y]$, we may use the relations (4.A.2b), (4.A.3c) and (4.A.3d) to extrapolate our solutions out to infinity. At leading order this is simple due to the exponentially decaying terms; we identify \bar{v}_0 with $v_\infty^{(0)}$ and rearrange (4.A.2b) for $v_\infty^{(0)}$ to find

$$v_\infty^{(0)} = \tilde{v}_0(Y) - \frac{\eta_\infty \xi}{\sigma} (\gamma - 1) \hat{T}_0(Y) - \frac{i k}{\eta_\infty} \hat{u}_0(Y). \quad (4.A.9)$$

For the pressure we simply find $p_\infty^{(0)} = p_0$. At first order consider the following: if

$$\tilde{v}_1(y) = \bar{v}_1 + (ay + b)e^{-\eta_\infty y} + (cy + d)e^{-\sigma\eta_\infty y} + ey, \quad (4.A.10)$$

which is the form of (4.A.3c), then in the limit $y \rightarrow \infty$

$$\tilde{v}_1(y) \sim \bar{v}_1 + ey. \quad (4.A.11)$$

Evaluating (4.A.3c) at $y = Y$ and rearranging to leave \bar{v}_1 and the terms linear in Y on the right hand side, as in (4.A.11), gives

$$\tilde{v}_1(Y) - (aY + b)e^{-\eta_\infty Y} - (cY + d)e^{-\sigma\eta_\infty Y} = \bar{v}_1 + eY. \quad (4.A.12)$$

We may identify \bar{v}_1 with $v_\infty^{(1)}$ and \bar{p}_1 with $p_\infty^{(1)}$, and thus use the extrapolated forms of (4.A.3c) and (4.A.3d) – which are of the form (4.A.12) – to rearrange for $p_\infty^{(1)}$ and $v_\infty^{(1)}$:

$$p_\infty^{(1)} = \tilde{p}_1(Y) - i(\omega - Mk)Yv_\infty^{(0)} - i\xi(\omega - Mk)(\gamma - 1) \left(2 + \beta - \frac{1}{\text{Pr}}\right) \hat{T}_0(Y), \quad (4.A.13a)$$

$$\begin{aligned} v_\infty^{(1)} = & \tilde{v}_1(Y) - \left(v_\infty^{(0)} + \frac{(\omega - Mk)^2 - k^2 - m^2}{\omega - Mk} ip_\infty^{(0)}\right) Y \\ & - \frac{i(\omega - Mk)(\gamma - 1)}{\sigma\eta_\infty} \left(\hat{T}_1(Y) - p_\infty^{(0)}\right) - \frac{ik}{\eta_\infty} \left(\hat{u}_1(Y) - \frac{kp_\infty^{(0)}}{\omega - Mk}\right) \\ & - \frac{im}{\eta_\infty} \left(\tilde{w}_0(Y) - \frac{mp_\infty^{(0)}}{\omega - Mk}\right) + \frac{\xi(\gamma - 1)}{2\sigma^2} \hat{T}_0(Y) + \frac{\xi k}{2(\omega - Mk)} \hat{u}_0(Y). \end{aligned} \quad (4.A.13b)$$

The effective impedance is then given by

$$Z_{\text{eff}} = \frac{p_\infty^{(0)} + \delta p_\infty^{(1)}}{v_\infty^{(0)} + \delta v_\infty^{(1)}}; \quad (4.A.14)$$

this is the function used in the dispersion relation (5.6.2) to find eigenmodes of the $\mathcal{O}(\delta)$ asymptotics.

4.B Solving the high frequency boundary layer equations

Here we solve equations (4.1.11) to $\mathcal{O}(\varepsilon^2)$. At leading order we find

$$\begin{aligned} \tilde{v}_0(y, \theta) &= A_0(y), & \check{u}_0(y, \theta) &= 0(y)e^{-\theta} - \frac{iU_y}{1 - UL} A_0(y), \\ \tilde{p}_0(y, \theta) &= F_0(y), & \check{T}_0(y, \theta) &= D_0(y)e^{-\sigma\theta} - \frac{iT_y}{1 - UL} A_0(y), \\ \tilde{w}_0 &= G_0(y)e^{-\theta} + \frac{N}{\rho(1 - UL)} F_0(y), \end{aligned} \quad (4.B.1)$$

where exponentially growing solutions have been excluded. The explicit y and θ dependencies will be dropped henceforth. Homogeneous boundary conditions on \check{u}_0 , \check{T}_0 and \tilde{w}_0 at $y = 0$ give

$$B_0(0) = iU_y(0)A_0(0), \quad D_0(0) = iT_y(0)A_0(0) = 0, \quad G_0(0) = -\frac{N}{\rho(0)}F_0(0). \quad (4.B.2)$$

The $D_0(0) = 0$ relation arises from our isothermal boundary condition $T_y(0) = 0$. Matching \tilde{p} and \tilde{v} to the outer solution will fix the values of $A_0(0)$ and $F_0(0)$ in section 4.B.1, and similarly at

subsequent orders.

At first order, we find secularity conditions by disallowing resonant terms. The first-order \tilde{v} equation is

$$\tilde{v}_{1,\theta} = -\frac{i(1-UL)}{\eta T} D_0 e^{-\sigma\theta} - \frac{iL}{\eta} B_0 e^{-\theta} - \left\{ \frac{T_y}{\eta T} A_0 - \frac{LU_y}{\eta(1-UL)} A_0 - \frac{T}{\eta} \left(\frac{A_0}{T} \right)_y \right\}, \quad (4.B.3)$$

where the curly brackets enclose terms that are functions of y only, and hence are resonant. To prevent powers of θ arising, we equate the curly brackets with zero and form the secularity condition for $A_0(y)$:

$$A_{0,y} - 2(\ln \eta T)_y A_0 = 0 \quad \Rightarrow \quad A_0(y) = \bar{A}_0(1-UL), \quad (4.B.4)$$

where \bar{A}_0 is a constant. In going from (4.B.3) to (4.B.4), the definitions of $\eta(y)$, (4.1.9), and its derivative are used. Similarly, the first-order \tilde{p} equation is

$$\tilde{p}_{1,\theta} = -\frac{1}{\eta} F_{0,y}, \quad (4.B.5)$$

where the right hand side is a function of y only and hence resonant. As above, we set this to zero to form the secularity condition for $F_0(y)$:

$$F_0(y) = \bar{F}_0, \quad (4.B.6)$$

where \bar{F}_0 is a constant. To ascertain \bar{A}_0 and \bar{F}_0 we could, for instance, force \tilde{v} and \tilde{p} to satisfy some impedance condition at the wall $y = 0$; or match to a known solution outside the boundary layer in the limit $y \rightarrow \infty$. Solving at first order now gives

$$\tilde{v}_1 = A_1 + \frac{iL}{\eta} B_0 e^{-\theta} + \frac{i(1-UL)}{\sigma\eta T} D_0 e^{-\sigma\theta}, \quad \tilde{p}_1 = F_1. \quad (4.B.7)$$

Expanding the first-order equation for \check{u} we find

$$\begin{aligned} \check{u}_{1,\theta\theta} - \check{u}_1 = & \frac{iU_y}{1-UL} \left(A_1 + \frac{iL}{\eta} B_0 e^{-\theta} + \frac{i(1-UL)}{\sigma\eta T} D_0 e^{-\sigma\theta} \right) - \frac{\bar{\delta}L}{\rho(1-UL)} F_0 \\ & + \frac{1}{\eta^2 T} \left((\eta T B_0)_y + \eta T B_{0,y} \right) e^{-\theta} + \frac{\sigma U_y}{\eta T} D_0 e^{-\sigma\theta}. \end{aligned} \quad (4.B.8)$$

The resonant³ terms on the right hand side of (4.B.8) are those $\propto \exp(-\theta)$. Equating the resonant terms with zero, we find

$$\frac{1}{\eta T} (\eta T B_0)_y - \frac{LU_y}{1-UL} B_0 + B_{0,y} = 0, \quad (4.B.9)$$

which may be written

$$B_{0,y} + \frac{3}{2} (\ln \eta T)_y B_0 = 0 \quad \Rightarrow \quad B_0(y) = B_0(0)(1-UL)^{-3/4}. \quad (4.B.10)$$

In the same vein, the secularity condition for G_0 can be found from the first-order \tilde{w} equation

$$\tilde{w}_{1,\theta\theta} - \tilde{w}_1 = -\frac{N}{\rho(1-UL)} F_1 + \frac{1}{\eta^2 T} \left((\eta T G_0)_y + \eta T G_{0,y} \right) e^{-\theta}, \quad (4.B.11)$$

³We use the term ‘resonant’ here even though these resonant terms are exponentially decaying.

where again the secular terms are $\propto \exp(-\theta)$. This leads to

$$G_{0,y} + \frac{1}{2}(\ln \eta T)_y G_0 = 0 \quad \Rightarrow \quad G_0(y) = G_0(0)(1 - UL)^{-1/4}. \quad (4.B.12)$$

For the first-order \check{T} equation

$$\begin{aligned} \frac{1}{\text{Pr}} \check{T}_{1,\theta\theta} - \check{T}_1 = \frac{iT_y}{1 - UL} \left(A_1 + \frac{iL}{\eta} B_0 e^{-\theta} + \frac{i(1 - UL)}{\sigma\eta T} D_0 e^{-\sigma\theta} \right) - \frac{\bar{\delta}}{\rho} F_0 \\ + \frac{1}{\sigma\eta^2 T} \left((\eta T D_0)_y + \eta (T D_0)_y \right) e^{-\sigma\theta} + \frac{2U_y}{\eta} B_0 e^{-\theta}, \end{aligned} \quad (4.B.13)$$

the secular terms are $\propto \exp(-\sigma\theta)$. Equating these with zero we find

$$\frac{1}{\eta T} (\eta T D_0)_y + \frac{1}{T} (T D_0)_y - \frac{T_y}{T} D_0 = 0, \quad (4.B.14)$$

which may be written

$$D_{0,y} + \frac{1}{2}(\ln \eta T)_y D_0 = 0 \quad \Rightarrow \quad D_0(y) = D_0(0)(1 - UL)^{-1/4}. \quad (4.B.15)$$

In fact, the boundary condition $D_0(0) = 0$ from (4.B.2) tells us that $D_0(y) \equiv 0$. This is a direct consequence of our isothermal wall condition $T_y(0) = 0$. The first-order solutions for \check{u} , \check{T} and \check{w} are then

$$\begin{aligned} \check{u}_1 = B_1 e^{-\theta} - \frac{iU_y}{1 - UL} A_1 + \frac{\bar{\delta}L}{\rho(1 - UL)} F_0, \quad \check{w}_1 = G_1 e^{-\theta} + \frac{N}{\rho(1 - UL)} F_1, \\ \check{T}_1 = D_1 e^{-\sigma\theta} + d_0 e^{-\theta} - \frac{iT_y}{1 - UL} A_1 + \frac{\bar{\delta}}{\rho} F_0, \end{aligned} \quad (4.B.16)$$

where

$$d_0(y) = \frac{\text{Pr}}{1 - \text{Pr}} \left(2U_y - \frac{LT_y}{1 - UL} \right) \frac{B_0}{\eta}. \quad (4.B.17)$$

No slip and isothermal wall boundary conditions at first order lead to

$$\begin{aligned} B_1(0) = iU_y(0)A_1(0) - \frac{\bar{\delta}L}{\rho(0)} F_0(0), \quad D_1(0) = -d_0(0) - \frac{\bar{\delta}}{\rho(0)} F_0(0), \\ G_1(0) = -\frac{N}{\rho(0)} F_0(0). \end{aligned} \quad (4.B.18)$$

At second order we find the secularity conditions for A_1 and F_1 by the same method as the preceding order, giving

$$A_{1,y} - 2(\ln \eta T)_y A_1 = \left[\bar{\delta}i(1 - UL) - \frac{\bar{\delta}i(L^2 + N^2)}{\rho(1 - UL)} \right] F_0, \quad (4.B.19a)$$

$$F_{1,y} = \bar{\delta}i\rho(1 - UL)A_0, \quad (4.B.19b)$$

which may be solved to find

$$A_1(y) = \bar{A}_1(1 - UL) + i\bar{\delta}(1 - UL) \int_0^y \left(1 - \frac{L^2 + N^2}{\rho(1 - UL)^2} \right) F_0 dy', \quad (4.B.20a)$$

$$F_1(y) = \bar{F}_1 + i\bar{\delta}\bar{A}_0 \int_0^y \rho(1 - UL)^2 dy'. \quad (4.B.20b)$$

The solution to the F_1 secularity condition in (4.B.20b), we see, is not in general a constant. The

high frequency forces variation in the acoustic pressure over the boundary layer at an order at which it was previously assumed to be constant (Brambley, 2011a). (Or, rather, the relationship between frequency and boundary layer thickness assumed here allows the pressure variation to jump to a lower order). Solving at second order with the secular terms removed,

$$\tilde{v}_2 = A_2 + \frac{iL}{\eta} B_1 e^{-\theta} + a_0 e^{-\theta} + \frac{i(1-UL)}{\sigma\eta T} D_1 e^{-\sigma\theta}, \quad \tilde{p}_2 = F_2, \quad (4.B.21)$$

where

$$a_0 = \frac{iLT}{\eta} \left(\frac{B_0}{\eta T} \right)_y + \frac{i(1-UL)}{\eta T} d_0 + \frac{i\bar{\delta}N}{\eta} G_0. \quad (4.B.22)$$

To find the secularity conditions for A_2 and F_2 which would close our solutions, we need solutions for \check{u}_2 and \check{T}_2 , and secularity conditions for B_1 and D_1 . The latter are found by removing resonant terms, as before, giving

$$B_{1,y} + \frac{3}{2} (\ln \eta T)_y B_1 = -\frac{U_y}{2T} d_0 - \frac{iU_y\eta}{2(1-UL)} a_0 + \frac{1}{2\eta T} (TB_{0,y})_y, \quad (4.B.23a)$$

$$D_{1,y} + \frac{1}{2} (\ln \eta T)_y D_1 = 0. \quad (4.B.23b)$$

Solving (4.B.23) leads to

$$B_1(y) = (1-UL)^{-3/4} \left\{ B_1(0) + \int_0^y (1-UL)^{3/4} \left[\frac{U_y}{2T} d_0 - \frac{iU_y\eta}{1-UL} \frac{a_0}{2} + \frac{1}{2\eta T} (TB_{0,y})_y \right] dy \right\} \quad (4.B.24a)$$

$$D_1(y) = D_1(0)(1-UL)^{-1/4}. \quad (4.B.24b)$$

The solutions for \check{u}_2 and \check{T}_2 are then found to be

$$\check{u}_2 = B_2 e^{-\theta} + b_0 e^{-\sigma\theta} - \frac{iU_y}{1-UL} A_2 + b_1, \quad (4.B.25a)$$

$$\check{T}_2 = D_2 e^{-\sigma\theta} + d_1 e^{-\theta} - \frac{iT_y}{1-UL} A_2 + d_2, \quad (4.B.25b)$$

where

$$b_0 = \frac{U_y}{\sigma\eta T} D_3, \quad b_1 = -\frac{i}{\eta^2 T} \left(\frac{TU_y A_0}{1-UL} \right)_{yy} + \frac{\bar{\delta}L}{\rho(1-UL)} F_1, \quad (4.B.26a)$$

$$d_1 = \frac{\text{Pr}}{1-\text{Pr}} \left\{ \left(2U_y - \frac{LT_y}{1-UL} \right) \frac{B_1}{\eta} + \frac{iT_y}{1-UL} a_0 - \frac{2U_y}{\eta^2} B_{0,y} + \frac{1}{\text{Pr}\eta^2 T} \left((\eta T d_0)_y + \eta (T d_0)_y \right) \right\}, \quad (4.B.26b)$$

$$d_2 = -\frac{i}{\eta^2 T} \left\{ \frac{1}{\text{Pr}} \left(\frac{TT_y A_0}{1-UL} \right)_{yy} + \frac{1-UL}{A_0} \left(\frac{TU_y^2 A_0^2}{(1-UL)^2} \right)_y \right\} + \frac{\bar{\delta}}{\rho} F_1. \quad (4.B.26c)$$

Although we are not solving for \tilde{v} and \tilde{p} to $\mathcal{O}(\varepsilon^3)$, we must use the third-order equations to form the secularity conditions for A_2 and F_2 . As before in (4.B.19), we find

$$A_{2,y} - 2(\ln \eta T)_y A_2 = -\frac{i(1-UL)}{T} d_2 - iLb_1 + \bar{\delta}i\gamma(1-UL)F_1 - \frac{\bar{\delta}iN^2}{\rho(1-UL)} F_1, \quad (4.B.27a)$$

$$F_{2,y} = \bar{\delta}i\rho(1-UL)A_1. \quad (4.B.27b)$$

Solving (4.B.27) we find

$$A_2(y) = (1 - UL) \left\{ \bar{A}_2 + i\bar{\delta} \int_0^y -\frac{i}{T} d_2 - \frac{iL}{1 - UL} b_1 + \bar{\delta} i \gamma F_1 - \frac{i\bar{\delta} N^2}{\rho(1 - UL)^2} F_1 dy' \right\}, \quad (4.B.28a)$$

$$F_2(y) = \bar{F}_2 + i\bar{\delta} \int_0^y \rho(1 - UL) A_1 dy', \quad (4.B.28b)$$

which are the final conditions needed to close our solutions for \tilde{v} and \tilde{p} to $\mathcal{O}(\varepsilon^2)$.

4.B.1 Matching the high frequency solutions to the outer flow

We must match the inner solutions found above:

$$\tilde{p}(y, \theta) = F_0(y) + \varepsilon F_1(y) + \varepsilon^2 F_2(y) + \mathcal{O}(\varepsilon^3), \quad (4.B.29a)$$

$$\begin{aligned} \tilde{v}(y, \theta) = & A_0(y) + \varepsilon \left[A_1(y) + \frac{iL}{\eta(y)} B_0(y) e^{-\theta} + \frac{i(1 - U(y)L)}{\sigma\eta(y)T(y)} D_0(y) e^{-\sigma\theta} \right] \\ & + \varepsilon^2 \left[A_2(y) + \frac{iL}{\eta} B_1(y) e^{-\theta} + a_0(y) e^{-\theta} + \frac{i(1 - U(y)L)}{\sigma\eta(y)T(y)} D_1(y) e^{-\sigma\theta} \right] + \mathcal{O}(\varepsilon^3). \end{aligned} \quad (4.B.29b)$$

with the outer solutions (4.1.6),

$$p_{\text{ui}}(1 - \delta y) = p_\infty + i\varepsilon\bar{\delta}(1 - ML)yv_\infty + \frac{1}{2}\varepsilon^2\bar{\delta}^2(N^2 - \bar{\alpha}^2)y^2p_\infty + \mathcal{O}(\varepsilon^3), \quad (4.B.30a)$$

$$v_{\text{ui}}(1 - \delta y) = v_\infty + i\varepsilon\bar{\delta}\frac{\bar{\alpha}^2 - N^2}{1 - ML}yp_\infty + \frac{1}{2}\varepsilon^2\bar{\delta}^2(N^2 - \bar{\alpha}^2)y^2v_\infty + \mathcal{O}(\varepsilon^3), \quad (4.B.30b)$$

in the limit $y \rightarrow \infty$.

Matching (4.B.29) with (4.B.30) at leading order leads to

$$\bar{F}_0 = p_\infty, \quad \bar{A}_0 = \frac{v_\infty}{1 - ML}. \quad (4.B.31)$$

Next, we write the secularity conditions (4.B.20) and (4.B.28) in terms of bounded integrals to aid matching:

$$F_1(y) = \bar{F}_1 + i\bar{\delta}\bar{A}_0(1 - ML)^2 \left[y - \int_0^y \bar{\chi}_0 dy' \right], \quad (4.B.32a)$$

$$\frac{A_1(y)}{1 - UL} = \bar{A}_1 + i\bar{\delta}\bar{F}_0 \left\{ \left(1 - \frac{L^2 + N^2}{(1 - ML)^2} \right) y + \frac{L^2 + N^2}{(1 - ML)^2} \int_0^y \bar{\chi}_1 dy' \right\}, \quad (4.B.32b)$$

$$\begin{aligned} F_2(y) = & \bar{F}_2 + i\bar{\delta}(1 - ML)^2 \bar{A}_1 \left[y - \int_0^y \bar{\chi}_0 dy' \right] - \bar{\delta}^2(L^2 + N^2)\bar{F}_0 \left\{ I_1 y \right. \\ & \left. - \int_0^y \bar{\chi}_0(y') \int_0^{y'} \bar{\chi}_1(y'') dy'' dy' + \int_0^y \left(\int_0^{y'} \bar{\chi}_1(y'') dy'' - I_1 \right) dy' \right\}, \\ & - \bar{\delta}^2(1 - ML)^2 \bar{F}_0 \left(1 - \frac{L^2 + N^2}{(1 - ML)^2} \right) \left[\frac{1}{2} y^2 - \int_0^y y' \bar{\chi}_0 dy' \right] \end{aligned} \quad (4.B.32c)$$

$$\begin{aligned} \frac{A_2(y)}{1 - UL} = & i\bar{\delta}\bar{F}_1 \left\{ \left(1 - \frac{L^2 + N^2}{(1 - ML)^2} \right) y + \frac{L^2 + N^2}{(1 - ML)^2} \int_0^y \bar{\chi}_1 dy' \right\} + i\xi(\gamma - 1)^2 \bar{A}_0 \int_0^y \bar{\chi}_\mu dy' \\ & + \bar{A}_2 - \bar{\delta}^2(1 - ML)^2 \bar{A}_0 \left\{ \left(1 - \frac{L^2 + N^2}{(1 - ML)^2} \right) \frac{y^2}{2} + \frac{L^2 + N^2}{(1 - ML)^2} \int_0^y y' \bar{\chi}_1 dy' \right\} \\ & + \bar{\delta}^2(1 - ML)^2 \bar{A}_0 \left\{ \frac{L^2 + N^2}{(1 - ML)^2} \int_0^y \bar{\chi}_1(y') \int_0^{y'} \bar{\chi}_0(y'') dy'' dy' \right. \\ & \left. + \left(1 - \frac{L^2 + N^2}{(1 - ML)^2} \right) I_0 y + \left(1 - \frac{L^2 + N^2}{(1 - ML)^2} \right) \int_0^y \left(\int_0^{y'} \bar{\chi}_0(y'') dy'' - I_0 \right) dy' \right\}, \end{aligned} \quad (4.B.32d)$$

where

$$\begin{aligned} I_0 &= \int_0^\infty \bar{\chi}_0 dy, & I_1 &= \int_0^\infty \bar{\chi}_1 dy, \\ \bar{\chi}_0 &= 1 - \frac{\rho(1-UL)^2}{(1-ML)^2}, & \bar{\chi}_1 &= 1 - \frac{(1-ML)^2}{\rho(1-UL)^2}, \end{aligned} \quad (4.B.33)$$

$$\bar{\chi}_\mu(y) = \frac{1}{1-UL} \left[\frac{1}{2\text{Pr}} (T^2)_{yyy} + (TU_y^2)_y + \frac{LT}{1-UL} (TU_y)_{yy} \right].$$

Matching at first order provides the relations

$$\bar{F}_1 = i\bar{\delta}I_0(1-ML)v_\infty, \quad \bar{A}_1 = -i\bar{\delta}I_1 \frac{L^2 + N^2}{(1-ML)^2} p_\infty, \quad (4.B.34)$$

while at second order we find

$$\bar{F}_2 = \bar{\delta}^2(I_0I_1 + I_{11} - I_{01})(L^2 + N^2)p_\infty - \bar{\delta}^2I_2((1-ML)^2 - L^2 - N^2)p_\infty \quad (4.B.35a)$$

$$\begin{aligned} \bar{A}_2 &= -i\xi(\gamma-1)^2 I_\mu \frac{v_\infty}{1-ML} + \bar{\delta}^2(I_0I_1 + I_3 - I_{10})(L^2 + N^2) \frac{v_\infty}{1-ML} \\ &\quad - \bar{\delta}^2I_{00}((1-ML)^2 - L^2 - N^2) \frac{v_\infty}{1-ML}, \end{aligned} \quad (4.B.35b)$$

where we have introduced

$$\begin{aligned} I_2 &= \int_0^\infty y\bar{\chi}_0 dy, & I_3 &= \int_0^\infty y\bar{\chi}_1 dy, & I_\mu &= \int_0^\infty \bar{\chi}_\mu dy, \\ I_{01} &= \int_0^\infty \bar{\chi}_0 \int_0^y \bar{\chi}_1(y') dy' dy, & I_{10} &= \int_0^\infty \bar{\chi}_1 \int_0^y \bar{\chi}_0(y') dy' dy, \\ I_{00} &= \int_0^\infty \left(\int_0^y \bar{\chi}_0(y') dy' - I_0 \right) dy, & I_{11} &= \int_0^\infty \left(\int_0^y \bar{\chi}_1(y') dy' - I_1 \right) dy. \end{aligned} \quad (4.B.36)$$

4.B.2 The effective impedance

To form the effective impedance we evaluate the pressure and velocity at the wall, $y = 0$:

$$\bar{p}(0) = F_0(0) + \varepsilon F_1(0) + \varepsilon^2 F_2(0), \quad (4.B.37)$$

$$\begin{aligned} \bar{v}(0) &= A_0(0) + \varepsilon \left[A_1(0) + \frac{iL}{\eta(0)} B_0(0) \right] \\ &\quad + \varepsilon^2 \left[A_2(0) + \frac{iL}{\eta(0)} B_1(0) + a_0(0) + \frac{i}{\sigma\eta(0)T(0)} D_1(0) \right], \end{aligned} \quad (4.B.38)$$

where the $A_j(0)$ and $F_j(0)$ are found in the previous section. The remaining required quantities are

$$B_0(0) = iU_y(0) \frac{v_\infty}{1-ML}, \quad B_1(0) = \left[\bar{\delta}I_1 U_y(0) \frac{L^2 + N^2}{(1-ML)^2} - \frac{\bar{\delta}L}{\rho(0)} \right] p_\infty, \quad (4.B.39a)$$

$$a_0(0) = -\frac{i\bar{\delta}N^2}{\eta(0)\rho(0)} p_\infty - \left[\frac{\text{Pr}}{1-\text{Pr}} \frac{2U_y(0)^2}{\eta(0)^2 T(0)} + \frac{5L^2 U_y(0)^2}{4\eta(0)^2} \right] \frac{v_\infty}{1-ML}, \quad (4.B.39b)$$

$$D_1(0) = -\frac{\bar{\delta}}{\rho(0)} p_\infty - \frac{\text{Pr}}{1-\text{Pr}} \frac{2iU_y(0)^2}{\eta(0)} \frac{v_\infty}{1-ML}, \quad (4.B.39c)$$

The wall impedance $Z = \bar{p}(0)/\bar{v}(0)$, so we may write

$$Z = \frac{p_\infty + \varepsilon i\bar{\delta}I_0(1-ML)v_\infty + \varepsilon^2 \bar{A}p_\infty}{\frac{v_\infty}{1-ML} \left[1 - \varepsilon \frac{LU_y(0)}{\eta(0)} + \varepsilon^2 \bar{\mathcal{B}} \right] + p_\infty \left[-\varepsilon i\bar{\delta}I_1 \frac{L^2 + N^2}{(1-ML)^2} + \varepsilon^2 \bar{\mathcal{C}} \right]} \quad (4.B.40)$$

where

$$\bar{\mathcal{A}} = \bar{\delta}^2(I_0 I_1 + I_{11} - I_{01})(L^2 + N^2) - \bar{\delta}^2 I_2((1 - ML)^2 - L^2 - N^2), \quad (4.B.41a)$$

$$\begin{aligned} \bar{\mathcal{B}} = & -i\xi(\gamma - 1)^2 I_\mu + \bar{\delta}^2(I_0 I_1 + I_3 - I_{10})(L^2 + N^2) - \bar{\delta}^2 I_{00}((1 - ML)^2 - L^2 - N^2) \\ & + \frac{\sigma(1 - \sigma)}{1 - \text{Pr}} \frac{2U_y(0)^2}{\eta(0)^2 T(0)} - \frac{5L^2 U_y(0)^2}{4\eta(0)^2}, \end{aligned} \quad (4.B.41b)$$

$$\bar{\mathcal{C}} = \bar{\delta} I_1 \frac{iLU_y(0)}{\eta(0)} \frac{L^2 + N^2}{(1 - ML)^2} - \frac{i\bar{\delta}(L^2 + N^2)}{\eta(0)\rho(0)} - \frac{i\bar{\delta}(\gamma - 1)}{\sigma\eta(0)}. \quad (4.B.41c)$$

Dividing top and bottom by v_∞ allows us to introduce the effective impedance $Z_{\text{eff}} = p_\infty/v_\infty$; rearranging for Z_{eff} gives

$$Z_{\text{eff}} = \frac{1}{1 - ML} \frac{Z - \varepsilon \frac{LU_y(0)}{\eta(0)} Z - \varepsilon i \bar{\delta} I_0 (1 - ML)^2 + \varepsilon^2 \bar{\mathcal{B}} Z}{1 + \varepsilon i \bar{\delta} I_1 \frac{L^2 + N^2}{(1 - ML)^2} Z + \varepsilon^2 (\bar{\mathcal{A}} - \bar{\mathcal{C}} Z)}. \quad (4.B.42)$$

which is equivalent to the result in the main text (4.1.13) once the expressions for ε , $\bar{\delta}$, ξ , $\eta(0)$, L and N are substituted, and the I_j integrals are written in terms of r . If the strict constraint $\delta = \varepsilon^3 \bar{\delta}$ is relaxed, and instead the weaker constraint $\delta = \varepsilon^{(2+n)}$, $n > 0$, is used, an expansion in powers of the two small parameters δ , ε can be found to $\mathcal{O}(\delta/\varepsilon^2)$ and shown to be asymptotically equivalent to (4.1.13) at $\mathcal{O}(\varepsilon)$ (see Appendix 4.C).

4.C Alternate high frequency asymptotics: two small parameters

Here we derive the high frequency solutions corresponding to a weaker constraint on the boundary layer thickness δ , and leave both δ and ε in the problem as two related yet independent small parameters. As before, the distinguished scaling for the WKB multiples scales approach gives $\omega = 1/\sqrt{\varepsilon}$, and by analysing the outer solutions (4.1.6) we need $\delta \ll \varepsilon^2$. We may constrain δ by the expression $\delta \sim \varepsilon^{(2+n)}$ for $n \in \mathbb{R}^+$. We then expand (1.1.13) in a thin boundary layer $r = 1 - \delta y$, and use the WKB multiple scales approach as in (4.1.8). The resulting governing equations are

$$\begin{aligned} \check{u}_{\theta\theta} - \check{u} = & \frac{iU_y \check{v}}{1 - UL} - \frac{\varepsilon}{\eta^2 T} [(\eta T \check{u}_\theta)_y + \eta T \check{u}_{\theta y} + \eta U_y \check{T}_\theta] - \frac{\varepsilon^2}{\eta^2 T} [(T \check{u}_y)_y + (U_y \check{T})_y] \\ & + \delta \left\{ -\frac{1}{\varepsilon^2} \frac{L}{\rho(1 - UL)} \check{p} - \frac{\delta}{\varepsilon^3} (1 + \beta) \frac{iL}{\eta} \check{v}_\theta - \frac{\delta}{\varepsilon^2} \frac{iL}{\eta^2 T} [(1 + \beta) T \check{v}_y + T_y \check{v}] \right. \\ & \left. + \frac{\varepsilon}{\eta} \check{u}_\theta + \frac{\varepsilon^2}{\eta^2 T} [T \check{u}_y + U_y \check{T}] \right\} + \mathcal{O}\left(\frac{\delta^3}{\varepsilon^4}\right), \end{aligned} \quad (4.C.1a)$$

$$\begin{aligned} \frac{1}{\text{Pr}} \check{T}_{\theta\theta} - \check{T} = & \frac{iT_y \check{v}}{1 - UL} - \frac{\varepsilon}{\eta^2 T} \left[\frac{1}{\text{Pr}} (\eta T \check{T}_\theta)_y + \frac{1}{\text{Pr}} \eta (T \check{T}_\theta)_y + 2\eta T U_y \check{u}_\theta \right] \\ & - \frac{\varepsilon^2}{\eta^2 T} \left[\frac{1}{\text{Pr}} (T \check{T})_{yy} + 2T U_y \check{u}_y + U_y^2 \check{T} \right] + \delta \left\{ -\frac{1}{\varepsilon^2} \frac{1}{\rho} \check{p} - \frac{\delta}{\varepsilon^2} \left[\frac{2iLU_y}{\eta^2} \check{v} \right. \right. \\ & \left. \left. - \frac{L^2 + N^2}{\eta^2} \check{T} \right] + \frac{\varepsilon}{\text{Pr} \eta} \check{T}_\theta + \frac{\varepsilon^2}{\text{Pr} \eta^2 T} (T \check{T})_{yy} \right\} + \mathcal{O}\left(\frac{\delta^3}{\varepsilon^2}\right), \end{aligned} \quad (4.C.1b)$$

$$\begin{aligned} \check{v}_\theta = & -\varepsilon \left[\frac{i(1 - UL)}{\eta T} \check{T} + \frac{iL}{\eta} \check{u} + \frac{T}{\eta} \left(\frac{\check{v}}{T} \right)_y \right] + \delta \left\{ \frac{1}{\varepsilon} [i(1 - UL) \frac{\gamma}{\eta} \check{p} - \frac{iN}{\eta} \check{w}] \right. \\ & \left. + \frac{\varepsilon}{\eta} \check{v} \right\} + \mathcal{O}\left(\frac{\delta^2}{\varepsilon}\right), \end{aligned} \quad (4.C.1c)$$

$$\begin{aligned} \tilde{p}_\theta = -\varepsilon \frac{\tilde{p}_y}{\eta} - \frac{\delta i \rho (1 - UL)}{\eta} & \left\{ \frac{1}{\varepsilon} \left[(2 + \beta) \tilde{v}_{\theta\theta} - \tilde{v} \right] + \left[\frac{(2 + \beta)}{\eta^2 T} \left((\eta T \tilde{v}_\theta)_y + \eta T \tilde{v}_{\theta y} \right) \right. \right. \\ & + (1 + \beta) \frac{iL}{\eta} \check{u}_\theta \left. \right] + \frac{\delta}{\varepsilon^2} (1 + \beta) \frac{iN}{\eta} \tilde{w}_\theta + \frac{\varepsilon}{\eta^2 T} \left[(1 + \beta) iLT \check{u}_y \right. \\ & \left. \left. + iL(\beta T_y \check{u} + U_y \check{T}) + (2 + \beta)(T \tilde{v}_y)_y \right] \right\} + \mathcal{O}\left(\frac{\delta^2}{\varepsilon}\right), \end{aligned} \quad (4.C.1d)$$

$$\begin{aligned} \tilde{w}_{\theta\theta} - \tilde{w} = -\frac{N}{\rho(1 - UL)} \tilde{p} - \frac{\varepsilon}{\eta^2 T} & \left[(\eta T \tilde{w}_\theta)_y + \eta T \tilde{w}_{\theta y} \right] - \frac{\varepsilon^2}{\eta^2 T} \left[(T \tilde{w}_y)_y \right. \\ & \left. + i\delta N(1 + \beta) \eta T \tilde{v}_\theta \right] + \mathcal{O}(\varepsilon^3), \end{aligned} \quad (4.C.1e)$$

where $\tilde{u} = \varepsilon^2 \check{u} / \delta$ and $\tilde{T} = \varepsilon^2 \check{T} / \delta$ and η is defined in (4.1.9). For different values of n , the term ordering in (4.C.1) may change. As an example, consider the three possibilities: if $0 < n < 1$ then $\delta^2 / \varepsilon^3 \gg \delta$; if $n = 1$ then $\delta^2 / \varepsilon^3 \sim \delta$; while if $1 < n < 2$ then $\delta^2 / \varepsilon^3 \ll \delta$. In fact this example shows the lowest order for which the term ordering changes (for these three ranges of n): lower order terms do not jump order, for instance $\delta / \varepsilon \gg \delta$, δ^2 / ε^3 for $0 < n < 2$.

We will solve (4.C.1) by assuming the following power series expansions for the acoustic quantities, where the subscript jk refers to the order of $\delta\varepsilon$,

$$\tilde{q} = \tilde{q}_{00} + \varepsilon \tilde{q}_{01} + \varepsilon^2 \tilde{q}_{02} + \delta \left(\frac{1}{\varepsilon^2} \tilde{q}_{1(-2)} + \frac{1}{\varepsilon} \tilde{q}_{1(-1)} + \left[\tilde{q}_{10} + \frac{\delta}{\varepsilon^3} \tilde{q}_{2(-3)} \right] \right), \quad (4.C.2)$$

where terms in the square brackets may jump order depending on the value of the exponent n , as discussed in the previous paragraph. The δ leading order – those terms that are not affected by the finite thickness of the shear layer, \tilde{q}_{0j} – may be solved independently of higher δ orders. This must be the case if the model is to be consistent with a zero-thickness boundary layer system.

At $\mathcal{O}(1)$, the radial velocity and pressure equations (4.C.1c) and (4.C.1d) may be integrated to give

$$\tilde{v}_{00} = A_{00}(y), \quad \tilde{p}_{00} = F_{00}(y), \quad (4.C.3)$$

which may be used in (4.C.1a), (4.C.1b) and (4.C.1e) to produce the solutions

$$\begin{aligned} \check{u}_{00} = B_{00}(y)e^{-\theta} - \frac{iU_y}{1 - UL} A_{00}(y), \quad \check{T}_{00} = D_{00}(y)e^{-\sigma\theta} - \frac{iT_y}{1 - UL} A_{00}(y), \\ \tilde{w}_{00} = G_{00}(y)e^{-\theta} + \frac{N}{\rho(1 - UL)} F_{00}(y), \end{aligned} \quad (4.C.4)$$

where exponentially growing solutions have been dropped. The functions of y in (4.C.3) and (4.C.4) are determined by secularity conditions at the next order in ε , and by boundary conditions. The explicit dependence of these functions on y will henceforth be dropped.

At $\mathcal{O}(\varepsilon)$, the analysis proceeds in much the same way as in Appendix 4.B. Equation (4.C.1c) is

$$\tilde{v}_{01,\theta} = -\frac{i(1 - UL)}{\eta T} \left(D_{00} e^{-\sigma\theta} - \frac{iT_y}{1 - UL} A_{00} \right) - \frac{iL}{\eta} \left(B_{00} e^{-\theta} - \frac{iU_y}{1 - UL} A_{00} \right) - \frac{T}{\eta} \left(\frac{A_{00}}{T} \right)_y, \quad (4.C.5)$$

where the solutions at $\mathcal{O}(1)$ have been inserted on the right hand side. Those terms in (4.C.5) that are only functions of y , and hence solve the homogeneous equation $\tilde{v}_{01,\theta} = 0$, are resonant and are set to zero:

$$\frac{i(1 - UL)}{\eta T} \frac{iT_y}{1 - UL} A_{00} + \frac{iL}{\eta} \frac{iU_y}{1 - UL} A_{00} - \frac{T}{\eta} \left(\frac{A_{00}}{T} \right)_y = 0. \quad (4.C.6)$$

Equation (4.C.6) is a first-order ordinary differential equation in y for the function $A_{00}(y)$, and

may be solved by rewriting in terms of a logarithmic derivative and integrating. The definition of $\eta(y)$ may then be used to express the solution as

$$A_{00}(y) = \bar{A}_{00}(1 - UL), \quad (4.C.7)$$

where \bar{A}_{00} is a constant determined by the boundary condition either at $y = 0$ or as $y \rightarrow \infty$. The resonant terms at $\mathcal{O}(\varepsilon)$ in the pressure equation (4.C.1d) are more simple, and we find the secularity condition

$$F_{00,y} = 0 \quad \implies \quad F_{00}(y) = \bar{F}_{00}, \quad (4.C.8)$$

with \bar{F}_{00} a constant. Solving for \tilde{v}_{01} and \tilde{p}_{01} with the resonant terms removed gives

$$\tilde{v}_{01} = A_{01} + \frac{iL}{\eta} B_{00} e^{-\theta} + \frac{i(1-UL)}{\sigma\eta T} D_{00} e^{-\sigma\theta}, \quad \tilde{p}_{01} = F_{01}. \quad (4.C.9)$$

Equation (4.C.1b) at $\mathcal{O}(\varepsilon)$ is

$$\begin{aligned} \frac{1}{\text{Pr}} \check{T}_{01,\theta\theta} - \check{T}_{01} &= \frac{iT_y}{1-UL} \left(A_{01} + \frac{iL}{\eta} B_{00} e^{-\theta} + \frac{i(1-UL)}{\sigma\eta T} D_{00} e^{-\sigma\theta} \right) \\ &+ \frac{1}{\sigma\eta^2 T} \left((\eta T D_{00})_y + \eta (T D_{00})_y \right) e^{-\sigma\theta} + \frac{2U_y}{\eta} B_{00} e^{-\theta}, \end{aligned} \quad (4.C.10)$$

and the secular terms are $\propto \exp(-\sigma\theta)$ (where the same murky definition of ‘‘secular’’ is exploited here as in the previous high frequency analysis in Appendix 4.B—a solution of the homogeneous system is considered secular, regardless of whether it grows or decays). Equating these terms with zero we find

$$\frac{1}{\eta T} (\eta T D_{00})_y + \frac{1}{T} (T D_{00})_y - \frac{T_y}{T} D_{00} = 0, \quad (4.C.11)$$

which may be solved to give

$$D_{00}(y) = D_{00}(0)(1 - UL)^{-1/4}. \quad (4.C.12)$$

The isothermal wall condition $T_y(0) = 0$ gives the boundary condition $D_{00}(0) = 0$ and hence $D_{00}(y) \equiv 0$. At $\mathcal{O}(\varepsilon)$, (4.C.1a) gives

$$\begin{aligned} \check{u}_{01,\theta\theta} - \check{u}_{01} &= \frac{iU_y}{1-UL} \left(A_{01} + \frac{iL}{\eta} B_{00} e^{-\theta} \right) \\ &+ \frac{1}{\eta^2 T} \left((\eta T B_{00})_y + \eta T B_{00,y} \right) e^{-\theta}. \end{aligned} \quad (4.C.13)$$

The resonant terms on the right hand side are those $\propto \exp(-\theta)$. Equating these terms with zero, we find

$$\frac{1}{\eta T} (\eta T B_{00})_y - \frac{LU_y}{1-UL} B_{00} + B_{00,y} = 0, \quad (4.C.14)$$

which gives the secularity condition

$$B_{00}(y) = B_{00}(0)(1 - UL)^{-3/4}, \quad B_{00}(0) = iU_y(0)A_{00}(0). \quad (4.C.15)$$

The boundary condition used to determine $B_{00}(0)$ is the viscous no slip condition. Similarly, the secularity condition for G_{00} can be found from (4.C.1e) at $\mathcal{O}(\varepsilon)$:

$$\tilde{w}_{01,\theta\theta} - \tilde{w}_{01} = -\frac{N}{\rho(1-UL)} F_{01} + \frac{1}{\eta^2 T} \left((\eta T G_{00})_y + \eta T G_{00,y} \right) e^{-\theta}, \quad (4.C.16)$$

where the secular terms are $\propto \exp(-\theta)$. This leads to the secularity condition

$$G_{00}(y) = G_{00}(0)(1 - UL)^{-1/4}, \quad G_{00}(0) = -\frac{N}{\rho(0)}F_{00}(0), \quad (4.C.17)$$

where again no slip sets the boundary value $G_{00}(0)$. Solving for \check{u}_{01} , \check{T}_{01} and \check{w}_{01} with the resonant terms suppressed then gives

$$\begin{aligned} \check{u}_{01} &= B_{01}e^{-\theta} - \frac{iU_y}{1 - UL}A_{01}, & \check{w}_{01} &= G_{01}e^{-\theta} + \frac{N}{\rho(1 - UL)}F_{01}, \\ \check{T}_{01} &= D_{01}e^{-\sigma\theta} + \psi_0e^{-\theta} - \frac{iT_y}{1 - UL}A_{01}, \end{aligned} \quad (4.C.18)$$

where

$$\psi_0(y) = \frac{\text{Pr}}{1 - \text{Pr}} \left(2U_y - \frac{LT_y}{1 - UL} \right) \frac{B_{00}}{\eta}. \quad (4.C.19)$$

At $\mathcal{O}(\varepsilon^2)$ we proceed as above, but now with both the $\mathcal{O}(1)$ and $\mathcal{O}(\varepsilon)$ solutions inserted into the governing equations (4.C.1). The secularity conditions on the \check{v}_{01} and \check{p}_{01} solutions are found to be

$$A_{01}(y) = \bar{A}_{01}(1 - UL), \quad F_{01}(y) = \bar{F}_{01}, \quad (4.C.20)$$

where the barred terms are constants. For completeness, solving (4.C.1c) and (4.C.1d) at this order, with the secular terms suppressed, gives

$$\check{v}_{02} = A_{02} + \left(\frac{iL}{\eta}B_{01} + \frac{iLT}{\eta} \left(\frac{B_{00}}{\eta T} \right)_y + \frac{i(1 - UL)}{\eta T} \psi_0 \right) e^{-\theta} + \frac{i(1 - UL)}{\sigma \eta T} D_{01} e^{-\sigma\theta}, \quad (4.C.21)$$

for the radial velocity and $\check{p}_{02} = F_{02}$ for the pressure, but these solutions will not be used as we will not determine the functions A_{02} and F_{02} . The secularity conditions for the solutions in (4.C.18) are found to be

$$B_{01,y} + \frac{3}{2} (\ln \eta T)_y B_{01} = \frac{U_y}{T} \psi_0 + \frac{LU_y T}{1 - UL} \left(\frac{B_{00}}{\eta T} \right)_y + \frac{1}{\eta T} (TB_{00,y})_y, \quad (4.C.22)$$

with $B_{01}(0) = iU_y(0)A_{01}(0)$ for \check{u}_{01} ;

$$D_{01}(y) = D_{01}(0)(1 - UL)^{-1/4}, \quad D_{01}(0) = \frac{\text{Pr}}{\text{Pr} - 1} \frac{2U_y(0)}{\eta(0)} B_{00}(0), \quad (4.C.23)$$

for \check{T}_{01} ; and

$$G_{01,y} + \frac{1}{2} (\ln \eta T)_y G_{01} = \frac{1}{\eta T} (TG_{00,y})_y, \quad G_{01}(0) = -\frac{N}{\rho(0)} F_{01}(0), \quad (4.C.24)$$

for \check{w}_{01} .

We now derive the δ expansion, which accounts for the finite thickness of the shear layer. At $\mathcal{O}(\delta/\varepsilon^2)$, (4.C.1c) is simply $\check{v}_{1(-2),\theta} = 0$, hence we find $\check{v}_{1(-2)} = A_{1(-2)}$. Similarly we find $\check{p}_{1(-2)} = F_{1(-2)}$. The equations (4.C.1a) and (4.C.1b) at this order are

$$\check{u}_{1(-2),\theta\theta} - \check{u}_{1(-2)} = \frac{iU_y}{1 - UL} A_{1(-2)} - \frac{L}{\rho(1 - UL)} F_{00}, \quad (4.C.25)$$

for \check{u} and

$$\frac{1}{\text{Pr}} \check{T}_{1(-2),\theta\theta} - \check{T}_{1(-2)} = \frac{iT_y}{1 - UL} A_{1(-2)} - \frac{1}{\rho} F_{00}, \quad (4.C.26)$$

for \check{T} , where now the forcing from the leading-order pressure appears on the right hand sides. Solving (4.C.25) and (4.C.26) gives

$$\check{u}_{1(-2)} = B_{1(-2)}e^{-\theta} - \frac{iU_y}{1-UL}A_{1(-2)} + \frac{L}{\rho(1-UL)}F_{00}, \quad (4.C.27a)$$

$$\check{T}_{1(-2)} = D_{1(-2)}e^{-\sigma\theta} - \frac{iT_y}{1-UL}A_{1(-2)} + \frac{1}{\rho}F_{00}. \quad (4.C.27b)$$

The next order is $\mathcal{O}(\delta/\varepsilon)$, at which equation (4.C.1c) is

$$\begin{aligned} \tilde{v}_{1(-1),\theta} = & -\frac{i(1-UL)}{\eta T} \left[D_{1(-2)}e^{-\sigma\theta} - \frac{iT_y}{1-UL}A_{1(-2)} + \frac{1}{\rho}F_{00} \right] \\ & -\frac{iL}{\eta} \left[B_{1(-2)}e^{-\theta} - \frac{iU_y}{1-UL}A_{1(-2)} + \frac{L}{\rho(1-UL)}F_{00} \right] \\ & -\frac{T}{\eta} \left(\frac{A_{1(-2)}}{T} \right)_y + \frac{i(1-UL)}{\eta} \gamma F_{00} - \frac{iN}{\eta} \left[G_{00}e^{-\theta} + \frac{N}{\rho(1-UL)}F_{00} \right]. \end{aligned} \quad (4.C.28)$$

As before, the resonant terms are those that are only functions of y ; we find the secularity condition

$$A_{1(-2),y} - 2(\ln \eta T)_y A_{1(-2)} = i(1-UL)F_{00} - \frac{i(L^2 + N^2)}{\rho(1-UL)}F_{00}. \quad (4.C.29)$$

The pressure equation (4.C.1d) at δ/ε is

$$\tilde{p}_{1(-1),\theta} = -\frac{1}{\eta}F_{1(-2),y} + \frac{i(1-UL)}{(\gamma-1)\eta T}A_{00}, \quad (4.C.30)$$

from which we find the secularity condition

$$F_{1(-2),y} = i\rho(1-UL)A_{00}, \quad (4.C.31)$$

where we have used the substitution $(\gamma-1)T = 1/\rho$. Solving for the pressure and radial velocity at this order, with the resonant terms suppressed, gives

$$\tilde{v}_{1(-1)} = A_{1(-1)} + \left(\frac{iL}{\eta}B_{1(-2)} + \frac{iN}{\eta}G_{00} \right) e^{-\theta} + \frac{i(1-UL)}{\sigma\eta T}D_{1(-2)}e^{-\sigma\theta}, \quad (4.C.32)$$

and $\tilde{p}_{1(-1)} = F_{1(-1)}$. For \check{u} and \check{T} we find the secularity conditions

$$B_{1(-2),y} + \frac{3}{2}(\ln \eta T)_y B_{1(-2)} = \frac{1}{2} \frac{NU_y}{1-UL}G_{00}, \quad (4.C.33)$$

with

$$B_{1(-2)}(0) = iU_y(0)A_{1(-2)}(0) - \frac{L}{\rho(0)}F_{00}(0); \quad (4.C.34)$$

and

$$D_{1(-2)}(y) = D_{1(-2)}(0)(1-UL)^{1/4}, \quad D_{1(-2)}(0) = -\frac{F_{00}}{\rho(0)}. \quad (4.C.35)$$

Solving with the resonant terms suppressed gives

$$\check{u}_{1(-1)} = B_{1(-1)}e^{-\theta} + \frac{U_y}{\sigma\eta T}D_{1(-2)}e^{-\sigma\theta} - \frac{iU_y}{1-UL}A_{1(-1)} + \frac{L}{\rho(1-UL)}F_{01}, \quad (4.C.36a)$$

$$\check{T}_{1(-1)} = D_{1(-1)}e^{-\sigma\theta} + \psi_1 e^{-\theta} - \frac{iT_y}{1-UL}A_{1(-1)} + \frac{1}{\rho}F_{01}, \quad (4.C.36b)$$

where

$$\psi_1 = \frac{\Pr}{1-\Pr} \left[\frac{2U_y}{\eta} B_{1(-2)} - \frac{T_y}{(1-UL)\eta} (LB_{1(-2)} + NG_{00}) \right]. \quad (4.C.37)$$

The final step is finding the secularity conditions to close the solutions at $\mathcal{O}(\delta/\varepsilon)$. At this order, the discussion of term ordering at the beginning of this section becomes important. The next largest asymptotic order is either $\mathcal{O}(\delta^2/\varepsilon^3)$ for $0 < n < 1$ or $\mathcal{O}(\delta)$ for $1 < n < 2$, or a balance of these two orders when $n = 1$. It turns out that to find the secularity conditions on $A_{1(-1)}$ and $F_{1(-1)}$ at the next order, we need to include the $\mathcal{O}(\delta)$ terms. Working to $\mathcal{O}(\delta^2/\varepsilon^3)$ does not produce equations that include either $\tilde{v}_{1(-1)}$ or $\tilde{p}_{1(-1)}$, and hence no closure conditions are found until the next order. For completeness the equations for $0 < n < 1$ would be

$$\tilde{v}_{2(-3),\theta} = \frac{i(1-UL)}{\eta} \gamma \tilde{p}_{1(-2)} - \frac{iN}{\eta} \tilde{w}_{1(-2)}, \quad (4.C.38a)$$

$$\tilde{p}_{2(-3),\theta} = \frac{i\rho(1-UL)}{\eta} [\tilde{v}_{1(-2)} - (2+\beta)\tilde{v}_{1(-2),\theta\theta}], \quad (4.C.38b)$$

which throw up another problem: the appearance of an $\mathcal{O}(\delta/\varepsilon^2)$ azimuthal velocity term, which we have been calculating to only leading order in δ in all preceding asymptotics. We thus make the judgement that by including $\mathcal{O}(\delta^2/\varepsilon^3)$ terms we would in fact be *opening* a new δ^2 expansion, rather than *closing* the desired δ expansion. So, working with the three guiding principles that (i) we want to close the system at $\mathcal{O}(\delta/\varepsilon)$, (ii) we do not want to calculate $\mathcal{O}(\delta^2)$ effects, and (iii) we do not want to calculate $\mathcal{O}(\delta)$ terms for the azimuthal velocity \tilde{w} , we choose to neglect $\mathcal{O}(\delta^2/\varepsilon^3)$ terms in favour of $\mathcal{O}(\delta)$ terms. This leads to the implicit restriction $1 \leq n < 2$, the equality at the lower bound because the resulting secularity conditions

$$A_{1(-1),y} - 2(\ln \eta T)_y A_{1(-1)} = i(1-UL)F_{01} - \frac{i(L^2 + N^2)}{\rho(1-UL)} F_{01}. \quad (4.C.39a)$$

$$F_{1(-1),y} = i\rho(1-UL)A_{01}, \quad (4.C.39b)$$

are unaffected by the inclusion of $\mathcal{O}(\delta^2/\varepsilon^3)$ terms in a formulation of the balanced-order equations for $n = 1$. In fact, the secularity conditions (4.C.39) would most likely be unchanged for the $0 < n < 1$ case, but would be found an order later.

To form an effective impedance boundary condition using the above high-frequency boundary layer solutions, we must match with the uniform flow outer solutions in the limit $y \rightarrow \infty$. Expanded near the boundary and in the high frequency limit, these outer solutions are

$$\tilde{p}_u \sim p_\infty^{(0)} + \varepsilon p_\infty^{(1)} + \frac{\delta}{\varepsilon^2} p_\infty^{(2)} + \frac{\delta}{\varepsilon} p_\infty^{(3)} + \frac{\delta}{\varepsilon^2} i(1-ML)y(v_\infty^{(0)} + \varepsilon v_\infty^{(1)}), \quad (4.C.40a)$$

$$\tilde{v}_u \sim v_\infty^{(0)} + \varepsilon v_\infty^{(1)} + \frac{\delta}{\varepsilon^2} v_\infty^{(2)} + \frac{\delta}{\varepsilon} v_\infty^{(3)} - \frac{\delta}{\varepsilon^2} \frac{(L^2 + N^2 - (1-ML)^2)}{1-ML} i y (p_\infty^{(0)} + \varepsilon p_\infty^{(1)}), \quad (4.C.40b)$$

where the expansions p_∞ and v_∞ have been expanded as in (4.C.2). We will apply the boundary conditions $\tilde{p}_{00}(0) = 1$, $\tilde{v}_{00}(0) = 1/Z$, and homogeneous boundary conditions at all subsequent orders. Thus, (4.C.7) implies $A_{00} = (1-UL)/Z$ which, in the limit $y \rightarrow \infty$, matches with (4.C.40b) to give

$$v_\infty^{(0)} = \frac{1}{Z}(1-ML). \quad (4.C.41)$$

Solving (4.C.8) gives $F_{00} = 1$, and matching with (4.C.40a) implies $p_\infty^{(0)} = 1$. At $\mathcal{O}(\varepsilon)$, homogeneous

boundary conditions on \tilde{v} and \tilde{p} imply $F_{01} = 0$ and

$$A_{01} = \frac{LU_y(0)}{\eta(0)Z}(1 - UL). \quad (4.C.42)$$

Matching in the limit $y \rightarrow \infty$ to (4.C.40) then gives

$$p_\infty^{(1)} = 0, \quad v_\infty^{(1)} = \frac{LU_y(0)}{\eta(0)Z}(1 - ML). \quad (4.C.43)$$

At $\mathcal{O}(\delta/\varepsilon^2)$, we may solve (4.C.29) with the boundary condition $A_{1(-2)}(0) = 0$ to find

$$A_{1(-2)} = i(1 - UL) \left\{ \left(1 - \frac{L^2 + N^2}{(1 - ML)^2} \right) y + \frac{L^2 + N^2}{(1 - ML)^2} \int_0^y \bar{\chi}_1 dy' \right\}, \quad (4.C.44)$$

and solve (4.C.31) with the boundary condition $F_{1(-2)}(0) = 0$ to find

$$F_{1(-2)} = \frac{i}{Z}(1 - ML)^2 \left\{ y - \int_0^y \bar{\chi}_0 dy' \right\}, \quad (4.C.45)$$

where $\bar{\chi}_0$ and $\bar{\chi}_1$ are defined in (4.B.33). In the limit $y \rightarrow \infty$ we see that the terms $\propto y$ in (4.C.44) and (4.C.45) match automaticall with those in (4.C.40). Matching the constant terms at this order gives

$$p_\infty^{(2)} = -\frac{i}{Z}(1 - ML)^2 I_0, \quad (4.C.46a)$$

$$v_\infty^{(2)} = i \frac{L^2 + N^2}{1 - ML} I_1, \quad (4.C.46b)$$

where again the definitions of I_0 and I_1 are as in (4.B.33). The final order is $\mathcal{O}(\delta/\varepsilon)$, at which the homogeneous \tilde{v} and \tilde{p} boundary conditions give

$$A_{1(-1)}(0) = \frac{i(\gamma - 1)}{\sigma\eta(0)} + \frac{i(L^2 + N^2)}{\eta(0)\rho(0)} \quad (4.C.47)$$

and $F_{1(-1)}(0) = 0$. Since $F_{01} \equiv 0$, the solution of (4.C.39a) is just $A_{1(-1)} = A_{1(-1)}(0)(1 - UL)$ and hence matching with (4.C.40b) in the limit $y \rightarrow \infty$ gives

$$v_\infty^{(3)} = \frac{i(1 - ML)}{\eta(0)} \left(\frac{(\gamma - 1)}{\sigma} + \frac{(L^2 + N^2)}{\rho(0)} \right). \quad (4.C.48)$$

The \tilde{p} problem (4.C.39b) has the same structure as the preceding order, and hence the solution is of the form (4.C.45). The terms $\propto y$ match exactly with those of (4.C.40a) as $y \rightarrow \infty$, while the constant terms match if

$$p_\infty^{(3)} = -\frac{iLU_y(0)}{\eta(0)Z}(1 - ML)^2 I_0. \quad (4.C.49)$$

The effective impedance is then just the ratio of the uniform flow wall-pressure and radial velocity:

$$Z_{\text{eff}} = \frac{p_\infty^{(0)} + \varepsilon p_\infty^{(1)} + \frac{\delta}{\varepsilon^2} p_\infty^{(2)} + \frac{\delta}{\varepsilon} p_\infty^{(3)}}{v_\infty^{(0)} + \varepsilon v_\infty^{(1)} + \frac{\delta}{\varepsilon^2} v_\infty^{(2)} + \frac{\delta}{\varepsilon} v_\infty^{(3)}}, \quad (4.C.50)$$

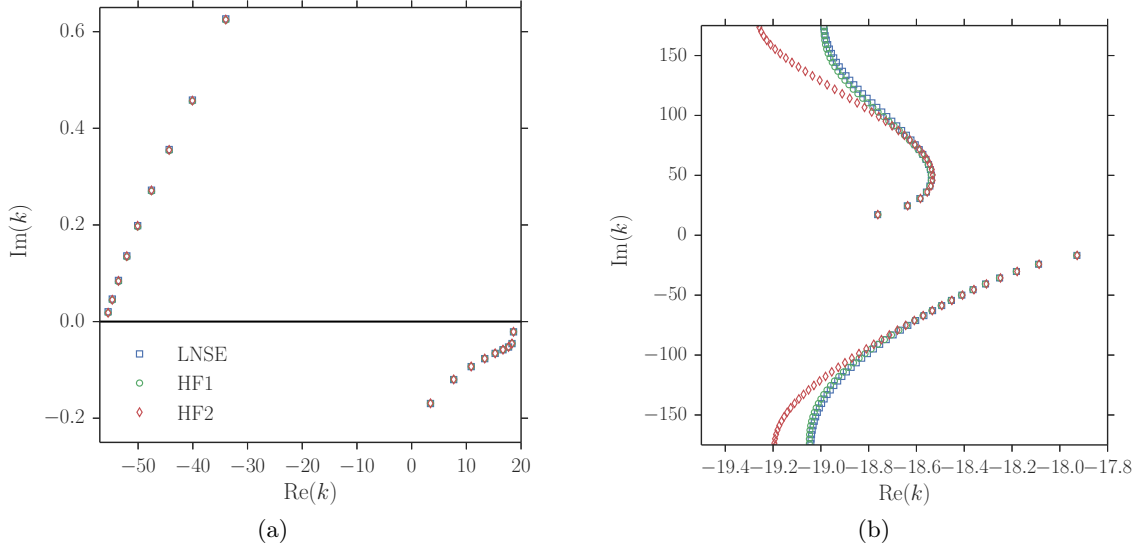


Figure 4.C.1. (a) Cut-on and (b) cut-off modes in the k -plane of the linearised compressible Navier–Stokes numerics (LNSE), the high-frequency asymptotic model (4.1.13) (HF1) and the alternate high-frequency asymptotic model (4.C.51) (HF2). Parameters are $\omega = 28$, $m = 0$, $M = 0.5$, $\delta = 2 \times 10^{-3}$, $\text{Re} = 5 \times 10^6$ with a boundary impedance of $Z = 3 + 4.16i$ and the hyperbolic boundary layer profiles in (3.1.1).

which may be rewritten as

$$Z_{\text{eff}} = \frac{1}{1 - ML} \frac{Z - \frac{\delta}{\varepsilon^2} i(1 - ML)^2 I_0 \left(1 + \varepsilon \frac{LU_y(0)}{\eta(0)}\right)}{1 + \varepsilon \frac{LU_y(0)}{\eta(0)} + \frac{\delta}{\varepsilon^2} \frac{L^2 + N^2}{(1 - ML)^2} iZI_1 + \frac{\delta}{\varepsilon} \frac{iZ}{\eta(0)} \left(\frac{(\gamma - 1)}{\sigma} + \frac{L^2 + N^2}{\rho(0)}\right)}. \quad (4.C.51)$$

This may be shown to be asymptotically equivalent to (4.B.42) to $\mathcal{O}(\delta/\varepsilon^2)$.

In figs. 4.C.1 and 4.C.2 the effective impedance boundary condition (4.C.51) is compared with the high-frequency asymptotic condition derived in the main part of the chapter, (4.1.13), and with numerical solutions of the linearised compressible Navier–Stokes equations, (3.1.2). The cut-on modes of (4.C.51) are close to those of the LNSE, fig. 4.C.1a; the cut-off modes of the LNSE are mostly predicted well by (4.C.51), with (4.1.13) faring slightly better. The high-frequency boundary conditions (4.1.13) and (4.C.51) predict surface modes of the LNSE with similar accuracy: fig. 4.C.2a shows an example where the surface mode lies in the region of asymptotic validity of the models, while fig. 4.C.2b shows an example where the surface mode lies outside the region of asymptotic validity.

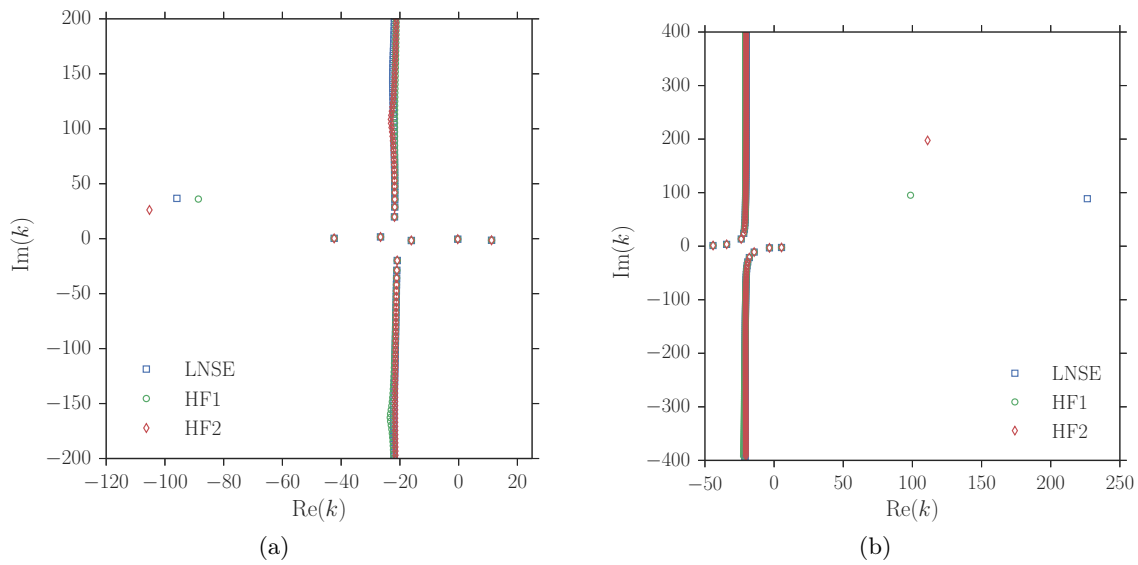


Figure 4.C.2. Mode spectra showing surface modes of the linearised compressible Navier–Stokes numerics (LNSE), the high-frequency asymptotic model (4.1.13) (HF1) and the alternate high-frequency asymptotic model (4.C.51) (HF2). Parameters are (a) $\omega = 31$, $m = 24$, $M = 0.5$, $\delta = 1 \times 10^{-3}$, $\text{Re} = 1 \times 10^6$, with a boundary impedance of $Z = 0.6 - 2i$ and (b) $\omega = 31$, $m = 24$, $M = 0.5$, $\delta = 2 \times 10^{-4}$, $\text{Re} = 2.5 \times 10^7$ with a boundary impedance of $Z = 2 + 0.6i$. The hyperbolic boundary layer profiles in (3.1.1) are used.

Chapter 5

Analytic solutions for the acoustics in a two-deck viscothermal boundary layer

In this chapter we seek to exploit the difference in viscous lengthscales between eddy viscosity and molecular viscosity in order to derive analytical solutions for the acoustics via matched asymptotic expansions in three scaling regions that cover an entire cylindrical, acoustically lined duct. This work has been submitted for publication in the *AIAA Journal* (Khamis & Brambley, 2016*c*); some of this work was presented at the AIAA Aeroacoustics conference (Khamis & Brambley, 2016*d*).

As is common in acoustics, we work predominantly in the frequency domain here. The results of such work are not always directly applicable to time-domain numerical solvers. Recent work has made progress in implementing an inviscid impedance boundary condition in the time domain to account for a finite region of shear (Brambley & Gabard, 2016). By incorporating the modified Myers boundary condition (reformulated in the time domain) into a linearised Euler solver, the unphysical numerical instabilities associated with time-domain formulations of the ill-posed classical Ingard–Myers boundary condition can be avoided. The physical surface wave instability is always present in the inviscid case (Khamis & Brambley, 2016*a*), however, so the time-domain implementation in Brambley & Gabard (2016) still yields instabilities. In the present chapter, we suggest a time-domain formulation that accounts for viscothermal effects in a thin, sheared boundary layer. Although the boundary condition is not implemented here, it is hoped that the good frequency-domain stability behaviour translates to a stable time-domain boundary condition, provided it is suitably implemented (Brambley & Gabard, 2016) and the boundary layer thickness and Reynolds number are chosen appropriately.

5.1 Governing equations

The dynamics of a viscous, compressible perfect gas are considered, as governed by the (dimensionless) Navier–Stokes equations (1.1.10). Using the linearisation scheme set out in section 1.1.2, the acoustics are governed by the linearised Navier–Stokes equations (LNSE) (1.1.13). The viscosities and thermal conductivity are taken to be linearly dependent on the temperature:

$$\mu = \frac{T}{T_0 \text{Re}}, \quad \mu_B = \frac{T}{T_0 \text{Re}} \frac{\mu_0^{B*}}{\mu_0^*}, \quad \kappa = \frac{T}{T_0 \text{Re} \text{Pr}}, \quad (5.1.1)$$

which is equivalent to setting the dimensionless viscosity function \mathcal{H} , introduced in (1.1.16), to be

$$\mathcal{H}(r, T) = \frac{T}{T_0}, \quad (5.1.2)$$

as in the previous two chapters. We want to solve (1.1.13) in the sheared boundary layer above an impedance lining with nonzero, non-constant viscosity and thermal conductivity without assuming a high- or low-frequency limit.

Outside the boundary layer, we assume the flow to be uniform and essentially inviscid, with the acoustics being well approximated by the Bessel function solutions (1.2.5) and (1.2.6). The relations (1.2.5) allow us to form an analytical expression for the effective impedance that the inviscid uniform flow solution sees at the wall,

$$Z_{\text{eff}} = \frac{\tilde{p}_u(1)}{\tilde{v}_u(1)} = (\omega - Mk) \frac{J_m(\alpha)}{i\alpha J'_m(\alpha)}. \quad (5.1.3)$$

We are interested in how the physics of the boundary layer effect connects the actual boundary impedance $\tilde{p}/\tilde{v} = Z$ to the effective impedance Z_{eff} .

5.2 Main boundary layer solution

It is thought that the Reynolds number of the flow in an aeroengine bypass duct is between 10^5 and 10^7 in-flight, and at take-off and landing (Jones *et al.*, 2005). Common assumptions for the thickness δ of the boundary layer are between 0.2 and 3% of the duct radius (Gabard, 2013). Experimental studies generally use fully developed turbulent boundary layers, and are a useful benchmark for choices of parameter values. In one such study, Renou & Aurégan (2011) report a Reynolds number of 3.38×10^5 (by the current definition); the boundary layer displacement (δ_d) and momentum (δ_m) thicknesses may be deduced from the data given in the reference to be $\delta_d \approx 5.1\%$ and $\delta_m \approx 3.9\%$ of the duct radius. The authors also give measurements of the (frequency dependent) acoustic boundary layer thickness, which lies in the range 0.26–0.67% of the duct radius, and is therefore far thinner than the mean flow boundary layer. In another study, Marx *et al.* (2010) report $\text{Re} \approx 2.4 \times 10^5$ (by the current definition); the boundary layer parameters were $\delta_d \approx 9\%$ and $\delta_m \approx 5\%$ of the duct radius. Assuming a laminar Blasius boundary layer gives the scaling $\delta \sim 1/\sqrt{\text{Re}}$; this choice of scaling generally underestimates the boundary layer thickness in aeroengines, possibly due to the boundary layer being turbulent. We propose the new scaling $\delta \sim \text{Re}^{-1/3}$, which models a slightly thicker boundary layer (or a slightly weaker viscosity) and is more in keeping with the scalings found in practice, as listed in table 5.1. Note, however, that we do not in any way model turbulence here.

The explicit boundary layer scaling used here is

$$r = 1 - \delta y, \quad \xi \delta^3 = 1/\text{Re}, \quad (5.2.1)$$

with $\xi = \mathcal{O}(1)$. The governing equations (1.1.13) are expanded in this regime, where y is the boundary layer variable. As in Brambley (2011a), the axial acoustic velocity and acoustic temperature perturbation are scaled as

$$\tilde{u} = \frac{\hat{u}}{\delta}, \quad \tilde{T} = \frac{\hat{T}}{\delta} \quad (5.2.2)$$

to balance the leading order of the continuity equation. The governing equations to first order in

δ	0.2%	1%	3%
Re			
10^5	2.5 : 1250	0.1 : 10	0.01 : 0.4
10^6	0.25 : 125	0.01 : 1	0.001 : 0.04
10^7	0.025 : 12.5	0.001 : 0.1	0.0001 : 0.004

Table 5.1. Values of $\xi_b; \xi_c$ where $\xi_b = 1/\text{Re}\delta^2$ is the Blasius scaling parameter, and $\xi_c = 1/\text{Re}\delta^3$ is the parameter for the new scaling proposed here. A value of ξ close to unity indicates a pertinent scaling choice. Boundary layer thicknesses given as a percentage of duct radius.

δ are

$$i(\omega - Uk)\hat{T} + ikT\hat{u} + T^2 \left(\frac{\tilde{v}}{T} \right)_y = \delta [\gamma i(\omega - Uk)T\tilde{p} + T\tilde{v} - imT\tilde{w}], \quad (5.2.3a)$$

$$i(\omega - Uk)\hat{u} - U_y\tilde{v} = \delta \left[\xi(\gamma - 1)^2 T(T\hat{u}_y + U_y\hat{T})_y + i(\gamma - 1)kT\tilde{p} \right], \quad (5.2.3b)$$

$$\tilde{p}_y = \delta \frac{i(\omega - Uk)}{(\gamma - 1)T} \tilde{v}, \quad (5.2.3c)$$

$$\frac{i(\omega - Uk)}{(\gamma - 1)^2 T} \tilde{w} = \frac{im}{\gamma - 1} \tilde{p} + \mathcal{O}(\delta), \quad (5.2.3d)$$

$$i(\omega - Uk)\hat{T} - T_y\tilde{v} = \delta \left[\frac{1}{\text{Pr}} \xi(\gamma - 1)^2 T(T\hat{T})_{yy} + \xi(\gamma - 1)^2 T(U_y^2\hat{T} + 2TU_y\hat{u}_y) + (\gamma - 1)i(\omega - Uk)T\tilde{p} \right]. \quad (5.2.3e)$$

It is clear from (5.2.3) that the choice of scaling (5.2.1) has pushed viscosity back to being a first order effect. This has the advantage that the leading order solution is exactly the inviscid uniform solution, with the correction at $O(\delta)$ including both shear and viscothermal corrections.

To solve the system (5.2.3) we expand the acoustic quantities in powers of δ : $\tilde{q} = \tilde{q}_0 + \delta\tilde{q}_1 + \mathcal{O}(\delta^2)$. At leading order, we use the relations

$$\hat{u}_0 = -\frac{iU_y}{\omega - Uk} \tilde{v}_0, \quad \hat{T}_0 = -\frac{iT_y}{\omega - Uk} \tilde{v}_0 \quad (5.2.4)$$

from (5.2.3b) and (5.2.3e) to rearrange the continuity equation (5.2.3a). The continuity equation reduces to

$$T(\omega - Uk) \left(\frac{\tilde{v}_0}{\omega - Uk} \right)_y = 0, \quad (5.2.5)$$

which has the solution $\tilde{v}_{m,0} = \bar{A}_0(\omega - Uk)$, where \bar{A}_0 is a constant and the subscript $m, 0$ denotes the leading order of the main boundary layer. Thus we may write $\hat{u}_{m,0} = -iU_y\bar{A}_0$ and $\hat{T}_{m,0} = -iT_y\bar{A}_0$. The pressure equation (5.2.3c) is readily integrated at leading order to produce $\tilde{p}_{m,0} = \bar{P}_0$, a constant. We may use this in equation (5.2.3d) to find $\tilde{w}_{m,0} = m(\gamma - 1)T\bar{P}_0/(\omega - Uk)$. This is the highest order of the azimuthal acoustic velocity solution that we need for the current study.

At first order, the \hat{u} and \hat{T} solutions may be written

$$\hat{u}_{m,1} = -\frac{iU_y}{\omega - Uk} \tilde{v}_{m,1} + \frac{(\gamma - 1)kT}{\omega - Uk} \bar{P}_0 - \xi\bar{A}_0 \frac{(\gamma - 1)^2 T}{\omega - Uk} (U_y T)_{yy}, \quad (5.2.6)$$

$$\hat{T}_{m,1} = -\frac{iT_y}{\omega - Uk} \tilde{v}_1 + (\gamma - 1)T\bar{P}_0 - \xi\bar{A}_0 \frac{(\gamma - 1)^2 T}{\omega - Uk} \left(\frac{1}{2\text{Pr}} (T^2)_{yyy} + (TU_y^2)_y \right), \quad (5.2.7)$$

where the subscript 1 denotes the first order. These are used in (5.2.3a) which, when integrated,

gives

$$\begin{aligned} \tilde{v}_{m,1} = & \bar{A}_1(\omega - Uk) + \bar{A}_0(\omega - Uk)y + i\bar{P}_0(\omega - Uk)y \left(1 - \frac{k^2 + m^2}{(\omega - Mk)^2}\right) \\ & + i\bar{P}_0(\omega - Uk) \frac{k^2 + m^2}{(\omega - Mk)^2} \int_0^y \chi_1 dy + i\xi \bar{A}_0(\gamma - 1)^2(\omega - Uk) \int_0^y \bar{\chi}_\mu dy, \end{aligned} \quad (5.2.8)$$

where \bar{A}_1 is a constant, and

$$\chi_1 = 1 - \frac{(\omega - Mk)^2}{\rho(\omega - Uk)^2}, \quad \bar{\chi}_\mu = \frac{1}{\omega - Uk} \left(\frac{(T^2)_{yyy}}{2\text{Pr}} + (TU_y^2)_y + \frac{kT}{\omega - Uk} (U_y T)_{yy} \right). \quad (5.2.9)$$

Note that viscous terms, identifiable by the parameter ξ , have arisen at this order in eqs. (5.2.6)–(5.2.8). The first order pressure is found by integrating (5.2.3c):

$$\tilde{p}_{m,1} = \bar{P}_1 + i\bar{A}_0(\omega - Mk)^2 y - i\bar{A}_0(\omega - Mk)^2 \int_0^y \chi_0 dy, \quad (5.2.10)$$

where \bar{P}_1 is a constant, and

$$\chi_0 = 1 - \frac{\rho(\omega - Uk)^2}{(\omega - Mk)^2}. \quad (5.2.11)$$

In summary, the solutions for the acoustic pressure and radial velocity in the main boundary layer, correct to first order, are

$$\begin{aligned} \tilde{v}_m = & (\omega - Uk) \left\{ \bar{A}_0 + \delta \bar{A}_1 + \delta \bar{A}_0 y + i\delta \bar{P}_0 y \left(1 - \frac{k^2 + m^2}{(\omega - Mk)^2}\right) \right. \\ & \left. + i\delta \bar{P}_0 \frac{k^2 + m^2}{(\omega - Mk)^2} \int_0^y \chi_1 dy + i\delta \xi \bar{A}_0(\gamma - 1)^2 \int_0^y \bar{\chi}_\mu dy \right\}, \end{aligned} \quad (5.2.12a)$$

$$\tilde{p}_m = \bar{P}_0 + \delta \bar{P}_1 + i\delta \bar{A}_0(\omega - Mk)^2 y - i\delta \bar{A}_0(\omega - Mk)^2 \int_0^y \chi_0 dy. \quad (5.2.12b)$$

These are identical in form to the pressure and radial velocity found by Brambley (2011*b*) by assuming an inviscid, thin-but-nonzero thickness boundary layer—but for the addition of the viscous integral $\bar{\chi}_\mu$ at first order in \tilde{v} . The constants \bar{A}_0 , \bar{A}_1 , \bar{P}_0 and \bar{P}_1 will be found by matching to the outer solution as $y \rightarrow \infty$.

The axial and azimuthal velocities in this scaling regime do not satisfy no slip at the wall $y = 0$. We have not, therefore, captured the full viscous dynamics of the boundary layer. The solutions (5.2.12) should be viewed as the *less* viscous main boundary layer solution that sits atop a viscous acoustic sublayer, which will be considered in section 5.3.

5.2.1 Matching the main boundary layer solution to the outer flow

The acoustics in the outer flow to which we asymptotically match are the uniform flow acoustics (1.2.5) expanded near the boundary in the limit $r \rightarrow 1$, as in (1.2.9). These are repeated here:

$$\tilde{p}_u(1 - \delta y) \sim p_\infty + \delta y i(\omega - Mk)v_\infty + \mathcal{O}(\delta^2), \quad (5.2.13a)$$

$$\tilde{v}_u(1 - \delta y) \sim v_\infty - \delta y \left(\frac{(\omega - Mk)^2 - k^2 - m^2}{i(\omega - Mk)} p_\infty - v_\infty \right) + \mathcal{O}(\delta^2), \quad (5.2.13b)$$

where

$$p_\infty = EJ_m(\alpha), \quad \text{and} \quad v_\infty = \frac{i\alpha EJ'_m(\alpha)}{(\omega - Mk)}. \quad (5.2.14)$$

We match (5.2.12) to (5.2.13) in the limit $y \rightarrow \infty$. At leading order we find

$$\bar{A}_0 = \frac{v_\infty}{\omega - Mk}, \quad \bar{P}_0 = p_\infty. \quad (5.2.15)$$

At first order, we require the terms proportional to y in (5.2.12) to match with the outer solutions, while the constant terms should cancel. Thus,

$$\bar{A}_1 = -ip_\infty \frac{k^2 + m^2}{(\omega - Mk)^2} I_1 - \frac{i\xi(\gamma - 1)^2}{\omega - Mk} v_\infty \bar{I}_\mu, \quad (5.2.16a)$$

$$\bar{P}_1 = i(\omega - Mk)v_\infty I_0 \quad (5.2.16b)$$

where

$$I_0 = \int_0^\infty \chi_0 dy, \quad I_1 = \int_0^\infty \chi_1 dy, \quad \bar{I}_\mu = \int_0^\infty \bar{\chi}_\mu dy. \quad (5.2.17)$$

The viscous integral (that of $\bar{\chi}_\mu$) is bounded as $y \rightarrow \infty$ because the gradients of the base flow are non-zero only inside the boundary layer.

5.2.2 Behaviour of the main boundary layer solutions near the boundary

Here we find the limiting behaviour of the solutions found in the previous section, (5.2.12), as $y \rightarrow 0$. This will be needed in section 5.3.1 when matching to the viscous sublayer solution. Expanding first the integrals, we find

$$\int_0^y \chi_0 dy \sim \left(1 - \frac{\rho(0)\omega^2}{(\omega - Mk)^2}\right) y + \mathcal{O}(y^2), \quad (5.2.18a)$$

$$\int_0^y \chi_1 dy \sim \left(1 - \frac{(\omega - Mk)^2}{\rho(0)\omega^2}\right) y + \mathcal{O}(y^2), \quad (5.2.18b)$$

$$\int_0^y \bar{\chi}_\mu dy \sim \frac{y}{\omega^2} \left(kT(0)^2 U'''(0) + kT(0)T''(0)U'(0) + 2\omega T(0)U'(0)U''(0) \right. \\ \left. + \frac{\omega}{\text{Pr}} T(0)T'''(0) \right) + \mathcal{O}(y^2), \quad (5.2.18c)$$

where we assume the base flow is non-slipping and satisfies isothermal wall conditions, $U(0) = 0$ and $T'(0) = 0$, such that $U(y) \sim U'(0)y$ and $T(y) \sim T(0)$, and similar for their derivatives. A prime denotes a derivative with respect to y . Thus for small y the pressure and velocity behave as

$$\tilde{v}_m^{(I)} \sim \bar{A}_0 \left(\omega - U'(0)ky - \frac{1}{2}U''(0)ky^2 \right) + \delta \bar{A}_1(\omega - U'(0)ky) + \delta \bar{A}_0 \omega y + i\delta y \bar{P}_0 \omega \\ - i\delta y \bar{P}_0 \frac{k^2 + m^2}{\rho(0)\omega} + i\delta y \xi \bar{A}_0 (\gamma - 1)^2 \omega \left(\frac{k}{\omega^2} T(0)^2 U'''(0) + \frac{k}{\omega^2} T(0)T''(0)U'(0) \right. \\ \left. + \frac{2}{\omega} T(0)U'(0)U''(0) + \frac{1}{\text{Pr}\omega} T(0)T'''(0) \right) + \mathcal{O}(\delta^2, \delta y^2, y^3), \quad (5.2.19a)$$

$$\tilde{p}_m^{(I)} \sim \bar{P}_0 + \delta \bar{P}_1 + i\delta y \bar{A}_0 \rho(0)\omega^2 + \mathcal{O}(\delta^2, \delta y^2). \quad (5.2.19b)$$

These forms, (5.2.19), will be used as the outer solutions to which the viscous sublayer solutions, derived in the next section, should match.

5.3 Viscous sublayer solution

We assume the existence of a thin viscous sublayer within which the base flow does not change quickly, but the acoustics change rapidly enough to satisfy viscous wall conditions at $r = 1$, $y = 0$. We scale into this sublayer by

$$y = \varepsilon z, \quad \varepsilon = \sqrt{\delta/\omega} \sim \text{Re}^{-1/6}, \quad (5.3.1)$$

as described in Appendix 5.A. We may expand the base flow near the wall using the no slip and isothermal wall conditions,

$$\begin{aligned} U &\sim \varepsilon z U'(0) + \frac{1}{2} \varepsilon^2 z^2 U''(0), & U_y &\sim U'(0) + \varepsilon z U''(0) + \frac{1}{2} \varepsilon^2 z^2 U'''(0), \\ U_{yy} &\sim U''(0) + \varepsilon z U'''(0) + \frac{1}{2} \varepsilon^2 z^2 U''''(0), & T &\sim T(0) + \frac{1}{2} \varepsilon^2 z^2 T''(0), \\ T_y &\sim \varepsilon z T''(0) + \frac{1}{2} \varepsilon^2 z^2 T'''(0), & T_{yy} &\sim T''(0) + \varepsilon z T'''(0) + \frac{1}{2} \varepsilon^2 z^2 T''''(0), \end{aligned} \quad (5.3.2)$$

where the derivatives and arguments of the base flow variables remain in terms of y , i.e.

$$U'(0) \equiv \left. \frac{d}{dy} U(y) \right|_{y=0}.$$

We will drop the argument 0 for all base flow variables in this section, as they will all be evaluated at the boundary: $U' \equiv U'(0)$, and so on.

Expanding (1.1.13) in powers of ε using (5.3.1) and (5.3.2) leads to the sublayer governing equations

$$\begin{aligned} \tilde{v}_z &= \varepsilon \left[-ik\hat{u} - \frac{i\omega}{T}\hat{T} \right] + \varepsilon^2 \left[ik\frac{U'}{T}z\hat{T} + \frac{T''}{T}z\tilde{v} \right] + \varepsilon^3 \left[(kU'' + \omega T'')\frac{i}{2T}z^2\hat{T} \right. \\ &\quad \left. + \frac{T'''}{2T}z^2\tilde{v} - im\omega\tilde{w} + i\gamma\omega^2\tilde{p} + \omega\tilde{v} \right], \end{aligned} \quad (5.3.3a)$$

$$\begin{aligned} \hat{u}_{zz} - \eta^2\hat{u} &= \frac{iU'}{\omega}\eta^2\tilde{v} - \varepsilon \left[\frac{kU'}{\omega}\eta^2z\hat{u} + \frac{U'}{T}\hat{T}_z - \frac{iU''}{\omega}\eta^2z\tilde{v} \right] - \varepsilon^2 \left[k\eta^2(\gamma-1)T\tilde{p} \right. \\ &\quad \left. - \frac{iU'''}{2\omega}\eta^2z^2\tilde{v} + \frac{kU''}{2\omega}\eta^2z^2\hat{u} + \frac{T''}{T}(z^2\hat{u}_{zz} + z\hat{u}_z) + \frac{U''}{T}(z\hat{T})_z \right], \end{aligned} \quad (5.3.3b)$$

$$\tilde{p}_z = \varepsilon^3 \left[\frac{i\omega^2}{(\gamma-1)T}\tilde{v} - \frac{i\omega^2(2+\beta)}{(\gamma-1)\eta^2T}\tilde{v}_{zz} \right], \quad (5.3.3c)$$

$$\tilde{w}_{zz} - \eta^2\tilde{w} = -\frac{m}{\omega}(\gamma-1)T\eta^2\tilde{p} + \mathcal{O}(\varepsilon), \quad (5.3.3d)$$

$$\begin{aligned} \frac{1}{\text{Pr}}\hat{T}_{zz} - \eta^2\hat{T} &= -\varepsilon \left[2U'\hat{u}_z + \frac{kU'}{\omega}\eta^2z\hat{T} - \frac{iT''}{\omega}\eta^2z\tilde{v} \right] - \varepsilon^2 \left[(\gamma-1)T\omega\eta^2\tilde{p} + 2U''z\hat{u}_z \right. \\ &\quad \left. - \frac{iT'''}{2\omega}\eta^2z^2\tilde{v} + \frac{kU''}{2\omega}\eta^2z^2\hat{T} + \frac{U'^2}{T}\hat{T} + \frac{1}{\text{Pr}}\frac{T''}{T} \left((z^2\hat{T}_z)_z + \hat{T} \right) \right], \end{aligned} \quad (5.3.3e)$$

where we have defined

$$\eta^2 = \frac{i}{\xi(\gamma-1)^2T(0)^2} \quad (5.3.4)$$

with $\text{Re}(\eta) > 0$. To find \tilde{p} and \tilde{v} to the desired order, we need to calculate \hat{u} and \hat{T} to $\mathcal{O}(\varepsilon^2)$ and \tilde{w} to $\mathcal{O}(1)$. The system (5.3.3) may be solved by expanding the acoustic quantities in powers of ε , $q = q_0 + \varepsilon q_1$ *et cetera*; details of this solution may be found in Appendix 5.B. The main results are expressions for the pressure and radial velocity in the acoustic boundary layer to $\mathcal{O}(\varepsilon^3)$,

$$\tilde{p}_s(z) = P_0 + \varepsilon P_1 + \varepsilon^2 P_2 + \varepsilon^3 \left(P_3 + \frac{i\omega^2}{(\gamma-1)T} A_0 z \right), \quad (5.3.5a)$$

$$\begin{aligned}\tilde{v}_s(z) = & A_0 + \varepsilon [A_1 + a_0 e^{-\eta z} + a_1 z] + \varepsilon^2 [A_2 + a_2 z + a_3 z^2 + (a_4 + a_5 z + a_6 z^2) e^{-\eta z} \\ & + a_7 e^{-\sigma \eta z}] + \varepsilon^3 [A_3 + a_8 z + a_9 z^2 + a_{10} z^3 + (a_{16} + a_{17} z + a_{18} z^2) e^{-\sigma \eta z} \\ & + (a_{11} + a_{12} z + a_{13} z^2 + a_{14} z^3 + a_{15} z^4) e^{-\eta z}],\end{aligned}\quad (5.3.5b)$$

where A_j and P_j are constants of integration, and a_j are linear combinations of the A_j and P_j given in Appendix 5.B. Here, $\sigma = \sqrt{\text{Pr}}$, and the subscript s denotes a solution in the viscous sublayer.

In the limit $z \rightarrow \infty$, \tilde{p} and \tilde{v} from (5.3.5) behave, to $\mathcal{O}(\varepsilon^3)$, as

$$\tilde{p}_s \sim P_0 + \varepsilon P_1 + \varepsilon^2 P_2 + \varepsilon^3 \left(P_3 + \frac{i\omega^2}{(\gamma-1)T} A_0 z \right), \quad (5.3.6a)$$

$$\tilde{v}_s \sim A_0 + \varepsilon (A_1 + a_1 z) + \varepsilon^2 (A_2 + a_2 z + a_3 z^2) + \varepsilon^3 (A_3 + a_8 z + a_9 z^2 + a_{10} z^3), \quad (5.3.6b)$$

where the exponentially small, necessarily viscous, terms in (5.3.5) vanish in this outer limit. We now match to the main boundary layer solution.

5.3.1 Matching with the main boundary layer solution

An intermediate variable is introduced to facilitate matching: let

$$\tau = y/\varepsilon^\lambda = z\varepsilon^{1-\lambda} \quad (5.3.7)$$

where $0 < \lambda < 1$. We then take the limit $\varepsilon \rightarrow 0$, holding τ fixed. For the acoustic pressure, the main boundary layer solution in the limit $y \rightarrow 0$, (5.2.19b), and the sublayer solution in the limit $z \rightarrow \infty$, (5.3.6a), may be rewritten in terms of the intermediate variable τ using (5.3.7). We find, as $\varepsilon \rightarrow 0$,

$$\tilde{p}_m \sim \bar{P}_0 + \varepsilon^2 \omega \bar{P}_1 + i\varepsilon^{2+\lambda} \tau \omega^3 \bar{A}_0 \rho(0) + \mathcal{O}(\varepsilon^4, \varepsilon^{2+2\lambda}) \quad (5.3.8a)$$

$$\tilde{p}_s \sim P_0 + \varepsilon P_1 + \varepsilon^2 P_2 + \varepsilon^{2+\lambda} \tau \frac{i\omega^2}{(\gamma-1)T(0)} A_0 + \varepsilon^3 P_3 + \mathcal{O}(\varepsilon^4, \varepsilon^{2+2\lambda}). \quad (5.3.8b)$$

Similarly, the \tilde{v} expansion in the limit $\varepsilon \rightarrow 0$ with τ held fixed gives

$$\begin{aligned}\tilde{v}_m \sim & \omega \bar{A}_0 - \varepsilon^\lambda \tau k U'(0) \bar{A}_0 - \varepsilon^{2\lambda} \tau^2 \frac{k U''(0)}{2} \bar{A}_0 - \varepsilon^{3\lambda} \tau^3 \frac{k U'''(0)}{6} \bar{A}_0 + \varepsilon^2 \omega^2 \bar{A}_1 \\ & + \varepsilon^{2+\lambda} \tau \left\{ \omega^2 \bar{A}_0 - k U'(0) \omega \bar{A}_1 + i\omega^2 \bar{P}_0 - i \frac{k^2 + m^2}{\rho(0)} \bar{P}_0 \right. \\ & \left. + i\xi(\gamma-1)^2 T(0)^2 \omega \bar{A}_0 \left(\frac{k U'''(0)}{\omega} + \frac{k T''(0) U'(0)}{\omega T(0)} + \frac{2U'(0)U''(0)}{T(0)} \right. \right. \\ & \left. \left. + \frac{1}{\text{Pr}} \frac{T'''(0)}{T(0)} \right) \right\} + \mathcal{O}(\varepsilon^{2+2\lambda}, \varepsilon^{4\lambda}),\end{aligned}\quad (5.3.9)$$

for the main boundary layer solution, and

$$\begin{aligned}\tilde{v}_s \sim & A_0 - \varepsilon^\lambda \tau \frac{k U'(0)}{\omega} A_0 + \varepsilon A_1 - \varepsilon^{2\lambda} \tau^2 \frac{k U''(0)}{2\omega} A_0 - \varepsilon^{3\lambda} \tau^3 \frac{k U'''(0)}{6\omega} A_0 \\ & - \varepsilon^{1+\lambda} \tau \frac{k U'(0)}{\omega} A_1 + \varepsilon^2 A_2 - \varepsilon^{1+2\lambda} \tau^2 \frac{k U''(0)}{2\omega} A_1 + \varepsilon^{2+\lambda} \tau \left\{ \omega A_0 + i\omega^2 P_0 \right. \\ & \left. - i(k^2 + m^2)(\gamma-1)T(0)P_0 - \frac{k U'(0)}{\omega} A_2 - \frac{1}{\eta^2} A_0 \left(\frac{T'''(0)}{\text{Pr} T(0)} + \frac{2U'(0)U''(0)}{T(0)} \right. \right. \\ & \left. \left. + \frac{k T''(0)U'(0)}{\omega T(0)} + \frac{k U'''(0)}{\omega} \right) \right\} + \varepsilon^3 A_3 + \mathcal{O}(\varepsilon^4, \varepsilon^{2+2\lambda})\end{aligned}\quad (5.3.10)$$

for the sublayer solution. These equations must match independently of $\lambda \in (0, 1)$.

We may identify from (5.3.8) that $P_0 = \bar{P}_0$ and $P_2 = \omega \bar{P}_1$. The $\mathcal{O}(\varepsilon)$ matching gives $P_1 = 0$. Because we want the matching to work for any value of the exponent $\lambda \in (0, 1)$, we set $P_3 = 0$. From the leading order of (5.3.9) and (5.3.10) we can readily identify $A_0 = \omega \bar{A}_0$. This is consistent with higher order terms of (5.3.9) and (5.3.10), and also with the $\mathcal{O}(\varepsilon^{2+\lambda})$ terms in the \bar{p} expansions (5.3.8) once we write $\rho(0) = 1/(\gamma - 1)T(0)$. At $\mathcal{O}(\varepsilon^2)$ we find $A_2 = \omega^2 \bar{A}_1$. Due to the absence of ε and ε^3 terms in (5.3.9), we set $A_1 = A_3 = 0$. The remaining terms at $\mathcal{O}(\varepsilon^{2+\lambda})$ match if the definition of η is inserted from (5.3.4).

5.4 Results for the mode shapes

All results presented here use hyperbolic velocity and temperature profiles,

$$U(r) = M \tanh\left(\frac{1-r}{\delta}\right) + M \left(1 - \tanh\left(\frac{1}{\delta}\right)\right) \left(\frac{1 + \tanh(1/\delta)}{\delta} r + (1+r)\right) (1-r) \quad (5.4.1a)$$

$$T(r) = T_0 + T_w \left(\cosh\left(\frac{1-r}{\delta}\right)\right)^{-1}, \quad (5.4.1b)$$

where δ is a measure of boundary layer thickness, with $U(1 - 3\delta) \approx 0.995M$. For the results presented here, $T_w = 0.104$.

First we show some examples of the acoustic mode shapes that result from the three different duct regions considered in the asymptotic analysis. The patchwork of regions of validity for the radial velocity can be seen in fig. 5.1: compared to the numerical solution of the full LNSE, the uniform flow outer solution \tilde{v}_u is valid for most of the duct, where the shear is negligible (fig. 5.1a); the main boundary layer solution \tilde{v}_m is accurate where the mean flow shear is important, but loses accuracy very close to the wall (fig. 5.1b); the viscous sublayer solution \tilde{v}_s is accurate in the acoustic boundary layer very close to the wall (fig. 5.1c). Figure 5.2 shows the mode shape of the acoustic pressure for the same parameters—we see that the sublayer solution is indeed the inner expansion of the main boundary layer solution (see fig. 5.2c). For the axial velocity we see a similar thing (fig. 5.3), except here the viscous sublayer solution is significantly different from the main boundary layer solution due to the sublayer solution satisfying no slip at the wall.

5.4.1 Composite solutions

Here we derive solutions for the acoustic mode shapes that are uniformly valid in r . We have defined three regions of the duct: the outer region, where the base flow is uniform and inviscid; the main boundary layer, where the base flow is sheared and viscosity is a first order perturbation; and the sublayer, where the base flow varies slowly, and viscous and inertial effects balance to enforce no slip and isothermal boundary conditions at the wall. In the outer region, the Bessel function solutions defined in (1.2.5) hold; in the main boundary layer the expansions (5.2.12) hold; while in the sublayer the expansions (5.3.5) hold.

For the pressure, since the sublayer solution (5.3.5a) is inviscid to $\mathcal{O}(\varepsilon^3)$, it transpires that the sublayer solution is exactly the inner expansion of the main boundary layer solution (5.2.12b) for small y ; this is why fig. 5.2c shows the main boundary layer solution continuing to perform well within the sublayer region. Thus, we need only form a composite of the outer solution $\tilde{p}_u = EJ_m(\alpha r)$ and the main boundary layer solution. This is equivalent to that found by Brambley for the modified Myers boundary condition (Brambley, 2011b). Using the definition of p_∞ from

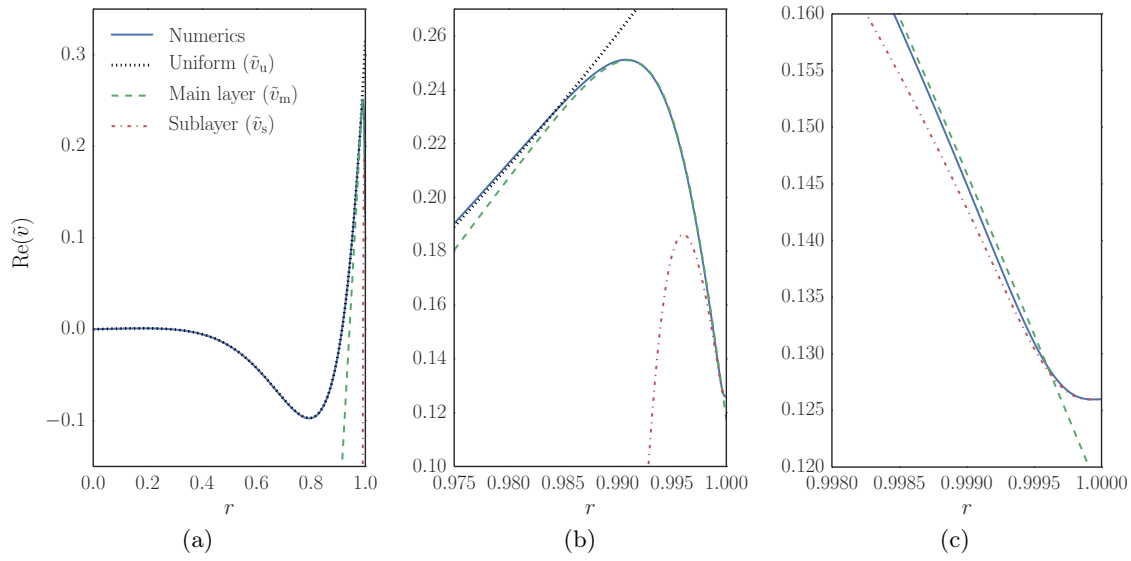


Figure 5.1. Acoustic mode shape for the radial velocity \tilde{v} found by numerically solving the LNSE, with the three asymptotic solutions overlaid, showing their patchwork of regions of validity. (a) shows the full duct $r \in [0, 1]$, (b) shows the main boundary layer, (c) shows the viscous sublayer. Parameters are $\omega = 5$, $k = -14 + 5i$, $m = 0$, $M = 0.5$, $\delta = 6 \times 10^{-3}$, $\text{Re} = 5 \times 10^6$.

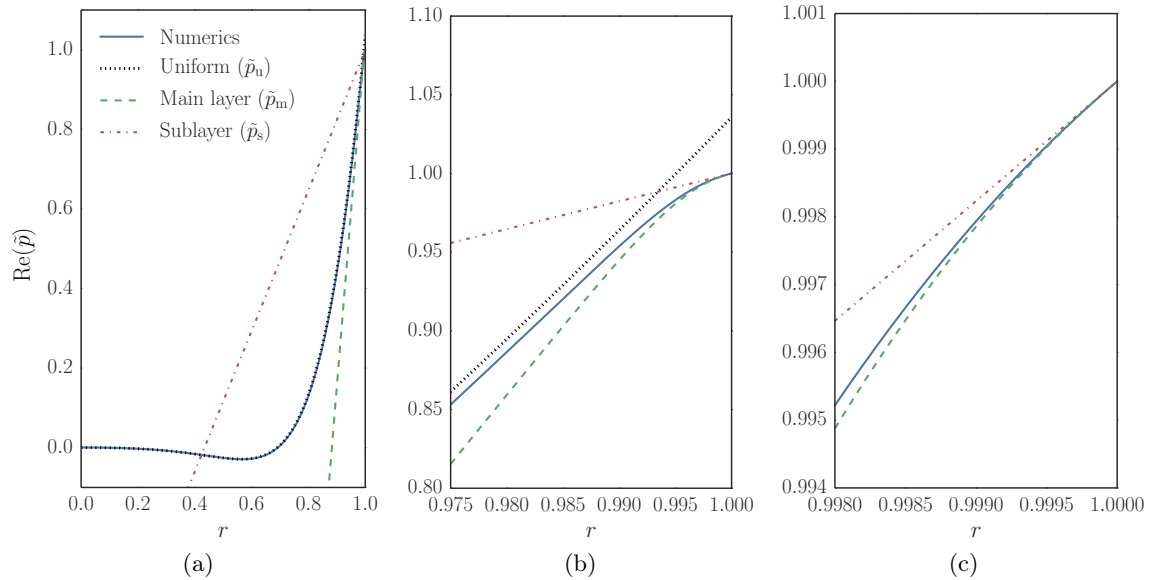


Figure 5.2. Acoustic mode shape for the acoustic pressure \tilde{p} found by numerically solving the LNSE, with the three asymptotic solutions overlaid, showing their patchwork of regions of validity. (a) shows the full duct $r \in [0, 1]$, (b) shows the main boundary layer, (c) shows the viscous sublayer. Parameters as in fig. 5.1.

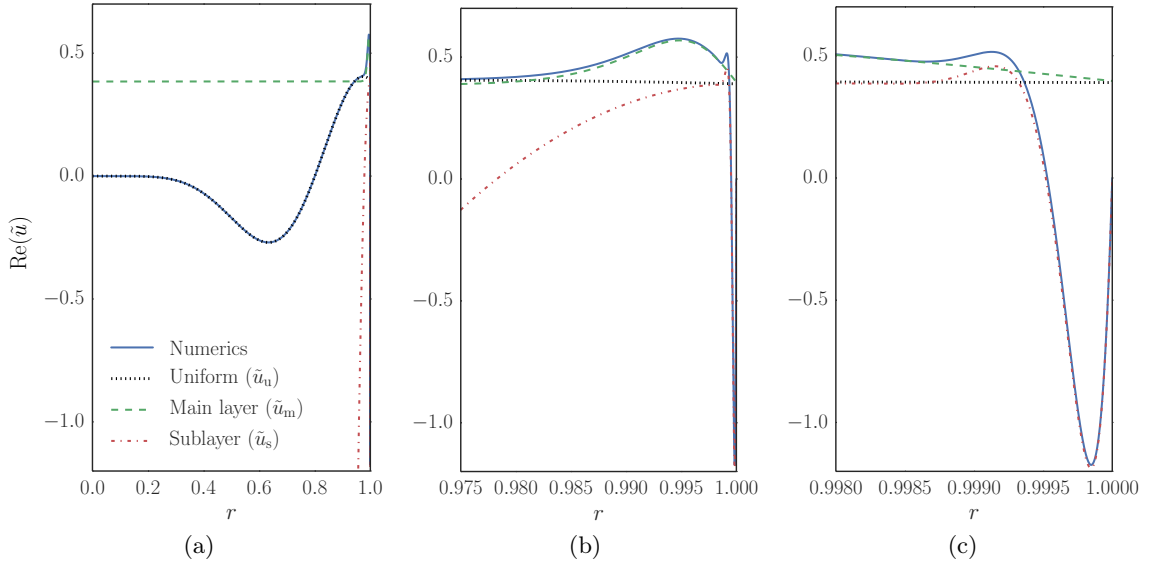


Figure 5.3. Acoustic mode shape for the axial velocity \tilde{u} found by numerically solving the LNSE, with the three asymptotic solutions overlaid, showing their patchwork of regions of validity. (a) shows the full duct $r \in [0, 1]$, (b) shows the main boundary layer, (c) shows the viscous sublayer. Parameters are $\omega = 15$, $k = 5 + 2i$, $m = 6$, $M = 0.5$, $\delta = 7 \times 10^{-3}$, $\text{Re} = 3 \times 10^6$.

(5.2.14), the uniformly valid composite solution \tilde{p}_c , valid across all regions, is given by

$$\frac{\tilde{p}_c}{p_\infty} = \frac{J_m(\alpha r)}{J_m(\alpha)} - \frac{\alpha J'_m(\alpha)}{J_m(\alpha)} \int_0^r 1 - \frac{\rho(\omega - Uk)^2}{(\omega - Mk)^2} dr. \quad (5.4.2)$$

Setting the amplitude of the wave, through the value of p_∞ , is the only degree of freedom remaining in (5.4.2).

Turning to the radial velocity, we may write the sublayer solution (5.3.5b) as

$$\tilde{v}_s = V_1(z; \varepsilon) + V_2(z; \varepsilon)e^{-\eta z} + V_3(z; \varepsilon)e^{-\sigma \eta z}. \quad (5.4.3)$$

Since the V_2 and V_3 terms decay exponentially as $z \rightarrow \infty$, and since the V_1 term is exactly the inner expansion of the main boundary layer solution \tilde{v}_m (5.2.12a) for small y , a composite of the main boundary layer and sublayer solutions is given by \tilde{v}_{cBL} ,

$$\tilde{v}_{cBL} = \tilde{v}_m + V_2(z; \varepsilon)e^{-\eta z} + V_3(z; \varepsilon)e^{-\sigma \eta z}. \quad (5.4.4)$$

We form a full composite expansion by additive composing \tilde{v}_{cBL} with the outer inviscid solution $\tilde{v}_u = i\alpha p_\infty J'_m(\alpha r)/J_m(\alpha)(\omega - Mk)$, giving the full composite solution $\tilde{v}_c = \tilde{v}_u + \tilde{v}_{cBL} - \tilde{v}_m^{(O)}$, where $\tilde{v}_m^{(O)}$ is the outer expansion as $y \rightarrow \infty$ of \tilde{v}_m given in (5.2.13b). In full, this composite solution is

$$\begin{aligned} \frac{\tilde{v}_c}{p_\infty} = & \frac{i\alpha J'_m(\alpha r)}{(\omega - Mk)J_m(\alpha)} + \frac{ik(M - U)}{(\omega - Mk)^2} \left(\frac{\alpha J'_m(\alpha)}{J_m(\alpha)} + (1 - r) \left[\frac{\alpha J'_m(\alpha)}{J_m(\alpha)} + (\alpha^2 - m^2) \right] \right) \\ & + \frac{(\omega - Uk)}{(\omega - Mk)^2} \left(\frac{(\gamma - 1)^2 \alpha J'_m(\alpha)}{\omega \text{Re}} \int_0^r \frac{\chi_\mu(r)}{\delta^3} dr - i(k^2 + m^2) \int_0^r \chi_1(r) dr \right) \\ & + \frac{\bar{V}_2(z; \varepsilon)}{J_m(\alpha)} e^{-(1-r)/\delta_{ac}} + \frac{\bar{V}_3(z; \varepsilon)}{J_m(\alpha)} e^{-\sigma(1-r)/\delta_{ac}}, \end{aligned} \quad (5.4.5)$$

where

$$\delta_{ac} = \frac{(\gamma - 1)T(1)}{\sqrt{i\omega \text{Re}}}; \quad \text{Re}(\delta_{ac}) > 0, \quad (5.4.6)$$

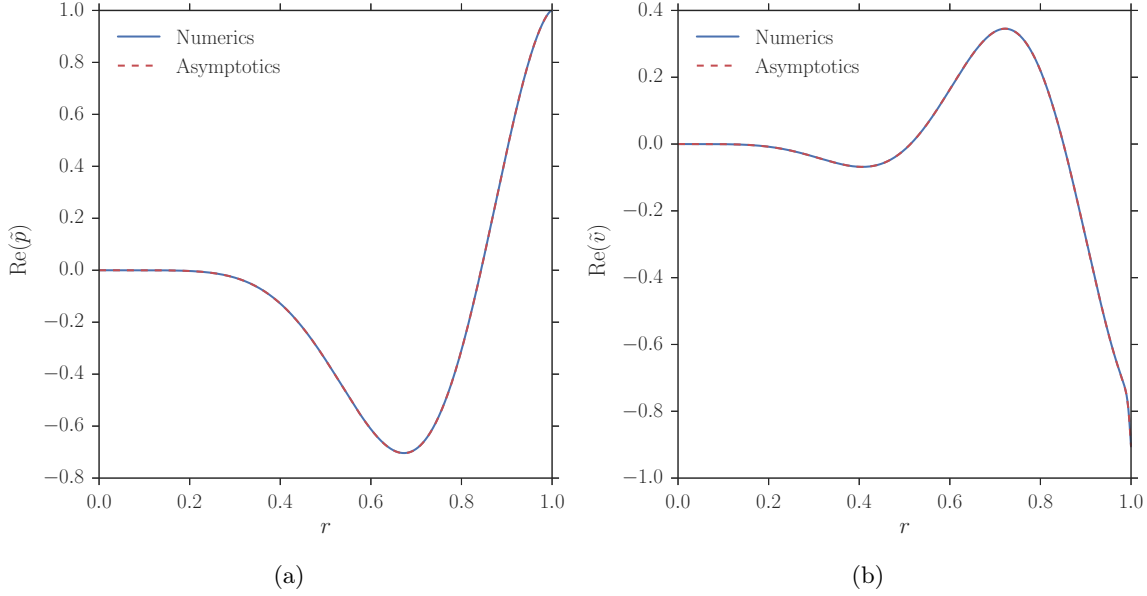


Figure 5.4. Comparison of the numerical LNSE mode shapes and the composite asymptotic mode shapes (5.4.2) and (5.4.5) for (a) the pressure \tilde{p} and (b) the radial velocity \tilde{v} . Parameters are $\omega = 15$, $k = 5 + 2i$, $m = 6$, $M = 0.5$, $\delta = 7 \times 10^{-3}$, $\text{Re} = 3 \times 10^6$.

and

$$\bar{V}_2(z; \varepsilon) = \varepsilon a_0 + \varepsilon^2(a_4 + a_5 z + a_6 z^2) + \varepsilon^3(a_{11} + a_{12} z + a_{13} z^2 + a_{14} z^3 + a_{15} z^4), \quad (5.4.7a)$$

$$\bar{V}_3(z; \varepsilon) = \varepsilon^2 a_7 + \varepsilon^3(a_{16} + a_{17} z + a_{18} z^2). \quad (5.4.7b)$$

Note, in (5.4.5) the integrals are with respect to r rather than the boundary layer variable y . For χ_1 the transformation is trivial; for χ_μ the derivatives of the base flow variables produce powers of δ such that

$$\chi_\mu(r) = -\omega \delta^3 \bar{\chi}_\mu(y), \quad (5.4.8)$$

with

$$\bar{\chi}_\mu(y) = \frac{1}{\omega - Uk} \left(\frac{1}{2\text{Pr}} (T^2)_{yyy} + (TU_y^2)_y + \frac{kT}{\omega - Uk} (U_y T)_{yy} \right), \quad (5.4.9)$$

as shown later in (5.5.8b) (we have also chosen to incorporate an ω in the definition of $\chi_\mu(r)$).

A comparison of (5.4.2) and (5.4.5) with the numerical LNSE for the same parameters as figs. 5.1–5.3 is given in fig. 5.4. Excellent agreement can be seen between the LNSE and composite solutions, suggesting that the composite solutions may be relied upon when mode shapes are required, rather than having the complication of three separate solutions, each with their own region of validity.

5.5 The effective impedance

The matched asymptotic expansions solutions for the acoustics derived in the previous sections, sections 5.2 and 5.3, and the uniform flow solution from section 1.2.1 are used here to construct an effective impedance boundary condition. The effective impedance is defined as the impedance seen by the inviscid, uniform flow acoustics (\tilde{p}_u and \tilde{v}_u here) if they were continued out of their region of validity to the wall at $r = 1$, and is given by (5.1.3). This definition allows us to apply the resulting boundary condition to an inviscid, slipping, uniform flow, meaning the thin boundary layer does not need to be resolved numerically. The effective impedance differs from the boundary impedance Z due to viscothermal effects and refraction through the sheared boundary layer. We

want to find Z_{eff} as a function of the boundary impedance Z .

5.5.1 Forming the effective impedance

We can use the information gleaned from matching the main boundary layer solution to the core flow in section 5.2.1, and from matching the main boundary layer solution to the viscous sublayer solution in section 5.3.1 to write the sublayer constants A_j , P_j in terms of the uniform flow constants p_∞ and v_∞ :

$$\begin{aligned} P_0 &= p_\infty, & P_2 &= i\omega(\omega - Mk)I_0v_\infty, & A_0 &= \frac{\omega}{\omega - Mk}v_\infty, \\ A_2 &= -i\omega^2 \frac{k^2 + m^2}{(\omega - Mk)^2} I_1 p_\infty - i\xi\omega(\gamma - 1)^2 \bar{I}_\mu \frac{\omega}{\omega - Mk} v_\infty, \end{aligned} \quad (5.5.1)$$

where I_0 , I_1 and \bar{I}_μ are defined in (5.2.17).

At the boundary, the wall-normal velocity is

$$\tilde{v}_s(0) = A_0 + \varepsilon a_0 + \varepsilon^2(A_2 + a_4 + a_7) + \varepsilon^3(a_{11} + a_{16}),$$

We may split a_{11} , a_{16} and A_2 up into terms proportional to v_∞ and p_∞ . Then we may write

$$\tilde{v}_s(0) = p_\infty (\varepsilon^2 \bar{R}_1 + \varepsilon^3 \bar{S}_1) + \frac{\omega}{\omega - Mk} v_\infty (1 + \varepsilon \bar{R}_2 + \varepsilon^2 \bar{S}_2 + \varepsilon^3 \bar{S}_3), \quad (5.5.2)$$

where

$$\bar{R}_1 = -i\omega^2 \frac{k^2 + m^2}{(\omega - Mk)^2} I_1, \quad (5.5.3a)$$

$$\bar{R}_2 = -\frac{kU'(0)}{\omega\eta}, \quad (5.5.3b)$$

$$\bar{S}_1 = i\omega \frac{k^2 + m^2}{(\omega - Mk)^2} \frac{kU'(0)}{\eta} I_1 - i(\gamma - 1)(k^2 + m^2) \frac{T(0)}{\eta} - \frac{i(\gamma - 1)\omega^2}{\sigma\eta}, \quad (5.5.3c)$$

$$\bar{S}_2 = -i\xi\omega(\gamma - 1)^2 \bar{I}_\mu + \frac{\sigma}{1 + \sigma} \frac{2U'(0)^2}{\eta^2 T(0)} - \frac{5k^2 U'(0)^2}{4\omega^2 \eta^2}, \quad (5.5.3d)$$

$$\begin{aligned} \bar{S}_3 &= i\xi(\gamma - 1)^2 \frac{kU'(0)}{\eta} \bar{I}_\mu - \frac{13k^2 U'(0)U''(0)}{8\omega^2 \eta^3} - \frac{kU'''(0)}{\omega\eta^3} - \frac{T'''(0)}{\sigma^3 \eta^3 T(0)} - \frac{151k^3 U'(0)^3}{32\omega^3 \eta^3} \\ &+ \frac{(7\sigma + 3)}{(1 + \sigma)^2} \frac{kU'(0)^3}{2\omega\eta^3 T(0)} + \frac{2(\sigma^3 + \sigma^2 - 2\sigma - 1)}{\sigma(1 + \sigma)^2} \frac{U'(0)T''(0)}{\omega\eta^3 T(0)} \\ &- \frac{(2\sigma^2 + 4\sigma + 1)}{(1 + \sigma)^2} \frac{kU'(0)T''(0)}{\omega\eta^3 T(0)}. \end{aligned} \quad (5.5.3e)$$

Similarly, we may write \tilde{p}_s at $z = 0$:

$$\tilde{p}_s(0) = p_\infty + \varepsilon^2 i\omega(\omega - Mk)I_0v_\infty. \quad (5.5.4)$$

Then, we use the definition of the boundary impedance, $Z = \tilde{p}_s(0)/\tilde{v}_s(0)$, with $\tilde{p}_s(0)$ and $\tilde{v}_s(0)$ defined in (5.5.2) and (5.5.4), and divide top and bottom of the ratio by v_∞ to introduce the effective impedance $Z_{\text{eff}} = p_\infty/v_\infty$:

$$Z = \frac{Z_{\text{eff}} + \varepsilon^2 i\omega(\omega - Mk)I_0}{\frac{\omega}{\omega - Mk} (1 + \varepsilon \bar{R}_2 + \varepsilon^2 \bar{S}_2 + \varepsilon^3 \bar{S}_3) + Z_{\text{eff}} (\varepsilon^2 \bar{R}_1 + \varepsilon^3 \bar{S}_1)}. \quad (5.5.5)$$

Rearranging, and writing in terms of r and primitive variables, then gives us our effective impedance

in terms of the boundary impedance Z ,

$$Z_{\text{eff}} = \frac{\omega}{\omega - Mk} \frac{Z + \frac{(\gamma-1)T(1)}{\sqrt{i\omega\text{Re}}} \frac{kU_r(1)}{\omega} Z - \frac{i}{\omega} (\omega - Mk)^2 \delta I_0 + (S_2 + S_3)Z}{1 + i(k^2 + m^2) \frac{\omega Z}{(\omega - Mk)^2} \delta I_1 + S_1 Z} + \mathcal{O}(\delta^2), \quad (5.5.6)$$

where

$$S_1 = \frac{(\gamma - 1)T(1)}{\sqrt{i\omega\text{Re}}} \left(\frac{k^2 + m^2}{(\omega - Mk)^2} ikU_r(1)\delta I_1 + \frac{i\omega}{\sigma}(\gamma - 1) + \frac{i}{\omega\rho(1)}(k^2 + m^2) \right), \quad (5.5.7a)$$

$$S_2 = \left(\frac{(\gamma - 1)T(1)}{\sqrt{i\omega\text{Re}}} \right)^2 \left(\frac{1}{T(1)^2} \frac{I_\mu}{\delta^2} + \frac{\sigma}{1 + \sigma} \frac{2U_r(1)^2}{T(1)} - \frac{5k^2}{4\omega^2} U_r(1)^2 \right), \quad (5.5.7b)$$

$$S_3 = \left(\frac{(\gamma - 1)T(1)}{\sqrt{i\omega\text{Re}}} \right)^3 \left(\frac{kU_r(1)}{\omega T(1)} \frac{I_\mu}{\delta^2} + \frac{13k^2}{8\omega^2} U_r(1)U_{rr}(1) + \frac{k}{\omega} U_{rrr}(1) + \frac{T_{rrr}(1)}{\sigma^3 T(1)} \right. \\ \left. + \frac{151k^3}{32\omega^3} U_r(1)^3 - \frac{(7\sigma + 3)kU_r(1)^3}{(1 + \sigma)^2 2\omega T(1)} - \frac{(\sigma^3 + \sigma^2 - 2\sigma - 1)2U_r(1)T_{rr}(1)}{\sigma(1 + \sigma)^2 \omega T(1)} \right. \\ \left. + \frac{(2\sigma^2 + 4\sigma + 1)kU_r(1)T_{rr}(1)}{(1 + \sigma)^2 \omega T(1)} \right), \quad (5.5.7c)$$

and

$$\delta I_0 = \int_0^1 1 - \frac{\rho(r)(\omega - U(r)k)^2}{(\omega - Mk)^2} dr, \quad \delta I_1 = \int_0^1 1 - \frac{(\omega - Mk)^2}{\rho(r)(\omega - U(r)k)^2} dr, \quad (5.5.8a)$$

$$\frac{I_\mu}{\delta^2} = \int_0^1 \frac{\chi_\mu}{\delta^3} dr, \quad \frac{\chi_\mu}{\delta^3} = \frac{-\omega}{\omega - Uk} \left(\frac{1}{2\text{Pr}} (T^2)_{rrr} + (TU_r^2)_r + \frac{kT}{\omega - Uk} (U_r T)_{rr} \right), \quad (5.5.8b)$$

where as mentioned in section 5.4.1 we have incorporated a power of ω in the definition of χ_μ compared to that of $\bar{\chi}_\mu$. Equation (5.5.6) is one of the main results of this chapter, and provides an effective impedance Z_{eff} to be applied to inviscid plug flow acoustics that accounts for the effect of the viscous boundary layer over a lining. The plot of the relative error between the asymptotic expression for Z_{eff} in (5.5.6) and the exact expression (5.1.3), fig. 5.1, shows that (5.5.6) is correct to the stated order of accuracy.

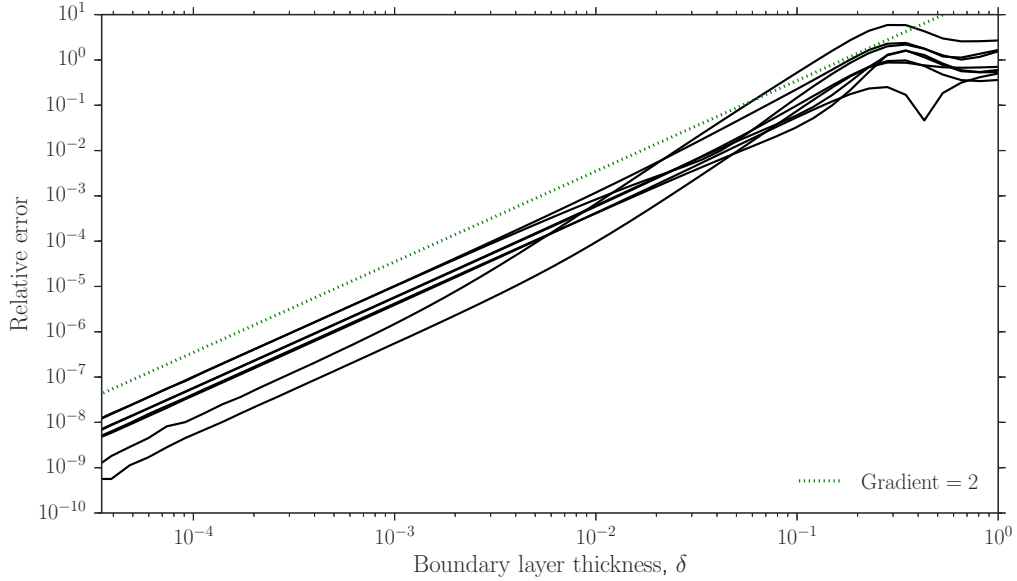


Figure 5.1. Relative error of Z_{eff} , defined as $|Z_{\text{eff}}(\tilde{p}_n(1)/\tilde{v}_n(1))/(\tilde{p}_u(1)/\tilde{v}_u(1)) - 1|$, calculated using (5.5.6) as compared to the analytical value found using (5.1.3). The ratio $Z = \tilde{p}_n(1)/\tilde{v}_n(1)$ is the boundary impedance as calculated from numerical solutions of the linearised Navier–Stokes equations (1.1.13), for $k = \pm 1 \pm i, \pm 1, \pm i$ and $\omega = 5, m = 0, M = 0.5, \text{Re} = 1/\delta^3$. The hyperbolic base flow (5.4.1) is used.

5.6 Results

To find duct modes of our new effective impedance boundary condition (5.5.6), we must first choose a model for the acoustic liner impedance. Here, we use a mass–spring–damper boundary with a mass d , spring constant b and damping coefficient R , which gives the impedance

$$Z(\omega) = i\omega d - ib/\omega + R. \quad (5.6.1)$$

The dispersion relation to be satisfied is then

$$Z_{\text{eff}}(Z) = \frac{\tilde{p}_u(1)}{\tilde{v}_u(1)} = (\omega - Mk) \frac{J_m(\alpha)}{i\alpha J'_m(\alpha)}, \quad (5.6.2)$$

to find values of k (or ω) when ω (or k) is specified (given m). This relation comes from our definition of the effective impedance as that impedance seen by the uniform flow inviscid solution at the wall. The function $Z_{\text{eff}}(Z)$ is the asymptotic effective impedance found using (5.5.6) with the boundary impedance Z from (5.6.1) as input. Examples of existing effective impedance boundary conditions are the Myers boundary condition (Ingard, 1959; Myers, 1980), which may be written

$$Z_{\text{eff}} = \frac{\omega}{\omega - Mk} Z, \quad (5.6.3)$$

and its first order correction (Brambley, 2011b) (called the modified Myers condition here),

$$Z_{\text{eff}} = \frac{\omega}{\omega - Mk} \frac{Z - \frac{i}{\omega}(\omega - Mk)^2 \delta I_0}{1 + i(k^2 + m^2) \frac{\omega Z}{(\omega - Mk)^2} \delta I_1}, \quad (5.6.4)$$

where δI_0 and δI_1 are as defined in (5.5.8). We will compare the new boundary condition (5.5.6) against these existing conditions, as well as against numerical solutions of the LNSE. As a way to test the importance of including the viscous sublayer in our asymptotic model, we will also

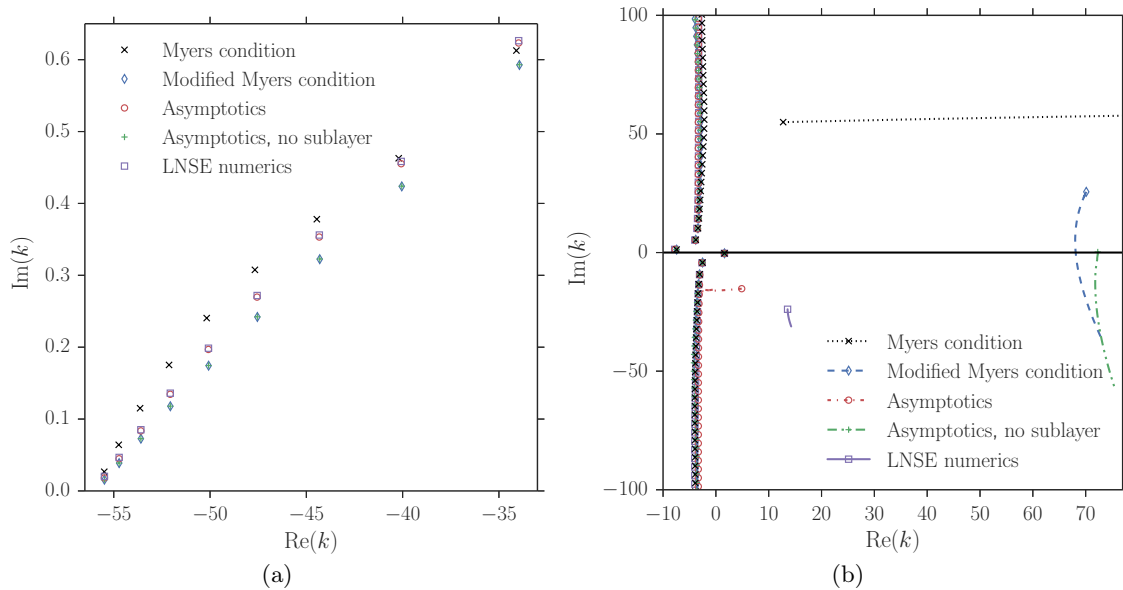


Figure 5.1. Duct modes in the complex k -plane of the Myers boundary condition (5.6.3), the modified Myers boundary condition (5.6.4), the new two-deck asymptotic condition (5.5.6), the one-deck (no sublayer) simplification of the new condition (5.6.5) and numerical solution of the LNSE (1.1.13). (a) shows upstream cut-on modes for each model, with $\omega = 28$, $m = 0$, $M = 0.5$, $\delta = 2 \times 10^{-3}$, and $\text{Re} = 5 \times 10^6$; (b) shows cut-off modes and one surface wave mode for each model, with $\omega = 5$, $m = 0$, $M = 0.5$, $\delta = 2 \times 10^{-3}$, and $\text{Re} = 2.5 \times 10^5$. Mode tracks follow the surface wave modes as $\text{Im}(\omega)$ is reduced from zero to $\text{Im}(\omega) \approx -8$ with $\text{Re}(\omega) = 5$ held fixed. In both (a) and (b), the boundary impedance is a mass–spring–damper (5.6.1) with mass $d = 0.15$, spring constant $b = 1.15$ and damping $R = 3$. The base flow (5.4.1) is used.

compute results using the boundary condition

$$Z_{\text{eff}} = \frac{\omega}{\omega - Mk} \frac{Z - \frac{i}{\omega}(\omega - Mk)^2 \delta I_0 + \frac{(\gamma-1)^2}{i\omega \text{Re}} \frac{I_\mu}{\delta^2}}{1 + i(k^2 + m^2) \frac{\omega Z}{(\omega - Mk)^2} \delta I_1}, \quad (5.6.5)$$

which is the effective impedance that would be obtained if the main boundary layer solutions were used to compute the boundary impedance, $\tilde{p}_m(0)/\tilde{v}_m(0) = Z$ (arguments in terms of y), rather than the viscous sublayer solutions. (That is, the Z_{eff} of a one-deck weakly viscous boundary layer above a lining.)

5.6.1 Wavenumber spectra

In fig. 5.1 a frequency is specified and (5.6.2) is solved to find allowed values of the axial wavenumber k . Figure 5.1a shows the upstream propagating cut-on modes for the new asymptotic model with, (5.5.6), and without, (5.6.5), the viscous sublayer, the Myers condition (5.6.3), the modified Myers boundary condition (5.6.4), and the viscous numerics (1.1.13). The damping of these propagating modes is predicted poorly by the Myers condition, which can lead to large errors in sound attenuation computations (up to 14dB (Gabard, 2013)) due to the effect of the nonzero boundary layer thickness. The new boundary condition (5.5.6) is shown to predict the damping of these modes well, and certainly better than the inviscid modified Myers condition, indicating that viscosity can play an important role in attenuation predictions. Figure 5.1a also shows the importance of calculating the contribution to the sound attenuation of the viscous sublayer: the one-deck weakly viscous model (5.6.5) predicts cut-on modes that are only marginally different to those of the inviscid modified Myers condition.

Figure 5.1b shows a surface wave mode for each model (those modes which exist only close to the lining). The two existing inviscid boundary conditions have surface wave modes in the upper half

k -plane, while the new boundary condition predicts a surface wave mode in the lower half k -plane, close to the real LNSE mode. The change in sign of $\Im m(k)$ between the inviscid and viscous surface modes has important ramifications for the flow stability. By plotting Briggs–Bers trajectories of the surface wave modes (shown in the same figure) where $\Re(\omega) = 5$ is held fixed and $\Im m(\omega)$ is reduced from zero, the stability may be investigated. Figure 5.1b shows the modified Myers surface mode crossing the real axis, indicating that the mode is convectively unstable. The surface modes of the new asymptotic boundary condition and the full LNSE are seen to remain in the lower half k -plane as $\Im m(\omega)$ is varied; thus the inviscid convective instability is stabilised by viscosity in the boundary layer. The surface mode of the one-deck model (5.6.5) is closer to the real axis than the modified Myers surface mode, but remains in the upper half plane; the plotted Briggs–Bers trajectory of the one-deck boundary condition mode, which crosses the real axis, therefore indicates that the convective instability is also present for this model. Thus, resolving the viscous sublayer has important ramifications for the stability of the boundary layer. The Briggs–Bers stability criteria cannot be applied for the Myers condition (Brambley, 2009).

5.6.2 Temporal stability

In contrast with the previous section, here we pick a real k and solve (5.6.2) for $\omega(k)$. The temporal growth rate of such a mode is given by $-\Im m(\omega)$. In fig. 5.2 the temporal stability of complex-frequency duct modes is investigated as k , real, is varied for the LNSE and the asymptotic boundary condition (5.5.6). Several stable modes can be seen in the upper right of the plot—these are representative of other stable modes outside of the plotted domain. The important modes for stability are those below the horizontal axis, as these are unstable. The unstable LNSE mode has a growth rate that increases to a maximum value (a characteristic growth rate of instability) before decreasing and finally restabilising for large, finite k . The unstable root for the asymptotic solution follows a qualitatively similar path until the point labelled ‘B’ on fig. 5.2. To the left of ‘B’, the asymptotic mode has a bounded growth rate. This suggests that the boundary condition (5.5.6) retains the regularisation – obtained in previous inviscid modified Myers boundary conditions by including a finite-thickness layer of shear – of the Myers condition vortex sheet instability (inherent in approximations ignoring $\mathcal{O}(\delta)$ terms). To the right of ‘B’ the asymptotic solution supports no unstable modes.

Figure 5.3 displays a diagnosis of the point ‘B’. As the asymptotic solution approaches the point ‘B’ from the left, the value of $|\omega - U(r)k|$ tends to zero, see fig. 5.3a. This is precisely the inviscid critical layer r_c , for which $\omega/k = U(r_c)$ and the perturbations are perfectly convected with the flow (Brambley *et al.*, 2012b). Close to the critical layer, the integrals I_μ and I_1 blow up (see fig. 5.3b), causing unphysical discontinuities in the acoustic solutions. Figure 5.4a shows the results of increasing the resolution of the numerical integration used to find these solutions. With higher numerical resolution of the integrals, the unstable asymptotic mode can be tracked closer to the real axis and stability, and closer to the critical layer. This adds weight to our conclusion that the unstable mode disappears into the critical layer at the point B .

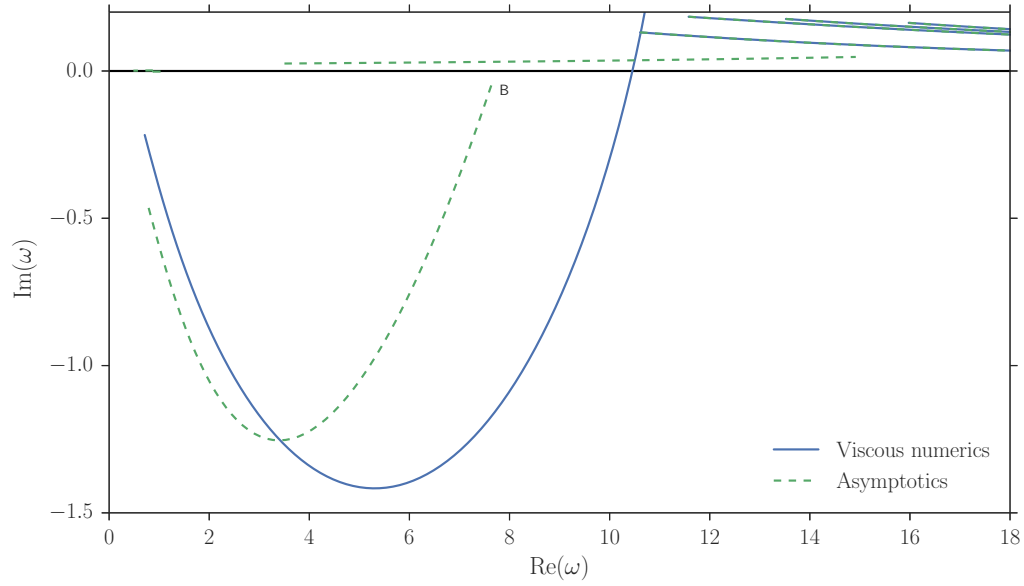


Figure 5.2. Modes in the ω plane as k , real, is increased, for LNSE numerics (solid) and the asymptotic solution (5.5.6) (dashed). The point labelled ‘B’ is where the regular unstable solution branch breaks down. Parameters are $m = 0$, $M = 0.5$, $\text{Re} = 7 \times 10^6$, $\delta = 5 \times 10^{-3}$, with a mass-spring-damper impedance (5.6.1) with mass $d = 0.15$, spring constant $b = 1.15$ and damping $R = 3$. The base flow (5.4.1) is used.

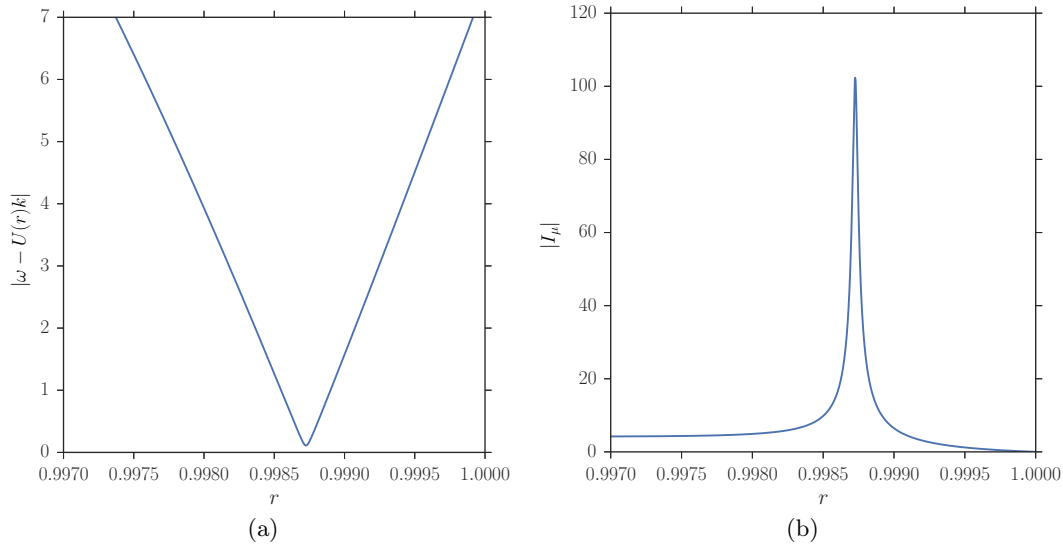


Figure 5.3. Evidence that the unstable solution in fig. 5.2 hits the critical layer at ‘B’. (a) $|\omega - U(r)k|$, and (b) $|I_\mu|$, for $(\omega, k) = (7.51 - 0.11i, 60.21)$, and for other parameters as in fig. 5.2

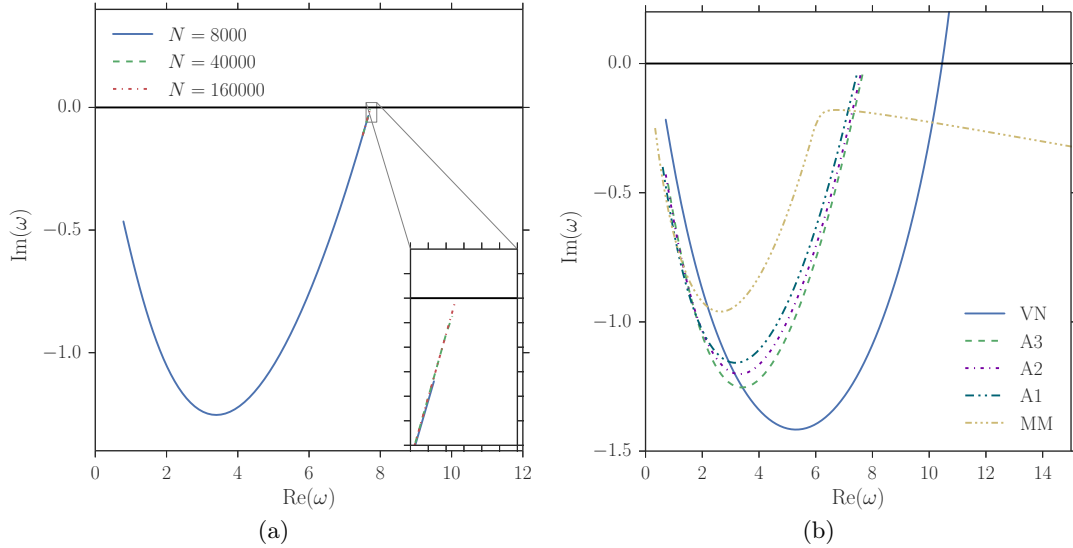


Figure 5.4. The behaviour of the unstable root in the ω -plane as k , real, is increased. (a) Results for the new asymptotic boundary condition (5.5.6) for three different discretisations, $N = 8000$, $N = 40000$, $N = 160000$. As the number of computational grid points is increased, the model is able to get closer to the inviscid critical layer $\omega - U(r_c)k = 0$, and the unstable mode is pushed closer to restabilisation, $\text{Im}(\omega) = 0$, before the solution breaks down. (b) Legend labels denote the viscous LNSE numerics (VN), the new asymptotic boundary condition (5.5.6) at $\mathcal{O}(\delta_{ac}^3)$ (A3), at $\mathcal{O}(\delta_{ac}^2)$ (A2), and at $\mathcal{O}(\delta_{ac})$ (A1), and the modified Myers condition (5.6.4) (MM). For both (a) and (b) all parameters as in fig. 5.2.

5.7 Suggestion of a time-domain formulation

In order to write down a simple time-domain formulation of the new asymptotic frequency-domain boundary condition (5.5.6), we choose to neglect high-order viscous terms that do not affect the qualitative behaviour of the boundary condition too acutely. Using the definition of the acoustic boundary layer thickness δ_{ac} from (5.4.6), we see that the S_j terms of (5.5.6), defined in (5.5.7), satisfy

$$S_j \sim \delta_{ac}^j. \quad (5.7.1)$$

Thus, retaining all three S_j terms means working to $\mathcal{O}(\delta_{ac}^3)$; neglecting only S_3 means working to $\mathcal{O}(\delta_{ac}^2)$; and neglecting both S_2 and S_3 means working to $\mathcal{O}(\delta_{ac})$. In all cases we retain the $\mathcal{O}(\delta)$ inviscid terms that account for the finite region of shear. Figure 5.4b shows the temporal stability plots for the three choices outlined above. Qualitatively, the behaviour of the $\mathcal{O}(\delta_{ac})$ form is the same as that of the $\mathcal{O}(\delta_{ac}^3)$ form. We choose, then, to forego the $\mathcal{O}(\delta_{ac}^3)$ in (5.5.6) in order to find the simplest time-domain formulation possible. (It transpires that the $\mathcal{O}(\delta_{ac}^2)$ terms do not add much complexity to the final formulation, so they are kept here for completeness.)

We choose a constant-then-linear mean flow profile with boundary layer thickness δ ,

$$U(r) = \begin{cases} U_0 \frac{(1-r)}{\delta}, & 1 - \delta \leq r \leq 1, \\ U_0, & 0 \leq r \leq 1 - \delta, \end{cases} \quad (5.7.2)$$

and a constant mean temperature and density, $T(r) = T_0$ and $\rho(r) = \rho_0$, respectively. This allows the boundary layer integrals I_j to be performed analytically:

$$\delta I_0 (\omega - U_0 k)^2 = \frac{2}{3} \delta U_0^2 k^2 - \delta U_0 k \omega, \quad \delta I_1 = \frac{\delta U_0 k}{\omega}, \quad \frac{I_\mu}{\delta^2} = 0. \quad (5.7.3)$$

Rearranging the effective impedance boundary condition (5.5.6) using (5.7.2) and (5.7.3), and

discarding the S_3 term as per the discussion in the previous paragraph, leads to

$$\left[\omega Z - \frac{U_0 k}{\delta \sqrt{\text{Re}}} \frac{Z}{\sqrt{i\omega}} + i\delta \rho_0 (U_0 k \omega - \frac{2}{3} U_0^2 k^2) + \omega Z S_2 \right] \tilde{v}_u = \left[(\omega - U_0 k) + i\delta U_0 k Z \frac{(k^2 + m^2)}{\rho_0 (\omega - U_0 k)} + (\omega - U_0 k) Z S_1 \right] \tilde{p}_u, \quad (5.7.4)$$

where the S_j terms simplify to

$$S_1 = \frac{1}{\sqrt{\text{Re}}} \left[\frac{(k^2 + m^2)}{\rho_0 (\omega - U_0 k)^2} U_0^2 k^2 \frac{1}{i\omega \sqrt{i\omega}} + \frac{1}{\sigma T_0} \sqrt{i\omega} - \frac{(k^2 + m^2)}{\rho_0} \frac{1}{i\omega \sqrt{i\omega}} \right], \quad (5.7.5a)$$

$$S_2 = \frac{1}{\delta^2 \text{Re}} \left[\frac{\sigma}{1 + \sigma} \frac{2U_0^2}{T_0} \frac{1}{i\omega} - \frac{5}{4} \frac{U_0^2 k^2}{\omega^2} \frac{1}{i\omega} \right]. \quad (5.7.5b)$$

To proceed, we follow Brambley & Gabard (2013) and Brambley & Gabard (2016) by introducing a number of new variables, the interpretation of which we leave until later. First, we appeal to the fact that \tilde{p}_u satisfies the inviscid linearised Euler equations in a uniform flow to make the substitution $k\tilde{p}_u/\rho_0(\omega - U_0 k) = \tilde{u}_u$. Then, we define $\tilde{v}_w = \tilde{p}_u/Z$ and $\tilde{v} = \tilde{v}_u/Z$, which arise when we divide (5.7.4) through by Z .

If in the frequency domain there exists a vector $\tilde{\mathbf{s}} = \tilde{\mathbf{u}}_u/i\omega$, where $\tilde{\mathbf{u}}_u = (\tilde{u}_u, \tilde{v}_u, \tilde{w}_u)$ is a vector of (the Fourier transform of) the acoustic velocity perturbations, then in the time domain

$$\frac{\partial \mathbf{s}'}{\partial t} = \mathbf{u}', \quad (5.7.6)$$

where a prime denotes an acoustic perturbation in the time domain. By (5.7.6) we may identify $\mathbf{s}' = (s'_1, s'_2, s'_3)$ as the acoustic displacement vector in the coordinate directions (x, r, θ) ; it follows that $\tilde{\mathbf{s}}$ is the frequency-domain Fourier transform of \mathbf{s}' . To deal with the fractional powers of ω , we introduce the fractional time-derivative operator $\partial_t^{\frac{1}{2}}$ (see, e.g., Beyer & Kempfle, 1995), which has the Fourier transform property

$$\mathcal{F}\{\mathbf{s}'\} = \tilde{\mathbf{s}} \quad \implies \quad \mathcal{F}\left\{\partial_t^{\frac{1}{2}} \mathbf{s}'\right\} = \sqrt{i\omega} \tilde{\mathbf{s}}. \quad (5.7.7)$$

Using (5.7.6) and (5.7.7) and the definitions in the previous paragraph, (5.7.4) may be written in the time-domain as

$$\begin{aligned} \frac{\partial v'}{\partial t} &= \left(\frac{\partial}{\partial t} + \mathbf{U}_0 \cdot \nabla \right) v_w + \delta \mathbf{U}_0 \cdot (\nabla_{\perp}^2 \mathbf{u}') + \delta \rho_0 \mathbf{U}_0 \cdot \nabla \left(\frac{\partial}{\partial t} + \frac{2}{3} \mathbf{U}_0 \cdot \nabla \right) v \\ &\quad - \frac{1}{\delta \sqrt{\text{Re}}} \mathbf{U}_0 \cdot \nabla \left(\partial_t^{\frac{1}{2}} s'_2 \right) + \frac{1}{\sqrt{\text{Re}}} \left\{ (\mathbf{U}_0 \cdot \nabla) \mathbf{U}_0 \cdot \nabla_{\perp}^2 \left(\partial_t^{\frac{1}{2}} \mathbf{e}' \right) \right. \\ &\quad \left. + \frac{1}{\sigma T_0} \left(\frac{\partial}{\partial t} + \mathbf{U}_0 \cdot \nabla \right) \left(\partial_t^{\frac{1}{2}} p' \right) + \frac{1}{\rho_0} \left(\frac{\partial}{\partial t} + \mathbf{U}_0 \cdot \nabla \right) \nabla_{\perp}^2 \left(\partial_t^{\frac{1}{2}} \phi' \right) \right\} \\ &\quad - \frac{1}{\delta^2 \text{Re}} \left\{ \frac{\sigma}{1 + \sigma} \frac{2}{T_0} |\mathbf{U}_0|^2 v' + \frac{5}{4} (\mathbf{U}_0 \cdot \nabla)^2 e'_2 \right\}, \end{aligned} \quad (5.7.8)$$

where ∇_{\perp} gives the gradient normal to the wall, and

$$\frac{\partial f'}{\partial t} = p', \quad \frac{\partial \phi'}{\partial t} = f', \quad \frac{\partial \mathbf{e}'}{\partial t} = \mathbf{s}', \quad (5.7.9)$$

and \mathbf{s}' is defined in (5.7.6). The subscript on the s'_j and e'_j scalars refer to the j th component of

the \mathbf{s}' and \mathbf{e}' vectors, respectively. Thus,

$$\frac{\partial e'_2}{\partial t} = s'_2, \quad \text{and} \quad \frac{\partial s'_2}{\partial t} = v', \quad (5.7.10)$$

as v' is the second component of the time-domain acoustic velocity vector \mathbf{u}' . Note that these new variables \mathbf{s} , \mathbf{e} , ν , v_w and ϕ are only ever needed on the lining at $r = 1$.

The physical interpretation of v_w and ν (of which \tilde{v}_w and $\tilde{\nu}$ are the Fourier transforms) is contained within the time domain boundary model (Brambley & Gabard, 2016). If v_w is the wall-normal velocity response of the wall due to an acoustic pressure p' through the impedance model $\mathcal{B}(p')$, then ν is the response through the same impedance model forced by the normal fluid velocity, $\mathcal{B}(v')$. For the mass–spring–damper model (5.6.1) that we have employed in previous sections of this chapter, v_w and ν satisfy

$$\frac{\partial v_w}{\partial t} = \frac{1}{d} [p' - b\psi - Rv_w], \quad \frac{\partial \psi}{\partial t} = v_w, \quad (5.7.11a)$$

$$\frac{\partial \nu}{\partial t} = \frac{1}{d} [v' - b\zeta - R\nu], \quad \frac{\partial \zeta}{\partial t} = \nu. \quad (5.7.11b)$$

The study of lossy waves in the time domain often leads to wave equations with fractional time derivatives (Carcione *et al.*, 2002; Holm & Näsholm, 2011). Therefore the appearance of the operator $\partial_t^{\frac{1}{2}}$ in (5.7.8) is expected, due to the inclusion of viscous and thermal dissipation. An implementation of the proposed time-domain formulation is left for future work, although it is hypothesised that a combination of the method used in Brambley & Gabard (2016) and the Grünwal–Letnikov finite difference scheme for the non-integer order derivatives (see, e.g., Scherer *et al.*, 2011) might be profitable.

5.8 Summary

The sheared and viscous boundary layer in a cylindrical acoustically lined duct was modelled as a two-deck system: a thick main layer with a weak viscosity; and a thin sublayer in which the mean flow is expanded about its wall value and viscosity balances inertia to enforce no slip. The scaled governing equations in each layer were analytically tractable, and allowed the asymptotic matching of solutions through to an inviscid uniform flow outside the boundary layer. In this way, a closed-form expression for the effective impedance was found, incorporating shear and viscosity and applicable in the frequency domain to a plug flow.

The temporal stability of the new boundary condition was shown to be well behaved away from the inviscid critical layer (which affects the weakly viscous main boundary layer), and with this as justification a time domain formulation of the two-deck effective impedance boundary condition was proposed.

In the final chapter, the attenuation properties of the asymptotic impedance boundary conditions derived in the current chapter and in chapters 2 and 4 are investigated via the test case of the reflection of an incident plane wave.

Appendix

5.A Determining the sublayer scaling

We imagine a thin sublayer, of thickness δ_{ac} , very close to the wall. We rescale into this sublayer from r -space via $r = 1 - \delta_{ac}z$, where z is the sublayer variable. We posit that y (the main boundary layer variable) and z are related by $y = \varepsilon z$, with $\varepsilon \ll 1$ to be determined.

Inside the sublayer, viscous and inertial terms must balance in order for viscous boundary conditions to be satisfied at the wall. The relevant terms in the linearised Navier–Stokes axial momentum equation are

$$i\rho(\omega - Uk)\tilde{u} \quad \text{and} \quad \frac{\gamma - 1}{\text{Re}}(T\tilde{u}_r)_r. \quad (5.A.1)$$

We want these two terms to balance the leading order of the sublayer governing axial momentum equation. Close to the wall, the base flow variables may be expanded for small y as

$$U(y) \sim yU'(0) + \mathcal{O}(y^2), \quad T(y) \sim T(0) + \mathcal{O}(y^2), \quad (5.A.2)$$

where we have used the no slip and isothermal boundary conditions $U(0) = 0$, $T'(0) = 0$. Using (5.A.2) in (5.A.1) and asserting that the leading order must balance we find

$$i\omega\tilde{u} \sim \frac{(\gamma - 1)^2 T(0)^2}{\delta_{ac}^2 \text{Re}} \tilde{u}_{zz}, \quad (5.A.3)$$

where we have written the r derivatives in terms of the sublayer variable z . The combination $(\gamma - 1)^2 T(0)^2$ is $\mathcal{O}(1)$: $(\gamma - 1) = 1/T_0$ is the reciprocal of the dimensionless centreline base temperature; the ratio $T(0)/T_0 \simeq 1.15$ for a compressible Blasius boundary layer. Thus we are left with

$$\omega\tilde{u} \sim \frac{1}{\delta_{ac}^2 \text{Re}} \tilde{u}_{zz}, \quad (5.A.4)$$

from which we may identify $\delta_{ac}^2 \sim 1/\omega \text{Re}$. This is the classical acoustic boundary layer scaling. We know that $\varepsilon\delta \sim \delta_{ac}$ from the relationships between r , y and z . We also know $\delta \sim 1/\text{Re}^{1/3}$ from our choice of main boundary layer scaling. Thus, we may define

$$\frac{1}{\text{Re}} = \xi\omega^3\varepsilon^6 \quad (5.A.5)$$

or equivalently $\varepsilon = \sqrt{\delta/\omega}$. The $\mathcal{O}(1)$ quantity ξ is the same as in (5.2.1). Relative to the main boundary layer the sublayer scales as $\varepsilon \sim \text{Re}^{-1/6}$, while relative to the duct it scales as $\varepsilon\delta \sim \text{Re}^{-1/2}$ which is the Blasius boundary layer scaling.

5.B Solving inside the sublayer

Here we show the details of the solution of the sublayer governing equations (5.3.3). Solving at leading order:

$$\tilde{v}_{0z} = 0 \quad \implies \tilde{v}_0 = A_0, \quad (5.B.1a)$$

$$\hat{u}_{0zz} - \eta^2 \hat{u}_0 = \frac{iU'}{\omega} \eta^2 \tilde{v}_0 \quad \implies \hat{u}_0 = B_0 e^{-\eta z} + C_0 e^{\eta z} - \frac{iU'}{\omega} A_0, \quad (5.B.1b)$$

$$\frac{1}{\text{Pr}} \hat{T}_{0zz} - \eta^2 \hat{T}_0 = 0 \quad \implies \hat{T}_0 = D_0 e^{-\sigma \eta z} + E_0 e^{\sigma \eta z}, \quad (5.B.1c)$$

$$\tilde{p}_{0z} = 0 \quad \Longrightarrow \quad \tilde{p}_0 = P_0, \quad (5.B.1d)$$

$$\tilde{w}_{0zz} - \eta^2 \tilde{w}_0 = -\frac{m}{\omega}(\gamma - 1)T\eta^2 \tilde{p}_0 \quad \Longrightarrow \quad \tilde{w}_0 = G_0 e^{-\eta z} + H_0 e^{\eta z} + \frac{m}{\omega}(\gamma - 1)TP_0, \quad (5.B.1e)$$

where A_j , P_j , B_j , C_j , D_j , E_j , G_j , and H_j are constants of integration. In the sublayer we want to satisfy no slip at the boundary $z = 0$ and match to the main boundary layer in the limit $z \rightarrow \infty$. Solutions that grow exponentially in z are therefore not allowed; $C_0 = E_0 = H_0 = 0$, and similarly at all orders. No slip and isothermal wall conditions give

$$B_0 = \frac{iU'}{\omega}A_0, \quad D_0 = 0, \quad G_0 = -\frac{m}{\omega}(\gamma - 1)TP_0. \quad (5.B.2)$$

At first order we find

$$\tilde{v}_1 = A_1 + a_0 e^{-\eta z} + a_1 z, \quad (5.B.3)$$

where

$$a_0 = \frac{ik}{\eta}B_0 = -\frac{kU'}{\omega\eta}A_0, \quad a_1 = ikB_0 = -\frac{kU'}{\omega}A_0. \quad (5.B.4)$$

Then,

$$\hat{u}_1 = b_0 + b_1 z + (B_1 + b_2 z + b_3 z^2)e^{-\eta z}, \quad (5.B.5)$$

$$\hat{T}_1 = D_1 e^{-\sigma\eta z} + d_0 z + d_1 e^{-\eta z}, \quad (5.B.6)$$

where

$$b_0 = -\frac{iU'}{\omega}A_1, \quad b_1 = -\frac{iU''}{\omega}A_0, \quad b_2 = \frac{3}{4}\frac{ikU'^2}{\omega^2}A_0, \quad b_3 = \frac{ikU'^2}{4\omega^2}\eta A_0, \\ d_0 = -\frac{iT''}{\omega}A_0, \quad d_1 = \frac{\text{Pr}}{1 - \text{Pr}}\frac{2iU'^2}{\omega\eta}A_0, \quad D_1 = -d_1.$$

No slip forces $B_1 = -b_0$. The first-order pressure contribution is $\tilde{p}_1 = P_1$. Higher orders of the azimuthal velocity \tilde{w} are not required to calculate \tilde{p} and \tilde{v} to the desired order.

At second order,

$$\tilde{v}_2 = A_2 + a_2 z + a_3 z^2 + (a_4 + a_5 z + a_6 z^2)e^{-\eta z} + a_7 e^{-\sigma\eta z} \quad (5.B.7)$$

where

$$a_2 = -ikb_0, \quad a_3 = -\frac{kU''}{2\omega}A_0, \quad a_4 = \left(-\frac{5}{4}\frac{k^2U'^2}{\omega^2\eta^2} - \frac{\text{Pr}}{1 - \text{Pr}}\frac{2U'^2}{\eta^2 T}\right)A_0 + \frac{ik}{\eta}B_1, \\ a_5 = -\frac{5}{4}\frac{k^2U'^2}{\omega^2\eta}A_0, \quad a_6 = -\frac{k^2U'^2}{4\omega^2}A_0, \quad a_7 = \frac{\text{Pr}}{1 - \text{Pr}}\frac{2U'^2}{\sigma\eta^2 T}A_0.$$

Then,

$$\hat{u}_2 = b_4 + b_5 z + b_6 z^2 + (B_2 + b_7 z + b_8 z^2 + b_9 z^3 + b_{10} z^4)e^{-\eta z} + b_{11} e^{-\sigma\eta z}, \quad (5.B.8)$$

$$\hat{T}_2 = d_2 + d_3 z + d_4 z^2 + (d_5 + d_6 z + d_7 z^2)e^{-\eta z} + (D_2 + d_8 z + d_9 z^2)e^{-\sigma\eta z}, \quad (5.B.9)$$

where

$$b_4 = \left(-\frac{iU'T''}{\omega\eta^2 T} - \frac{iU'''}{\omega\eta^2}\right)A_0 + k(\gamma - 1)TP_0 - \frac{iU'}{\omega}A_2, \quad b_5 = -\frac{iU''}{\omega}A_1, \\ b_6 = -\frac{iU'''}{2\omega}A_0, \quad b_7 = \left(\frac{41}{32}\frac{ik^2U'^3}{\omega^3\eta} + \frac{3}{8}\frac{ikU'U''}{\omega^2\eta}\right)A_0 + \frac{3kU'}{4\omega}B_1,$$

$$\begin{aligned}
 b_8 &= \left(\frac{21}{32} \frac{ik^2U'^3}{\omega^3} + \frac{3}{8} \frac{ikU'U''}{\omega^2} \right) A_0 + \frac{kU'\eta}{4\omega} B_1, \\
 b_9 &= \left(\frac{11}{48} \frac{ik^2U'^3}{\omega^3} \eta + \frac{ikU'U''}{12\omega^2} \eta + \frac{iU'T''}{6\omega T} \eta \right) A_0, & b_{10} &= \frac{ik^2U'^3}{32\omega^3} \eta^2 A_0, \\
 b_{11} &= -\frac{\text{Pr}}{1 - \text{Pr}} \frac{2iU'^3}{\omega\sigma\eta^2 T} A_0,
 \end{aligned}$$

with no slip giving $B_2 = -(b_4 + b_{11})$; and

$$\begin{aligned}
 d_2 &= \left(-\frac{2iU'U''}{\omega\eta^2} - \frac{iT'''}{\text{Pr}\omega\eta^2} \right) A_0 + (\gamma - 1)T\omega P_0, & d_3 &= -\frac{iT'''}{\omega} A_1, & d_4 &= -\frac{iT'''}{2\omega} A_0, \\
 d_5 &= \frac{\text{Pr}}{(1 - \text{Pr})^2} \left(\frac{5 + 3\text{Pr}}{2} \frac{ikU'^3}{\omega^2\eta^2} + \frac{4iU'U''}{\omega\eta^2} - \frac{2ikU'T''}{\omega^2\eta^2} \right) A_0 + \frac{\text{Pr}}{1 - \text{Pr}} \frac{2U'}{\eta} B_1, \\
 d_6 &= \frac{\text{Pr}}{1 - \text{Pr}} \left(\frac{5}{2} \frac{ikU'^3}{\omega^2\eta} - \frac{ikU'T''}{\omega^2\eta} + \frac{2iU'U''}{\omega\eta} \right) A_0, & d_7 &= \frac{\text{Pr}}{1 - \text{Pr}} \frac{ikU'^3}{2\omega^2} A_0, \\
 d_8 &= -\frac{\text{Pr}}{1 - \text{Pr}} \frac{ikU'^3}{2\omega^2\eta} A_0, & d_9 &= -\frac{\text{Pr}\sigma}{1 - \text{Pr}} \frac{ikU'^3}{2\omega^2} A_0,
 \end{aligned}$$

with $D_2 = -(d_2 + d_5)$ from the boundary condition at $z = 0$. For the pressure we find $\tilde{p}_2 = P_2$.

At third order we find

$$\begin{aligned}
 \tilde{v}_3 &= A_3 + a_8z + a_9z^2 + a_{10}z^3 + (a_{11} + a_{12}z + a_{13}z^2 + a_{14}z^3 + a_{15}z^4)e^{-\eta z} + \\
 &\quad (a_{16} + a_{17}z + a_{18}z^2)e^{-\sigma\eta z}, \tag{5.B.10}
 \end{aligned}$$

$$\tilde{p}_3 = P_3 + \frac{i\omega^2}{(\gamma - 1)T} A_0 z. \tag{5.B.11}$$

The constants are defined by

$$\begin{aligned}
 a_8 &= \left(i\omega^2 - i(k^2 + m^2)(\gamma - 1)T \right) P_0 - \left(\frac{T'''}{\eta^2 \text{Pr} T} \right. \\
 &\quad \left. + \frac{2U'U''}{\eta^2 T} + \frac{kT''U'}{\eta^2 \omega T} + \frac{kU'''}{\eta^2 \omega} - \omega \right) A_0 - \frac{kU'}{\omega} A_2, \\
 a_9 &= -\frac{kU''}{2\omega} A_1, & a_{10} &= -\frac{kU'''}{6\omega} A_0,
 \end{aligned}$$

$$\begin{aligned}
 a_{11} &= -A_0 U' \left(\frac{151k^3U'^2}{32\eta^3\omega^3} + \frac{13k^2U''}{8\eta^3\omega^2} + \frac{k\text{Pr}((\text{Pr} - 3)T'' + 4U'^2)}{\eta^3(\text{Pr} - 1)^2 T\omega} \right. \\
 &\quad \left. - \frac{2(\text{Pr} - 3)\text{Pr}U''}{\eta^3(\text{Pr} - 1)^2 T} \right) + 8i\eta(\text{Pr} - 1)\omega^2 \left(B_1 U' \left[5k^2(\text{Pr} - 1)T \right. \right. \\
 &\quad \left. \left. - \frac{\text{Pr}}{4\eta^3(\text{Pr} - 1)^2 T\omega} \right] + \frac{B_2 k - (\gamma - 1)m^2 P_0 T}{8\eta^2(\text{Pr} - 1)\omega^2} \right),
 \end{aligned}$$

$$\begin{aligned}
 a_{12} &= U' \left(\frac{k \left(A_0 \text{Pr} (6U'^2 - 4T'') + \frac{5iB_1 k}{32\eta\omega^3} \right)}{4\eta^2(\text{Pr} - 1)T\omega} - \frac{151A_0 k^3 U'^2}{32\eta^2\omega^3} \right. \\
 &\quad \left. - \frac{13A_0 k^2 U''}{8\eta^2\omega^2} + \frac{2A_0 \text{Pr} U''}{\eta^2(\text{Pr} - 1)T} \right),
 \end{aligned}$$

$$a_{13} = kU' \left(8\omega^2 \left(\frac{A_0(-\text{Pr}T'' + \text{Pr}U'^2 + T''')}{16\eta(\text{Pr} - 1)T\omega^3} + \frac{iB_1 k}{32\omega^3} \right) - \frac{55A_0 k^2 U'^2}{32\eta\omega^3} - \frac{5A_0 k U''}{8\eta\omega^2} \right),$$

$$a_{14} = -\frac{A_0 k U'}{48T\omega^3} (17k^2 T U'^2 + 4k T U'' \omega + 8T'' \omega^2), \quad a_{15} = -\frac{A_0 \eta k^3 U'^3}{32\omega^3},$$

$$a_{16} = -\frac{3A_0\eta^3 kTU^3\omega}{2(\text{Pr}-1)} + \frac{iD_2\eta^5 T\omega^3}{\sigma}, \quad a_{17} = -\frac{\sigma}{1-\text{Pr}} \frac{A_0 kU^3}{2\eta^2 T\omega},$$

$$a_{18} = \frac{\text{Pr}}{1-\text{Pr}} \frac{A_0 kU^3}{2\eta T\omega}.$$

5.C Details of the viscous sublayer–main boundary layer matching

One important thing to note, which becomes clear when studying (5.3.8), is that the error term $\mathcal{O}(\varepsilon^{2+2\lambda})$ in (5.3.8a) has no analogue in (5.3.8b). In fact, if you were to solve for the pressure to $\mathcal{O}(\varepsilon^4)$ in the sublayer, there would exist a term $\propto \varepsilon^4 z^2$; written in terms of the intermediate matching variable τ , (5.3.7), this would become $\propto \varepsilon^{2+2\lambda}\tau^2$. We must, however, choose a point to stop our expansions—we do not want to solve to $\mathcal{O}(\varepsilon^4)$ in order to match an error term. Although it is not true that $\varepsilon^{2+2\lambda} \ll \varepsilon^3$ in general, and hence keeping $\mathcal{O}(\varepsilon^3)$ terms whilst neglecting $\mathcal{O}(\varepsilon^{2+2\lambda})$ seems counter-intuitive, the $\mathcal{O}(\varepsilon^{2+2\lambda})$ error term is artificial, created by truncating the expansion of the base flow at a certain point. When forming a composite solution, we would be able to identify that the truncated sequence

$$\omega - \varepsilon U'(0)kz - \frac{\varepsilon^2}{2}U''(0)kz^2 + \mathcal{O}(\varepsilon^3) \quad (5.C.1)$$

is actually the inner expansion of the convective term $(\omega - Uk)$ and is not, despite what (5.C.1) forecasts, the source of an $\mathcal{O}(\varepsilon^3)$ error. (In fact, for the acoustic pressure it must be the case that the sublayer solution is exactly the near-wall expansion of the main boundary layer solution, as both are inviscid at all retained orders.)

The subtlety of this issue is shown more clearly by dissecting the \tilde{v} expansions in the limit $\varepsilon \rightarrow 0$ with τ held fixed,

$$\tilde{v}_{m,0}^{(I)} = \omega \bar{A}_0 - \varepsilon^\lambda \tau k U'(0) \bar{A}_0 - \varepsilon^{2\lambda} \tau^2 \frac{kU''(0)}{2} \bar{A}_0 - \varepsilon^{3\lambda} \tau^3 \frac{kU'''(0)}{6} \bar{A}_0 + \mathcal{O}(\varepsilon^{4\lambda}), \quad (5.C.2a)$$

$$\begin{aligned} \delta \tilde{v}_{m,1}^{(I)} = & \varepsilon^2 \omega^2 \bar{A}_1 + \varepsilon^{2+\lambda} \tau \left\{ \omega^2 \bar{A}_0 - kU'(0)\omega \bar{A}_1 + i\omega^2 \bar{P}_0 - i \frac{k^2 + m^2}{\rho(0)} \bar{P}_0 \right. \\ & + i\xi(\gamma - 1)^2 T(0)^2 \omega \bar{A}_0 \left(\frac{kU'''(0)}{\omega} + \frac{kT''(0)U'(0)}{\omega T(0)} + \frac{2U'(0)U''(0)}{T(0)} \right. \\ & \left. \left. + \frac{1}{\text{Pr}} \frac{T'''(0)}{T(0)} \right) \right\} + \mathcal{O}(\varepsilon^{2+2\lambda}), \end{aligned} \quad (5.C.2b)$$

for the main boundary layer solution, and

$$\tilde{v}_{s,0}^{(O)} = A_0, \quad (5.C.3a)$$

$$\varepsilon \tilde{v}_{s,1}^{(O)} = \varepsilon^\lambda \tau a_1 + \varepsilon A_1, \quad (5.C.3b)$$

$$\varepsilon^2 \tilde{v}_{s,2}^{(O)} = \varepsilon^{2\lambda} \tau^2 a_3 + \varepsilon^{1+\lambda} \tau a_2 + \varepsilon^2 A_2, \quad (5.C.3c)$$

$$\varepsilon^3 \tilde{v}_{s,3}^{(O)} = \varepsilon^{3\lambda} \tau^3 a_{10} + \varepsilon^{1+2\lambda} \tau^2 a_9 + \varepsilon^{2+\lambda} \tau a_8 + \varepsilon^3 A_3, \quad (5.C.3d)$$

for the sublayer solution. The $\mathcal{O}(\varepsilon^{4\lambda})$ error in (5.C.2a) that seems to be unaccounted for in (5.C.3) is duly of the form described in (5.C.1); it is less clear from (5.C.2b), but the $\mathcal{O}(\varepsilon^{2+2\lambda})$ error has the same origin. Thus, while $\varepsilon^{4\lambda} \gg \varepsilon^{2+2\lambda}$ necessarily, and while it is not true in general that $\varepsilon^{4\lambda} \ll \varepsilon^3$ and $\varepsilon^{2+2\lambda} \ll \varepsilon^3$, a composite solution or effective impedance boundary condition utilising the two expansions (5.2.12) and (5.3.5) would not be liable to have errors of $\mathcal{O}(\varepsilon^{4\lambda})$ for

an unknown $\lambda \in (0, 1)$. This is supported by comparison with numerical solutions of the linearised Navier–Stokes equations.

Chapter 6

A study of the attenuation properties of various boundary models via plane wave reflection coefficients

It is important for acoustic engineers to know how well acoustic liners attenuate sound in a non-quiescent fluid. It is therefore vital that a simplified acoustic boundary condition for use in plug flow (that incorporates the effects of the thin boundary layer into an effective impedance of the liner) has the correct attenuation properties. Gabard (2013) tested existing inviscid impedance boundary conditions by the benchmark problem of a plane wave incident on a shear layer above a lined wall. Numerical solutions of the Pridmore-Brown (1958) equation were compared with analytical expressions for the reflection coefficients obtained using the Myers boundary condition (Ingard, 1959; Myers, 1980) and its various first order corrections Brambley (2011*b*); Rienstra & Darau (2011). It was found that the finite thickness of the boundary layer can be significant, and that use of the Myers condition can lead to large errors in sound attenuation predictions (Gabard, 2013). Chapter 3 of this thesis has shown that viscosity and thermal conduction can play a large role in the damping rate of cut-on modes and the physical onset of instability; investigating their effects on the attenuation of sound via the calculation of reflection coefficients is a worthwhile supplement to the data presented there.

In this chapter, the work of Gabard (2013) is extended to include viscothermal effects in the sheared boundary layer above a lined wall. Numerical solutions of linearised compressible Navier–Stokes equations are presented and the reflection coefficients calculated and compared to the corresponding inviscid results. In addition to this, the analytical expressions for the reflection coefficients of the asymptotic closed-form effective impedance boundary conditions derived in chapters 2, 4 and 5 are derived and compared to the numerics.

6.1 Mathematical formulation

We consider a Cartesian coordinate system $\mathbf{x} = (x, y, z)$ with a mean flow $\mathbf{U} = (U(y), 0, 0)$ above a lined wall situated at $y = 0$ for all x and z . Above some point $y \sim \delta > 0$, the mean flow is uniform, such that $U(y) = M$ for $y \gtrsim \delta$. Below this point, the mean flow follows some sheared profile down to the wall upon which no slip is satisfied.

In the uniform flow region, the acoustic velocity potential, ϕ' , satisfies the convected wave

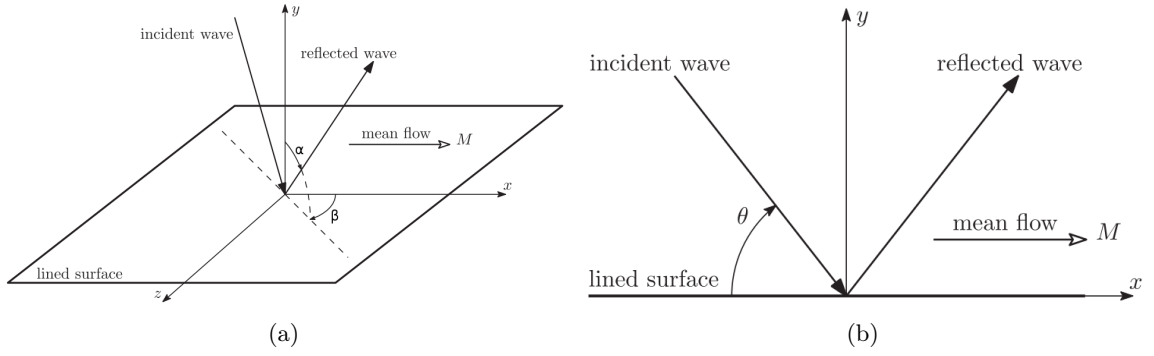


Figure 6.1. The arrangement of the angles defining the incident and reflected wave directions with respect to the coordinate directions. Adapted from Gabard (2013).

equation

$$\frac{D^2 \phi'}{Dt^2} - \nabla^2 \phi' = 0, \quad (6.1.1)$$

where $D/Dt = \partial/\partial t + M\partial/\partial x$ is the material derivative. In the frequency domain we may write a plane wave solution of (6.1.1) as

$$\tilde{\phi} = e^{i(\omega t - K\boldsymbol{\theta}_i \cdot \mathbf{x})} + R e^{i(\omega t - K\boldsymbol{\theta}_r \cdot \mathbf{x})}, \quad (6.1.2)$$

where $K = \omega/D$ is the acoustic wavenumber, for Doppler factor $D = 1 + M\boldsymbol{\theta}_i \cdot \mathbf{e}_x$, and the two terms correspond to: an incident wave of unit amplitude travelling in the direction $\boldsymbol{\theta}_i \cdot \mathbf{x}$; and a reflected wave of amplitude R travelling in the direction $\boldsymbol{\theta}_r \cdot \mathbf{x}$. The vectors $\boldsymbol{\theta}_i$ and $\boldsymbol{\theta}_r$ are therefore the angles of incidence and reflection, respectively, and are defined as

$$\boldsymbol{\theta}_i = \sin \alpha \cos \beta \mathbf{e}_x - \cos \alpha \mathbf{e}_y + \sin \alpha \sin \beta \mathbf{e}_z, \quad (6.1.3a)$$

$$\boldsymbol{\theta}_r = \sin \alpha \cos \beta \mathbf{e}_x + \cos \alpha \mathbf{e}_y + \sin \alpha \sin \beta \mathbf{e}_z, \quad (6.1.3b)$$

in three dimensions, and

$$\boldsymbol{\theta}_i = \cos \theta \mathbf{e}_x - \sin \theta \mathbf{e}_y, \quad \boldsymbol{\theta}_r = \cos \theta \mathbf{e}_x + \sin \theta \mathbf{e}_y, \quad (6.1.4)$$

in two dimensions (see fig. 6.1). In 3D the Doppler factor is $D = 1 + M \sin \alpha \cos \beta$; in 2D the Doppler factor is $D = 1 + M \cos \theta$. In both cases (6.1.3) and (6.1.4), the reflected wave has a positive sign in the \mathbf{e}_y direction where the incident wave has a negative; for convenience, and to avoid the confusion of hidden negative signs, we shall define $k_y = K\boldsymbol{\theta}_r \cdot \mathbf{e}_y$ as the acoustic wavenumber in the y direction, in both 2D and 3D.

6.1.1 Asymptotic reflection coefficients

The effective impedance boundary conditions derived in this thesis (in chapters 2, 4 and 5), and those proposed elsewhere (by Ingard (1959) and Myers (1980), and by Brambley (2011*b*)), may be expressed in the general form

$$Z_{\text{eff}} = \frac{\omega}{\omega - Mk_x} \frac{Z + F}{1 + G}, \quad (6.1.5)$$

where the functions F and G may depend on, in general: the mean velocity and temperature profiles and centreline Mach number, the modal wavenumbers and frequency, the boundary layer thickness, and the Reynolds and Prandtl numbers. The parameter $k_x = K\boldsymbol{\theta}_i \cdot \mathbf{e}_x$ is the wavenumber in the x direction, and correspondingly $k_z = K\boldsymbol{\theta}_i \cdot \mathbf{e}_z$ is the wavenumber in the z direction (in 3D).

These replace the notation used in all previous chapters of this thesis to denote the wavenumbers in the coordinate directions that are not normal to the lined wall (k and m , previously).

Using the definitions of k_x and D , we may derive the convenient formulae

$$\omega - Mk_x = K, \quad \frac{\omega}{\omega - Mk_x} = D, \quad (6.1.6)$$

and use them to rewrite (6.1.5) as

$$\tilde{p}(0)(1 + G) = -\tilde{v}(0)D(Z + F), \quad (6.1.7)$$

where the arguments of \tilde{p} and \tilde{v} are in terms of y , and the definition $Z_{\text{eff}} = \tilde{p}(0)/[-\tilde{v}(0)]$ is used. Now, the pressure and radial velocity may be deduced from the velocity potential in uniform flow via $\tilde{p} = -D\tilde{\phi}/Dt$ and $\tilde{v} = \partial\tilde{\phi}/\partial y$, leading to

$$\tilde{p}(y = 0) = -iK(1 + R), \quad \tilde{v}(y = 0) = -ik_y(R - 1), \quad (6.1.8)$$

where the common exponential terms have been ignored. Inserting the expressions (6.1.8) into (6.1.7), we may rearrange the resulting equation to find R :

$$R = \frac{D\boldsymbol{\theta}_r \cdot \mathbf{e}_y(Z + F) - (1 + G)}{D\boldsymbol{\theta}_r \cdot \mathbf{e}_y(Z + F) + (1 + G)}. \quad (6.1.9)$$

Gabard (2013) gives the general form for the reflection coefficient as

$$R = \frac{Z(D\boldsymbol{\theta}_r \cdot \mathbf{e}_y + iT_1) - 1 + iT_0}{Z(D\boldsymbol{\theta}_r \cdot \mathbf{e}_y - iT_1) + 1 + iT_0}, \quad (6.1.10)$$

where the T_j are real-valued. The form (6.1.10) may be consolidated with (6.1.9) by observing that

$$iT_0 = D\boldsymbol{\theta}_r \cdot \mathbf{e}_y F, \quad iT_1 = -\frac{1}{Z}G, \quad (6.1.11)$$

although for the effective impedance boundary conditions derived in this thesis (6.1.11) results in complex-valued T_j , meaning the form (6.1.10) is less instructive. For the sake of continuity, however, we will define the reflection coefficients of the second-order inviscid model of chapter 2, the high-frequency viscous model of chapter 4, and the two-deck viscous model of chapter 5 in relation to the form (6.1.10) by giving the forms of the parameters T_0 and T_1 .

Rederiving the second-order inviscid boundary condition from chapter 2 for the flat Cartesian geometry considered here leads to (6.1.5) with

$$F = \frac{iK^2}{\omega}\delta I_0 + (\delta I_0\delta I_1 + \delta^2 I_3 - \delta^2 I_{10})K_{\perp}^2 Z - (K^2 - K_{\perp}^2)\delta^2 I_{00}Z, \quad (6.1.12a)$$

$$G = -iK_{\perp}^2 \frac{DZ}{K}\delta I_1 + K_{\perp}^2(\delta I_0\delta I_1 + \delta^2 I_{11} - \delta^2 I_{01}) - (K^2 - K_{\perp}^2)\delta^2 I_2, \quad (6.1.12b)$$

where $K_{\perp}^2 = k_x^2 + k_z^2$. Comparing (6.1.5) and (6.1.12) with the cylindrical form (2.2.8) illustrates the extra complexity due to curvature appearing at $\mathcal{O}(\delta^2)$. The reflection coefficient predicted by the effective impedance boundary condition (6.1.5) with (6.1.12) is then given by (6.1.10) with

$$T_0 = D\boldsymbol{\theta}_r \cdot \mathbf{e}_y \left[-\frac{K}{D}\delta I_0 - i(\delta I_0\delta I_1 + \delta^2 I_3 - \delta^2 I_{10})K_{\perp}^2 Z + i(K^2 - K_{\perp}^2)\delta^2 I_{00}Z \right], \quad (6.1.13a)$$

$$T_1 = -\frac{K_\perp^2 D}{K} \delta I_1 + i(\delta I_0 \delta I_1 + \delta^2 I_{11} - \delta^2 I_{01}) \frac{K_\perp^2}{Z} - i(K^2 - K_\perp^2) \delta^2 I_2 \frac{1}{Z}. \quad (6.1.13b)$$

The reflection coefficient for the high-frequency Z_{eff} model given in (4.1.13) may be defined by the parameters

$$T_0 = \boldsymbol{\theta}_r \cdot \mathbf{e}_y \left[\frac{i(\gamma-1)T(0)}{\sqrt{i\omega \text{Re}}} \frac{k_x U_y(0)}{K} Z - K \delta I_0 - iDBZ \right], \quad (6.1.14a)$$

$$T_1 = -\frac{K_\perp^2 D}{K} \delta I_0 + \frac{i\mathcal{A}}{Z} + i\mathcal{C}, \quad (6.1.14b)$$

and (6.1.10), where

$$\mathcal{A} = K_\perp^2 (\delta I_0 \delta I_1 + \delta^2 I_{11} - \delta^2 I_{01}) - (K^2 - K_\perp^2) \delta^2 I_2, \quad (6.1.15a)$$

$$\begin{aligned} \mathcal{B} = & K_\perp^2 (\delta I_0 \delta I_1 + \delta^2 I_3 - \delta^2 I_{10}) - (K^2 - K_\perp^2) \delta^2 I_{00} + \frac{(\gamma-1)^2}{i\omega \text{Re}} \left(\frac{I_\mu}{\delta^2} \right. \\ & \left. - \frac{2\sigma}{1+\sigma} T(0) U_y(0)^2 - \frac{5k_x^2}{4\omega^2} T(0)^2 U_y(0)^2 \right), \end{aligned} \quad (6.1.15b)$$

$$\mathcal{C} = \frac{(\gamma-1)T(0)}{\sqrt{i\omega \text{Re}}} \left(-\frac{ik_x U_y(0)}{K^2} K_\perp^2 \delta I_1 + \frac{i}{\omega} K_\perp^2 (\gamma-1)T(0) + \frac{i\omega}{\sigma(\gamma-1)} \right), \quad (6.1.15c)$$

where $\sigma^2 = \text{Pr}$.

For the two-deck viscothermal boundary condition derived in the preceding chapter, (5.5.6), the T_j parameters are

$$T_0 = \boldsymbol{\theta}_r \cdot \mathbf{e}_y \left[\frac{i(\gamma-1)T(0)}{\sqrt{i\omega \text{Re}}} \frac{k_x U_y(0)}{K} Z - K \delta I_0 - iD(S_2 + S_3)Z \right], \quad (6.1.16a)$$

$$T_1 = -\frac{K_\perp^2 D}{K} \delta I_1 + iS_1, \quad (6.1.16b)$$

where

$$S_1 = \frac{(\gamma-1)}{\sqrt{i\omega \text{Re}}} \left(-\frac{ik_x U_y(0)}{K^2} T(0) \delta I_1 K_\perp^2 + \frac{i}{\rho(0)} \left[\frac{T(0)}{\omega} K_\perp^2 + \frac{\omega}{\sigma} \right] \right), \quad (6.1.17a)$$

$$S_2 = \frac{(\gamma-1)^2}{i\omega \text{Re}} \left(\frac{I_\mu}{\delta^2} + \left[\frac{2\sigma}{1+\sigma} - \frac{5k_x^2}{4\omega^2} T(0) \right] T(0) U_y(0)^2 \right), \quad (6.1.17b)$$

$$\begin{aligned} S_3 = & \left(\frac{(\gamma-1)}{\sqrt{i\omega \text{Re}}} \right)^3 \left\{ -\frac{k_x I_\mu}{\delta^2 \omega} U_y(0) T(0)^2 - \frac{13k_x^2}{8\omega^2} U_{yy}(0) U_y(0) T(0)^3 - \frac{k_x}{\omega} U_{yyy}(0) T(0)^3 \right. \\ & - \frac{1}{\sigma} T_{yyy}(0) T(0)^2 - \frac{151k_x^3}{31\omega^3} U_y(0)^3 T(0)^3 + \frac{7\sigma+3}{(1+\sigma)^2} \frac{k_x}{2\omega} U_y(0)^3 T(0)^2 \\ & + \frac{1}{\sigma} \frac{\sigma \text{Pr} + \text{Pr} - 2\sigma - 1}{(1+\sigma)^2} \frac{2T_{yy}(0)}{\omega} U_y(0) T(0)^2 \\ & \left. - \frac{2\text{Pr} + 4\sigma + 1}{(1+\sigma)^2} \frac{k_x T_{yy}(0)}{\omega} U_y(0) T(0)^2 \right\}. \end{aligned} \quad (6.1.17c)$$

Using (6.1.16) in (6.1.10) gives the reflection coefficient.

6.1.2 Computational method

A computational domain is created in $y \in [0, y_N]$ where y_N is chosen such that n_λ wall-normal uniform flow wavelengths fit inside the domain. The wall-normal uniform flow wavelength is given by $\lambda_y = 2\pi/k_y$ for $k_y^2 = (\omega - Mk_x)^2 - k_x^2 - k_z^2$; then, $y_N = n_\lambda \lambda_y$ gives the upper bound of the

domain. The lined wall is situated at $y = 0$, and a non-uniform grid y_i , $i = 1, 2, \dots, N$ (with more points clustered near the wall to fully resolve the boundary layer) is mapped to a uniform computational grid ξ_i via the mapping

$$\xi_i = \frac{y_N}{A} \operatorname{arcsinh} \left(\frac{y_i}{y_N} \sinh A \right), \quad (6.1.18)$$

for a real-valued parameter A that governs the severity of the grid stretching. In general the parameters $N = 10000$, $A = 8.5$ and $n_\lambda = 3$ gave satisfactory results.

The linearised compressible Navier–Stokes equations (LNSE), given in (1.1.13), are solved in the domain, with a 6th order unoptimized (Brambley, 2016) finite difference scheme used to approximate derivatives with respect to y (reducing to a 4th order scheme near the domain boundaries). The viscothermal effects are modelled as having linear dependence on the temperature, as in (3.1.4). A sheared mean flow profile is applied, with the mean velocity U and temperature T having the forms

$$U(y) = M \tanh \frac{4y}{\delta}, \quad T(y) = T_0 + \tau \operatorname{sech} \frac{4y}{\delta}, \quad (6.1.19)$$

where $\tau \approx 0.104$ approximates the compressible Blasius profile wall temperature, and $T_0 = 1/(\gamma-1)$ defines the free stream temperature, for γ the ratio of specific heats.

An incident plane wave of unit amplitude is used as a boundary condition at the top of the domain via the expression

$$\tilde{\phi}_y + ik_y \tilde{\phi} = 2ik_y e^{-iKy_N \theta_i \cdot \mathbf{e}_y}, \quad (6.1.20)$$

where R has been eliminated and common exponential factors have been cancelled. This creates a problem, as the inviscid plane wave (6.1.2) is not a solution of the viscous governing equations (1.1.13). A plane wave applied at the top of a viscous uniform flow will not propagate at a constant amplitude, as shown in fig. 6.2, destroying our ability to calculate the reflection coefficient reliably. To get around this, viscous effects are smoothly, but rapidly, “turned off” at the top of the shear layer, when the velocity and temperature reach their free stream values. This is achieved by multiplying the viscous terms by the sigmoid-type function

$$h_\mu(y) = \begin{cases} 1, & y < y_s, \\ 2 - \frac{2}{1 + \exp(-\nu(y - y_s))}, & y > y_s, \end{cases} \quad (6.1.21)$$

where $y = y_s$ marks the edge of the shear layer and $\nu \approx 60$ governs the speed at which the function h_μ approaches zero above y_s . The use of (6.1.21) is not the ideal way to treat this problem, but ensures that the calculated reflection coefficient does not depend on domain size or number of grid points.

To calculate the reflection coefficient, we use the complementary expression to (6.1.20) in which the unit amplitude incident wave is eliminated,

$$\tilde{\phi}_y - ik_y \tilde{\phi} = -2iRk_y e^{-ik_y y_N}, \quad (6.1.22)$$

and use the uniform flow relationships $\tilde{\mathbf{u}} = \nabla \tilde{\phi}$, $\tilde{p} = -D\tilde{\phi}/Dt$ and $\tilde{T} = \tilde{p}/\rho_0$ to transform (6.1.22) into an expression for each acoustic variable (noting that $\rho_0 \equiv 1$ in the scheme of nondimensionalisation used here). Then, we may rearrange the resulting expressions to find the reflection

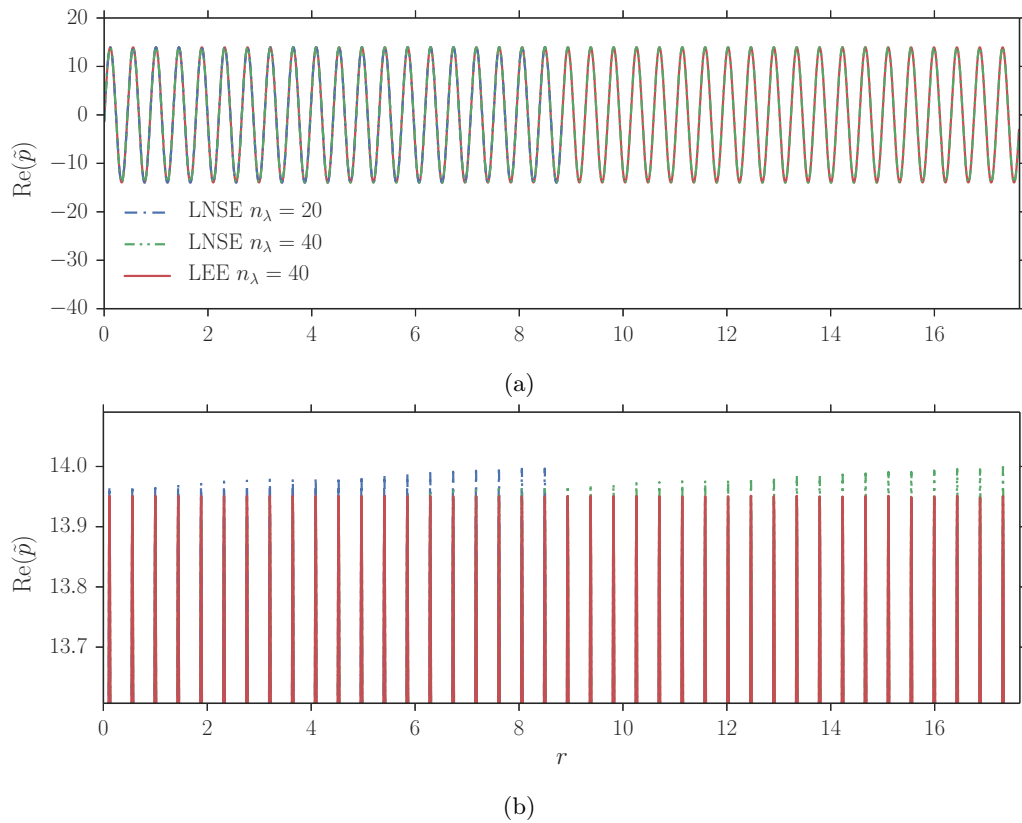


Figure 6.2. Mode shapes of the acoustic pressure, \tilde{p} , for the solutions of the linearised Navier–Stokes equations (LNSE) *without* using the viscosity damping function (6.1.21) to turn off viscosity at the top of the shear layer, for a domain containing 20 and 40 wavelengths. Also plotted are the mode shapes for the solution of the linearised Euler equations (LEE) for a domain containing 40 wavelengths. (a) shows the full solutions, while (b) shows a close-up of the wave peaks. The LNSE solutions grow to the right at different rates depending on the domain size. The LEE solution retains a constant amplitude throughout the region of uniform flow.

coefficient:

$$R_u = -(2k_x k_y)^{-1} e^{ik_y y_N} (\tilde{u}_y(y_N) - ik_y \tilde{u}(y_N)), \quad (6.1.23a)$$

$$R_v = -(2k_y^2)^{-1} e^{ik_y y_N} (\tilde{v}_y(y_N) - ik_y \tilde{v}(y_N)), \quad (6.1.23b)$$

$$R_w = -(2k_z k_y)^{-1} e^{ik_y y_N} (\tilde{w}_y(y_N) - ik_y \tilde{w}(y_N)), \quad (6.1.23c)$$

$$R_p = -(2K k_y)^{-1} e^{ik_y y_N} (\tilde{p}_y(y_N) - ik_y \tilde{p}(y_N)), \quad (6.1.23d)$$

$$R_t = -(2K k_y)^{-1} e^{ik_y y_N} (\tilde{T}_y(y_N) - ik_y \tilde{T}(y_N)), \quad (6.1.23e)$$

where the five expressions for the R_j should all result in the same value (a useful test of the numerical method). The standard deviation¹ of the R_j values in the test cases presented here was generally of the order of 10^{-8} , so error bars, considered unnecessary, have not been plotted. Taking the mean of the R_j from (6.1.23) then gives us the value of R which we compare with the asymptotic approximations, derived above, and the inviscid numerical result that may be attained using the same code in the inviscid limit.

6.2 Results

Here we plot results for the reflection coefficient of a plane wave incident on a boundary layer above a lined wall at any angle in two and three dimensions. The two viscous asymptotic expressions (6.1.14) and (6.1.16) are compared to the viscous numerics; the inviscid second order expression (6.1.13) is compared to the inviscid numerics; and the viscous numerics are compared to the inviscid numerics. Also plotted are the reflection coefficients found using the Ingard–Myers (Ingard, 1959; Myers, 1980) condition and its first order correction (the modified Myers condition, Brambley, 2011*b*) (given below) so as to evaluate existing inviscid boundary conditions by comparing with the new inviscid condition derived in this thesis, (6.1.13), and by judging how important their neglect of viscosity is for attenuation predictions. The reflection coefficient of the Myers condition, (1.2.17), is defined by (6.1.10) with $T_0 = T_1 = 0$. The modified Myers boundary condition, (1.2.18), is defined by (6.1.10) with

$$T_0 = -k_y \delta I_0, \quad T_1 = -\frac{K_{\perp}^2 D}{K} \delta I_1. \quad (6.2.1)$$

Gabard (2013) uses five test cases to compare impedance boundary conditions, and we adhere to those cases here. The parameter values of these five cases are typical of a turbofan engine duct, and are outlined in table 6.1. Gabard (2013) reports that case A corresponds to the near-fan flow conditions at the inlet of a turbofan engine at blade passing frequency; case B represents the flow upstream of the fan where the boundary layer would be thinner; case C tests the double frequency

¹Standard deviation defined here as $\sigma_{SD}^2 = \frac{1}{N_R} \sum (|R_j| - |R_{\mu}|)^2$, where N_R is the number of R values (four in 2D, five in 3D) and R_{μ} is the mean of the N_R R values.

Case	Frequency ω	Shear thickness δ (%)	Mach number M	Impedance Z
A	28	1.4	0.55	$5 - i$
B	28	0.7	0.55	$5 - i$
C	56	1.4	0.55	$5 - i$
D	28	1.4	0.3	$5 - i$
E	28	3	0.55	$3 - 0.5i$

Table 6.1. Test cases for reflection coefficient calculations, as used in Gabard (2013).

harmonic of the blade passing frequency; case D tests a lower Mach number flow; and case E corresponds to the thicker boundary layer and altered impedance of the bypass duct.

6.2.1 Two dimensions

In this section we constrain the incident wave to lie in the same plane as the direction of the mean flow, as in fig. 6.1b. The angle θ is varied between 0 and π , so that the wave is incident anywhere between directly downstream and directly upstream. Figure 6.3 shows results in decibels for a high Reynolds number, where the subfigure labels correspond to the ‘‘Case’’ column in table 6.1. All the models collapse approximately onto a single line when the incident wave is perpendicular to the mean flow. If the mean temperature was constant, this would be exactly true for the inviscid case (Gabard, 2013) as the standard wave equation is recovered. For the viscous case the standard wave equation is never recovered, but the reflection coefficient still collapses approximately to the single line followed by the inviscid models. In particular, in all cases the greatest discrepancy between inviscid and viscous reflection comes when the wave is incident in an upstream direction, as was seen in fig. 3.6 previously. This could be due to the refraction of upstream propagating waves away from the lining by the mean flow shear, and the resulting increase in the importance of viscosity to the attenuation rate. This feature is well captured by the high frequency asymptotic solution, and partially captured by the two-deck weakly viscous model. We also recover the result of Gabard (2013) that the Myers boundary condition is ill-suited for attenuation calculations, with the reflection coefficient of waves incident at shallow angles being predicted with errors of up to 10dB with respect to inviscid numerics.

Figure 6.4 shows results for relatively lower values of Re . As intuition suggests, this separates the viscous and inviscid models by a greater amount, particularly for upstream propagating waves. In figs. 6.4A, 6.4C and 6.4E the benefits of using the second-order accurate inviscid boundary condition over the modified Myers condition may be seen, with the modified Myers condition having errors of more than 1dB for upstream propagating incident waves. The second order inviscid condition consistently predicts the reflection coefficient in line with the inviscid numerics across all angles of incidence. The two-deck weakly viscous model is seen to either over-predict or under-predict R for upstream propagating waves (e.g. figs. 6.4B and 6.4C) compared with the viscous numerics, although the model out-performs the inviscid models in capturing the features of the viscous numerics. The high-frequency asymptotic boundary condition is extremely accurate with respect to the viscous numerics in all cases. The poor accuracy of the Myers condition is again evident in all cases at shallow angles of incidence.

6.2.2 Three dimensions

In this section we use the angle definitions indicated in fig. 6.1a, allowing the incident wave to enter the boundary layer at a cross-flow angle (nonzero β). In fig. 6.5 results for Case A at $Re = 4 \times 10^5$ are plotted, where the colour bar scale is in decibels. Figures 6.5a–6.5c show the viscous models, while figs. 6.5e–6.5h show the inviscid models. At steep angles of incidence ($\alpha \lesssim \pi/8$) the viscous and inviscid results vary only slightly, as in the 2D case. At shallower angles, the features of the viscous and inviscid density plots start to change, with greater attenuation occurring in the viscous case in the upstream direction (as β approaches π or $-\pi$). This is seen more easily in fig. 6.5d, which shows the error, in decibels, of the inviscid LEE numerics (fig. 6.5e) with respect to the viscous LNSE numerics (fig. 6.5a). Large regions in (α, β) space show discrepancies of more than 3dB between the inviscid and viscous attenuation predictions, with a maximum error being

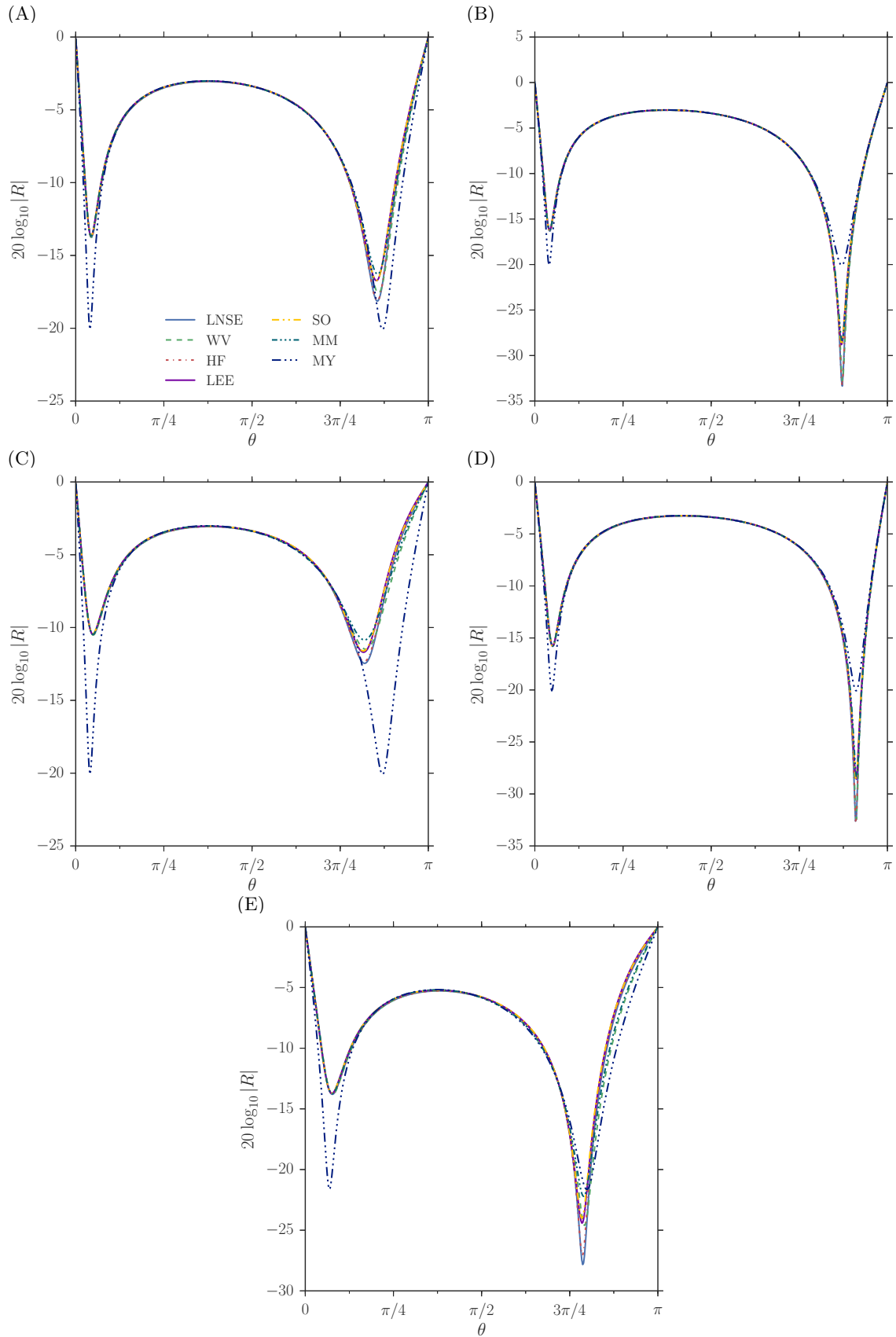


Figure 6.3. Reflection coefficient in decibels for the five cases in table 6.1. Legend acronyms are linearised Navier–Stokes equations (LNSE), weakly viscous two-deck (WV), high frequency viscous (HF), linearised Euler equations (LEE), second order inviscid (SO), modified Myers (MM) and Myers (MY). Reynolds numbers are (A,C,D) $\text{Re} = 5 \times 10^6$, (B) $\text{Re} = 2 \times 10^7$, (E) $\text{Re} = 1 \times 10^6$.

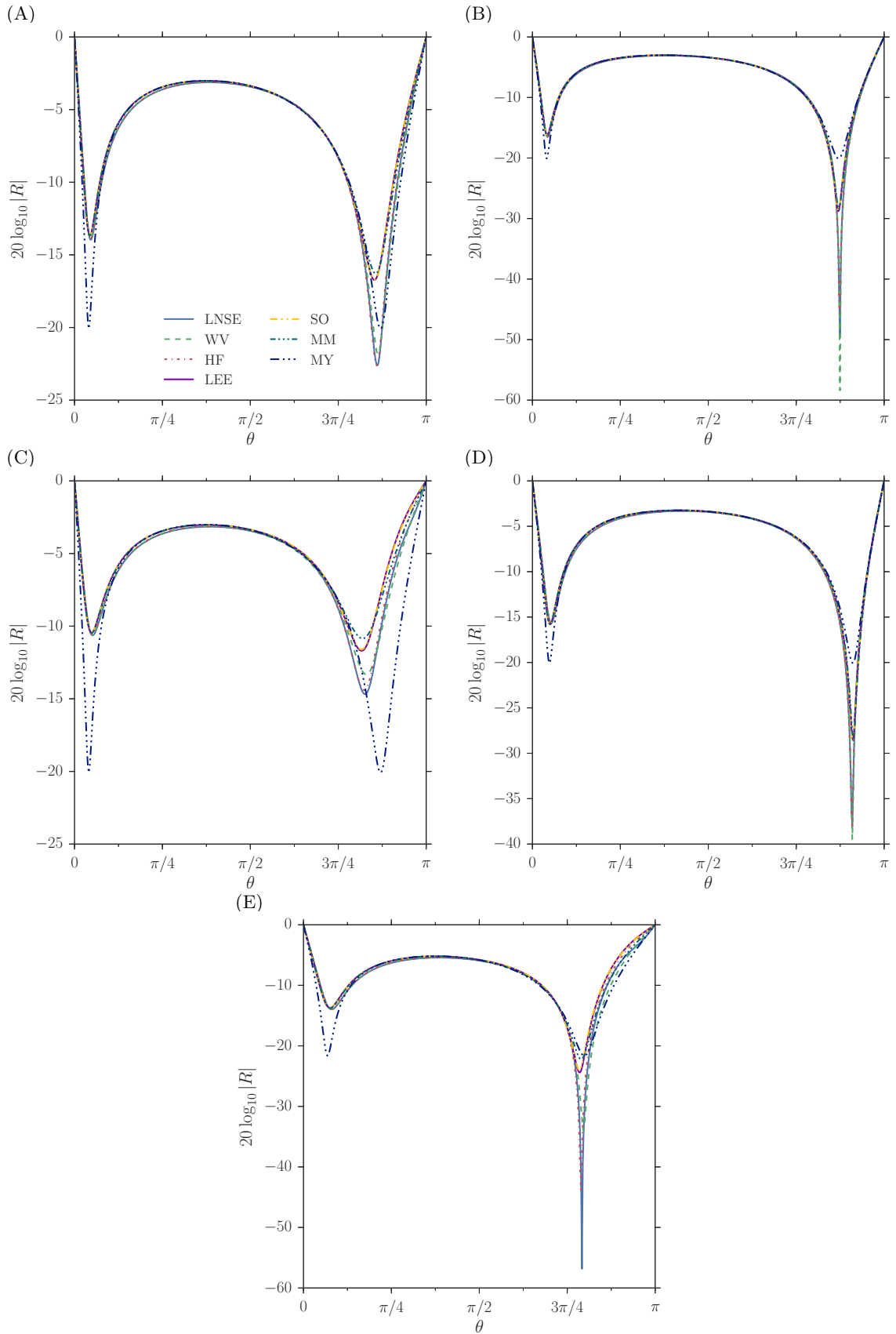


Figure 6.4. Reflection coefficient in decibels for the five cases in table 6.1. Legend acronyms are linearised Navier–Stokes equations (LNSE), weakly viscous two-deck (WV), high frequency viscous (HF), linearised Euler equations (LEE), second order inviscid (SO), modified Myers (MM) and Myers (MY). Reynolds numbers are (A,C,D) $Re = 4 \times 10^5$, (B) $Re = 3 \times 10^6$, (E) $Re = 1 \times 10^5$.

an under-prediction of ~ 17 dB by the inviscid numerics for upstream propagating incident waves entering the boundary layer at shallow angles.

The features of the viscous LNSE numerics, shown in fig. 6.5a, are captured well by the two viscous asymptotic models, figs. 6.5b and 6.5c. The second-order inviscid boundary condition, fig. 6.5f, performs well in 3D, accurately reproducing the features of the inviscid LEE numerics, fig. 6.5e. The Myers condition, fig. 6.5h, fails to capture the complicated changes in reflection coefficient that occur as β is varied for shallow entry angles ($\alpha \gtrsim 3\pi/8$).

More substantial differences between the viscous and inviscid attenuation predictions can be seen in fig. 6.6, which shows results for Case E at $\text{Re} = 1 \times 10^5$. The inclusion of viscosity creates patches of very intense attenuation (compare the LNSE results fig. 6.6a with the LEE results fig. 6.6e), leading to a maximum under-prediction by the inviscid numerics of 32dB. The median absolute error is ± 0.3 dB between the LNSE and LEE numerics, but this belies the significant effect of viscosity at shallow angles of incidence and directions of propagation away from downstream. It is also worth noting the change in polarity of the discrepancy between the LNSE and LEE numerics as the direction of propagation varies between upstream propagating and cross-flow propagating (see fig. 6.6d). Neglecting viscosity leads to an under-prediction of attenuation near $\beta = \pm\pi$ where the wave is propagating almost directly upstream, but this switches to an over-prediction for $-5\pi/8 \lesssim \beta \lesssim 5\pi/8$ where the wave is propagating either across the mean flow or downstream. Again, the asymptotic boundary conditions derived in chapters 2, 4 and 5 perform well, capturing the complexities of the attenuation patterns of the numerics in (α, β) space.

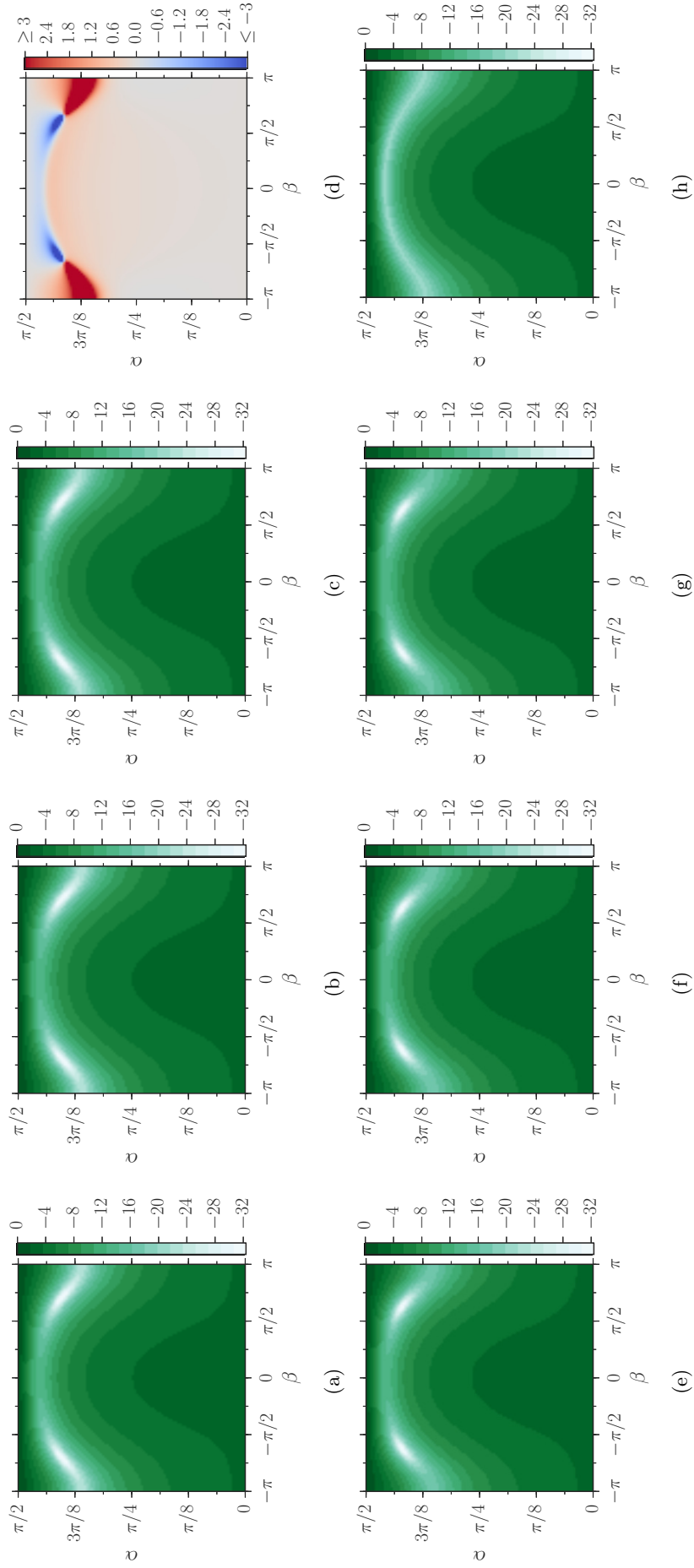


Figure 6.5. Reflection coefficient in decibels for case A from table 6.1. The Reynolds number is $Re = 4 \times 10^5$. (a) LNSE, (b) HF, (c) WV, (d) Error in the LEE prediction compared with the viscous LNSE prediction, (e) LEE, (f) SO, (g) MM, (h) MY. The maximum absolute discrepancy in the hot spots of (d) is ~ 17 dB, while the median is ~ 0.2 dB.

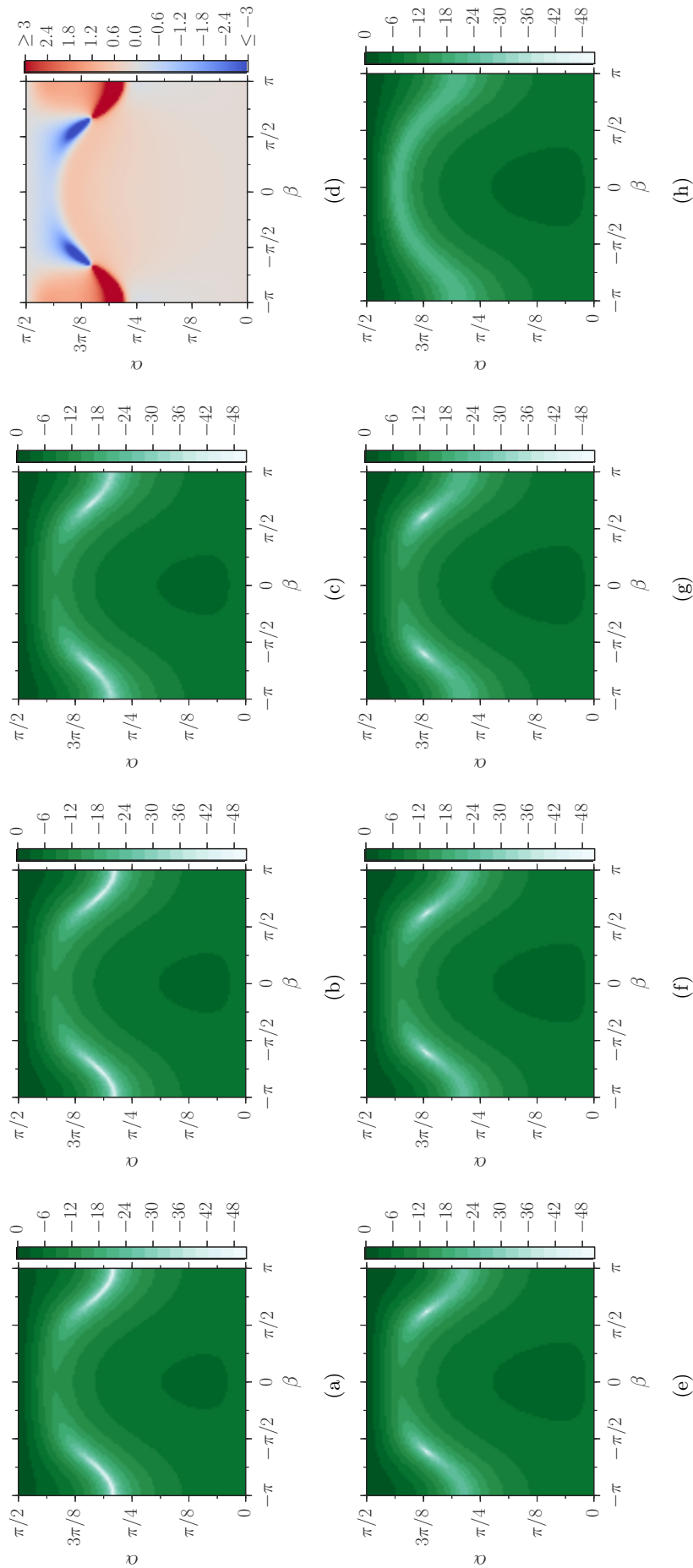


Figure 6.6. Reflection coefficient in decibels for case E from table 6.1. The Reynolds number is $Re = 1 \times 10^5$. (a) LNSE, (b) HF, (c) WV, (d) Error in the LEE prediction compared with the viscous LNSE prediction, $20 \log_{10} |R_{LEE} / R_{LNSE}|$, (e) LEE, (f) SO, (g) MM, (h) MY. The maximum absolute discrepancy in the hot spots of (d) is ~ 32 dB, while the median is ~ 0.3 dB.

6.3 Summary

This chapter has studied the attenuation of a sound wave incident on a sheared boundary layer above an impedance wall. By numerically computing the reflection coefficient (the amplitude of the reflected wave) for an inviscid and viscous system, the importance of viscosity for accurate prediction of the attenuation of upstream and cross-flow propagating sound was shown quantified. Understanding the damping of upstream propagating sound is vitally important for targeting fan and compressor noise in the forward arc, see figs. 1.1 and 1.2. The analysis presented here is a useful extension to both the numerical investigation in chapter 3, and the inviscid study of Gabard (2013).

This chapter also used the problem of an incident plane wave as a testing ground for the asymptotic impedance boundary conditions derived in this thesis. In support of the conclusions drawn by Gabard (2013), the results presented here show that the Myers boundary condition fails to capture the influence of mean flow shear on sound attenuation, leading to significant errors. The damping of upstream and downstream propagating sound, in two and three dimensions, is poorly predicted by the Myers boundary condition. The second-order inviscid boundary condition of chapter 2 was shown to accurately reproduce the attenuation properties of the linearised Euler equations (LEE) numerics, consistently outperforming the first-order modified Myers condition (Brambley, 2011*b*) in two and three dimensions.

The viscous impedance boundary conditions derived in chapters 4 and 5 were shown to accurately predict the attenuation properties of the linearised Navier–Stokes equations (LNSE). The two-deck boundary condition with the weakly viscous main boundary layer, of chapter 5 did not fully capture the large effect of viscosity on the attenuation of upstream propagating sound; the multiple scales high frequency boundary condition, of chapter 4, performed well across all test cases.

Chapter 7

Conclusion

This thesis has sought to extend the current theory of sound propagation over impedance surfaces. Although much focus has been given to the derivation of acoustic boundary conditions that aim to further the capabilities of numerical codes and mathematical studies, the analysis performed in the preceding chapters also allows a greater insight into and understanding of boundary layer stability, the role of viscosity in sound attenuation and the behaviour and number of surface wave modes.

In chapter 2 the problem of sound in an inviscid, sheared boundary layer is studied. The work of Brambley (2011*b*) is extended by deriving, via an expansion in terms of the boundary layer thickness $0 < \delta \ll 1$, a second-order accurate impedance boundary condition applicable to plug flows. A non-asymptotic boundary condition capable of treating short-wavelength, high-frequency sound in thick boundary layers is proposed, which utilises numerical integration techniques to derive an approximate solution for the effective impedance of an inviscid shear layer over an acoustic lining.

In chapter 3 a numerical investigation is performed to quantify the importance of viscous and thermal conductive effects, with regard to mean flow shear effects, for acoustic calculations in sheared boundary layers of impedance linings. The chapter compares numerical solutions of the linearised compressible Navier–Stokes equations (LNSE) with numerical solutions of the linearised compressible Euler equations (LEE), and compares the LEE numerics with analytical acoustic solutions attainable in inviscid uniform duct flow. The study compares the following: the ratio \bar{p}/\bar{v} at the lined wall, where \bar{v} is not constrained; the position of both cut-on and cut-off modes in the k -plane; the number and position of surface wave modes; and the stability properties via Briggs–Bers (Bers, 1983; Briggs, 1964) analysis.

In chapter 4 two asymptotic analyses are presented of a viscous, sheared boundary layer over an acoustic lining. A relatively simple boundary layer rescaling, assuming the laminar Blasius scaling relationship between boundary layer thickness and Reynolds number, $\delta \sim 1/\text{Re}^{1/2}$, leads to a reduced system of governing equations for the acoustics in a viscous boundary layer which must be solved numerically. The assumption of a high sound frequency leads to the second asymptotic regime analysed in chapter 4. This analysis leads to an analytically tractable set of high-frequency governing equations by utilising the multiple scales method with a WKB-type ansatz for the acoustic quantities, allowing the effective impedance of a viscous, sheared boundary layer above an impedance lining to be expressed in closed form.

In chapter 5 asymptotic analysis of a novel two-deck boundary layer is presented and compared to numerical solutions of the LNSE. An assumption of weak viscosity in the outer deck of the boundary layer leads to analytically tractable governing equations; the inner deck equations are made tractable by assuming that the mean flow deviates from its wall state only slightly across

the thin sublayer. Acoustic solutions are asymptotically matched between the two decks of the boundary layer and the outer region of inviscid uniform flow to form uniformly valid solutions for the acoustics and an expression for the effective impedance.

In chapter 6, the problem of a plane wave incident on a sheared boundary layer above an impedance surface is treated numerically and asymptotically, in two and three dimensions, for both an inviscid and a viscous fluid. The effects of viscosity on the reflection coefficient are investigated by comparisons of the viscous and inviscid numerics. The suitability for use in attenuation predictions of the asymptotic effective impedance boundary conditions derived throughout this thesis, and existing boundary conditions derived elsewhere, is tested by comparing asymptotic calculations of the reflection coefficient with numerical solutions.

The effective impedance boundary conditions derived in this thesis are summarised in table 7.1. The table contains concise descriptions of when each boundary condition should be used, and when each model is prone to fail.

Modelling in the frequency domain

Analytical modelling of sound propagation in lined ducts with uniform flow, where the acoustic pressure modes may be written in terms of Bessel functions, requires an impedance boundary condition to be applied at the duct wall in order to form a dispersion relation. By applying one of the closed-form effective impedance boundary conditions, the capabilities of such analytical modelling may be improved. The second-order inviscid model, (2.2.8), has been shown to predict with greater accuracy both cut-on and cut-off modes, as well as surface wave modes. When the boundary layer thickness δ is small and the wavenumber and frequency satisfy $k, \omega \ll 1/\delta$, the second-order boundary condition consistently and accurately reproduces the results found via numerical solution of the Pridmore-Brown equation, improving on the modified Myers condition (Brambley, 2011*b*) and retaining its well-posedness. By applying the high-frequency boundary condition (4.1.13) or the two-deck model (5.5.6), it would be possible to form analytical mode shapes for acoustics that account for a viscothermal shear layer of finite thickness $0 < \delta \ll 1$ above the lining. Alternatively, the uniformly valid composite expansions (5.4.2) and (5.4.5) may be used. These composite expansions give the correct asymptotic behaviour when evaluated in each of the three duct regions defined in chapter 5, and are shown to agree well with the full LNSE numerics.

For inviscid numerics in the frequency domain, the boundary conditions derived in chapter 2 may be easily applied in their general forms, (2.2.8) and (2.3.11), or simplified by assuming a specific shear profile; for example, a linear profile leads to expressions (2.5.2) and (2.5.4). For sufficiently thin boundary layers, the second-order asymptotic condition (2.2.8) allows the accurate prediction of growth rates and characteristic wavelengths of inviscid instability. The effect of the shear is modelled more precisely than in previous inviscid modifications of the Myers condition (Brambley, 2011*b*; Joubert, 2010; Myers & Chuang, 1984; Rienstra & Darau, 2011), improving predictions of the position of cut-on modes in the k -plane. This should increase the accuracy of attenuation calculations, with the results of chapter 6 supporting this claim. For thick boundary layers, or high wavenumbers or frequencies outside the region of asymptotic validity, the single-step implicit Runge–Kutta boundary condition (2.3.11) could be carefully used, with the associated caveats kept in mind. It has been evidenced here that the implicit Runge–Kutta condition can produce very accurate predictions of the effective impedance. The scheme performs poorly, however, when predicting the wavenumber and behaviour of surface modes and modes with sharp changes in the boundary layer forced by the shear, owing to its poor resolution of waves in the boundary layer. A higher order implicit method could solve this problem, but for such a method a closed form of the

BC	When does it work well	When does it work poorly
SO	<p>Accurate reproduction of LEE solutions across wide range of frequencies;</p> <p>Well-behaved temporal stability away from inviscid critical layer;</p> <p>Easily applicable as a boundary condition in the frequency domain.</p>	<p>Should not be used outside region of asymptotic validity, $k, \omega \ll 1/\delta$, due to accuracy loss and spurious solutions;</p> <p>Undefined at inviscid critical layer $\omega - U(r_c)k = 0$;</p> <p>Spurious singularity at $(\omega - Mk)^2 = k^2 + m^2$.</p>
IR	<p>Accurate Z_{eff} prediction at extremities of wavenumber plane, due to non-asymptotic nature;</p> <p>Useful when asymptotic models fail, outside of their region of validity.</p>	<p>Cannot resolve surface modes due to low number of sample points in boundary layer;</p> <p>Small-δ analysis not always sufficient when choosing the correct square root sign, see Appendix 2.D.</p>
VF	<p>Accurate reproduction of LNSE results across wide range of frequencies;</p> <p>Well-behaved temporal stability, captures viscous phenomena of mode restabilisation for finite k;</p> <p>Model could be incorporated into an inviscid numerical code as a boundary solver;</p>	<p>No closed-form expression for the boundary condition;</p> <p>Region of asymptotic validity confined to $k, \omega \ll 1/\delta$</p>
HF	<p>Very accurate prediction of LNSE cut-on modes at high frequencies with respect to scaling regime $\omega \gg 1$, $\omega \sim \delta^{-2/3}$, $k/\omega \lesssim \mathcal{O}(1)$;</p> <p>Captures the full effects of viscosity throughout both the acoustic and mean flow boundary layers;</p> <p>Accuracy of cut-on mode prediction remains fair for moderate to low frequencies.</p>	<p>Scaling regime means the model is ill-suited to investigate temporal stability, for which important regimes are $\omega = \mathcal{O}(1)$ and $k/\omega \gg 1$;</p> <p>Fails to predict surface modes that lie outside the region of asymptotic validity.</p>
TD	<p>Unrestricted frequency allows time-domain formulation;</p> <p>Accurate reproduction of LNSE solutions across parameter space;</p> <p>Well-behaved temporal stability away from inviscid critical layer.</p>	<p>Main boundary layer sensitive to $\delta \sim \text{Re}^{-1/3}$ scaling, meaning viscous information may be lost;</p> <p>Main boundary layer suffers from interaction with inviscid critical layer, so model cannot capture restabilisation of modes at small wavelengths.</p>

Table 7.1. Summary of the effective impedance boundary conditions derived in this thesis, with a description of where they perform well and where they perform badly. Acronyms in Boundary Condition (BC) column are SO: $\mathcal{O}(\delta^2)$ Inviscid, (2.2.8); IR: Implicit Runge–Kutta Model, (2.3.11); VF: $\mathcal{O}(\delta)$ Viscous, (4.1.2); HF: High-frequency Model, (4.1.13); TD: Two-deck Model, (5.5.6).

boundary condition would be overly complicated. Alternatively, a careful application of an explicit scheme might be profitable, if the blow up of solutions could be avoided.

When full viscous numerics are not practical, it should be possible to make use of the asymptotic models presented in chapters 4 and 5 in frequency domain computations. The boundary layer model in §4.1.1 may be seen as an extension of the viscous Myers model of Brambley (2011*a*) in order to account for a nonzero-thickness viscous shear layer by including $\mathcal{O}(\delta)$ terms, or indeed as an extension of the inviscid modified Myers model of Brambley (2011*b*) to include viscothermal terms—in effect, §4.1.1 gives a viscous modified Myers condition. Although no closed-form solution for the effective impedance can be found for such a model, the reduced governing equations could be incorporated into an inviscid aeroacoustic numerical code as a boundary solver. The relatively few assumptions that are made in the derivation of the model (4.1.2) mean the resulting boundary condition performs well for a wide range of parameters, and also yields the correct stability properties, see figs. 4.4 and 4.5. If one is concerned with high frequency sound (such as is common in aeroacoustics), the analytical effective impedance boundary condition (4.1.13) may be easily applied in the frequency domain at the wall of an inviscid uniform flow. It is shown in §4.2.3 that the high frequency asymptotics predict the cut-on modes of the linearised compressible Navier–Stokes equations well even at relatively low frequencies down to $\omega \sim \mathcal{O}(1)$.

In deriving the effective impedance boundary condition (5.5.6), no assumptions about the sound being low or high frequency, nor about the velocity or temperature profiles of the mean flow boundary layer, have been made—unlike previous works which have found such assumptions necessary in order to give analytic solutions. This effective impedance boundary condition can be applied to acoustics in slipping inviscid flow, and accounts for the effects of shear and viscosity within the boundary layer. It is anticipated that this boundary condition could be used in frequency-domain numerics to avoid having to mesh finely and solve for the acoustics within the thin boundary layers at the walls.

The asymptotic models derived in chapters 2, 4 and 5 are shown to be suitable for attenuation calculations through favourable comparisons with numerical solutions in chapter 6. This is in contrast with the performance of the classical Ingard–Myers boundary condition, which does not accurately predict the effects of mean flow shear on sound absorption for either upstream or downstream propagating sound in 2D, figs. 6.3 and 6.4 and cannot capture the complicated effects of cross-flow sound propagation at shallow angles of incidence in 3D, figs. 6.5 and 6.6.

Surface wave modes

The new second-order asymptotic condition predicts surface modes with a higher degree of accuracy than the modified Myers condition, but also predicts additional spurious surface modes. Asymptotic analysis of the $k/\omega \gg 1$ regime has shown that the new condition predicts a possible 14 surface modes, compared to the six of the modified Myers condition (Brambley, 2013) and four of the Myers condition (Rienstra, 2003). By comparison with computations, it is suggested that the extra modes predicted by the second-order condition are spurious, and are easily recognised by being far out of the range of asymptotic validity. Analysis of the single-step implicit scheme boundary condition leads to a prediction of six surface modes, matching the prediction of the modified Myers model. Also introduced at the second-order of the asymptotic expansion is the spurious singularity when $(\omega - Mk)^2 = k^2 + m^2$, near which the first-order condition or implicit Runge–Kutta condition could be used instead.

It is shown in chapter 3 that a viscous boundary layer over an acoustic lining can support a greater number of surface wave modes than a corresponding inviscid boundary layer, fig. 3.7.

This indicates that inviscid models may be inadequate for comprehensive analyses, as these surface modes have important ramifications for stability. The viscous reduced boundary layer governing equations (4.1.2) may be used as part of an inviscid numerical solver in order to capture the notable effects of viscosity close to the boundary. The closed-form viscous boundary conditions (4.1.13) and (5.5.6) adequately predict viscous surface modes within their regions of asymptotic validity, figs. 4.3b and 5.1b; however, surface modes inhabit the regime $k/\omega \gg 1$ (Brambley, 2013) meaning it is possible for them to lie outside of the regions of asymptotic validity of the models, fig. 4.4.

Implications for impedance eduction

The success of commonly-used impedance eduction techniques, which connect the “far-field” acoustic response of a liner to its on-surface impedance, depends upon the quality of the liner model employed. The accuracy with which the second-order inviscid model, (2.2.8), and the viscous closed-form boundary conditions from chapters 4 and 5, (4.1.13) and (5.5.6), predict cut-on modes (see figs. 2.5, 4.3a and 5.1a) suggests that these models would be a useful tool in such impedance eduction methods, in either inviscid or viscous studies, if the asymptotic regimes are respected. Moreover, these three closed-form boundary conditions have more degrees of freedom (the δI_j integrals) than previous inviscid (such as that of Brambley, 2011*b*) or viscous (such as that of Aurégan *et al.*, 2001) models with which to achieve a better fit to the data (or, indeed, with which to “back out” some information about the base flow).

Effects of viscosity on attenuation

Although it is not always feasible to include viscous and thermal conductive effects in all aeroacoustic computations, it is shown here that there should be more careful thought about the situations in which they should be included, and an understanding of the size of the errors introduced by omitting them. Certainly, at low frequencies and for thin boundary layers the acoustics can be significantly affected by viscosity, with errors being introduced by its neglect that are of the same order of magnitude as the errors introduced by neglecting shear (e.g. fig. 3.3a). The existence of the anomalous region (Brambley, 2011*a*), in $\Re(k) > \omega/M$, $\Im(k) < 0$, can also lead to significant errors in inviscid computations.

In general, the damping of upstream propagating well cut-on modes – an important parameter for the understanding of fan forward noise – is found to be poorly predicted by inviscid numerics (see fig. 3.6), showing that small errors can lead to significant variations in important small quantities. This point is corroborated and extended by the numerical study in chapter 6. Viscosity is shown to greatly affect the attenuation of upstream propagating plane waves that enter the boundary layer at shallow angles, figs. 6.4, 6.5d and 6.6d; it is also shown that for cross-flow propagating sound, inviscid calculations can in fact over-predict the damping rate, figs. 6.5d and 6.6d (rather than under-predict, as is the case for upstream propagating sound). This finding is intrinsically linked to the importance of incorporate a swirling mean flow into an impedance boundary condition—cross-flow swirl alters the effective angle between the mean flow and the direction of sound propagation, hence altering how viscosity affects the attenuation.

The importance of viscosity in the boundary layer is demonstrated in figs. 5.1–5.3 by the major effect of the viscous sublayer on the acoustic mode shapes. Figure 5.4b suggests that shear effects dominate viscous effects within the mean flow boundary layer, while viscosity dominates within the viscous sublayer.

Stability

Viscosity is also indispensable when investigating the physical onset of instability, and in particular the growth rate of the instability is strongly dependent on viscosity (see fig. 3.9). The flow appears to be totally stabilized if viscosity is strong enough, which for the parameters considered here (see fig. 3.9) occurred at Reynolds numbers around $\text{Re} = 4 \times 10^5$.

The temporal stability properties of the full LNSE are well approximated by the $\mathcal{O}(\delta)$ boundary layer model (4.1.2): the model is well-posed and has a well-defined maximum growth rate of instability, and captures the damping of small wavelengths by viscosity. The high frequency asymptotic model derived in §4.1.2 is not well suited to temporal stability analysis due to the scaling assumptions $\omega \gg 1$ and $k/\omega \lesssim \mathcal{O}(1)$ made in its derivation; this suggests that it may not perform well if adapted to time domain applications, but should be suitable for use in the frequency domain where temporal instability is excluded.

For the parameters used in chapter 5, flow over an acoustic liner is unstable, as shown in figs. 5.1b and 5.2 for the full LNSE. The asymptotics of chapter 5 correctly reproduce this stability behaviour away from the critical layer. Near the critical layer the integrals become singular and the asymptotic solution breaks down (fig. 5.3). Inviscid solutions similarly break down at or near the critical layer (Brambley *et al.*, 2012b), and this is often not limiting when used in practice, although if accurate details are required around the critical layer a full LNSE solutions is probably advisable with high resolution around the critical layer to avoid numerical inaccuracies (see, e.g., fig. 10 of Brambley *et al.*, 2012b).

Modelling in the time domain

The application of impedance conditions in grazing flow in the time domain is an open question. The Myers condition has been applied in the time domain in many different ways, and is still a topic of current research (e.g. Gabard & Brambley, 2014). The use of the modified Myers condition in the time domain has been only recently studied (Brambley & Gabard, 2013, 2016), and application of the new inviscid impedance boundary conditions derived here in the time domain would be interesting future work. Previous investigations of viscous impedance boundary conditions have avoided the time domain. Due to the good temporal stability behaviour of the asymptotic boundary condition presented in chapter 5, a time-domain formulation of (5.5.6) is proposed in section 5.7. Equation (5.7.8) is the first time-domain impedance boundary condition to incorporate viscothermal effects. Implementation of this boundary condition as part of a time-domain LEE solver is beyond the scope of this thesis, and would constitute interesting future work. The recent success of an inviscid time-domain implementation (Brambley & Gabard, 2016) gives hope that the formulation proposed here will prove useful.

Implications for aeroengine design

The parameters used to produce most of the figures throughout this thesis (for example figs. 4.3a, 5.1a, 6.3 and 6.4) have been chosen to represent realistic aeroengine conditions. The large difference between viscous results and results found using the Myers boundary condition, particularly for upstream propagating cut-on modes, suggests that inlet liners may be incorrectly optimized at present. By incorporating the effects of viscosity and thermal conduction in optimization codes, engineers could make savings of several decibels—which could be vitally important in achieving the targeted 50% noise reduction by 2020 (ACARE, 2001).

Boundary layer instabilities could have detrimental effects on engine performance, so the ability to correctly predict when these instabilities occur is of practical importance. Triggering instabili-

ties in the flow over acoustic linings could lead to inefficiencies of the fan; the association of surface modes with convective instabilities (see fig. 3.8) means that instabilities would likely interact with the fan blade tips, heightening the adverse effect on performance. This thesis has shown that to correctly model boundary layer instabilities viscous effects need to be accounted for, with the characteristic growth rate and wavelength of instability strongly linked to the Reynolds number, and the phenomena of restabilisation at small wavelengths missing from inviscid models (see fig. 3.9).

7.1 Further work

Here, a discussion is presented of possible extensions to the current work and interesting future directions.

- In chapter 5, a mean flow with a high Reynolds number Re , a subsonic Mach number $0 \leq M < 1$, and a thin mean-flow boundary layer of thickness $\delta \sim Re^{-1/3}$ is assumed. This boundary layer is thicker than the laminar Blasius boundary layer thickness of $O(Re^{-1/2})$, and is motivated by realistic aircraft engine flows and laboratory experiments investigating flows over acoustic linings. A mean flow boundary layer wider than predicted by laminar Blasius theory might be due to a turbulent boundary layer and the effects of an eddy viscosity; modelling such phenomena is one aspect lacking from the work in this thesis. Since in most cases high Reynolds number boundary layers are turbulent, this would be an interesting avenue of future research. One way to address this would be by altering the choice of viscous function \mathcal{H} in (1.1.16) to contain some radially dependent eddy viscosity that is strong at the edge of the boundary layer and weak very close to the wall (Marx & Aurégan, 2013). A reformulation of the analyses in chapters 4 and 5 with such a modified \mathcal{H} would be a pertinent extension, as would inclusion of the effects of the eddies themselves on the acoustics.
- Results are presented throughout this thesis assuming a homogeneous impedance boundary, which may not be achieved in practice. Ongoing numerical investigations (Tam *et al.*, 2014; Zhang & Bodony, 2016) may illumine the important effects of inhomogeneities that could be included in theoretical studies. Comparison of these results to direct numerical simulations (DNS) and experiments (such as Alomar & Aurégan, 2016) would help validate these assumptions. Measurements of parameter values from aeroengines in flight (in particular boundary layer thicknesses) would be useful both to inform the relevant asymptotic regimes of interest in future theoretical work, and to predict the impact of the current theoretical work on aeroengine noise.
- The effects of swirl on the acoustics in a duct, neglected here, are known to be appreciable (Mathews *et al.*, 2016). Incorporating a swirling mean flow would lead to a frequency-domain boundary condition applicable in such situations as that studied in Mathews *et al.* (2016), where the current standard is the classical and ill-posed inviscid Ingard–Myers boundary condition. The importance of swirl for attenuation, stability, and the number of surface modes could be investigated.
- Find the response of the new boundary conditions derived here to a point source forcing via a Green’s functions treatment. This should allow the response to turbulent gusts to be built up by using a turbulent spectra and superposition of point source-type inputs.
- Implement the time-domain formulation of the two-deck boundary layer model (5.7.8), and incorporate it into a time-domain LEE code to account for a viscous, sheared boundary layer through the new boundary condition.
- Investigate scattering at a hard–soft junction in a viscous, sheared boundary layer. It may be possible to make use of the asymptotic boundary conditions derived here to form approximate solutions, which may be compared to a full solution found through a combination of triple-deck theory and the Wiener–Hopf method. A comparison with the inviscid treatment of Rienstra (2007), which used the Myers condition, would be interesting.

- Study the effects of slowly varying liner impedance or more realistic geometry, with application to liner splices or non-cylindrical engines. A related problem is the treatment of slowly varying effects of a non-parallel mean flow: in this work, no axial variation of the thin boundary layer is assumed.
- Investigate the absolute stability of viscous flow over a liner. An absolute instability would dominate a convective instability for large times; gaining an understanding of the effect of viscosity on the absolute stability properties may therefore be valuable, although our expectation is that absolute instabilities will be confined to extremely thin boundary layers at extremely high Reynolds numbers (Brambley, 2013).
- Investigate the effects of boundary layer profile on acoustics in a viscous fluid. It has been shown that in an inviscid fluid, the details of the mean flow profile are not as important to attenuation calculations as parameters such as the displacement or momentum thickness of the boundary layer (Gabard, 2013; Nayfeh *et al.*, 1974). However, the shape of the boundary layer profile can effect the behaviour and number of surface modes in an inviscid fluid (Brambley, 2013).
- Application of impedance boundary conditions to acoustics in free jets, where the interface between fluids moving with different velocities can be thought of as an impedance surface.
- Investigate nonlinear effects on the acoustics in the boundary layer and on the interaction between the acoustics and the impedance lining.

Bibliography

- ACARE 2001 *European Aeronautics: A Vision for 2020*. European Commission, http://www.acare4europe.org/sites/acare4europe.org/files/document/Vision%202020_0.pdf [Accessed 22/08/2016].
- ALOMAR, A. & AURÉGAN, Y. 2016 PIV Measurement of a Porous Liner in a Duct with Flow. In *22nd AIAA/CEAS Aeroacoustics Conference*. American Institute of Aeronautics and Astronautics.
- AURÉGAN, Y. & LEROUX, M. 2008 Experimental evidence of an instability over an impedance wall in a duct with flow. *Journal of Sound and Vibration* **317**, 432–439.
- AURÉGAN, Y., STAROBINSKI, R. & PAGNEUX, V. 2001 Influence of grazing flow and dissipation effects on the acoustic boundary conditions at a lined wall. *The Journal of the Acoustical Society of America* **109** (1), 59–64.
- AYTON, L. J. 2014 Asymptotic Approximations for the Sound Generated by Aerofoils in Unsteady Subsonic Flows. PhD thesis, University of Cambridge.
- BERS, A. 1983 Space-time evolution of plasma instabilities – absolute and convective. In *Basic Plasma Physics, Handbook of Plasma Physics, Vol. 1* (ed. A. A. Galeev & R. N. Sudan), pp. 451–517. North-Holland.
- BEYER, H. & KEMPFLE, S. 1995 Definition of Physically Consistent Damping Laws with Fractional Derivatives. *Zeitschrift Angewandte Mathematik und Mechanik* **75**, 623–635.
- BOYER, G., PIOT, E. & BRAZIER, J.-P. 2011 Theoretical investigation of hydrodynamic surface mode in a lined duct with sheared flow and comparison with experiment. *Journal of Sound and Vibration* **330**, 1793–1809.
- BRAMBLEY, E. J. 2009 Fundamental problems with the model of uniform flow over acoustic linings. *Journal of Sound and Vibration* **322**, 1026–1037.
- BRAMBLEY, E. J. 2011a Acoustic implications of a thin viscous boundary layer over a compliant surface or permeable liner. *Journal of Fluid Mechanics* **678**, 348–378.
- BRAMBLEY, E. J. 2011b Well-Posed Boundary Condition for Acoustic Liners in Straight Ducts with Flow. *AIAA Journal* **49** (6), 1272–1282.
- BRAMBLEY, E. J. 2013 Surface modes in sheared boundary layers over impedance linings. *Journal of Sound and Vibration* **332**, 3750–3767.
- BRAMBLEY, E. J. 2015 DRP schemes perform badly for decaying or growing oscillations. AIAA Paper 2015-2540.

- BRAMBLEY, E. J. 2016 Optimized finite-difference (DRP) schemes perform poorly for decaying or growing oscillations. *Journal of Computational Physics* **324**, 258–274.
- BRAMBLEY, E. J., DARAU, M. & RIENSTRA, S. W. 2012a The critical layer in linear-shear boundary layers over acoustic linings. *Journal of Fluid Mechanics* **710**, 545–568.
- BRAMBLEY, E. J., DAVIS, A. M. J. & PEAKE, N. 2012b Eigenmodes of lined flow ducts with rigid splices. *Journal of Fluid Mechanics* **690**, 399–425.
- BRAMBLEY, E. J. & GABARD, G. 2013 Time domain simulations using the Modified Myers boundary condition. AIAA Paper 2013-2218.
- BRAMBLEY, E. J. & GABARD, G. 2016 Time-domain implementation of an impedance boundary condition with boundary layer correction. *Journal of Computational Physics* **321** (321), 755–775.
- BRAMBLEY, E. J. & PEAKE, N. 2006 Classification of aeroacoustically relevant surface modes in cylindrical lined ducts. *Wave Motion* **43**, 301–310.
- BRAMBLEY, E. J. & PEAKE, N. 2008 Stability and acoustic scattering in a cylindrical thin shell containing compressible mean flow. *Journal of Fluid Mechanics* **602**, 403–426.
- BRAND, R. S. & NAGEL, R. T. 1982 Reflection of sound by a boundary layer. *Journal of Sound and Vibration* **85** (1), 31–38.
- BRIGGS, R. J. 1964 *Electron-stream Interaction with Plasmas*. MIT.
- BURAK, M., BILLSON, M., ERIKSSON, L.-E. & BARALON, S. 2008 Validation of a Time & Frequency Domain Grazing Flow Acoustic Liner Model. AIAA Paper 2008-2929.
- BURAK, M. O., BILLSON, M., ERIKSSON, L.-E. & BARALON, S. 2009 Validation of a Time- and Frequency-Domain Grazing Flow Acoustic Liner Model. *AIAA Journal* **47** (8), 1841–1848.
- CARCIONE, M. J., CAVALLINI, F., MAINARDI, F. & HANYGA, A. 2002 Time-domain modeling of constant-q seismic waves using fractional derivatives. *Pure and Applied Geophysics* **159** (7), 1719–1736.
- CRAMER, M. S. 2012 Numerical estimates for the bulk viscosity of ideal gases. *Physics of Fluids* **24** (6).
- DAI, X. & AURÉGAN, Y. 2016 Influence of shear flow on liner impedance computed by multimodal method. In *22nd AIAA/CEAS Aeroacoustics Conference*. American Institute of Aeronautics and Astronautics.
- DOAK, P. E. & VAIDYA, P. G. 1970 Attenuation of plane wave and higher order mode sound propagation in lined ducts. *Journal of Sound and Vibration* **12** (2), 201–224.
- DOKUMACI, E. 2014 On the effect of viscosity and thermal conductivity on sound propagation in ducts: A re-visit to the classical theory with extensions for higher order modes and presence of mean flow. *Journal of Sound and Vibration* **333** (21), 5583–5599.
- EVERSMAN, W. 1973 Approximation for thin boundary layers in the sheared flow duct transmission problem. *The Journal of the Acoustical Society of America* **53** (5), 1346–1350.
- EVERSMAN, W. & BECKEMEYER, R. J. 1972 Transmission of sound in ducts with thin shear layer – convergence to the uniform flow case. *Journal of the Acoustical Society of America* **52** (1B), 216–220.

- GABARD, G. 2013 A comparison of impedance boundary conditions for flow acoustics. *Journal of Sound and Vibration* **332** (4), 714–724.
- GABARD, G. 2016 Boundary layer effects on liners for aircraft engines. *Journal of Sound and Vibration* **381**, 30–47.
- GABARD, G. & BRAMBLEY, E. J. 2014 A full discrete dispersion analysis of time-domain simulations of acoustic liners with flow. *Journal of Computational Physics* **273**, 310–326.
- GREENSPAN, M. 1959 Rotational Relaxation in Nitrogen, Oxygen and Air. *Journal of the Acoustical Society of America* **31**, 155–160.
- HAIRER, E., NØRSETT, S. P. & WANNER, G. 1993 *Solving ordinary differential equations I: Nonstiff problems*. Springer-Verlag.
- HINCH, E. J. 1991 *Perturbation Methods*. Cambridge University Press, Cambridge Books Online.
- HOLM, S. & NÄSHOLM, S. P. 2011 A causal and fractional all-frequency wave equation for lossy media. *The Journal of the Acoustical Society of America* **130** (4), 2195–2202.
- INGARD, U. 1959 Influence of fluid motion past a plane boundary on sound reflection, absorption, and transmission. *Journal of the Acoustical Society of America* **31**, 1035–1036.
- INGARD, U. 2010 *Noise Reduction Analysis. Infinity Science Series*. Jones & Bartlett Learning.
- JONES, M. G., WATSON, W. R. & PARROTT, T. L. 2005 Benchmark Data for Evaluation of Aeroacoustic Propagation Codes with Grazing Flow. AIAA Paper 2005-2853.
- JOUBERT, L. 2010 Asymptotic approach for the mathematical and numerical analysis of the acoustic propagation in a strong shear flow. PhD thesis, École Polytechnique.
- KADOYA, K., MATSUNAGA, N. & NAGASHIMA, A. 1985 Viscosity and Thermal Conductivity of Dry Air in the Gaseous Phase. *J. Phys. Chem. Ref. Data* **14** (4), 947–970.
- KHAMIS, D. & BRAMBLEY, E. J. 2015 The Effective Impedance of a Finite-Thickness Viscothermal Boundary Layer Over an Acoustic Lining. AIAA Paper 2015-2229.
- KHAMIS, D. & BRAMBLEY, E. J. 2016a Acoustic boundary conditions at an impedance lining in inviscid shear flow. *Journal of Fluid Mechanics* **796**, 386–416.
- KHAMIS, D. & BRAMBLEY, E. J. 2016b Analytic model and concise impedance boundary condition for viscous acoustics in ducted shear flow. AIAA Paper 2016-2976.
- KHAMIS, D. & BRAMBLEY, E. J. 2016c Analytic solutions for the acoustics in a two-deck viscothermal boundary layer. Submitted to AIAA Journal.
- KHAMIS, D. & BRAMBLEY, E. J. 2016d Viscous effects on the acoustics and stability of a shear layer over a non-rigid wall. Submitted to J. Fluid Mech.
- KO, S.-H. 1971 Sound Attenuation in Lined Rectangular Ducts with Flow and Its Application to the Reduction of Aircraft Engine Noise. *Acoustical Society of America Journal* **50**, 1418–1432.
- KO, S.-H. 1972 Sound attenuation in acoustically lined circular ducts in the presence of uniform flow and shear flow. *Journal of Sound and Vibration* **22** (2), 193–210.
- LANDAU, L. D. & LIFSHITZ, E. M. 1987 *Fluid Mechanics*, 2nd edn. Elsevier, New York.

- MARX, D. & AURÉGAN, Y. 2013 Effect of turbulent eddy viscosity on the unstable surface mode above an acoustic liner. *Journal of Sound and Vibration* **332** (15), 3803–3820.
- MARX, D., AURÉGAN, Y., BAILLIET, H. & VALIÈRE, J-C. 2010 PIV and LDV evidence of hydrodynamic instability over a liner in a duct with flow. *Journal of Sound and Vibration* **329**, 3798–3812.
- MATHEWS, J. R., PEAKE, N. & BIANCHI, S. 2016 Asymptotic and numerical Green’s functions in a lined duct with realistic shear and swirl. AIAA Paper 2016-2922.
- MCALPINE, A., ASTLEY, R. J., HUI, V. J. T., BAKER, N. J. & KEMPTON, A. J. 2006 Acoustic scattering by an axially-segmented turbofan inlet duct liner at supersonic fan speeds. *Journal of Sound and Vibration* **294** (4–5), 780–806.
- MIKHAIL, M. N. & EL-TANTAWY, M. R. 1994 The acoustic boundary layers: a detailed analysis. *Journal of Computational and Applied Mathematics* **51**, 15–36.
- MILES, J. W. 1957 On the reflection of sound at an interface of relative motion. *The Journal of the Acoustical Society of America* **29** (2), 226–228.
- MUNGUR, P. & GLADWELL, G. M. L. 1969 Acoustic wave propagation in a sheared fluid contained in a duct. *Journal of Sound and Vibration* **9** (1), 28–48.
- MYERS, M. K. 1980 On the acoustic boundary condition in the presence of flow. *Journal of Sound and Vibration* **71** (3), 429–434.
- MYERS, M. K. & CHUANG, S. L. 1984 Uniform Asymptotic Approximations for Duct Acoustic Modes in a Thin Boundary-Layer Flow. *AIAA Journal* **22** (9), 1234–1241.
- NAYFEH, A. H. 1973 Effect of the acoustic boundary layer on the wave propagation in ducts. *J. Acoust. Soc. Am.* **54**, 1737–1742.
- NAYFEH, A. H., KAISER, J. E. & SHAKER, B. S. 1974 Effect of mean-velocity profile shapes on sound transmission through two-dimensional ducts. *Journal of Sound and Vibration* **34** (3), 413–423.
- NAYFEH, A. H., KAISER, J. E. & TELIONIS, D. P. 1975 Acoustics of Aircraft Engine-Duct Systems. *AIAA Journal* **13** (2), 130–153.
- PEAKE, N. & PARRY, A. B. 2012 Modern Challenges Facing Turbomachinery Aeroacoustics. *Annual Review of Fluid Mechanics* **44** (1), 227–248.
- PIERCE, A. D. 1994 *Acoustics*, 3rd edn. Acoustical Society of America.
- PINKERTON, J. M. M. 1947 A Pulse Method for the Measurement of Ultrasonic Absorption in Liquids: Results for Water. *Nature* **160**, 128–129.
- PRIDMORE-BROWN, D. C. 1958 Sound Propagation in a Fluid Flowing Through an Attenuating Duct. *Journal of Fluid Mechanics* **4** (4), 393–406.
- RENOU, Y. & AURÉGAN, Y. 2010 On a Modified Myers Boundary Condition to Match Lined Wall Impedance Deduced from Several Experimental Methods in Presence of a Grazing Flow. AIAA Paper 2010-3945.
- RENOU, Y. & AURÉGAN, Y. 2011 Failure of the Ingard-Myers boundary condition for a lined duct: An experimental investigation. *Journal of the Acoustical Society of America* **130** (1), 52–60.

- RIBNER, H. S. 1957 Reflection, Transmission, and Amplification of Sound by a Moving Medium. *The Journal of the Acoustical Society of America* **29** (4), 435–441.
- RICE, E. J. 1969 Propagation of Waves in an Acoustically Lined Duct with a Mean Flow. *NASA Special Publication* **207**, 345.
- RIENSTRA, S. W. 2003 A Classification of Duct Modes Based on Surface Waves. *Wave Motion* **37** (2), 119–135.
- RIENSTRA, S. W. 2006 Impedance models in time domain, including the extended helmholtz resonator model. AIAA Paper 2006-2686.
- RIENSTRA, S. W. 2007 Acoustic Scattering at a Hard-Soft Lining Transition in a Flow Duct. *Journal of Engineering Mathematics* **59** (4).
- RIENSTRA, S. W. & DARAU, M. 2011 Boundary-layer thickness effects of the hydrodynamic instability along an impedance wall. *Journal of Fluid Mechanics* **671**, 559–573.
- RIENSTRA, S. W. & VILENSKI, G. G. 2008 Spatial Instability of Boundary Layer Along Impedance Wall. AIAA Paper 2008-2932.
- SCHERER, R., KALLA, S. L., TANG, Y. & HUANG, J. 2011 The grünwald–letnikov method for fractional differential equations. *Computers & Mathematics with Applications* **62** (3), 902–917, special Issue on Advances in Fractional Differential Equations II.
- STEWART, H. J. 1942 The Energy Equation for a Viscous Compressible Fluid. *Proc Natl Acad Sci USA* **28** (5), 161–164.
- TACK, D. H. & LAMBERT, R. F. 1965 Influence of Shear Flow on Sound Attenuation in a Lined Duct. *The Journal of the Acoustical Society of America* **38** (4), 655–666.
- TAM, C. K. W. & MORRIS, P. J. 1980 The radiation of sound by the instability waves of a compressible plane turbulent shear layer. *Journal of Fluid Mechanics* **98** (2), 349–381.
- TAM, C. K. W., PASTOUCHENKO, N. N., JONES, M. G. & WATSON, W. R. 2014 Experimental validation of numerical simulations for an acoustic liner in grazing flow: Self-noise and added drag. *Journal of Sound and Vibration* **333** (13), 2831–2854.
- TESTER, B. J. 1973 Some Aspects of “Sound” Attenuation in Lined Ducts containing Inviscid Mean Flows with Boundary Layers. *Journal of Sound and Vibration* **28**, 217–245.
- TRITTON, D. J. 1988 *Physical Fluid Dynamics*. Oxford Science Publications . Clarendon Press.
- VILENSKI, G. G. & RIENSTRA, S.W. 2007 On hydrodynamic and acoustic modes in a ducted shear flow with wall lining. *Journal of Fluid Mechanics* **583**, 45–70.
- ZHANG, Q. & BODONY, D. J. 2012 Numerical investigation and modelling of acoustically excited flow through a circular orifice backed by a hexagonal cavity. *Journal of Fluid Mechanics* **693**, 367–401.
- ZHANG, Q. & BODONY, D. J. 2016 Numerical investigation of a honeycomb liner grazed by laminar and turbulent boundary layers. *Journal of Fluid Mechanics* **792**, 936–980.